

# Computational Modeling of Rupture Risk in Abdominal Aortic Aneurysms

Andreas Maier



# Computational Modeling of Rupture Risk in Abdominal Aortic Aneurysms

Andreas Maier

Bericht Nr. 16 (2012)  
Lehrstuhl für Numerische Mechanik  
Professor Dr.-Ing. Wolfgang A. Wall  
Technische Universität München

## Bibliografische Information der Deutschen Nationalbibliothek

Die Deutsche Nationalbibliothek verzeichnet diese Publikation in der Deutschen Nationalbibliografie; detaillierte bibliografische Daten sind im Internet über <http://dnb.d-nb.de> abrufbar.

ISBN 978-3-8439-1066-8

Berichte können bezogen werden über:



Lehrstuhl für Numerische Mechanik  
Technische Universität München  
Boltzmannstraße 15  
D-85747 Garching bei München  
<http://www.inm.mw.tum.de>

© Verlag Dr. Hut, München 2013  
Sternstr. 18, 80538 München  
Tel.: 089/66060798

Die Informationen in diesem Buch wurden mit großer Sorgfalt erarbeitet. Dennoch können Fehler, z.B. bei der Beschreibung des Gefahrenpotentials von Versuchen, nicht vollständig ausgeschlossen werden. Verlag, Autoren und ggf. Übersetzer übernehmen keine juristische Verantwortung oder irgendeine Haftung für eventuell verbliebene fehlerhafte Angaben und deren Folgen.

Alle Rechte, auch die des auszugsweisen Nachdrucks, der Vervielfältigung und Verbreitung in besonderen Verfahren wie fotomechanischer Nachdruck, Fotokopie, Mikrokopie, elektronische Datenaufzeichnung einschließlich Speicherung und Übertragung auf weitere Datenträger sowie Übersetzung in andere Sprachen, behält sich der Autor vor.

1. Auflage 2013

# TECHNISCHE UNIVERSITÄT MÜNCHEN

Lehrstuhl für Numerische Mechanik

## Computational Modeling of Rupture Risk in Abdominal Aortic Aneurysms

Andreas Maier

Vollständiger Abdruck der von der Fakultät für Maschinenwesen der Technischen Universität München zur Erlangung des akademischen Grades eines

Doktor-Ingenieurs (Dr.-Ing.)

genehmigten Dissertation.

Vorsitzender: Univ.-Prof. Dr.-Ing. Michael W. Gee

Prüfer der Dissertation:

1. Univ.-Prof. Dr.-Ing. Wolfgang A. Wall
2. Univ.-Prof. Dr. med. Hans-Henning Georg Ulrich Eckstein
3. Assoc. Prof. C. Alberto Figueroa, Ph.D.,  
King's College London, UK

Die Dissertation wurde am 28. Juni 2012 bei der Technischen Universität München eingereicht und durch die Fakultät für Maschinenwesen am 11. Oktober 2012 angenommen.



## Danksagung

Der Großteil dieser Arbeit wurde während meiner Zeit als Stipendiat der International Graduate School of Science and Engineering (IGSSE) der TUM am Lehrstuhl für Numerische Mechanik angefertigt. An erster Stelle möchte ich mich bei meinem Doktorvater Herrn Professor Wolfgang A. Wall für die Ermöglichung der Anfertigung dieser Doktorarbeit und das in mich gesetzte Vertrauen herzlich bedanken. Ich bin stets gern an den Lehrstuhl gekommen, was am tollen Kollegium, der Vielseitigkeit in den Forschungsthemen und nicht zuletzt auch an einer guten Mischung aus doktorväterlicher Betreuung und selbständig freiheitlicher Arbeitsweise am Institut gelegen hat. Der IGSSE und dessen Team danke ich für die Finanzierung des Forschungsprojektes und die gute Betreuung in den letzten Jahren.

Mein besonderer Dank gilt auch meinem IGSSE-Teamleiter Professor Michael W. Gee für die stets kompetente Betreuung während meiner Zeit am Lehrstuhl und die Übernahme des Prüfungsvorsitzes. Als Teamleiter konnte Professor Gee immer eine Richtung vorgeben, auch wenn wir oft genug mit unserer Forschung in bis dato wenig vertraute Themen vordringen und viele medizinische Gegebenheiten erst lernen mussten.

Weiterhin möchte ich meinem Bürokollegen Mahmoud Ismail meinen Dank aussprechen, den ich nicht nur fachlich sehr schätze, sondern der auch ein sehr guter Freund geworden ist. Hamman de Vaal danke ich für das Korrekturlesen vieler Journal-Artikel und auch dieser Arbeit. Jonas Biehler, Sebastian Kehl und Susanna Tinkl danke ich für die thematische Zusammenarbeit am Lehrstuhl und für die Übernahme vieler Aufgaben am Ende meiner Promotionszeit. Herrn Kei Müller möchte ich an dieser Stelle in seiner Funktion als sehr guter Freund erwähnen. Obwohl ich nicht alle Kollegen namentlich aufzählen kann, so gebührt mein Dank dennoch jedem, der zur Entwicklung der verwendeten FE Software oder einfach nur zu meinem Wohlbefinden am Lehrstuhl beigetragen hat. Nicht vernachlässigen will ich die Unterstützung durch meine Semestranten und Diplomanden, deren Arbeiten an verschiedenen Stellen auch in die Dissertation miteingeflossen sind.

Weiterhin möchte ich mich bei Herrn Professor Hans-Henning Eckstein, Direktor der Klinik und Polyklinik für Vaskuläre und Endovaskuläre Chirurgie am Klinikum rechts der Isar der TUM, für die Offenheit zur interdisziplinären Forschung am Aortenaneurysma und für die Übernahme der Prüfung der Dissertation bedanken.

Zu Dank verpflichtet bin ich auch den Mitarbeitern an der Klinik und Polyklinik für Vaskuläre und Endovaskuläre Chirurgie am Klinikum rechts der Isar. Hervorheben möchte ich an dieser Stelle Herrn PD Dr. Christian Reeps, der in meinen Augen nicht nur ein hervorragender Arzt ist, sondern der als Ideengeber und mit seinem unnachgiebigen Einsatz maßgeblich für die erzielten Forschungserfolge mitverantwortlich ist. Beeindruckend habe ich empfunden, dass sich Herr Christian Reeps immer Zeit für ein Gespräch mit mir genommen hat, auch wenn er gelegentlich zuvor schon 20 Stunden durchgehend operiert hat. Weiterhin möchte ich Herrn Professor Markus Essler, Frau Verena Grabher-Meier, Herrn Dr. Felix Härtl, Herrn PD Dr. Jaroslav Pelisek, Frau Dr. Julia Pongratz und Herrn Dr. Alexander Zimmermann für Ihre Unterstützung und die Zusammenarbeit auf dem Forschungsthema danken.

Herrn Professor M. L. Raghavan, Ph.D., danke ich für die freundliche Aufnahme in seine Arbeitsgruppe an der University of Iowa, Iowa City, während meines Auslandsaufenthalts in den USA und Herrn Chaid Schwarz für seine Hilfsbereitschaft und Freundschaft während dieser

## *Danksagung*

---

Zeit. Herrn Alberto Figueroa, Ph.D., danke ich für die Übernahme der Aufgaben als Prüfer im Promotionsverfahren.

Ein herzlicher Dank gebührt meinen Eltern und Geschwistern und meiner Freundin Barbara für die außeruniversitäre Unterstützung. Sie haben stets dafür gesorgt, dass ich an der Universität den Kopf für die Forschungsthemen frei hatte. Ohne ihre Rücksicht und Hilfe hätte sich die Anfertigung der vorliegenden Arbeit deutlich schwerer dargestellt.

Andreas Maier

## Abstract

An abdominal aortic aneurysm (AAA) is defined as a balloon-like dilation of the abdominal aorta of more than 3.5 cm. More than 200,000 people are affected in Germany. In case of AAA rupture, there is a terminal outcome for 90 % of these patients. However, since only 25 % of all AAAs actually rupture, combined with the fact that prophylactic surgery is associated with mortality rates of 4 %, it becomes clear that the surgeon has to balance the individual patient's risk of AAA rupture and the risk of elective surgery. So far, a maximum diameter criterion has been applied in clinical practice to identify patients at risk, which however sometimes fails to reliably predict AAA rupture. Within the current work, comprehensive experiments on mechanical properties of AAA wall, investigations on biological processes within the AAA wall measured by medical imaging techniques and sophisticated finite element (FE) simulations to determine *in vivo* acting wall stress were performed to clarify the so far poorly understood interplay of these mechanical and biological factors during AAA development. Additionally, mechanics-based indices were examined and shown to provide a more reliable AAA rupture risk prediction than the maximum diameter criterion.

The current work starts by presenting the software framework developed to automatically perform sophisticated FE analyses for patient-specific AAAs, forming part of an ever increasing, consistent AAA data base. Stringent segmentation and meshing protocols are presented. Furthermore, implications for the FE modeling are discussed in the cardiovascular setting, including the material modeling and prestressing of AAA geometries reconstructed from computed tomography (CT) images.

In order to improve current AAA risk stratification, [18F]-fluorodeoxyglucose positron emission tomography/CT (FDG-PET/CT) was investigated as a potential biomarker for non-invasive *in vivo* AAA evaluation. The role of FDG-PET/CT in the non-invasive AAA evaluation has been disputed in literature and needs to be explored in more detail. Therefore, a profound study on the interaction of mechanical AAA wall quantities and the intensity of metabolic processes as obtained by FDG-PET/CT imaging was conducted. FDG-PET/CT data sets of 52 patients were included and mechanotransduction processes in the AAA wall were investigated. A strong correlation was found between maximum von Mises stresses in the AAA wall and maximum local FDG-metabolism ( $r = 0.576$ ,  $P = 2E - 5$ ). The findings indicated that unphysiologically high mechanical stresses in the AAA wall were one trigger for mechanobiological reaction processes, which in turn caused elevated FDG-glucose metabolism. In a small number of patients, other stress-independent causes for increased mural FDG-metabolism were conceivable, which were discussed in detail.

In an approach to experimentally investigate the mechanical properties of AAA wall, 163 wall specimens from 50 patients were harvested during open surgery and investigated in uniaxial tensile tests. The mean thickness of the specimens was  $1.67 \pm 0.49$  mm with a median of 1.57 mm. Since no anisotropy was evident, the elastic behavior of the specimens was fitted to the hyperelastic, isotropic strain energy function  $W = \frac{\alpha}{6} (I_1 - 3) + \beta (I_1 - 3)^2$ . Thereby,  $\alpha$  ( $0.399 \pm 0.229$  MPa, median 0.314 MPa) and  $\beta$  ( $4.33 \pm 3.97$  MPa, median 3.11 MPa) were the fitted material parameters. The failure stretch had a mean of  $1.48 \pm 0.19$  with a median of 1.45. Failure tension and wall strength (both in terms of 1.PK stresses) were  $1.52 \pm 0.56$  MPa (median 1.42 MPa) and  $1.06 \pm 0.49$  MPa (median 0.95 MPa), respectively. Additionally, non-invasively available patient data was collected for the individual wall specimens and correlated

---

to the testing results in an attempt to explain the variations in mechanical wall properties. Wall thickness was shown to be correlated to the intensity of the FDG-metabolism at the specimen excision site, as preoperatively measured by FDG-PET/CT ( $r = 0.601$ ,  $P < 1E-9$ ). Failure properties were dependent on individual patient's medical history, where a decrease in failure tension was observed especially in patients suffering from chronic kidney disease (CKD) and in patients with increased blood test values of creatinine, potassium and urea - all of which are related to kidney malfunction. Multiple linear regression was applied to create stochastic models for the non-invasive and preoperative prediction of patient-specifically varying mechanical quantities, such as wall thickness, elastic properties, failure tension and wall strength.

In a final investigation, it was tested whether the consideration of patient-specific variations in wall thickness and failure properties via the proposed stochastic models enabled a more reliable distinction between stable and rupture-prone AAAs. Thereby, 80 non-ruptured, electively repaired AAAs and 20 ruptured AAAs were simulated and evaluated with respect to maximum AAA diameter, maximum wall stresses and maximum rupture risk indices (RRI) (considering failure tension and wall strength models). Maximum diameters of non-ruptured and ruptured AAAs differed by 27.2%. A slightly better distinction between these groups was enabled by the evaluation of maximum wall stresses under consideration of patient-specific wall stress distributions ( $\delta = 38.0\%$ ). The best distinction between non-ruptured AAAs and ruptured AAAs was achieved by the investigation of maximum RRIs, where uniform wall thickness was applied for all patients in combination with a patient-specific failure tension model. The average difference in the RRI between the two patient groups was 63.8% ( $P < 1E-5$ ).

In conclusion, this work showed that CKD should be rated as a risk factor for AAA rupture and that its inclusion can improve clinical decision making even on basis of the maximum diameter criterion. Rupture risk stratification can be improved even further by performance of patient-specific FE simulations where the most reliable rupture risk stratification was achieved for FE models with constant wall thickness in combination with a patient-specific failure tension model. Future work should also include more detailed investigations on other AAA constituents, such as the intraluminal thrombus (ILT), in which the pressure transmission phenomena from the blood lumen to the AAA wall are supposed to play a pivotal role for wall stress calculations.

# Contents

<b>1</b>	<b>Introduction</b>	<b>1</b>
1.1	Medical Background . . . . .	2
1.2	The Clinical Management Dilemma . . . . .	5
1.3	Engineering Solutions & Outline of the Work . . . . .	6
<b>2</b>	<b>From Imaging to Simulation</b>	<b>11</b>
2.1	Imaging . . . . .	11
2.2	Segmentation . . . . .	13
2.2.1	A Condensed Version of the Segmentation Protocol . . . . .	14
2.3	FE Mesh Generation . . . . .	16
2.4	Nonlinear Elasticity . . . . .	17
2.4.1	Kinematics . . . . .	17
2.4.2	Stress and Equilibrium . . . . .	19
2.4.3	Elasticity . . . . .	21
2.5	Materials . . . . .	23
2.5.1	Intraluminal Thrombus (ILT) . . . . .	23
2.5.2	Calcification . . . . .	31
2.5.3	Arterial Wall of AAAs . . . . .	46
2.6	Numerical Solution . . . . .	56
2.6.1	Boundary Value Problem . . . . .	56
2.6.2	Prestressing . . . . .	56
2.6.3	Solution and Performance Details . . . . .	58
2.7	Postprocessing . . . . .	59
<b>3</b>	<b>Some Statistical Methods</b>	<b>63</b>
3.1	Hypothesis Testing and Statistical Significance . . . . .	63
3.1.1	Hypothesis Testing . . . . .	63
3.1.2	Statistical Significance: The P-Value . . . . .	64
3.1.3	Types of Statistical Tests . . . . .	65
3.2	Regression and Outlier Detection . . . . .	68
3.2.1	Regression Analysis . . . . .	68
3.2.2	Outlier Detection . . . . .	70
<b>4</b>	<b>Mechanotransduction in Abdominal Aortic Aneurysms</b>	<b>75</b>
4.1	FDG-PET/CT Imaging for Engineers . . . . .	76
4.2	Literature Review . . . . .	77
4.3	Correlation of Metabolic Activity to Biomechanical Loading . . . . .	85

4.3.1	Methods	85
4.3.2	Results	89
4.3.3	Discussion	93
4.4	Conclusion - Mechanotransduction in AAA	96
<b>5</b>	<b>Mechanical Testing of AAA Wall</b>	<b>99</b>
5.1	Methods	100
5.1.1	Study Population and Tissue Sampling	100
5.1.2	Mechanical Testing	102
5.1.3	Assessment of Testing Results	103
5.1.4	Non-invasively Assessable Explanatory Variables	105
5.2	Tensile Test Results	108
5.3	Simple Regression	109
5.3.1	Regression Results	110
5.3.2	Interpretation and Discussion of the Results	120
5.4	Normal Abdominal Aortic (AA) Wall	125
5.4.1	Tensile Test Results for Normal AA Wall	125
5.4.2	Comparison between AAA Wall and Normal AA Wall	127
5.4.3	Interpretation and Discussion	130
5.5	Multiple Regression	132
5.5.1	Methods	132
5.5.2	Results	133
5.5.3	General Discussion of Multiple Linear Regression Models	146
5.6	Conclusion	147
<b>6</b>	<b>Incorporating Testing Results into FE Analysis of Patient-Specific AAAs</b>	<b>149</b>
6.1	Methods	149
6.1.1	Study Population	149
6.1.2	AAA Geometry Reconstruction, Model Variations and FE Analysis	150
6.1.3	Statistical Evaluation	151
6.2	Results	152
6.3	Discussion	152
6.3.1	Interpretation of the Results	152
6.3.2	Limitations	154
6.4	Conclusion	155
<b>7</b>	<b>Conclusion and Outlook</b>	<b>157</b>
<b>A</b>	<b>Appendix: Segmentation</b>	<b>159</b>
A.1	Structure of the AAA Data Base	159
A.2	Segmentation Protocol	159
A.3	Meshing Protocol	164
<b>B</b>	<b>Appendix: Biomechanics and PET/CT</b>	<b>167</b>
	<b>Bibliography</b>	<b>171</b>

# Nomenclature

## Mathematical styles, operators and symbols

$c$	style for a scalar value
$\mathbf{x}$	style for vectors and tensors
$\bar{\mathbf{S}}$	style for a tensor in Voigt notation
$\mathbf{0}$	zero tensor
$\mathbf{1}$	identity tensor
$\otimes$	dyadic product
$\frac{\partial}{\partial(\cdot)}$	partial differentiation with respect to $(\cdot)$
$\det$	determinant
$\operatorname{div}$	spatial divergence operator
$\operatorname{Div}$	material divergence operator
$\operatorname{Grad}$	material gradient
$\lim$	limes
$\operatorname{tr}$	trace

## Nonlinear continuum mechanics

$a, A$	area in deformed/reference configuration
$\mathbf{b}, \mathbf{C}$	left, right Cauchy-Green deformation tensors
$\mathbf{C}$	material tangent
$\mathbf{d}$	displacement vector
$\mathbf{e}$	Euler-Almansi strain tensor
$\mathbf{E}$	Green-Lagrange strain tensor
$\mathbf{F}$	deformation gradient
$I_j, \bar{I}_j$	j-th principal invariant, j-th modified invariant
$J$	Jacobian
$\mathbf{m}, \mathbf{M}$	principal axes in deformed/reference configuration
$\mathbf{n}, \mathbf{N}$	surface normal vector in deformed/reference configuration
$p, p_0$	hydrostatic pressure in deformed/reference configuration
$\mathbf{P}$	first Piola-Kirchhoff stress tensor
$\mathbf{Q}, \mathbf{R}$	rotation tensors
$\mathbf{S}$	second Piola-Kirchhoff stress tensor
$\mathbf{t}$	traction vector
$\mathbf{U}, \mathbf{v}$	right and left stretch tensor
$v, V$	volume in deformed/reference configuration
$W, W_{iso}, W_{vol}$	strain energy, isochoric contribution, volumetric contribution

$\mathbf{x}, \mathbf{X}$	position in deformed/reference configuration
$\lambda_i$	principal stretches
$\boldsymbol{\sigma}$	Cauchy stress tensor
$\Omega, \Omega_0$	deformed/reference configuration
$\partial\Omega, \partial\Omega_0$	boundary of deformed/reference configuration
$\chi$	mapping from reference to deformed configuration

### Physical quantities

$c, c_1, c_2, c_i$	(isotropic) material parameters
$D_1, D_2$	(isotropic) material parameters
$E$	Young's modulus/referential stiffness
$G$	shear modulus (linear elasticity theory)
$HU$	radiodensity, attenuation coefficient (Hounsfield Units)
$P_{max}$	wall strength (1.PK stress)
$t$	wall thickness
$T_{max}$	failure tension (1.PK stress)
$T_{max,Cauchy}$	failure tension (Cauchy stress)
$k_1, k_2, k_3$	(anisotropic) material parameters
$\alpha, \beta$	(isotropic) material parameters
$\alpha_{HU}$	HU-dependent material parameters
$\beta$	numerical parameter
$\kappa$	bulk modulus
$\mu$	shear modulus (nonlinear elasticity theory)
$\nu$	Poisson's ratio
$\rho$	fiber dispersion parameter
$\sigma_{max}$	wall strength (Cauchy stress)

### Statistics

$\bar{x}$	style for mean values
$\hat{y}$	style for fitted values
$A, B, D$	samples
$CD$	Cook's Distance
$f$	number of degrees of freedom
$H_0, H_1$	null hypothesis, alternative hypothesis
$\mathbf{H}, h_{ii}$	hat matrix, leverages (diagonal entries of $\mathbf{H}$ )
$n$	sample size, number of observations
$p$	number of parameters
$P$	P-value

$r$	Pearson's product-moment correlation coefficient
$\mathbf{r}$	residual
$R^2$	coefficient of determination
$s$	sample standard deviation, standard error
$s^2$	sample variance
$sd$	standard deviation, standard error
$t$	test statistic
$t_i$	studentized residual
$\mathbf{x}, \mathbf{X}$	independent (explanatory) variable, design matrix
$\mathbf{y}$	dependent (response) variable
$\alpha$	significance level
$\beta$	regression coefficients/parameters
$\delta$	difference in expectations
$\mu$	expectation of a distribution

**Abbreviations**

1Q, 3Q	first/third quartile
AA	(healthy) abdominal aorta
AAA	abdominal aortic aneurysm
ACE	angiotensin-converting-enzyme
ASA	acetylsalicylic acid
CD	Cook's distance
CHD	coronary heart disease
CKD	chronic kidney disease
CT	computed tomography
DM	diabetes mellitus
EVAR	endovascular aortic repair
FDG	fluorodeoxyglucose
FE	finite element
IA	inverse analysis
ILT	intraluminal thrombus
hsCRP	high-sensitivity C-reactive protein
HU	Hounsfield Units
LS	least squares
MMP	matrix metalloproteinase
MRI	magnetic resonance imaging
MSE	mean square error
MTM	mean tangential modulus
MULF	modified updated Lagrangean formulation
NORD	normalized diameter
PET	positron emission tomography
PK	Piola-Kirchhoff
PVD	peripheral vascular disease
ROI	region of interest
RPI	rupture potential index
RRI	rupture risk index
R&V	Raghavan & Vorp
SEF	strain energy function
SEM	standard error of the mean
SMC	smooth muscle cell
SUV	standardized uptake value
TAA	thoracic aortic aneurysm

# 1 Introduction

“The patient’s rapid recovery made me think that the surgery for aortic aneurysm may become infinitely simple.”

- Sir Astley Cooper, 1817

Physician Sir Astley Cooper commented on his patient Charles Hutson after the first surgery of an aortic aneurysm in 1817. The patient died 48 hours after surgery [25].

“I want to go when I want. It is tasteless to prolong life artificially. I have done my share, it is time to go. I will do it elegantly.”

- Albert Einstein, April 15, 1955

Albert Einstein was one of the most famous AAA patients and victims. He underwent a first surgery of his large aneurysm in 1948. Six years later, assumedly on April 12, 1955, his aneurysm started leaking. Physicians advised immediate surgery, which he refused saying the above words. Albert Einstein died on the morning of April 18, 1955 [30].

Cardiovascular incidents are responsible for about 45 % of deaths for men who die between the age of 65 to 74 years. Thereby, ischaemic heart disease, stroke and *abdominal aortic aneurysm* (AAA) related deaths are the three major causes of death [186]. What most cardiovascular diseases (e.g. atherosclerosis, coronary heart disease, carotid artery stenosis, existence of an AAA) have in common is that they can be easily diagnosed, while the associated risk for the patient to suffer from a potentially fatal incident remains difficult to predict. Furthermore, prophylactic surgical interventions are costly and sometimes more dangerous for the patient than the disease itself. Consequently, patients at risk of a cardiovascular incident need to be identified and treated, whereas the other patients should not be exposed to the risks of unnecessary surgeries. The process of identifying patients at risk is known as *risk assessment* or *risk stratification*. However, clinical decision making for or against elective interventions is often based on empirical statistics and does not always meet the individual patient's circumstances. Pathophysiological processes present during the development of a cardiovascular disease and biological reactions of the affected vessel differ between individual patients. A better understanding of patient-specific pathophysiological processes would improve risk assessment and ensure that the individual patient receives the most appropriate therapy. In recent years, the efforts on this issue have become a field of interdisciplinary research between the established medicine and innovative engineering sciences. Engineering approaches include the application of fluid and structural continuum mechanics principles in the formerly purely medical problems. Examples are the role of wall shear stress in the development of atherosclerosis and stenoses or the consideration of tensile stresses in atherosclerotic plaque rupture or aneurysm rupture.

The presented work aims to bridge the gap between classical medicine and engineering mechanics, although more emphasis is put on the engineering side. The focus of this work is the mechanical evaluation of the abdominal aortic aneurysm. The current chapter starts by giving some medical background on AAAs and explains the dilemma of decision making after AAA diagnosis in more detail. In a brief outlook on the current work, it finally lists some ideas how engineering science can contribute to alleviate the clinical management dilemma of AAAs and how engineering approaches may help to better understand the pathogenesis and development of AAAs.

## 1.1 Medical Background

### Epidemiology

The AAA is a permanent dilation of the abdominal aorta as a consequence of a preceding wall degeneration. The presence of an AAA can lead to rupture of the aorta with a terminal outcome for most patients. In case of rupture, 90 % of the patients die before reaching the hospital. Mortality rates for patients with ruptured AAA being treated operatively vary from 35 % to 70 % [151]. The prevalence of AAAs with a diameter of more than 3 cm is about 5 % within male population over 65 years [186] and up to 10 % within male population over 80 years [31]. About 30 % of the AAAs have a maximum diameter larger than 4.5 cm [186]. In Germany, more than 200,000 people have an AAA with a maximum diameter of 3.5 – 4 cm or more [46]. Due to the high prevalence and high rupture mortality, AAA related deaths are among the leading causes of death in western societies.

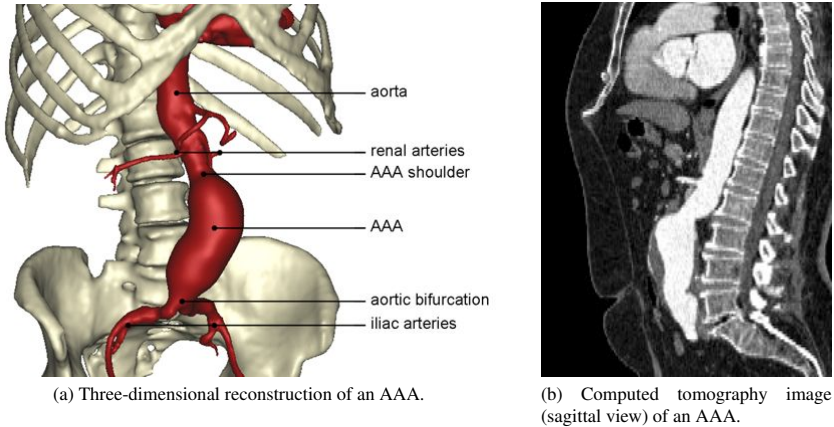


Figure 1.1: Infrarenal abdominal aortic aneurysm.

### Classification

The AAA is the most common form of aortic aneurysms, where the dilation affects the aorta distal to diaphragm. Dependent on the location of the AAA, it is distinguished between:

**Infrarenal AAA**, where the proximal AAA shoulder lies distal to the renal artery bifurcation, see Figure 1.1. This is the most common form of AAAs (~90% of all AAAs, [79]).

**Suprarenal AAA**, where the complete AAA is located proximal to the renal artery bifurcation.

**Juxtarenal AAA**, where the AAA starts proximal to the renal artery bifurcation and ends between the renal artery bifurcation and the aortic bifurcation into the iliac arteries.

As opposed, the thoracic aortic aneurysm (TAA) affects the ascending aorta, the aortic arch and/or the descending thoracic aorta. It occurs more infrequently. Other predilection sites for aneurysms are the iliac arteries and the popliteal arteries. Another morphological differentiation between AAAs that is very famous among physicians, but which is often poorly understood by engineers, is the **fusiforme** (cylindrical, symmetrical) and the **sacciforme** AAA (e.g. eccentric bulges).

The formation of an AAA only occurs as a consequence to a preceding degeneration of the aortic wall. In case of a **false** aneurysm, the degeneration can be a tear in the intima or a mechanical separation of the different layers of the aorta (*tunicae intima, media* and *adventitia*), with subsequent hemorrhage into the vessel wall [205]. Such a mechanical separation can be caused by e.g. an aortic dissection, where the separation mainly occurs at the middle third of the *tunica media* of the aortic wall [32]. These aneurysms are sometimes also called *dissecting* aortic aneurysms. Most AAAs, however, are **true** aneurysms, where all the wall layers are

mechanically intact. In these cases, a change in the microstructural composition of the wall leads to a structural degeneration. In most cases, but not exclusively, the initial degeneration is a reduction of the amount of elastic fibers (elastin) [24, 78], which are mainly found in the *membrana elastica interna* (a layer between the intima and the media) and within the media of a healthy artery [55]. The loss of elastin has been associated with a change of the prestretch in the remaining wall constituents [232], which are mainly smooth muscle cells and collagen. Continuous collagen remodeling, sometimes in combination with overcompensatory collagen net production [15], can subsequently lead to AAA growth. Other causes for the imbalance in the microstructural composition of arterial wall are e.g. Marfan syndrome (connective tissue disorder) or Ehlers-Danlos syndrome (deficient type I and III collagen synthesis) [159]. The latter two examples are genetic disorders, where fatal consequences often occur at a young age. In these cases, the clinical decision making is mostly unambiguous. Otherwise, the AAA mainly occurs in the elderly population, where accumulated risk factors drive the development of an AAA. Known risk factors for the development of a true AAA are male sex, age, smoking, hypertension and hypercholesterolemia [52]. To make matters worse, the risk factors of AAA development only barely overlap with the risk factors of AAA rupture, which are female sex, AAA diameter and hypertension, but not male sex or age [204].

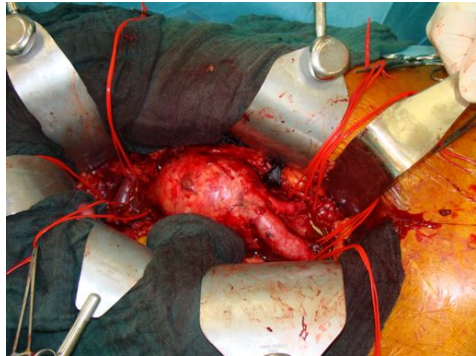
### Clinical Presentation

A clinically important differentiation is made between **asymptomatic** (about 80 % of all clinical presentations), **symptomatic** (5 – 10 %) and **ruptured** AAAs (10 – 15 %). The ruptured AAA is a clinical emergency. But also symptomatic AAAs necessitate an urgent clinical intervention. They are characterized by sudden onset of abdominal pain and aortic pressure pain (other potential painful abdominal or thoracic disorders need to be excluded). If left untreated, symptomatic AAAs are known to have a rupture probability of 90 % within two years following diagnosis [149]. Since most AAAs are asymptomatic, their diagnosis is often an incidental finding, although recently, ultrasound (US) screening programs for elderly people have increasingly been performed [45, 186]. Screening programs benefit from the fast and inexpensive US techniques used to reliably detect and monitor AAAs [126, 136]. Once detected, monitoring and, if a certain size is approaching or rapid growth is seen on serial US images, elective therapy is the clinical standard for the asymptomatic AAAs. In the case of elective therapy, computed tomography (CT) (Figure 1.1 (b)) or magnetic resonance imaging (MRI) remains inevitable to confirm the diagnosis and to plan the surgery [212].

### Surgical Treatment

Since the beginning of successful operative treatments, the conventional open AAA repair has been the gold standard for operative therapy of non-ruptured and ruptured AAAs. In general, transabdominal access to the AAA (Figure 1.2) is used to suture a prosthesis to the nondilated aorta and the iliac arteries in order to bridge the affected segment of the aorta. The open AAA repair is a highly invasive technique, however, it enables the surgeon to adjust the operative technique to the actual *in situ* anatomical conditions, which might not have been correctly interpreted from CT data. After a successful surgery, the prosthesis usually serves the patient to the end of his life. Potential early complications include myocardial, visceral and limb ischaemia,

Figure 1.2: Situation during conventional open repair of a non-ruptured AAA. Transabdominal access is used to reach the AAA. A prosthesis (not shown in this picture) will be used to bridge the affected segment of the aorta.



as well as renal failure, due to embolic complications. Life-threatening long term complications can be wound and graft material infections [11].

In the early nineties, endovascular aortic repair (EVAR) was introduced as a less invasive surgical therapy and as an alternative to conventional open surgery with the potential to reduce mortality and morbidity for both elective and emergency repair. During EVAR, an endograft composed of a fabric graft and a metal stent is delivered transluminally to exclude the AAA from blood flow and pressure [180]. The EVAR technique demands precise quantitative preoperative planning to decide on patient eligibility and for the choice of the correct device. Patient eligibility requires a nondilated, thrombus-free infrarenal neck for endograft attachment and excludes kinks  $> 75^\circ$  in the iliac arteries that could hinder delivery. Different studies showed patient eligibility ranging from 30 % to slightly more than 50 % [184]. Major complications with EVAR can be occlusion of renal, mesenteric or iliac arteries, as well as endoleaks that can hamper the proper AAA exclusion and again lead to a state susceptible to secondary rupture [180, 184].

In summary, neither of the two elective therapies is without potential risk. According to the largest randomized control trial performed by Greenhalg *et al.* [71], open surgical intervention is related to a 30-day perioperative all-cause mortality of approximately 4.0 % and EVAR to 1.7 %.

## 1.2 The Clinical Management Dilemma

Considering that asymptomatic AAAs can be stable for the patient's lifetime and that only 25 % of all AAAs actually rupture [34], the dilemma of clinical decision making for or against elective therapy becomes clear: There is a large number of patients with asymptomatic AAA, whereas only few of them are at risk of rupture. On the other hand prophylactic elective therapy is related to a significant mortality and morbidity. Consequently, physicians have to balance the risk of AAA rupture with the risk of elective therapy. Most commonly, the simple but well evaluated maximum diameter criterion, often complemented by parameters of AAA morphology and growth rate, is used in clinical practice to identify patients at risk of AAA rupture. The maximum diameter criterion is based on empirical studies, which have shown that the risk of

AAA rupture increases with the maximum diameter of the AAA [45, 151, 204]. For a certain threshold of the AAA diameter (mostly 5.5 cm), the annual risk of rupture then exceeds the average perioperative mortality of elective therapy. From a statistical point of view, the patient then benefits from elective therapy, giving indication for surgery.

However, some AAAs rupture below the well accepted maximum diameter thresholds. Scott *et al.* [187] report a maximum potential rupture rate of 2.1 % per year for AAAs with a maximum diameter between 3.0 cm and 4.4 cm and a maximum potential rupture rate of 10.2 % for AAAs with a maximum diameter between 4.5 cm and 5.9 cm. Other studies report even higher rupture rates of 12.8 % for AAAs with a maximum diameter below 5.0 cm [34], whereas AAAs with a maximum diameter of more than 5.0 cm are stable in 60 % of all cases. Consequently, improvements to the well established diameter criterion are necessary or, alternatively, novel and more precise methods to predict AAA rupture need to be introduced to support clinical decision making for or against elective therapy.

### 1.3 Engineering Solutions & Outline of the Work

Mechanically, the maximum diameter criterion is based on the Law of Laplace, which states a linear relationship between lumen diameter and wall stress for cylindrical geometries with constant wall thickness under luminal pressure. Not surprisingly, the Law of Laplace fails to predict realistic loading for more complex geometries, such as AAAs [171].

A promising approach for a more patient-specific rupture risk estimation which has emerged within the last decade, is based on biomechanical determinants such as stress distribution and strength of the AAA wall. Basic mechanical knowledge indicates that rupture occurs when wall stress exceeds wall strength. In this regard, non-invasive computational approaches based on patient-specific AAA geometry reconstruction from medical images and finite element (FE) analysis have increasingly been performed to calculate the stresses acting in the vessel wall. Contrary to the diameter criterion following the law of Laplace, the FE method enables consideration of patient-specific complex AAA morphology and interplay of different constituents such as intraluminal thrombus (ILT), calcification and the diseased arterial wall. Probably the first noteworthy approaches of non-invasive computational FE analysis to compute AAA wall stresses were thereby presented by Inzoli *et al.* [106], Mower *et al.* [147], Raghavan & Vorp (R&V) [164] and Fillinger *et al.* [48, 49], while a potentially variable wall strength was not yet considered. Nevertheless, it was shown in [48], and later on by Truijers *et al.* [211] or Heng *et al.* [82], that the evaluation of the maximum wall stresses already allowed for a better distinction between rupture-prone and stable AAAs than the maximum diameter criterion. Since then, computational FE analyses of AAAs have been gradually enhanced. Examinations on thrombus effects [41, 63, 231], calcifications [125, 132, 195], prestressing methods [38, 64, 66, 128, 129] or surrounding tissue [60, 145] have helped to obtain increasingly realistic simulation results. Nevertheless, the proper consideration of all these different modeling assumptions in nonlinear FE analysis is still under discussion in literature [131, 169]. Chapter 2 of the current work is devoted to a more detailed literature review of this topic. It also illustrates the workflow necessary to create an up-to-date FE model of an AAA and to perform a wall stress analysis using the FE method, as it will be performed multiple times throughout the course of the presented work. The focus is thereby on structural approaches to estimate the rupture risk of AAA configura-

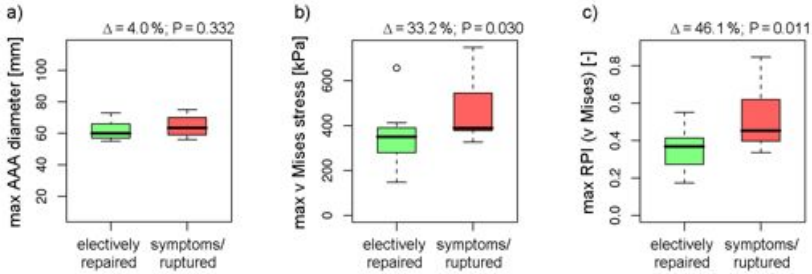


Figure 1.3: A success story for engineering principles in AAA risk stratification: Comparison of a) diameter criterion, b) maximum wall stress and c) maximum RPI between diameter matched groups of electively repaired ( $n = 13$ ) and symptomatic or ruptured AAAs ( $n = 12$ ).  $\Delta$ -values on top of the diagrams indicate the relative difference of the means with respect to the group of electively repaired AAAs. Pictures adapted from Maier *et al.* [133].

tions at the time of imaging. Growth and remodeling simulations [102, 239] or fluid-structure interactions (FSI) [65, 236] are not in the focus of this work. The reader is specifically referred to [203] for detailed investigations of these topics omitted here. With regard to the neglect of FSI in AAAs, however, it was shown in [122] that FSI and purely structural approaches lead to similarly good stress results to be used in the status quo rupture risk prediction for given AAA geometries.

Another reason why the diameter criterion sometimes fails to properly predict rupture is that it does not consider patient-specific variations of wall composition, degradation or stability, which are associated with AAA formation. Unfortunately, much less is known about AAA wall strength as opposed to wall stress calculations. Only one reasonable contribution on spatial wall strength distribution by Vande Geest *et al.* [222] could be found in literature. Therein, local thrombus thickness, local AAA diameter, AAA family history and sex were identified to have statistically significant influence on AAA wall strength. These quantities were then used to design a stochastic model for the non-invasive prediction of patient-specific wall strength distributions. Vande Geest *et al.* [222] also defined the quotient of wall stress and strength as the *rupture potential index (RPI)*. Later on, this stochastic strength model was used by other groups [62, 104, 118, 133, 218] to investigate whether the RPI could help to more precisely identify rupture-prone AAAs. Thereby, the two largest investigations by Gasser *et al.* [62] and Maier *et al.* [133] came to surprisingly similar results and conclusions. Whereas the diameter criterion completely failed to identify rupture-prone AAAs from diameter matched subgroups of electively repaired AAAs and ruptured AAAs per definition, maximum wall stresses and maximum RPIs were statistically significantly higher in the groups of ruptured AAAs (maximum wall stresses:  $\Delta = 17\%$ ,  $P = 0.021$  in [62] and  $\Delta = 33.2\%$ ,  $P = 0.030$  in [133]; maximum RPI:  $\Delta = 43\%$ ,  $P = 0.016$  in [62] and  $\Delta = 46.1\%$ ,  $P = 0.009$  in [133]). Selected results obtained by Maier *et al.* [133] are shown in Figure 1.3. Both studies concluded unanimously that the inclusion of wall strength reinforces rupture risk indices derived from computational FE models. What the term “statistically significant” or the P-value actually mean is dealt within

Chapter 3. Statistical test methods to check whether one approach yields significantly different results from a second approach (“hypothesis testing”) are discussed. Moreover, Chapter 3 also deals with regression methods and outlier detection used for the derivation of stochastic models as e.g. performed in the above-mentioned work by Vande Geest *et al.* [222].

Nevertheless, despite the promising outcomes of the above mentioned computational studies, the application of a wall-stress criterion or a RPI criterion to support the clinical decision making is a long way from everyday clinical practice. One problem is the missing of a standardized procedure for the AAA model generation and the performance of the FE analysis between different research groups. However, another more important point is that patient-specificity, especially with regard to mechanical properties and biological processes within the AAA wall, is still lacking in computational FE models. Consequently, the proper consideration of patient-specific variations in mechanical AAA wall properties and biological processes by means of non-invasive techniques would be essential to improve rupture risk stratification. In this regard, [18F]-fluorodeoxyglucose positron emission tomography/CT (FDG-PET/CT) has attracted the interest of physicians as a potential non-invasive biomarker for *in vivo* evaluation of AAAs [114, 168, 179, 210]. FDG-PET/CT is used to measure the (FDG-)glucose metabolism within the patient and therewith it provides data on the intensity of biological processes within the AAA vessel wall. In the first clinical studies, a large variation in the intensity of the FDG metabolism in AAA wall was observed between patients, where an increased metabolic activity was associated with inflammation [39, 169], rapid AAA expansion and rupture risk [168, 179, 210]. Thereby, it has also been hypothesized that increased FDG metabolism may be caused by unphysiologically high wall stresses through mechanotransduction processes [130, 237]. However, the histopathological changes [51] and consequently the clinical implications for patients with increased FDG metabolism are not undisputed [113]. In order to shed light on this discussion, a profound study on the interaction of mechanical quantities as obtained by FE analysis and the metabolic activity as measured by FDG-PET/CT is performed in Chapter 4. Thereby, the chapter starts with a short introduction of PET/CT imaging from an engineering perspective. A thorough literature review is performed and already existing approaches to assess the mechanotransduction processes in AAAs are presented. Finally, a comprehensive study on the correlation of mechanical quantities to metabolic activity in the AAA wall is conducted for the statistically relevant number of 50 patients.

Interestingly, the presence of variations in wall degradation, intensity of metabolic processes and consequently in the mechanical properties (AAA wall thickness, elastic properties and failure properties) is known - but has so far not been addressed sufficiently. The standard FE simulation of an AAA found in literature still uses the assumption of population-averaged, uniform material properties for the AAA wall. This applies most of all to the assumption of uniform wall thickness and uniform parameters for the hyperelastic material model. The main issue in this regard is that experimental studies usually only report the mean and median values for the mechanical AAA wall properties, complemented by confidence intervals, standard errors or standard errors of the mean. However, the proper measuring and modeling of the observed variations to be used for preoperative prediction of patient-specific variations of mechanical AAA wall properties, e.g. as done for the stochastic model for wall strength prediction in [222], is scarce. Consequently, non-invasive prediction of patient-specific variations in AAA wall properties is still an unsolved problem of realistic rupture risk stratification, as also stated in e.g. [21, 101, 203]. Thus, the prediction of spatial and patient-specific changes of mechanical AAA

wall properties, based on clinically available data, would be an essential contribution to a more reliable rupture risk prediction. The measuring and modeling of such patient-specific changes in AAA wall properties is the topic of Chapter 5. In preparation for this chapter, AAA wall specimens were harvested from 50 patients during open AAA surgery and thickness, elastic properties and failure properties of the specimens were measured in uniaxial tensile tests. Additionally, a set of non-invasively assessable patient-specific parameters was acquired for each specimen. Experimental results from uniaxial tensile tests were then correlated to these parameters. Significant parameters were identified and regression models were generated to be used for non-invasive prediction of patient-specific distributions of mechanical AAA wall properties. In Chapter 6, these regression models are applied in FE simulations of 100 AAA patients in order to check for their validity and to investigate whether these enable a more reliable distinction between rupture-prone and stable AAAs.

Chapter 7 concludes with a summary of the key findings and open questions left by the present work. Finally, some potential directions for future research are suggested that might help to further improve AAA rupture risk prediction and promote computational FE analysis of AAAs as a tool to support physicians in clinical decision finding.



## 2 From Imaging to Simulation

As already introduced in the previous chapter, FE simulation of patient-specific AAAs is a promising approach for a more reliable AAA rupture risk stratification [48, 62, 133]. In general, a realistic FE simulation of an AAA requires detailed information about the patient-specific AAA morphology, the different AAA constituents and their material properties, complemented by adequate boundary conditions and nonlinear modeling theories. The aim of the current chapter is to explain the workflow to perform such a FE simulation, which is briefly depicted in Figure 2.1:

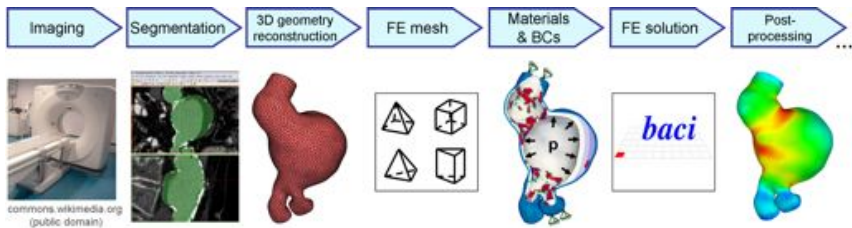


Figure 2.1: Illustration of the workflow for a FE simulation of an AAA, starting with the imaging in the hospital until the postprocessing of the results.

One peculiarity in this project was introduced by the large number of AAAs that were investigated in the present work. This required methods that ensured consistency and quality for all the AAAs models and allowed for automatization of individual steps. In the current work, a batch process was created that included automated assignment of the boundary conditions and material parameters, the numerical solution and the postprocessing of the simulation results. This, however, also means that the image segmentation and the meshing still needed to be done manually. Stringent protocols for these steps were necessary in order not to introduce operator bias. The use of the batch process further introduced some flexibility to the simulation procedure (e.g. quick changes to material parameters and wall thickness, etc.) with subsequent automatic recalculation of results. All the steps, whether manually performed or automated, are explained in the following sections.

### 2.1 Imaging

For patients diagnosed with AAA, the diameter of the AAA is usually monitored using ultrasound. In case the diameter reaches a critical threshold, contrast enhanced CT images are commonly acquired to plan the surgery. Medical imaging data utilized in this work was provided by the university hospital Rechts der Isar of the Technische Universität München. CT was

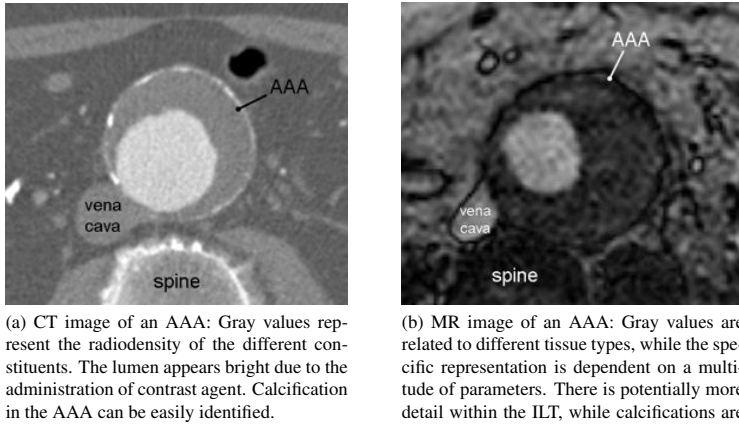


Figure 2.2: Examples of transversal CT/MR images of AAA patients.

most frequently used for the patients included in the present work. MRI was less frequently used and was commonly reserved to AAA patients with intolerance against the contrast agent administered for CT imaging. Basically, both imaging routines can be used in the modeling chain, whereas there are specific advantages and disadvantages for each modality (concerning both the patient and the simulation workflow).

In CT images, regions and organs of the human body can be differentiated based on the *Hounsfield Units* (HU). The HU is a measure for the attenuation of X-rays (=radiodensity) of the imaged material. The radiodensity is a physical quantity of the material and consequently the image information is always the same independent of the CT scanner utilized. Typically, the HU for the human body ranges from  $-1000$  HU for air to about  $3075$  HU for tooth enamel [14]. The image resolution that was almost consistently available for all patients was in the order of  $0.6$  mm. The drawbacks of this imaging modality are the low soft tissue contrast (especially without administration of contrast agent) and that the patient is exposed to harmful radiation. An extract of a CT image of an AAA patient is given in Figure 2.2 (a).

MRI makes use of the principle of nuclear magnetic resonance, a magnetic alignment of atomic nuclei (mainly hydrogen nuclei, protons) under the influence of a strong static magnetic field, the precession of these nuclei when exposed to resonant radiofrequency pulses and a time-delayed realignment (relaxation) of the nuclei creating a measurable radiofrequency signal. Relaxation times of nuclei are dependent on chemical compositions and neighboring molecules, which vary for different tissue types and can be used for the creation of images. MRI comes with the advantage that the patient is not exposed to harmful radiation. Flexible scanner settings can be adapted to enhance the contrast between different aspects of soft tissues or even to visualize the blood flow (velocity encoded phase-contrast MRI) [111, 214]. However, this also means that the MR image information is not consistent over different scanners or scanner settings. MR imaging usually comes with longer scanning time than CT. Images itself are often at lower

resolution and prone to artifacts. Calcification is often hardly visible, but there is potentially more detail available for the intraluminal thrombus. Neither CT nor MRI can be used to assess material properties of any of the AAA constituents directly or can be used to reliably detect the AAA wall thickness [21]. An example of a MR image of an AAA patient is given in Figure 2.2 (b).

## 2.2 Segmentation

“Segmentation” is the partitioning of medical images (CT or MRI), into different anatomical structures. Resulting masks from the segmentation in a stack of 2D images can be used to calculate 3D reconstructions of the geometries. In this work, the goal was to derive the 3D reconstructions of the AAAs and, ideally, also the different constituents, which are the blood lumen, intraluminal thrombus (ILT), calcifications and the AAA wall. The following explanations refer to CT images, which were provided for the majority of the patients in this study. In CT images without prior administration of contrast agent, the blood lumen features an attenuation of 20 HU to 40 HU [76]. The attenuation of the blood, and therewith the contrast to surrounding tissue or ILT (28 HU to 45 HU), is increased by administration of contrast agent (contrast enhanced blood: approximately 150 HU to 500 HU). Calcifications range from about 200 HU [37] to 1000 HU. The AAA wall, or the arterial wall in general, features an attenuation which is close to the attenuation of non-contrast enhanced blood, ILT or surrounding tissue. This issue together with the circumstance that available CT resolution is close to wall thickness dimensions, makes a segmentation of the AAA with reliable wall thickness reconstruction impossible [21, 43, 49, 143, 169]. Approaches for wall thickness reconstruction have been presented in [139, 189], which however are elusive. The assumption of an idealized, non-patient-specific wall thickness is consequently the standard in literature [49, 60, 62, 196, 211]. Still, it is clear that knowledge on the actual, patient-specific AAA wall thickness is important for the determination of realistic wall stress distributions or for rupture risk prediction in general. This is also a major topic of the present work which will be elaborated upon in Chapter 5. To start with, the rest of this present section deals with the segmentation of the lumen and the ILT, while an idealized AAA wall is assumed at this stage. A practical method of including calcification in FE models is explained in Section 2.5.2.

Generally speaking, it would be desirable to have an automated segmentation method for the reconstruction of the AAA geometries. This would not only help to get rid of the tedious manual interaction, but would also lead to operator-independent, consistent segmentation results. Studies have shown that manual segmentation of the same AAA performed by different operators can lead to non-negligible variations in the results [197]. Nevertheless, the fact that every AAA features a somehow individual morphology, prevents a fully automated segmentation process and is the reason why no algorithm or software exists that can reliably extract any arbitrary AAA geometry without user intervention. Even in the company M2S Inc. (West Lebanon, NH, USA), which has collected and evaluated medical images of more than 200,000 aortic aneurysms for clinical trials or preoperative planning, manual segmentation is still seen as the most reliable way of AAA geometry reconstruction [from personal conversation with Prof. ML Raghavan, University of Iowa, IA, USA, Sept. 2011]. Nevertheless, there are possibilities and approaches that convey mechanical principles to image segmentation in order to obtain at

least semi-automated segmentation methods that minimize user intervention as e.g. proposed in [4] and incorporated in the commercial software A4clinics (Vascops GmbH, Vienna, Austria). The good intra and inter-operator reproducibility of the results using such semi-automated methods was shown in [104]. Analogously, to obtain segmentation results as reproducible as possible, a detailed segmentation protocol was developed for application in the present work. As far as possible, the protocol makes use of unambiguous automated software functions. For all the AAAs dealt within the present work, segmentation and 3D geometry reconstruction were performed using the commercial software Mimics (Materialise, Leuven, Belgium). The following descriptions are especially based on the workflow as performed in this software, but can be likewise conveyed to other image segmentation software (e.g. Matlab (The MathWorks Inc., Natick, MA, USA), the open source software packages 3D Slicer (<http://www.slicer.org>) or Seg3D (SCI, University of Utah, Salt Lake City, UT, USA)). A condensed version of the protocol which was utilized to process all AAAs within this study is given in the following. The complete protocol can be found in the Appendix A.

### 2.2.1 A Condensed Version of the Segmentation Protocol

Transversal CT or MR images were used for segmentation to attain a consistent orientation of the AAA models in the xyz-space and to obtain best segmentation results. Sufficient segmentation results at justifiable effort were obtained for slice distances  $\leq 3$  mm and pixel sizes  $\leq 1$  mm.

**Lumen** The lumen was quickly and reliably segmented using some standard software functions. The workflow is concisely outlined by the following steps:

1. Threshold the blood lumen (selects all voxels within a certain HU range and groups them in one mask). The correct choice of the upper and lower bounds for thresholding is thereby dependent on the administration and amount of contrast agent in the blood lumen. A rule of thumb is to set the lower bound as high as possible but such that all pixels inside the lumen are selected, and the upper bound such that only single pixels are noticeably missing.
2. Cut the mask proximal to the celiac artery bifurcation and close to the common iliac artery bifurcations.
3. Shrink the mask by 1 pixel (8-connectivity in transversal planes).
4. Cut off the renal arteries and the inferior mesenteric artery.
5. Perform a region grow (selects only these regions of the active mask which are still connected to the lumen).
6. Dilate the mask by 1 pixel (8-connectivity in transversal planes) and close voids inside the lumen.
7. Check contour and manually repair inaccuracies.

An example of a final lumen looks like in Figure 2.3.

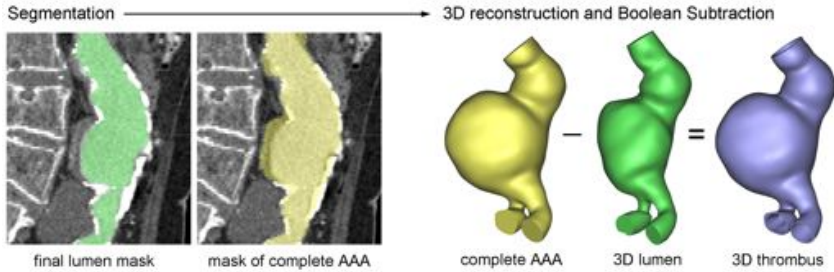


Figure 2.3: Illustration of the segmentation workflow. Left: 2D masks of segmented lumen and complete AAA geometry. Right: 3D reconstructions of lumen, complete geometry and ILT.

**Intraluminal Thrombus (ILT)** A very practical way to extract the intraluminal thrombus was to segment and three-dimensionally reconstruct the complete AAA geometry (including lumen and thrombus) and then create the ILT by a 3D Boolean subtraction of the lumen from the complete geometry, see e.g. Figure 2.3. The required mask of the complete geometry was thereby created by a slice-wise, manual selection of the complete geometry, which is briefly depicted by the points:

1. Copy the lumen mask.
2. Add ILT to this mask (in Mimics: Use *Multiple Slice Edit*).
3. Check and repair the mask, if applicable.

If calcifications exist, the inner half should be included in the mask and the outer half should be excluded. An example for the final mask of a complete AAA geometry (lumen and ILT) is depicted in Figure 2.3.

**3D Reconstruction** With the masks of lumen and complete geometry available, the 3D reconstructions of lumen and complete geometry were calculated. The 3D reconstructions were smoothed using Laplacian [224] and advanced volume preserving algorithms [202]. Centerlines for these geometries were saved (e.g. for later calculation of local radius/diameter) and the geometries were cut at the branching of the renal arteries and 2 cm distal to the aortic bifurcation at the iliac arteries. The 3D ILT geometry was obtained by Boolean subtraction of the 3D lumen from the complete 3D geometry. The fully detailed protocol for the calculation of the 3D geometries from the masks, smoothing, centerline generation, cutting and processing of the 3D ILT geometry (including Mimics software parameters and software specific hints) is given in the Appendix A.2. The 3D geometries of lumen and ILT were saved in stl(stereolithography)-file format.

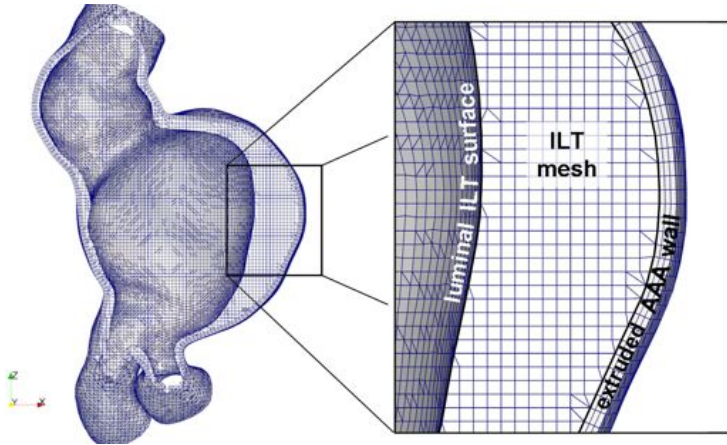


Figure 2.4: Cut-view of a hexahedron-dominant mesh of ILT and AAA wall. Edge length size was  $h = 1$  mm for elements representing the ILT. The AAA wall was extruded to the lumen or the abluminal ILT surface, whereas the wall thickness and the number of element layers can be freely adjusted (here: 1.2 mm over 3 layers of elements).

## 2.3 FE Mesh Generation

The segmented and reconstructed AAA geometries needed to be discretized (“meshed”) for FE simulation. In the current work, the mesh generation was performed using the commercial software Harpoon (Sharc Ltd, Manchester, UK). This software is capable of generating hexahedron-dominant meshes even for irregular geometries such as AAAs. All AAAs were meshed following a fixed meshing protocol, which is given in the Appendix A.3. In short, the 3D geometry of the ILT was loaded into the software (if the AAA did not feature any ILT the lumen geometry was used instead) and divided into luminal and abluminal ILT surfaces, inlet and two outlets for later definition of boundary conditions. The geometry was then meshed using an element edge length of  $h = 1$  mm. The created mesh was checked visually especially at in and outlets and at sites of thin ILT, where meshing errors were most likely to occur. In case of meshing errors the edge length was varied within the range  $0.95 \text{ mm} < h < 1.05 \text{ mm}$ , which frequently resolved meshing errors sufficiently. Missing elements were also added manually. Since the AAA wall could not be segmented from CT images, an idealized AAA wall was extruded to the abluminal ILT surface or onto the lumen if ILT was not present. Wall thickness and numbers of element layers over the wall could be adjusted in a custom extrusion algorithm. At this stage, a spatially constant wall thickness of  $t = 1.2 \text{ mm}$  was assumed and distributed over three layers of elements. A cut-view of a meshed AAA is shown in Figure 2.4. Numbers of elements for the AAAs included in this study ranged from about 20,000 elements for an ILT-free AAA to about 730,000 elements for AAAs with large ILT burden. An ordinary AAA mesh typically consisted of about 250,000 elements.

## 2.4 Nonlinear Elasticity

The mathematical formulation of the movements and deformations of continuous bodies under loading is part of the field of continuum mechanics. In the cardiovascular system, arteries can undergo significant diameter changes over a heart cycle with related systolic/diastolic pressure changes at the inside of the vessel. For the application of mechanics in the evaluation of AAAs, it is consequently necessary to account for large deformations. Concurrent formulations for the description of large deformations that differ in the choice of their reference systems, are the *material* (also *Lagrangian*) *formulation* and the *spatial* (also *Eulerian*) *formulation*. In a material formulation, the reference system is a material frame, where the movement of a reference point is followed during the deformation of a body. In a spatial formulation, the reference system is fixed and the flux of quantities over the borders of control volumes is a key factor. The material formulation is typically used to describe the kinematics of solids, which is consequently applied in the current work. In a material formulation, one generally differentiates between a *reference* (*material, initial, undeformed*) *configuration* of a body and a *deformed* (*current, spatial*) *configuration* of a body. For standard engineering problems, the reference configuration is usually known and the deformed configuration has to be determined in an inherently nonlinear solution process. It will be pointed out in Section 2.6.2 that this does not directly apply to cardiovascular problems, where the reference configuration of e.g. an artery is not known from the beginning, since the patients are alive and consequently the CT image of the artery is acquired under physiological loading.

This section summarizes some aspects of nonlinear continuum mechanics that provide the basis for the subsequent chapters. It describes the kinematics for large deformations, the concept of stress and fundamentals of elasticity. In the context of the present work, it is most of all needed for the physically correct evaluation of the experiments and for the correct description of the mechanical behavior of the different AAA constituents. For more detailed information beyond the scope of this short summary, the reader is referred to the works in [7, 57, 90, 91, 153, 240].

### 2.4.1 Kinematics

This paragraph describes the common deformation measures for solids in a material formulation. Consider an undeformed body in its reference configuration  $\Omega_0$ . The position of any generic material point of that body is given as  $\mathbf{X}$  (capital letters usually refer to quantities in the reference configuration) in a 3D Euclidean space  $\mathbb{R}^3$ . When the body is loaded and deformed into a spatial deformed configuration  $\Omega$ , the same point is shifted to a position described by the vector  $\mathbf{x}$  (small letters usually refer to quantities in the deformed configuration) using the same Cartesian orthogonal base. Hence, the current position  $\mathbf{x}$  of any point may be described by the mapping function  $\chi$ , which transforms  $\Omega_0$  to  $\Omega$ :

$$\chi : \begin{cases} \Omega_0 \rightarrow \Omega \\ \mathbf{x} = \chi(\mathbf{X}) \end{cases} \quad (2.1)$$

The determination of the vector function  $\chi$  is required as part of the solution of the finite elasticity problem and is analogous to the solution for the displacement vector field  $\mathbf{d}$ :

$$\mathbf{d} = \mathbf{x} - \mathbf{X}. \quad (2.2)$$

The fundamental kinematic variable is the material *deformation gradient*  $\mathbf{F}$  defined as

$$\mathbf{F}(\mathbf{X}) := \text{Grad } \mathbf{x} = \frac{\partial \mathbf{x}}{\partial \mathbf{X}} = \mathbf{1} + \frac{\partial \mathbf{d}}{\partial \mathbf{X}}. \quad (2.3)$$

$\mathbf{F}$  is constrained to

$$J = \det(\mathbf{F}) > 0, \quad (2.4)$$

where the determinant of  $\mathbf{F}$  is commonly denoted the *Jacobian*  $J$ . The Jacobian  $J$  is a measure for the volume change. Condition (2.4) ensures that a generic volume remains positive under deformation. An interpretation of the deformation gradient  $\mathbf{F}$  is that it transforms an incremental line element  $d\mathbf{X}$  into its spatial counterpart:

$$d\mathbf{x} = \mathbf{F}d\mathbf{X} \quad (2.5)$$

Further, respective transformations of infinitesimal areas and volumes read:

$$da = J\mathbf{F}^{-T}dA \quad (2.6)$$

$$dv = JdV \quad (2.7)$$

A mapping described by the deformation gradient  $\mathbf{F}$  can contain contributions of rigid body motion and actual stretch. The splitting of  $\mathbf{F}$  into these two parts is denoted *polar decomposition*:

$$\mathbf{F} = \mathbf{R}\mathbf{U} = \mathbf{v}\mathbf{R} \quad (2.8)$$

$\mathbf{R}$  is the orthogonal rotation tensor ( $\mathbf{R}\mathbf{R}^T = \mathbf{R}^T\mathbf{R} = \mathbf{1}$ ,  $\mathbf{1}$  is the identity tensor).  $\mathbf{U}$  and  $\mathbf{v}$  are the right (material) and the left (spatial) stretch tensor, respectively.  $\mathbf{U}$  and  $\mathbf{v}$  are positive definite and symmetric tensors. The normalized eigenvectors  $\mathbf{M}_1, \mathbf{M}_2, \mathbf{M}_3$  and the corresponding eigenvalues  $\lambda_1, \lambda_2, \lambda_3$  of the right stretch tensor  $\mathbf{U}$  are given by the eigenvalue problem

$$\mathbf{U} \cdot \mathbf{M}_i = \lambda_i \cdot \mathbf{M}_i, \quad \text{with } i = 1, 2, 3. \quad (2.9)$$

$\mathbf{M}_i$  can thereby be interpreted as the principal axes in the material configuration and  $\lambda_i$  as the corresponding principal stretches. Analogously,  $\mathbf{m}_1, \mathbf{m}_2, \mathbf{m}_3$  are the normalized eigenvectors and  $\lambda_1, \lambda_2, \lambda_3$  the eigenvalues of the left stretch tensor  $\mathbf{v}$  such that

$$\mathbf{v} \cdot \mathbf{m}_i = \lambda_i \cdot \mathbf{m}_i, \quad \text{with } i = 1, 2, 3. \quad (2.10)$$

Again,  $\mathbf{m}_i$  represent the principal axes in the deformed configuration and  $\lambda_i$  the principal stretches.  $\mathbf{U}$  and  $\mathbf{v}$  share the same eigenvalues/principal stretches. The spectral decompositions of  $\mathbf{U}$  and  $\mathbf{v}$  are obtained with

$$\mathbf{U} = \sum_{i=1}^3 \lambda_i \mathbf{M}_i \otimes \mathbf{M}_i, \quad \mathbf{v} = \sum_{i=1}^3 \lambda_i \mathbf{N}_i \otimes \mathbf{N}_i, \quad (2.11)$$

where  $\otimes$  represents the dyadic product.

The deformation gradient  $\mathbf{F}$  is a two-point tensor since it is referred to both the material and the deformed configuration. It is also possible to delineate deformation measures that are completely related to either the material or the deformed configuration. A common deformation

measure related to the reference configuration is the *right Cauchy-Green deformation tensor*  $\mathbf{C}$ . It is defined as

$$\mathbf{C} = \mathbf{F}^T \mathbf{F} = \mathbf{U}^2. \quad (2.12)$$

$\mathbf{C}$  has the same eigenvectors as  $\mathbf{U}$ . The eigenvalues of  $\mathbf{C}$  are  $\lambda_i^2$ . Additionally, the *Green-Lagrange strain tensor*  $\mathbf{E}$  is defined as

$$\mathbf{E} = \frac{1}{2} (\mathbf{C} - \mathbf{1}). \quad (2.13)$$

Both the right Cauchy-Green and the Green-Lagrange tensors are symmetric. A deformation measure that is only related to the deformed configuration is the *left Cauchy-Green deformation tensor*  $\mathbf{b}$ . It is defined as

$$\mathbf{b} = \mathbf{F} \mathbf{F}^T = \mathbf{v}^2. \quad (2.14)$$

Again,  $\mathbf{b}$  and  $\mathbf{v}$  feature the same eigenvectors. The eigenvalues of  $\mathbf{b}$  are  $\lambda_i^2$ . Another deformation measure that is defined within the deformed configuration is the *Euler-Almansi strain tensor* that is defined by

$$\mathbf{e} = \frac{1}{2} (\mathbf{1} - \mathbf{b}^{-1}). \quad (2.15)$$

The first three *principal invariants* that are associated with  $\mathbf{C}$  and  $\mathbf{b}$  are

$$I_1 = I_1(\mathbf{C}) = I_1(\mathbf{b}) = \text{tr} \mathbf{C} = \lambda_1^2 + \lambda_2^2 + \lambda_3^2 \quad (2.16)$$

$$I_2 = I_2(\mathbf{C}) = I_2(\mathbf{b}) = \frac{1}{2} [(\text{tr} \mathbf{C})^2 - \text{tr}(\mathbf{C}^2)] = \lambda_1^2 \lambda_2^2 + \lambda_1^2 \lambda_3^2 + \lambda_2^2 \lambda_3^2 \quad (2.17)$$

$$I_3 = I_3(\mathbf{C}) = I_3(\mathbf{b}) = \det \mathbf{C} = \lambda_1^2 \lambda_2^2 \lambda_3^2 = J^2 \quad (2.18)$$

## 2.4.2 Stress and Equilibrium

Stress is a measure for the force acting per unit area, whereas both forces and areas can be likely defined in either reference or deformed configuration resulting in different stress measures. The best starting point for the derivation of a stress measure is thereby a body in its deformed configuration  $\Omega$  that is held in equilibrium by external forces. The internal forces acting on a generic cut section of the body can be obtained by the *methods of section* (= splitting the body by an imaginary cut). The resultant forces exerted by the material that has been “cut away” acting on a surface element  $\Delta a$  on the boundary  $\partial\Omega = \Gamma$  are denoted  $\Delta \mathbf{f}$ . The *traction vector*  $\mathbf{t}$  is then defined as the resultant force acting on an infinitesimal surface area:

$$\mathbf{t} = \lim_{\Delta a \rightarrow 0} \frac{\Delta \mathbf{f}}{\Delta a} = \frac{d\mathbf{f}}{da} \quad (2.19)$$

The traction  $\mathbf{t}$  is a stress vector that is dependent on the orientation of the cut surface. The *Cauchy stress tensor*  $\boldsymbol{\sigma}$ , which is independent of this orientation, is then obtained via the *Cauchy theorem*:

$$\mathbf{t} = \boldsymbol{\sigma} \cdot \mathbf{n}, \quad (2.20)$$

where the projection of  $\boldsymbol{\sigma}$  to the normal vector  $\mathbf{n}$  is equal to the traction  $\mathbf{t}$ .  $\boldsymbol{\sigma}$  is symmetric and represents the real stresses in the deformed configuration. In other words, the traction  $\mathbf{t}$  can be interpreted as “real force divided by deformed cross-sectional area”.

In static translational equilibrium and in the absence of body forces, the integral of contact forces over the complete boundary  $\partial\Omega$  of the deformed configuration must be zero:

$$\int_{\partial\Omega} \mathbf{t} da = \int_{\partial\Omega} \boldsymbol{\sigma} \mathbf{n} da = \mathbf{0} \quad (2.21)$$

Considering that this equilibrium applies to any infinitesimal small subregion of  $\Omega$ , the local point-wise equilibrium condition can be delineated following an application of Gauss' divergence theorem:

$$\operatorname{div}(\boldsymbol{\sigma}) = \mathbf{0}, \quad (2.22)$$

where  $\operatorname{div}(\cdot)$  is the divergence operator on  $\Omega$ . The Cauchy stress tensor is completely related to the deformed configuration of a body, which is at an *a priori* unknown state. This exacerbates the solution for Eq. (2.22) and motivates the definition of further stress measures. For instance, insertion of Eq. (2.6) into Eq. (2.21) yields

$$\int_{\partial\Omega_0} \boldsymbol{\sigma} J \mathbf{F}^{-T} \mathbf{N} dA = \int_{\partial\Omega_0} \mathbf{P} N dA = \mathbf{0} \quad (2.23)$$

where  $J \mathbf{F}^{-1} \boldsymbol{\sigma} = \mathbf{P}$  has been applied.  $\mathbf{P}$  is the unsymmetric *first Piola-Kirchhoff (1.PK) stress tensor*, which is related to both the reference and the spatial configuration (“real force divided by undeformed cross-sectional area”). Application of Gauss' divergence theorem leads to the local point-wise equilibrium condition:

$$\operatorname{Div}(\mathbf{P}) = \mathbf{0}, \quad (2.24)$$

where  $\operatorname{Div}(\cdot)$  is the divergence operator with respect to the reference configuration  $\Omega_0$ .

A complete pull-back of  $\boldsymbol{\sigma}$  into the reference configuration  $\Omega_0$  yields the frequently used second Piola-Kirchhoff stress tensor  $\mathbf{S}$  that is defined as

$$\mathbf{S} = \mathbf{F}^{-1} \mathbf{P} = J \mathbf{F}^{-1} \boldsymbol{\sigma} \mathbf{F}^{-T}. \quad (2.25)$$

The second Piola-Kirchhoff stress tensor  $\mathbf{S}$  is symmetric. It has no intelligible physical interpretation, in that it would be defined as “force that is pulled back to reference configuration divided by undeformed cross-sectional area”. It is commonly used during the solution process for the translational equilibrium

$$\operatorname{Div}(\mathbf{F}\mathbf{S}) = \mathbf{0}. \quad (2.26)$$

To round off, the transformations of the different stress measures into each other are briefly summarized by

$$\boldsymbol{\sigma} = J^{-1} \mathbf{P} \mathbf{F}^T = J^{-1} \mathbf{F} \mathbf{S} \mathbf{F}^T, \quad (2.27)$$

$$\mathbf{P} = J \boldsymbol{\sigma} \mathbf{F}^{-T} = \mathbf{F} \mathbf{S}, \quad (2.28)$$

$$\mathbf{S} = J \mathbf{F}^{-1} \boldsymbol{\sigma} \mathbf{F}^{-T} = \mathbf{F}^{-1} \mathbf{P}. \quad (2.29)$$

### 2.4.3 Elasticity

Elastic properties of solids under large deformation can be described by means of strain energy functions  $W$  (SEFs), which describe the energetic potential that is stored by the material during the deformation. In case of an isothermal, homogeneous material which is assumed for the current work, the stored energy  $W$  is only a function of the deformation (strain) measure and described by the SEF. Suitable strain measures can thereby be delineated from energy conjugated stress-strain pairs. For instance the deformation gradient  $\mathbf{F}$  forms an energy-conjugated stress-strain pair with the first Piola-Kirchhoff stress tensor  $\mathbf{P}$ . In absence of volumetric constraints,  $\mathbf{P}$  can then be calculated by differentiation of  $W$  with respect to  $\mathbf{F}$ :

$$\mathbf{P} = \frac{\partial W}{\partial \mathbf{F}} \quad (2.30)$$

Such a relation of stress to strain is generally called the *constitutive equation*. In case of an incompressibility constraint, the analogue to Eq. (2.30) becomes

$$\mathbf{P} = \frac{\partial W}{\partial \mathbf{F}} - p\mathbf{F}^{-1}, \quad J = 1, \quad (2.31)$$

where  $p$  is a Lagrange multiplier that enforces the material incompressibility and  $J = 1$  is the incompressibility condition.

Analogously, the second Piola-Kirchhoff stress and the Green-Lagrange strain form an energy-conjugated stress-strain pair. The constitutive equation reads:

$$\mathbf{S} = \frac{\partial W}{\partial \mathbf{E}} = 2 \frac{\partial W}{\partial \mathbf{C}}. \quad (2.32)$$

SEFs for the application in FE methods are frequently formulated with respect to  $\mathbf{C}$ . The material tangent  $\mathbb{C}$  in the reference configuration, which is needed in linearization-based solutions of the boundary value problem (Section 2.6.1), can then be calculated with

$$\mathbb{C} = \frac{\partial^2 W}{\partial \mathbf{E}^2} = 4 \frac{\partial^2 W}{\partial \mathbf{C}^2}. \quad (2.33)$$

In case of an isotropic material, the strain energy  $W$  must be independent of rotations of the reference system. For SEFs written with respect to  $\mathbf{C}$ , the strain energy  $W(\mathbf{C})$  can be equivalently described by the invariants  $I_1, I_2, I_3$  of the argument  $\mathbf{C}$ :

$$W = W(I_1(\mathbf{C}), I_2(\mathbf{C}), I_3(\mathbf{C})) \quad (2.34)$$

For anisotropic materials, the first three invariants are not sufficient to correctly describe the strain energy  $W$ . Additional invariants are needed for transversely isotropic or fully anisotropic materials to fully capture the relevant deformations provided by  $\mathbf{C}$ . It is referred to [90] and [153] for a detailed elaboration. In the case of compressibility,  $\mathbf{F}$  can be split in an *isochoric* (volume preserving, deviatoric) part and *volumetric* (volume changing, dilational) part using multiplicative decomposition. This yields

$$\mathbf{F} = J^{\frac{1}{3}} \bar{\mathbf{F}}, \quad (2.35)$$

where  $J^{\frac{1}{3}}$  represents the volumetric part and  $\bar{\mathbf{F}}$  the isochoric part, respectively. The strain energy  $W$  can then be described by isochoric and volumetric contributions. This approach was probably first introduced by Flory [50]:

$$W(F) = W_{iso}(\bar{\mathbf{F}}) + W_{vol}(J), \quad (2.36)$$

where the strain measures in the isochoric contribution are just substituted by their *modified* counterparts. For instance, the modified right Cauchy-Green deformation tensor and the modified invariants are given by

$$\bar{\mathbf{C}} = J^{-\frac{2}{3}}\mathbf{C}, \quad \bar{I}_1 = J^{-\frac{2}{3}}I_1, \quad \bar{I}_2 = J^{-\frac{4}{3}}I_2, \quad \bar{I}_3 = \det \bar{\mathbf{C}} = 1. \quad (2.37)$$

The specific forms of SEFs which were used for the constitutive modeling of biological soft tissues, will be presented in the following sections dealing with the different AAA constituents (Sections 2.5.1, 2.5.2 and 2.5.3). However, independent of the specific form, there are some conditions that any SEF has to fulfill and which are briefly discussed in the following: One of these conditions is that stored energy/stresses must vanish in a residual-stress-free reference configuration  $\Omega_0$ . This can be described by

$$W(\mathbf{F} = \mathbf{1}) = 0, \quad \frac{\partial W}{\partial \mathbf{F}}(\mathbf{1}) - p_0 \mathbf{1} = \mathbf{0} \text{ (incomp.)}, \quad \frac{\partial W}{\partial \mathbf{F}}(\mathbf{1}) = \mathbf{0} \text{ (comp.)}, \quad (2.38)$$

where  $\mathbf{0}$  is the zero tensor and  $p_0$  is the hydrostatic pressure in the reference configuration  $\Omega_0$ . This configuration is called the *natural configuration*. However, it is also possible that a body is not stress-free despite the absence of external loads on  $\partial\Omega_0$ . Such existing stresses are called *residual stresses*.

Another requirement on SEFs is *objectivity*, which describes the independence of stored energy from rigid body modes (translations and rotations). Since translations do not affect the deformation gradient  $\mathbf{F}$ , we can limit ourselves to the investigation of rotations: Applying an arbitrary rotation  $\mathbf{Q}$  ( $\mathbf{Q}$  is the orthogonal rotation tensor with  $\det \mathbf{Q} = 1$  and  $\mathbf{Q}^T = \mathbf{Q}^{-1}$ ) transforms the deformation gradient  $\mathbf{F}$  to  $\mathbf{QF}$ . Consequently, the objectivity condition reads

$$W(\mathbf{F}) = W(\mathbf{QF}). \quad (2.39)$$

From polar decomposition (Eq. (2.8)) and for the example  $\mathbf{Q} = \mathbf{R}^T$ , which is a feasible choice for an arbitrary rotation, we can rewrite the objectivity condition in Eq. (2.39) as

$$W(\mathbf{F}) = W(\mathbf{U}). \quad (2.40)$$

This implies that any SEF is *a priori* objective if it is only dependent on the stretch contribution  $\mathbf{U}$  of  $\mathbf{F}$ , e.g. if it is formulated with respect to  $\mathbf{U}$  ( $W = W(\mathbf{U})$ ). Furthermore, the right Cauchy-Green deformation tensor  $\mathbf{C}$  and the Green-Lagrange strain tensor  $\mathbf{E}$  can be written as functions of  $\mathbf{U}$ . Consequently, any SEF written as a function of  $\mathbf{C}$ ,  $\mathbf{E}$  or their invariants is automatically objective.

For stability reasons in numerical application, SEFs should further fulfill the conditions of *convexity*. Briefly, convexity guarantees the uniqueness of solutions stating that any local minimum is also the global minimum. This is especially important for the application of linearization methods to obtain a stable and unique solution of nonlinear problems. It is referred to [7] for an in-depth discussion of this aspect.

## 2.5 Materials

On the macroscopic level (e.g. visual observation during open AAA repair or in CT images), one can distinguish three different AAA constituents: The intraluminal thrombus, calcifications and the diseased arterial wall itself. In this section, the biological background is summarized for each of these three constituents, followed by a literature review of mechanical experiments and existent mechanical models. Detailed explanations on the choice of material models and on the specific implementation within the current work are given for each constituent.

### 2.5.1 Intraluminal Thrombus (ILT)



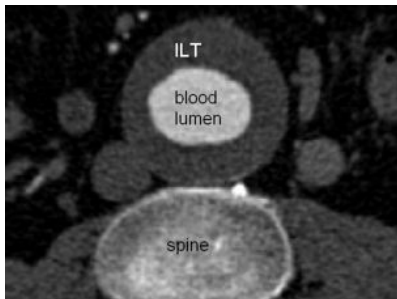
(a) ILT removed from the AAA: Its consistency can range from “jelly-like (dt. Wackelpudding)” ...



(b) ... to “solidified porridge (dt. erkalteter Griesbrei)” (terminology thanks to Felix Härtl, MD).



(c) An abluminal layer sample (left) can be visually distinguished from a luminal layer sample (right) by color and structural integrity.



(d) In contrast enhanced CT images, the ILT can be distinguished from the blood lumen, but the different ILT layers are not resolved.

Figure 2.5: Intraluminal thrombus is a deposition of coagulated blood at the luminal side of the AAA wall which is removed during open AAA repair.

### Biology of ILT

Intraluminal thrombus is a product of blood coagulation that adheres to the arterial wall. The depositions can be centimeters thick, filling out the AAA sac and narrowing the blood lumen. ILT consists mainly of fibrin bundle networks, which are the final product of complex activation cascades with a multitude of coagulation factors [205]. Thereby, the main processes are activation of prothrombin to thrombin, the conversion of fibrinogen by thrombin to fibrin and the formation of fibrin bundle networks. Erythrocytes may also be trapped in the fibrin network [205, 208]. It has also been found from histological and immunohistochemical investigations that the formation and growth of ILT leads to pathological changes in the AAA wall: Vorp *et al.* [226] found that partial pressure of oxygen decreases over ILT thickness leading to hypoxia in AAA wall adjacent to thick ILT burden. This was in agreement with their expectations from previous poor computer models [227]. Hypoxia in turn mediates inflammation and mural neo-vascularization. Kazi *et al.* [110] showed that the AAA wall is thinner behind ILT, which was expected to be induced by a reduction of the contents of elastin fibers and smooth muscle cells (SMCs), while there were more signs of inflammation.

For mechanical considerations, most literature distinguishes between luminal, medial and abluminal ILT layers. The degeneration from the luminal to the abluminal layers in surgically removed ILT is also visible to the human eye (Figures 2.5 (a) through (c)). However, the layers cannot be distinguished based on CT images (Figure 2.5 (d)). In scanning electron microscopy images, it can be seen that the luminal layer is made up of randomly oriented thick fibrin bundles that can branch and cross-link each other [233]. This fibrin network is partly degenerated in the medial layer and it is almost completely degenerated in the abluminal layer [230]. In most literature, it is assumed that from a mechanical point of view, the ILT exerts a two-fold cushioning effect on the AAA wall: Firstly, it narrows the lumen and therewith minimizes the surface that the blood pressure acts on. Secondly, due to its structural integrity, it can counteract the blood forces and provide some load bearing effect. This was e.g. shown in early computational models [147] and by *in vitro* pressure measurements in ILT samples [83]. Pressure transmission in ILT was also the main question in a series of publications by Hinnen *et al.* [83, 84, 85, 86, 87], which investigated influences of test set-ups on pressure measurements in ILT. Surprisingly, they did not perform a single *in vivo* pressure measurement for validation. Some earlier findings by Schurink *et al.* [185], however, indicate that ILT might actually not reduce the pressure load on the AAA wall. In consequence, the effects of ILT on pressure transmission remain disputed and there is no proof that the above mentioned assumptions in literature do really capture the physiology and the mechanical behavior of ILT. More research effort on this topic is necessary to clarify this issue.

### Literature Review - Experiments and Strain Energy Functions

Various mathematical/mechanical formulations are used in the literature to describe the nonlinear material behavior of ILT. This section is devoted to the literature review on ILT experiments and associated constitutive laws. Where possible, the present work uses the concept of “referential stiffness” to compare stiffness values measured by different groups. The referential stiffness represents the initial stiffness of a material under assumption of uniaxial tension/compression without consideration of softening or stiffening of the material at higher strains. In the theory of linear elasticity, the referential stiffness coincides with the Young’s modulus. In contrast,

the mean tangential modulus (MTM), which is also often used in literature, generally denotes the average stiffness of a nonlinear material over an investigated strain range and is susceptible to the chosen stress-strain range and the type of stress description (e.g. Cauchy, 1./2.PK). For example, a material with stiffening behavior features a higher MTM than referential stiffness.

Probably the first experimental study on mechanical characterization of ILT was performed by Di Martino *et al.* [41]. Circumferentially oriented specimens ( $n = 21$ ) were cut from ILTs using a die. Tensile tests exhibited a referential stiffness of 131 kPa. Mean strength was 85 kPa (1.PK stress), failure stretch was  $\lambda_{max} = 1.64$ . The well described experimental set-up and results were complemented by a too simple 2D FE investigation of ILT effects on wall stress results.

Wang *et al.* [230] were the first to propose a finite strain constitutive model for ILT according to their tensile test results. Fifty ILT specimens were tested. The luminal thrombus region was found to be stiffer and stronger than the medial region (luminal: MTM= 550 kPa, strength 530 kPa (Cauchy stress); medial: MTM= 300 kPa, strength= 260 kPa (Cauchy stress)). Differences between mechanical behavior in circumferential or longitudinal testing directions were shown to be not significant. In consequence, an isotropic constitutive law was proposed:

$$W = c_1 (I_2 - 3) + c_2 (I_2 - 3)^2 \quad (2.41)$$

Parameters for this SEF derived from the testing results are given in [230]. In addition, the ILT microstructure was investigated using scanning electron microscopy, which revealed that there was no preferred orientation of the constituents [230].

Vande Geest *et al.* [221] performed biaxial tension tests on  $n = 9$  ILT specimens. They concluded that ILT material behaves isotropic. Referential stiffness ranged from 201 kPa to 231 kPa. The two-parametric SEF

$$W = c_1 (I_1 - 3) + c_2 (I_1 - 3)^2 \quad (2.42)$$

was proposed. Numbers without units were given for the material parameters, e.g. “ $c_1 = 7.98$ ”. The intuitive assumption of the units being N/cm<sup>2</sup>, however, would yield too stiff material models ( $E_{ref} = 6 \cdot c_1 = 478$  kPa, if  $c_1 = 7.98$  N/cm<sup>2</sup>). The work is not conclusive in this regard.

Hinnen *et al.* [86] performed shear and compression tests. Ten specimens were frozen at  $-80^\circ\text{C}$  for two weeks and equalized to room temperature before testing. Results from compression tests (using a fluid filled “compression box”) were not listed in detail. Nevertheless, it was concluded that “the Poisson’s ratio of human fibrinous thrombus must be close to 0.5” [86]. Some more quantitative information on the compression test results would have been helpful. The shear modulus  $G$  was measured in dynamic shear tests using 1% shear and frequencies between 0.8 Hz and 3.9 Hz. The Young’s modulus was calculated using the formula  $E = 2(1 + \nu)G$ , with  $\nu = 0.5$ . The Young’s modulus was obtained to 37 – 39 kPa and was independent of the strain-rate/frequency.

Gasser *et al.* [63] performed the largest study on ILT properties so far, including  $n = 112$  specimens. In cyclic tensile tests, ILT specimens showed only a very slightly nonlinear material behavior and negligible hysteresis. Excision sites from luminal, medial or abluminal layers were resolved. Referential stiffness decreased from the luminal layer (62.9 kPa) to the medial layer (47.5 kPa) to the abluminal layer (41.5 kPa). Ultimate strength in terms of Cauchy-stresses

ranged from 47.7 kPa (abluminal) to 156.5 kPa (luminal). An Ogden-type SEF [144, 153] was proposed for the modeling of the mechanical ILT behavior:

$$W = c \sum_{i=1}^3 (\lambda_i^4 - 1), \quad (2.43)$$

with  $\lambda_i$  as the  $i$ -th principal stretch. Plane stress FE models of the ILT specimens were used to calculate the correct material parameters in an inverse analysis (IA). The material parameters  $c$  for the luminal, medial and abluminal layers were determined to  $c = 2.62$  kPa, 1.98 kPa and 1.73 kPa, respectively [63].

Van Dam *et al.* [216] put emphasis on the investigation of the viscoelastic behavior of ILT. ILT specimens from 7 patients (number of specimens was not given) were stored at  $-80^\circ\text{C}$  and thawed for testing. A Maxwell-model was proposed and shear tests were performed to derive the parameters. They measured a referential stiffness of 5.1 kPa for the elastic response.

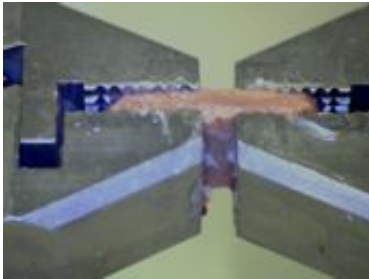
Ashton *et al.* [3] performed unconfined compression tests on  $n = 47$  (18 luminal, 15 medial, 14 abluminal) ILT specimens and reported compressive elastic moduli at 5% strain. Elastic moduli of luminal, medial and abluminal layers were determined to 1.5 kPa, 2.5 kPa and 19.3 kPa, which describes an increase of the compressive elastic moduli from the luminal to the abluminal layers. Ashton *et al.* did not propose a SEF or parameters to be used with other existent SEFs.

Monstadt *et al.* [146] performed both compression and tensile tests on fresh, artificially grown ILT from human and porcine blood. They used test rigs specially designed for testing of ILT. The referential stiffness for different samples was 2 – 4 kPa in tensile tests and 500 kPa in compression tests. Specimens showed a linear stress-strain curve during tensile tests over the complete strain range until failure at approximately 10 kPa (1.PK stress). A linear behavior during compression was obtained until 70% of compression. Results may have been hampered by the use of fresh, artificially grown ILT.

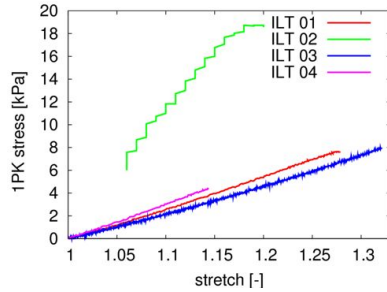
Tong *et al.* [208] investigated  $n = 67$  ILT specimens with special regard to anisotropic mechanical behavior. They found a mean referential stiffness ranging from 90 kPa for fresh thrombus to 206 kPa for luminal ILT specimens. Increased anisotropy was stated for  $n = 10$  luminal ILT specimens, whereas the mean referential stiffness for these specimens ranged from 208 kPa in circumferential to 291 kPa in longitudinal direction. Strength in terms of 1.PK stresses ranged from 28 kPa to 60.5 kPa. Tong *et al.* hypothesized that cracks were likely to be initiated by the hooks used for specimen mounting. They proposed a Holzapfel-like strain energy function for the constitutive modeling:

$$W = \mu(I_1 - 3) + \frac{k_1}{k_3} (\exp\{k_2[(1 - \rho)(I_1 - 3)^2 + \rho(I_4 - 1)^2]\} - 1) \quad (2.44)$$

with  $\mu$  as the shear modulus for the isotropic contribution,  $k_1$  to  $k_3$  as anisotropic material parameters, and  $\rho$  as the fiber dispersion parameter (with values provided in [208]).  $I_4$  is the fourth invariant of the right Cauchy-Green deformation tensor  $\mathbf{C}$ , which is equal to the stretch in fiber direction. The study was complemented by a description of ILT microstructure constituents over different aging phases. It is to note that only few specimens (10 out of 67) featured markedly increased anisotropy at all. Therefore, the proposal of an anisotropic material law by Tong *et al.* is surprising, since the behavior of the majority of ILT specimens would be captured more accurately using an isotropic law. Another discrepancy of the study by Tong *et al.* was that



(a) Clamped ILT specimen. It was glued to the grips using cyanoacrylate to prevent slipping whilst squeezing was basically avoided.



(b) Stress-stretch curves (loading branches only) for the 4 tested ILT specimens. Stiffness values ranged from 24 kPa to 104 kPa.

Figure 2.6: Own ILT experiments: Samples were obtained during open surgery and cut into smaller rectangular specimens suitable for uniaxial tensile testing. Specimens were exposed to 20 cycles of sinusoidal loading at 0.5 Hz. Data from the last cycle was used for the evaluation of mechanical properties.

the mean referential stiffness was 208 kPa for the circumferential direction and 291 kPa for the longitudinal direction, which was both higher than the mean isotropic referential stiffness of 206 kPa.

In 2009, own experiments were performed on ILT specimens. ILT was harvested from a 70 year old male patient during elective AAA repair and stored in Lactated Ringer's solution (Figure 2.5 (b)). Prior to uniaxial tensile testing, the ILT was cut into 4 smaller rectangular specimens which dimensions were measured using digital calipers. Typical specimen dimensions were 20 mm in length, 10 mm in width and 3 mm in thickness. Specimens from the abluminal ILT layer had dark brown color, those from the luminal layer had light brown color (Figure 2.5 (c)). Uniaxial tensile tests were performed at room temperature using an ElectroForce 3100 (Bose Corp., Eden Prairie, USA) test machine. Specimens were glued to the clamps using cyanoacrylate to prevent slipping of the specimen from the clamps while being careful to avoid squeezing the specimens, see Figure 2.6 (a). Cyclic sinusoidal loading was then applied to the specimens at frequency  $f = 0.1$  Hz. As the strain-stress response of biological tissue changes during first cycles of periodical testing [58, 98], 19 cycles of loading and unloading were used for preconditioning. The loading branches from the 20th cycles were used for the evaluation of mechanical ILT properties. Measured stress-stretch curves are plotted in Figure 2.6 (b), revealing an almost linear stress-stretch behavior of the investigated ILT material. The stiffness of the specimens ranged from 24 kPa to 104 kPa. The experiments were stopped due to the publication of the comprehensive study by Gasser *et al.* [63]. Results from the own experiments were not published, since tests were not performed for a statistically relevant number of specimens.

A summary of the review is given in Table 2.1. To conclude with the review, the studies consistently distinguished between three ILT layers. In all tensile tests, the referential stiffness decreased from the luminal to the abluminal layer. The study by Gasser *et al.* [63] resolved the different mechanical behavior of all three layers most accurately. The situation was vice versa

Table 2.1: Review of mechanical ILT tests in literature:

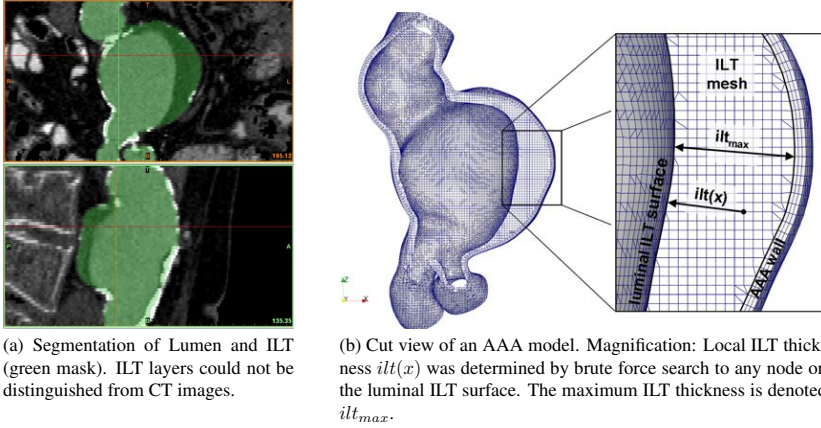
Group	Test set-up	Experimentally measured referential stiffness	No. specs.	Comments
Di Martino <i>et al.</i> (1998) [41]	uniaxial tension	131 kPa (all circumferential)	n=21	Linear stress-strain behavior; strength=0.085MPa, $\lambda_{max}=1.64$
Wang <i>et al.</i> (2001) [230]	uniaxial tension	300 kPa (med.) - 550 kPa (lum.)	n=50	No difference between circ./long. orientation; SEF based on $I_2$
Vande Geest <i>et al.</i> (2006) [221]	biaxial tension	201 kPa (circ.), 231 kPa (long.)	n=9	Isotropy confirmed; isotropic SEF, no units for params.!
Hinnen <i>et al.</i> (2007) [86]	shear	37 - 39 kPa	n=10	strain-rate independency (extended phys. frequency range)
Gasser <i>et al.</i> (2008) [63]	uniaxial tension	41 kPa (abl.) - 63 kPa (lum.)	n=112	Ogden-type SEF with parameters derived by IA; ILT layers resolved
van Dam <i>et al.</i> (2008) [216]	shear	5.1 kPa	unkn.	Emphasis was put on modeling the viscoelastic behavior
Ashton <i>et al.</i> (2009) [3]	compress.	19 kPa (abl.) - 1.5 kPa (lum.)	n=47	Unconfined-compression tests; stiffness at 5% strain
Monstadt <i>et al.</i> (2009) [146]	compress. & tension	2 - 4 kPa (tension), 500 kPa (compression)	n=11	Artificial ILT; linear behavior in tension and 70% compression
Tong <i>et al.</i> (2011) [208]	biaxial tension	105 kPa (abl.) - 200 kPa (lum.); 208 kPa (circ.), 291 kPa (long.)	n=67	Influence of hooks; anisotropy stated for 10 luminal specimens
own tests (2009)	uniaxial tension	24 kPa - 104 kPa	n=4	unpublished results

in compression tests, where the stiffness increased from the luminal to the abluminal layer. Actually, knowledge on the *in vivo* stress-state (tension/compression) would therefore be of major importance for the correct assignment of material parameters and their gradients. This thought should be included in future work. It seems reasonable to assume that ILT behaves isotropic. The two studies by Wang *et al.* [230] and Vande Geest *et al.* [221], which were specially designed to investigate anisotropic effects, concluded that ILT material behaves isotropic. Tong *et al.* stated distinct anisotropy for only 10 out of their 67 ILT specimens [208]. However, preferential stiffening directions detected by Wang *et al.* [230] (circumferential) and Tong *et al.* [208] (longitudinal) were in disagreement. This further substantiates that the assumption of an isotropic ILT behavior is adequate.

Without going into detail, purely computational studies which focused on the investigation of ILT effects on AAA FE simulation results can be found in [143, 147, 160, 227, 231]. More complex models additionally consider the fluid mechanics [12] or fluido-chemical interactions [238] during the ILT formation process.

## Implementation Issues

This paragraph deals with the ILT model selected for the present work and implementation issues for usage with the FE solver BACI (Institute for Computational Mechanics, TUM, Munich,



(a) Segmentation of Lumen and ILT (green mask). ILT layers could not be distinguished from CT images.

(b) Cut view of an AAA model. Magnification: Local ILT thickness  $ilt(x)$  was determined by brute force search to any node on the luminal ILT surface. The maximum ILT thickness is denoted  $ilt_{max}$ .

Figure 2.7: Segmentation of the ILT from CT images (a) and realization in the FE model (b).

Germany) [229]. If ILT was present in an AAA, it could be easily identified in both contrast enhanced CT images (28 HU to 45 HU) or MR images. Using the previously introduced segmentation and meshing protocol, the 3D geometry of the ILT could be easily reconstructed and a hexahedron-dominated mesh was created. A representative ILT mask during the segmentation process and an associated cut-view of the 3D ILT mesh are shown in Figure 2.7. Although the ILT material exhibited distinct layer specific properties in mechanical tests and microstructural investigations, there was no chance of distinguishing between different layers in CT images based on the HU. More potential is seen for the usage of MR to derive layer specific properties [21, 61]. A sophisticated method to reliably derive mechanical ILT properties from MR images, however, is still far from application.

In order to account for the spatially variable mechanical properties of ILT nonetheless, the material model proposed by Gasser *et al.* [63] was applied for constitutive modeling in the current work. The suggested SEF in Eq. (2.43) can be rewritten in terms of invariants:

$$W = c(I_1^2 - 2I_2 - 3) \quad (2.45)$$

This material model resolves the mechanical behavior of three different ILT layers, whereas stiffness values of 62.9 kPa ( $c = 2.62$  kPa) for the luminal, 47.5 kPa ( $c = 1.98$  kPa) for the medial and 41.5 kPa ( $c = 1.73$  kPa) for the abluminal layer were reported. This model has the further advantage, that the reported stiffness values represent the median values of current literature (Table 2.1) and that these are in good agreement with own uniaxial tensile tests that yielded stiffness values between 24 kPa and 104 kPa. In the current work, the categorization of any ILT material point into either luminal, medial or abluminal layer was based on a brute force search to compute the distance of any ILT node to the luminal ILT surface (denoted  $ilt(x)$ , see also Figure 2.7 (b) and [68]). The luminal ILT layer was then defined by  $ilt(x) \leq \frac{1}{3}ilt_{max}$ , the medial layer by  $\frac{1}{3}ilt_{max} < ilt(x) \leq \frac{2}{3}ilt_{max}$  and the abluminal layer by  $\frac{2}{3}ilt_{max} < ilt(x)$ , respectively. Figure 2.8 displays a representative AAA where the ILT is divided into luminal, medial and

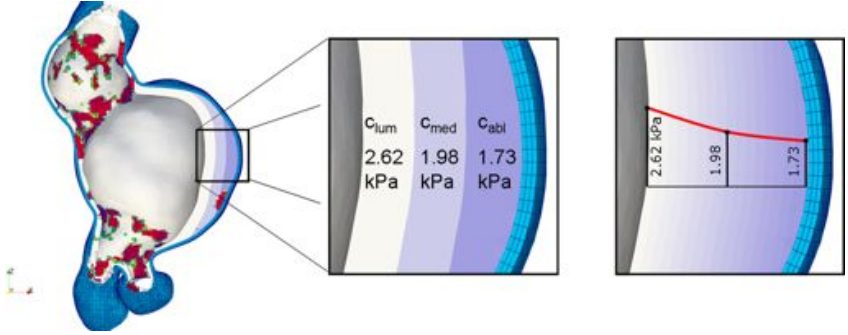


Figure 2.8: Left: Cut view of a representative AAA. White to violet color indicates ILT layers. Red color indicates calcification. First magnification: Distinct luminal, medial and abluminal layers with parameters as proposed by Gasser *et al.* [63]. Second magnification: Material parameters were linearly interpolated between the luminal surface ( $c = 2.62$  kPa), the 50 %-ILT-thickness sampling point ( $c = 1.96$  kPa) and the point of maximum ILT thickness ( $c = 1.73$  kPa) to obtain a continuous parameter distribution.

abluminal layers. In the final BACI-implementation, however, the parameters followed a continuous distribution to avoid stiffness jumps within the ILT (Figure 2.8 right). The parameter  $c$  was thereby linearly interpolated between the luminal surface, the 50 %-ILT-thickness and the point of max ILT thickness. For the modeling of a slightly compressible ILT material, the energetic potential stored by the material during the deformation was split into volumetric and isochoric contributions yielding  $W = W_{iso} + W_{vol}$  (see Section 2.4). Eq. (2.45) then reads in terms of modified invariants:

$$W_{iso} = c(\bar{I}_1^2 - 2\bar{I}_2 - 3) \quad (2.46)$$

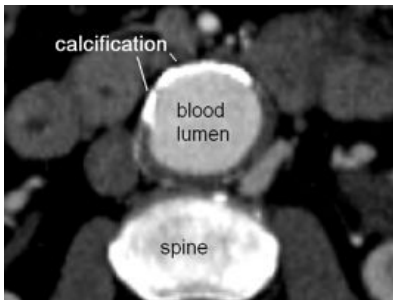
Different forms of volumetric SEFs have been proposed in literature [42, 144, 152, 191, 192, 201]. The model for the volumetric strain energy contribution in the current work was chosen as an Ogden-Simo-Miehe type of SEF:

$$W_{vol} = \frac{\kappa}{\beta^2}(\beta \ln J + J^{-\beta} - 1), \quad (2.47)$$

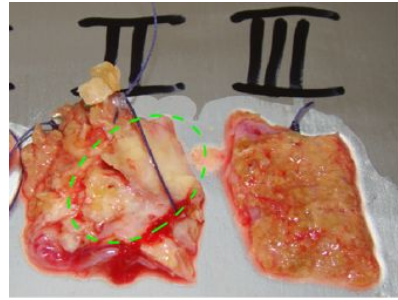
where  $\kappa$  is the bulk modulus and  $\beta$  an additional parameter. The parameter  $\beta$  was originally introduced to provide better fits of the models to experimental data, whereas meanwhile the choice of  $\beta = -2$  is suggested for numerical stability reasons [42]. Based on the previous literature research, a Poisson's ratio  $\nu = 0.48$  was assumed [40, 86]. With the material parameter  $c$  (Eq. (2.46)) and the Poisson's ratio available, the bulk modulus could be roughly calculated using  $\kappa = 8\frac{c}{1-2\nu}$ . It is to note that in case of spatially variable stiffness the bulk modulus needed to be adapted for each element to model a spatially constant Poisson's ratio. If the bulk modulus was not adapted, odd results occurred especially in case of large variation in the material parameter  $c$ , as e.g. shown in the term paper by Marc Hirschvogel [88].

## 2.5.2 Calcification

Calcifications are products of late stage atherosclerosis. Processes that lead to calcification are basically the same in AAAs and in the non-aneurysmal aorta [141]. The first paragraph in this current section outlines some of the related biology in arterial wall that has been associated with atherosclerosis and calcification. An abundant literature review of experiments and computational models is given in the following. The detailed explanation how calcifications were included in the present work closes this section.



(a) Calcification has a high X-ray attenuation yielding high HU values. It is shown in white color in CT images. It is an evidence for late stages of atherosclerosis.



(b) AAA wall samples harvested during open repair: Sample “II” features visible calcification (green dashed line) on its luminal side. Sample “III” shows no calcification.

Figure 2.9: Calcification is one of the AAA constituents that can be visually detected from CT images (a) and/or visually at the luminal side of AAA wall samples (b).

### Biology of Calcification

Complex cellular processes in the pathogenesis of atherosclerosis occur over years, whereas the exact mechanisms involved are still disputed [54, 205]. The initiation is most probably a mechanically caused damage to the endothelial cell layer. Local alterations of blood flow conditions (vortices/recirculations, reduced blood velocity and reduced wall shear stress) leading to damage of the arterial endothelial layer are thought to play a key role [33, 99, 134]. The risk factors hypercholesterolemia, hypertension, smoking, hyperlipidemia and diabetes mellitus (DM) promote the initiation and development of atherosclerosis [205]. Lipids, especially the low density lipoproteins (LDL), can cross the damaged endothelial barrier, where they are oxygenated (oxLDL) and accumulated. At the same time, thrombocytes adhere to the damaged endothelial layer and form aggregates. The aggregates excrete growth factors (platelet derived growth factor “PDGF” and transforming growth factor “ $\text{TFG-}\beta$ ”) that activate a proliferation of SMCs and their migration into the sub-endothelial space [54]. This finally leads to a formation of the fibrous cap, which also contains collagen and proteoglycans in its extracellular matrix. Simultaneously, the thrombocyte aggregates and the damaged endothelial cells (due

to the presence of oxLDL in the intima) express chemotactical substances that attract monocytes, which subsequently migrate into the sub-endothelial space where they differentiate into macrophages. This is basically an inflammatory response of the immune system. Within the intima, the macrophages secrete the monocyte-chemoattractive proteins “MCP-1” to recruit further monocytes and cytokines that promote the migration and proliferation of SMCs from the media into the intima. The macrophages then take up the oxLDL while transforming into immobile *foam cells*. The intracellular decomposition of LDL can lead to accumulation of cholesterol in the foam cells, if not transported away by the functional high density lipoproteins (HDL). The whole process leads to the formation of a visible *atheroma* at the luminal surface of the arterial wall, which is often referred to as the *atherosclerotic plaque* [205]. Calcification occur in the further stages of atherosclerosis, however, the sequence of events leading to vascular calcification are disputed in literature. In [198, 199, 205], calcification has been regarded as a passive, degenerative process within advanced atherosclerotic plaques: Hypoxia leads to degeneration and death of immobilized foam cells and SMCs which subsequently undergo necrosis. Calcium salts are discarded to the surrounding area of the necrotic core [205] forming calcifications. Other groups suggest that vascular calcification are active physiologic mechanisms [161] that are similar to regulated ossification in human bone [1], acting as a physiologic defense against progressive atherosclerosis [54]. It has also been shown that arterial calcification and calcium deposits in human bone are identical in their chemical compositions and that they primarily exist in the form of calcium phosphates (e.g. hydroxyapatite) [19, 120, 138]. However, independent of the exact mechanisms responsible for its formation, calcification does not occur in healthy vessel wall. It is always an evidence of local atherosclerosis [54]. Calcifications in AAAs can inhibit vessel expansion, but also put the patient at risk of plaque rupture, which in turn can lead to subsequent perforations in the degenerated aortic wall [132].

### Literature Review - Experiments and Strain Energy Functions

At the beginning of this paragraph it is to note that this work distinguishes between *calcified tissue* and *calcification*. “Calcified tissue” denotes the compound of aortic/AAA tissue with disperse calcification, while “calcification” denotes plain calcification without surrounding fibrous components. Both types are dealt within literature and are considered in this review. Further, no difference was made whether the experimentally investigated calcification stemmed from non-dilated aortic tissue or AAA tissue, since the underlying pathological processes are similar - as pointed out in the previous paragraph.

The probably first study to derive mechanical properties of calcified tissue was performed by Lee *et al.* [120] in 1991. Fibrous caps of atherosclerotic plaques from the abdominal aorta were harvested during autopsies and classified into cellular (SMCs and extracellular matrix,  $n = 7$ ), hypocellular (mainly extracellular matrix with only rare cells,  $n = 9$ ) and calcified (with calcium deposits) ( $n = 11$ ) plaques. In dynamic compression tests, in which specimens were loaded with a pressure of 9.3 kPa (equivalent to 70 mmHg) at 0.5 Hz, an average Young’s modulus of 2.03 MPa for the calcified plaques was measured. The stiffness was increased to 2.34 MPa (+13 %) for a loading frequency of 2 Hz. A complementary histological investigation of the plaques revealed a highly significant relation between stiffness and histological composition. It was concluded that “calcified caps were 4 – 5 times stiffer than cellular caps” [120].

In 1994, Loree *et al.* [127] investigated the uniaxial tensile behavior of circumferentially oriented samples of atherosclerotic plaques. Plaques were grouped in cellular ( $n = 12$ ), hypocellular ( $n = 9$ ) and calcified ( $n = 5$ ) tissue. For the calcified tissue, the average tangential modulus at 25 kPa was  $1.466 \pm 1.284$  MPa [it is to note that they obtained 25 kPa at approximately 1 % engineering strain, what they considered as “physiologic” stress and strain]. However, they also found that calcified tissue exhibited highly nonlinear behavior. For instance, they measured a tangential modulus  $32.0 \pm 55.9$  MPa at 20 % engineering strain. Two specimens of calcified tissue were additionally investigated for their ultimate strength, whereby these specimens yielded highest (701 kPa, 1.PK) and lowest strength (149 kPa, 1.PK) of the whole study, respectively. Tangential moduli of the three groups (cellular, hypocellular, calcified) at 25 kPa stress were shown to be not significantly different. Strangely, in the abstract of this publication, Loree *et al.* only listed the value  $1.466 \pm 1.284$  MPa for the tangential modulus of calcified tissue. Imprudently, this value was subsequently used in the constitutive modeling of calcifications by other renowned groups (e.g. [26, 96, 125, 195]). In Speelman *et al.* [195], the value of  $1.466 \pm 1.284$  MPa was even used as Young’s modulus in combination with a NeoHookean material model. The NeoHookean material, however, has a softening behavior that does definitely not meet the stiffening behavior stated by Loree *et al.* [127].

Beattie *et al.* [9] used inflation tests (internal pressurization) of ring segments from atherosclerotic aorta. The strain field was determined using particle tracking from images taken during the experiments at different internal pressures. Material properties were assessed using inverse FE analysis. One aortic ring segment had calcified deposits. The FE mesh used for inverse analysis was fine enough to resolve the calcified deposits. An initial stiffness of 3.99 MPa was calculated for calcifications, the stiffness prior to breaking at  $\lambda_{max} = 1.053$  was 10.7 MPa.

Plain calcification was investigated in a well organized study by Holzapfel *et al.* [95]. Anisotropic mechanical properties of 8 different tissue components of atherosclerotic lesions from human iliac arteries were considered. Among the tests, 4 calcified specimens underwent uniaxial tension in both axial and circumferential direction. Calcifications featured “very stiff and linear mechanical responses” [95] with an average Young’s modulus of  $12.6 \pm 4.7$  MPa. The average strength of calcifications was 179 kPa (Cauchy), the associated failure stretch was  $\lambda_{max} = 1.02$  (only two specimens were tested on failure properties, because of too small dimensions of the other ones). Both failure strength and stretch were smaller than the values for each of the other investigated tissues. Holzapfel *et al.* did not promote the use of a particular SEF to be used for the constitutive modeling of calcifications nor did they state anisotropy.

A very well presented study on mechanical properties of plain calcifications was performed by Marra *et al.* [138]. The study also contained morphological investigations of calcification microstructure by scanning electron microscopy and elemental analyses confirming the predominance of the chemical elements phosphorus and calcium over smaller amounts of mainly oxygen and carbon. For the mechanical testing, Marra *et al.* used a nanoindentation system to test very small specimens of plain calcification. Twelve specimens from 12 patients were harvested from the intimal side of excised AAA wall. Four separate indentations/measurements in the order of  $3 \mu\text{m}^2$  were made for each specimen. Depending on mounting methods and assumptions on Poisson’s ratio ( $0.1 \leq \nu \leq 0.4$ ), they obtained elastic moduli from 20.5 GPa to 24.5 GPa. They concluded that the “average elastic modulus of 22.7 GPa is three orders of magnitude stiffer than AAA wall ... and in the range of cortical bone” [138].

Table 2.2: Literature review of mechanical tests of calcification:

Group	Test set-up	Experimentally measured stiffness	No. specs.	Comments
Lee <i>et al.</i> (1991) [120]	dynamic compress.	2.03 MPa - 2.34 MPa	n=11	Calcified tissue from atherosclerotic aorta; 4-5 times stiffer than "normal" atherosclerotic tissue
Loree <i>et al.</i> (1994) [127]	uniaxial tension	1.47 MPa at 1% strain, 32 MPa at 20% strain	n=5	Calcified tissue from atherosclerotic aorta; no significant difference to non-calcified tissue; often misinterpreted
Beattie <i>et al.</i> (1998) [9]	inflation tests	3.99 MPa - 10.7 MPa	n=1	Material parameters of calcified deposits derived by IA
Holzappel, <i>al.</i> (2004) [95]	uniaxial tension	12.6 MPa	n=4	Plain calcification; isotropic, linear stress-strain behavior; different from properties of other tissues
Marra <i>et al.</i> (2006) [138]	nanoin-dentation	20.5 GPa - 24.5 GPa	n=12	Plain calcification from AAAs; 3 orders of magnitude stiffer than AAA wall
Maier <i>et al.</i> (2010) [132]	uniaxial tension	40 MPa (calcified tissue); 450 MPa (plain calc.)	n=3	Calcified tissue and plain calcification; calcium deposits causative for AAA morphology (indentations)

Our own group investigated dispersedly calcified and heavily calcified tissue (calcification over complete sample length) harvested during open AAA repair and plain calcification from iliac arteries [132]. In uniaxial tensile tests, an almost linear elastic behavior of plain calcification and highly calcified tissue was stated. In contrast, tissue with only disperse calcification ("calcified tissue") featured mechanical characteristics close to the properties of non-calcified AAA tissue (nonlinearity, "J-shape", hysteresis). The stiffness of heavily calcified tissue (40 MPa) and plain calcification (450 MPa) was drastically increased compared to the stiffness of tissue with only disperse calcification or without calcification. Strength could not be tested. In complementary FE analyses, it was shown that calcifications were causative for local indentations in the individual AAA morphology. A NeoHookean SEF with  $W = c_1(I_1 - 3)$  and  $c_1 = 8.9 \text{ MPa}$  was proposed for constitutive modeling of calcifications.

An overview on the studies investigating mechanical properties of calcified tissues and calcifications is given in Table 2.2. This overview again stresses that it should be distinguished between calcified tissue and plain calcification. Calcified tissue still featured the material non-linearity characteristic for soft tissue. Stiffness values measured for dispersedly calcified tissue ranged from 1.48 MPa to 32 MPa. In contrary, the calcified deposits featured a linear stress-strain behavior and experimentally measured stiffness ranged from 3.99 MPa to 24.5 GPa. The studies consistently stated an increased stiffness of calcified tissue or calcification to non-calcified tissue. Strength values could not be measured reliably [127, 95]. Among the previously introduced studies, only our own group proposed a SEF for the modeling of calcifications in [132]. Other groups mainly used the measurements of Loree *et al.* [127] to create constitutive models to be used in nonlinear FE analysis. For instance, Huang *et al.* [96] used a curve fitting

algorithm to derive material properties for the SEF

$$W = D_1(\exp(D_2(I_1 - 3)) - 1). \quad (2.48)$$

The material parameters were  $D_1 = 18.8 \text{ kPa}$  and  $D_2 = 20$ , representing a nonlinear behavior with notable stiffening. This adequately describes the behavior of calcified tissue. In [26, 96, 125], this material model, however, was used for the constitutive modeling of plain calcifications. But even worse, in Speelman *et al.* [195], a NeoHookean material law with a Young's modulus of  $1.48 \text{ MPa}$  was used for calcifications. This resulted in calcifications being softer than AAA wall modeled with standard literature material models (e.g. by the Raghavan & Vorp (R&V) material model [164], which is discussed in more detail on page 50). To avoid such mistakes, it is suggested to plot stress-stretch curves for test cases (e.g. uniaxial tension under the assumption of incompressibility) for the material models to interpret SEFs and their material parameters. This is exemplarily done in Figure 2.10.

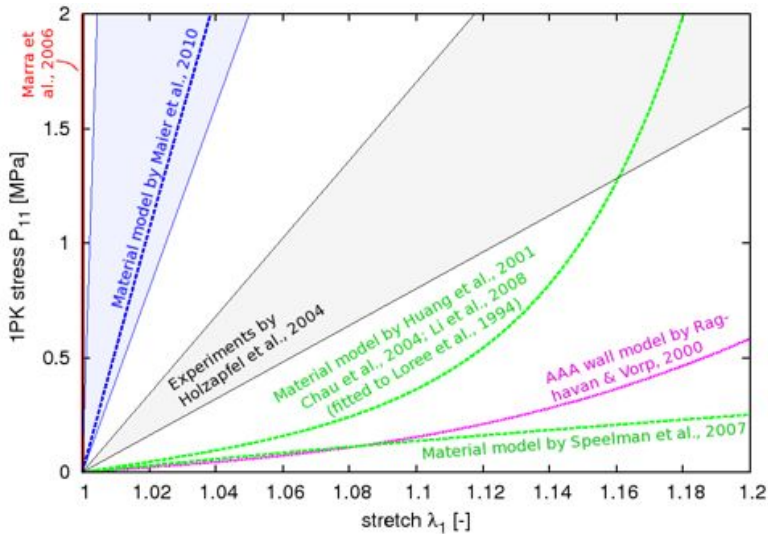


Figure 2.10: Stiffness ranges for calcification measured in experiments (solid lines) by Holzapfel *et al.* (gray), Marra *et al.* (red) and Maier *et al.* (blue). Stress-stretch curves of different material models for the case of uniaxial tension are plotted with dashed lines. The material model utilized by Huang *et al.*, Chau *et al.* and Li *et al.*, respectively, yielded a characteristic stress-stretch curve for calcified tissue. The calcification model by Speelman *et al.* yielded a stress-stretch response that was softer than the AAA wall material model by Raghavan & Vorp over a wide strain range.

## Literature Review - Computational Modeling of Calcified AAAs

Impact of calcifications has only been rarely treated in computational AAA wall stress analyses so far. Neglecting calcifications is common practice in literature. However, calcifications are frequently present in atherosclerotic lesions of AAAs [141] within the intima or at the interface between intima and media as consequence of the biological processes explained previously. More infrequently, calcifications can also be found in the ILT of AAAs [181]. Transmural calcification within the adventitia is exceptional for AAAs and is more commonly found in patients suffering from arterial occlusive disease with diabetes [161] and end stage renal disease [182].

To my knowledge, there are only five original research contributions that incorporate the influence of calcifications in computational AAA wall stress analyses. The first investigation was already performed in 1993 by Inzoli *et al.* [106]. Idealized AAA geometries were used in this FE analysis, in which they made use of the small strain theory. For the modeling of calcifications, they chose a Young's modulus of  $E = 20$  MPa and a Poisson's ratio of  $\nu = 0.5$ . The choice of the parameters, however, could not be tracked back based on the references given. Inzoli *et al.* stated that existent calcifications could increase the stress in adjacent AAA wall 1.1 to 3.1 times, dependent on the location of the calcification. However, one should not overrate these findings, since first idealized AAA geometries together with fictitious locations of calcifications were used and second, details of the incorporation of calcifications were missing. Beside the work by Inzoli *et al.* [106], there were four major investigations on AAA calcification by de Putter *et al.* [37], Speelman *et al.* [195], Li *et al.* [125] and our own group [132] which used four different approaches that are discussed in more detail in the following:

In 2006, de Putter *et al.* [37] presented three different methods for the CT-image-based incorporation of calcifications in preexistent FE meshes. Their ideas are noteworthy, but in the application the authors missed to bridge the gap from highly idealized geometries (a brick of AAA wall with an embedded calcification) to something close to an idealized or realistic AAA geometry. The calcifications were modeled using a NeoHookean law with shear moduli  $G$  ranging from 1.5 MPa to 100 MPa. The inclusion of calcification was performed subsequently to the creation of an initial FE mesh for the complete structure domain (the artificial brick which represented the AAA wall). The coordinates of the FE mesh and the CT data were linked such that the calcification seen in CT images was located within the FE domain. The HU information from the CT images was therefore available within the FE framework. In the first method, de Putter *et al.* calculated iso-HU-intensity surfaces within the FE mesh and used a threshold of 200 HU to define the existence of calcification. After tetrahedral remeshing material properties of calcification were applied to the inside of the isosurface whereas the outside was considered as normal AAA wall. In the second method, the HU within the original CT image was calculated at the location of each finite element. Elements that featured a HU above the threshold were considered as calcification. In the third method, they assumed a linear relation between the HU in the CT image and the tissue stiffness, whereas just the shear modulus was adapted for each element with a HU above the threshold. The formula they applied for the adjustment of the shear modulus  $G(\mathbf{X})$  of each element was

$$G(\mathbf{X}) = G_{tissue} + \frac{HU(\mathbf{X}) - HU_{thres}}{HU_{max} - HU_{thres}} (G_{calc} - G_{tissue}). \quad (2.49)$$

$G_{tissue}$  and  $G_{calc}$  were the shear moduli for non-calcified tissue and calcification, respectively.  $HU(\mathbf{X})$ ,  $HU_{thres}$  and  $HU_{max}$  were the HU at location  $\mathbf{X}$ , the threshold for the existence of calcification and the maximum HU within the image. In subsequent FE calculations (the bricks under uniaxial tension), Putter *et al.* stated an increase in stress at the interface between calcification and surrounding tissue for most combinations of methods and shear moduli [this is of course not surprising if one introduces a second stiffer material into a brick that would otherwise feature completely homogeneous material parameters]. They proposed to discard method 1 due to uncertainties of locating the iso-surfaces mediated by too coarse CT resolution. To conclude with this work, the idea by Putter *et al.* to use the HU for the adaptation of element-specific stiffness is acknowledged, while the computational results should definitely not be subscribed to real AAA geometries.

In Speelman *et al.* [195], six real (but a little bit too excessively smoothed) AAA geometries were investigated. If calcification was present at the location of AAA wall, the complete wall was considered as calcified wall (all elements over the wall thickness - there were no elements left which represented the non-calcified part of the wall). Calcifications were not incorporated as separate constituents of the AAA, as e.g. seen in Putter *et al.* [37], but were rather combined to one material with the non-calcified adventitia or other fibrous parts of the arterial wall. Since Speelman *et al.* [195] used only one constitutive law for this compound and changed material parameters if calcifications were present, this method will be called *implicit* modeling in the following. Methods that consider calcifications as separate constituents (as e.g. by Putter *et al.* [37]) will be called *explicit* modeling methods in the following.

Speelman *et al.* used the Raghavan & Vorp material law [164] for the modeling of non-calcified AAA wall and a NeoHookean material law for the wall compound if calcifications were present. They investigated the influence of three different elastic moduli for calcified wall compound on wall stress results. Surprisingly, the elastic moduli for the calcified compound were chosen to 0.19 MPa, 1.47 MPa and 2.75 MPa. This correlated to the specification of calcified tissue in the abstract of the work by Loree *et al.* [127] - which was intended to resemble the stiffness of calcified tissue at 1% strain. However, Loree *et al.* also stated that there was a drastic increase of stiffness at increasing strain [127], which was not considered in the contribution by Speelman *et al.* [195]. In consequence, the choice of the three above mentioned elastic moduli did not reflect a meaningful representation for calcifications: For the case of  $E = 0.19$  MPa, calcifications yielded a material behavior that was softer than the behavior of AAA wall modeled by the R&V material law. For  $E = 1.47$  MPa, calcifications behaved slightly stiffer than R&V AAA wall initially, but became softer at larger strain due to the softening behavior of the NeoHookean material. This circumstance is also depicted in Figure 2.10. Only for the choice of  $E = 2.75$  MPa, calcifications behaved stiffer than AAA wall over the complete physiological strain range. Not surprisingly, Speelman *et al.* could only state a consistent increase of peak wall stress for the choice of  $E = 2.75$  MPa. Results for  $E = 0.19$  MPa were not even mentioned.

The implicit modeling method by Speelman *et al.* comes along with a series of drawbacks: Implicit modeling is associated with stiffening of wall elements (premise: Correct choice of material parameters for calcifications). This naturally leads to stress concentrations and increased stress in these elements. However, this method makes it impossible to distinguish whether the high stress acts in calcifications or the fibrous part of the vessel wall. Investigations of interface phenomena between calcification and adjacent AAA wall or also growth and remodeling extensions to the FE analysis become impossible. Finally, failure criteria for AAA wall as e.g.

introduced in [222] are not applicable any more. With regard to the series of modeling errors and limitations for later rupture risk evaluation, the implicit modeling method as proposed by Speelman *et al.* should be discarded.

On the contrary, a method of explicit modeling of calcifications was presented by Li *et al.* [125]. Therein, calcifications were treated and modeled as separate constituents of the AAA, leaving the vessel wall mechanics unchanged. In total, 20 AAAs were investigated by Li *et al.* [125]. Calcifications were identified and segmented manually by means of thresholding in a commercial software. The segmentation effort in [125] has to be appreciated, leading to inclusion of all calcifications which were assumed to be embedded within the AAA wall. After the meshing, however, some of the calcifications were not embedded any more but they rather represented the only wall constituent that was left at these locations. The material law for calcifications was adapted from measurements by Loree *et al.* [127] (SEF and parameters according to Eq. (2.48)). It could not be concluded from the article, whether Li *et al.* measured the peak wall stress only in the non-calcified wall or also within the calcification. Nonetheless, the authors stated a general increase of peak wall stress when calcifications were included in the FE calculation. They did not find a correlation between the increase in peak wall stress and the amount of calcification. They concluded that the location of calcifications was more important for the determination of peak wall stress rather than the amount of calcification.

The most recent study on calcification in AAA wall stress analysis was published by our own group (Maier *et al.* [132]), which included FE simulation of three patient-specific AAAs. For the model creation, calcifications were identified by manual segmentation from CT images such that they were limited to the region of previously segmented ILT geometry as shown in Figure 2.11 (a). Calcifications were modeled as separate AAA constituents adjacent to the luminal side of the AAA wall (Figure 2.11 (b)). The approach was motivated by the fact that in most cases during AAA wall sample preparation, calcifications were visible to the human eye from the luminal side of the AAA wall. Further, it was also motivated by the aspect that atherosclerotic processes especially occur within the intima and media of the vessel wall. Also the increased collagen remodeling and production in the media and adventitia of AAAs [15, 180] might entail an accumulation of calcifications close to the luminal side of AAA wall. Potentially existent intimal layers covering the calcifications from the luminal side were neglected in that study. All constituents were meshed as separate parts with matching grids. AAA wall was modeled with the material law proposed by Raghavan & Vorp [164], while ILT and calcifications, respectively, took a coupled-form of the NeoHookean material law [89] given as

$$W = c_1(I_1 - 3) + \frac{c_1}{\beta}(J^{-2\beta} - 1). \quad (2.50)$$

For ILT, the material parameters in Eq. (2.50) were set to  $c_1 = 18 \text{ kPa}$  and  $\beta = 4.5$ . For calcifications the parameters were chosen to  $c_1 = 8.929 \text{ MPa}$  and  $\beta = 2.0$  in accordance to the measurements that were performed within the same study [132] (Table 2.2, Figure 2.10). FE simulations were performed for models considering calcifications (denoted *wCa*) and for models neglecting calcifications (*noCa*). The *noCa*-models could be easily generated by changing the material parameters of calcifications to material parameters used for ILT, while the geometry and the mesh were left unchanged. Large deformation FE solutions (including physiological prestress) were calculated for a constant luminal pressure of  $p = 121 \text{ mmHg}$  consistently applied for all patients.

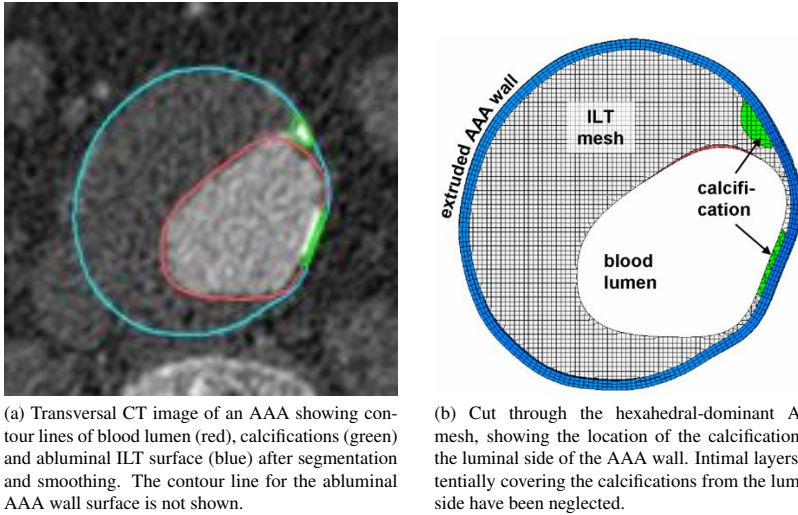


Figure 2.11: Calcifications were segmented manually from CT images (a). They were meshed as separate constituents with matching grids to ILT or AAA wall (b). Pictures adapted from Maier *et al.* [132].

FE simulations showed that presence of calcifications consistently reduced the average wall stress in all patients. The maximum wall stress decreased in two patients, while one patient featured an increased maximum wall stress when calcifications were included. Maximum stresses in calcifications were higher than maximum stresses in the AAA wall for all patients. Wall stress distributions for the three patients who were considered in this study by Maier *et al.* are shown in Figures 2.12 through 2.14. Each figure depicts first the locations of calcifications in the AAA, then the stress distribution in the AAA wall obtained for the wCa-model and finally the wall stress distribution for the noCa-model. For the wCa-model, AAA wall stress was markedly decreased at locations of calcification. In noCa models, regions of high von Mises stress were located at concave shaped areas and indentations of the AAA wall. Visual comparison of calcified regions with the FE results, however, revealed that high stress areas of the noCa-models matched regions where actually severe calcification was present. Indeed, the same regions exhibited very low wall stress in wCa-simulations. In Figure 2.15, it can be nicely seen that at such regions the outer wall was held almost stress-free, while higher stresses occurred in the underlying calcifications. The wall stress distribution along the circumference of the same cut is given in Figure 2.16, where both the wall stress distributions for the noCa- and the wCa-model are given. Regions with underlying calcifications are indicated by gray background color. This figure suggests that stress peaks can occur in the wall close to the borders of calcifications. Such stress peaks can occur due to sudden stiffness changes between the calcification, ILT, and AAA wall in simulation. However, it was questioned, whether such stress peaks were physiologi-

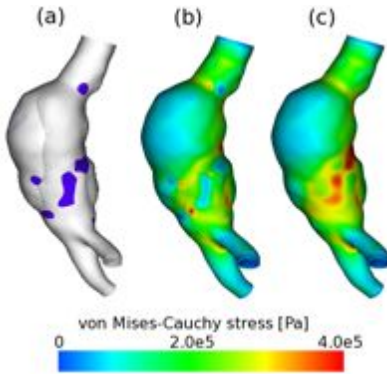


Figure 2.12: Patient 1: Slightly calcified AAA. (a) Violet color indicates calcification. (b) Wall stress results for wCa model. (c) Wall stress results for noCa model. Pictures adapted from Maier *et al.* [132].

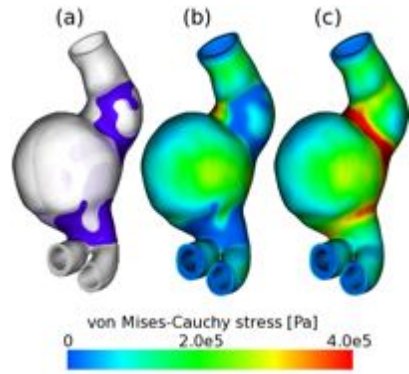


Figure 2.13: Patient 2: Severely calcified AAA. (a) Violet color indicates calcification. (b) Wall stress results for wCa model. (c) Wall stress results for noCa model. Pictures adapted from Maier *et al.* [132].

cal, since remodeling processes were likely to counteract at these sites. Also a more smooth modeling of the material transitions was expected to reduce such stress peaks.

The main findings of the study by Maier *et al.* [132] were that indentations at the AAA wall and calcified regions matched very well. It was hypothesized that existent calcification were causative for the individual patient's AAA morphology. Inclusion of calcifications into FE simulations is therefore crucial to obtain reliable wall stress results especially for patients with severe AAA calcification. It was also stated that maximum wall stress did not generally increase in case of AAA calcification. This is also in agreement with the clinical study by Siegel *et al.* [190], showing that the percentage of rupture is the same for calcified and non-calcified AAAs.

Compared to the earlier studies by Speelman *et al.* [195] and Li *et al.* [125], the approach by Maier *et al.* has the advantage that it can distinguish between stresses acting in calcifications and stresses acting in the fibrous part of the wall (media and adventitia). This is due to the fact that the explicit modeling method proposed by Maier *et al.* incorporates calcification as separate parts. Hereby, mechanical properties of the fibrous part of the vessel wall remain unchanged. Remodeling processes, damage modeling, and failure criteria for the fibrous part of the wall can still be applied to the AAA wall. While the implicit method by Speelman *et al.* leads to increased stress in the complete AAA wall when calcification was present, the proposed explicit method leads to stress concentrations within the much stiffer calcifications and decreased stress in the AAA wall. In contrast to the results obtained by the implicit method, explicit modeling does not always entail increased peak wall stress. This discrepancy also leads to different evaluation of the patient's AAA rupture risk. The relation between individual AAA morphology and existent calcifications becomes most clear in the study by Maier *et al.* [132]. This also proves that large calcification can prevent the dilation of adjacent AAA wall, resulting in bulges especially at calcification-free regions.

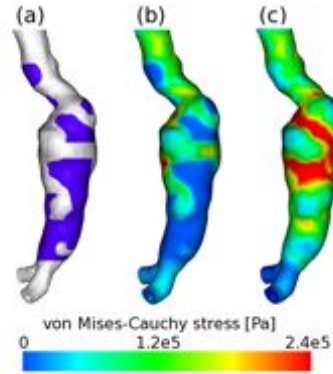


Figure 2.14: Patient 3: Heavily calcified AAA. (a) Violet color indicates calcification. (b) Wall stress results for wCa model. (c) Wall stress results for noCa model. Pictures adapted from Maier *et al.* [132].

### Implementation Issues

Calcifications may be small, widely separated foci, measuring only a few mm, or large plate-like structures of irregular shape that vary in size and can even measure several cm in length [54, 138]. Several of the above mentioned studies showed that calcifications might influence the stress level in the adjacent AAA wall and also stress peaks can occur locally at the borders of small calcifications. Generally, calcifications can be easily detected in CT images due to their high X-ray attenuation. However, their irregular shape and the vast number of separated foci make a manual segmentation of calcifications almost impossible. Manual segmentation of calcifications was performed in the studies by Li *et al.* [125] and by our own group [132] - but this method also came along with several drawbacks:

- **Time-consumption**  
To give a guesstimate, the segmentation and mesh generation for the three calcified AAAs in the study by Maier *et al.* [132] presented on the preceding pages, took about 50 hours per AAA. Already for that reason, the manual segmentation does not provide a feasible method to be applied to a multitude of AAAs.
- **Location**  
The method proposed by Maier *et al.* [132] only allowed for calcifications adjacent to the luminal side of the AAA wall, but not within the intima or the media. Actually, the atherosclerotic processes which are responsible for the existence of calcifications mainly occur in the intima and the media of the vessel wall. This should be accounted for in a more advanced method.
- **Resolution of material transitions**  
The previous methods revealed the appearance of stress peaks at transitions from calcifications to AAA wall. However, it is doubted whether such stress peaks are physiologically feasible. Firstly, remodeling processes within the AAA wall would probably lead to net collagen production at such high stress regions over a longer period of time [112], which in turn would counteract stress peaks. Secondly, stress singularities in the FE model occur

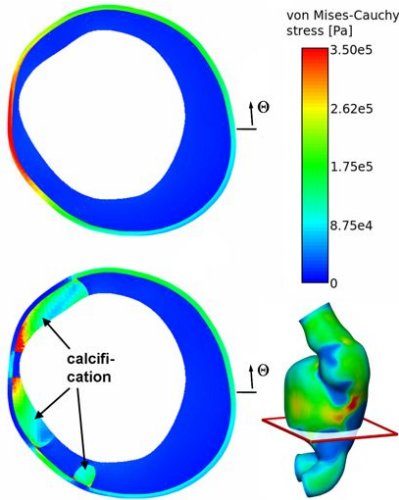


Figure 2.15: Cut through the AAA of patient 2. Color visualizes the von Mises-Cauchy stresses in the noCa (top) and wCa-model (bottom), respectively. The 3D view marks the position of the cut plane in the AAA. Picture adapted from Maier *et al.* [132].

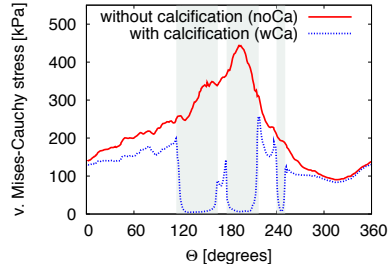


Figure 2.16: Wall stress along the circumference of the cut plane displayed in Figure 2.15. The diagram shows the von Mises-Cauchy stress in the innermost layer of wall elements for the noCa-model (red) and the wCa-model (blue). Regions with calcifications are shaded light gray. Stress peaks can be noted in the wCa-model close to the borders of calcifications. Adapted from Maier *et al.* [132].

due to the sudden material transition. A better resolution of the potentially more gradual transition between calcifications and the embedding tissue is expected to reduce such singularities.

- Resolution of gaps and cracks  
Small gaps or cracks between calcification - even if captured during segmentation - can usually not be preserved during smoothing and meshing, yielding a final model that does not resolve these features any more.
- Horizontal edges  
Manual segmentation sometimes brought about calcifications with a predominantly circumferential orientation and edges perpendicular to the superior-inferior AAA axis. This can be seen in Figure 2.14 (a), where some of the calcifications feature sudden horizontal edges. This phenomena is attributable to segmentation in transversal CT images with non-isotropic voxels (larger voxel edge length over slice thickness than in-plane) which does not reflect the actual geometry of calcifications.

To overcome the aforementioned drawbacks, the current work used the method of Hounsfield Unit mapping (“HU mapping”) to incorporate calcifications into FE analysis. This approach

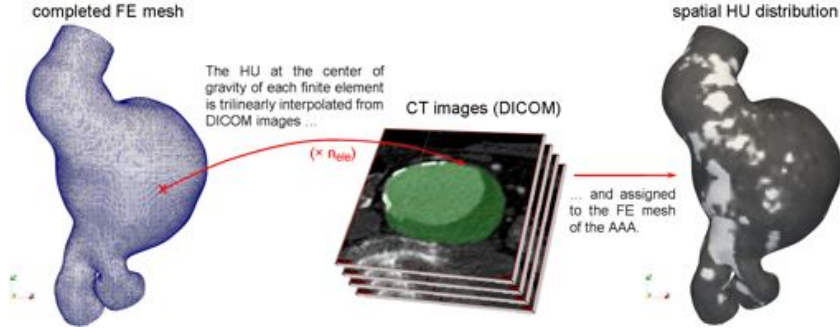


Figure 2.17: HU mapping: The HU at the center of gravity of each finite element was trilinearly interpolated from the DICOM image data (same CT image sequence as used for segmentation!) and assigned to the mesh yielding the spatial HU distribution on the AAA geometry.

was inspired by the work of de Putter *et al.* [37], who made use of a relation between the HU in the CT image and the stiffness of the tissue, but who did not apply this method for realistic AAA geometries. Some preliminary work on this method was also performed in term papers by Sophia Lauterbach [119] and Marc Hirschvogel [88]. The HU mapping-method set in after segmentation and mesh generation, which already reveals its great advantage: There was no need to modify the segmentation and meshing protocol as introduced in Sections 2.2 and 2.3. Instead, the HU mapping made use of the already existing FE mesh. The FE mesh was processed using a custom-made algorithm, which trilinearly interpolated the HU at the center of gravity of each element from the CT images. The interpolated values were written to the FE mesh, which resulted in a spatial representation of the HU values from the CT images as indicated in Figure 2.17.

Each element, independent of representing a part of the ILT or the AAA wall, was now assigned the HU as obtained at its location within the CT data. Although there is no exact relation (the equation in de Putter *et al.* [37] was just a rough guess, too), a strong positive correlation between the locally measured HU and the stiffness of the tissue/calcification was assumed. Under this premise, it was possible to assign material properties to each element, based on the underlying HU. A very concise and viable approach was the addition of a SEF representing the mechanical behavior of calcifications to the already existent material model (SEF) for the AAA wall or the ILT, respectively:

$$W_{calcified\_ILT} = W_{ILT} + W_{calc.}, \quad (2.51)$$

$$W_{calcified\_wall} = W_{wall} + W_{calc.}, \quad (2.52)$$

where  $W_{ILT}$  and  $W_{wall}$  are the standard SEFs (isochoric & volumetric contributions) for non-calcified ILT and wall, respectively.  $W_{calc.}$  implies both the isochoric and the volumetric contributions for the calcifications. The formulation of  $W_{calc.}$  must satisfy  $W_{calc.} = 0$  for non-calcified elements to retain the behavior of the original material and  $W_{calc.} \gg 0$  for elements representing calcification. Due to the fact that the stiffness of calcifications is orders of magnitudes higher

than the stiffness of AAA wall or ILT (as shown in experiments by Holzapfel *et al.* [95], Marra *et al.* [138] and Maier *et al.* [132]),  $W_{ILT}$  and  $W_{wall}$  become comparably small for calcified regions. The almost linear stress-strain behavior of calcification that was experienced can e.g. be modeled by a NeoHookean material combined with the previously introduced Ogden-Simo-Miehe type volumetric contribution (Eq. (2.47)):

$$W_{calc.} = W_{calc,iso} + W_{calc,vol} = \alpha_{HU}(\bar{I}_1 - 3) + \frac{\kappa}{\beta^2}(\beta \ln J + J^{-\beta} - 1) \quad (2.53)$$

The mentioned requirements on  $W_{calc.}$  could be incorporated by a spatial adaptation of  $\alpha_{HU}$  according to the HU of the respective element. In the present study, the function for the adjustment of  $\alpha_{HU}$  was set to

$$\alpha_{HU} = \begin{cases} 0, & HU \leq HU_{min}, \\ \frac{1}{2} \left( \sin\left(\frac{\pi(HU - HU_{min})}{HU_{max} - HU_{min}}\right) - \frac{\pi}{2} \right) + 1 \alpha_{max}, & HU_{min} < HU < HU_{max}, \\ \alpha_{HU,max}, & HU \geq HU_{max}. \end{cases} \quad (2.54)$$

In Eq. (2.54),  $HU_{min}$  is the lower threshold at which the transition from the embedding tissue to calcification was initiated. Below this threshold  $\alpha_{HU}$  was zero and the material behavior of the tissue remains unchanged.  $HU_{max}$  is the upper threshold, above which pure calcification with  $\alpha_{HU,max} = 8.929 \text{ MPa}$  [132] was assumed. The sine function that was applied for HU values in between  $HU_{min}$  and  $HU_{max}$  was chosen to mimic a smooth transition from non-calcified to calcified regions. There were no requirements on continuous differentiability of  $\alpha_{HU}$ . A schematic curve for  $\alpha_{HU}$  is given in Figure 2.18. Concerning the volumetric contribution in Eq. (2.53), investigations in the term paper by Marc Hirschvogel [88] recommended to set  $\kappa$  and  $\beta$  in such a way that the Poisson's ratio of the already existent material (ILT/AAA wall) and the Poisson's ratio of calcifications match. This was achieved by the element-wise adaptation of the bulk modulus to the parameter  $\alpha_{HU}$  using the formula  $\kappa = \frac{2\alpha_{HU}}{1-2\nu}$ .

It is to note, that it was not possible to derive an *exact* relation between the HU and the stiffness of calcifications. The choices for the stiffness value for calcifications ( $\alpha_{HU}$ ) and the function used for the material transition remained a very subjective decision. The same applied to the adjustment of the upper threshold. A reference value, however, was found for the lower threshold  $HU_{min}$ , since in literature the presence of calcifications was indicated by  $HU > 200$  [37]. Unfortunately, the attenuation in the blood lumen, enhanced by contrast agent, already exceeded 200 HU in almost any AAA. The choice of  $HU_{min} = 200$  would lead to spill-over-effects from the blood lumen into the innermost layers of ILT or AAA wall and accordingly lead to an artificial stiff crust next to the blood lumen. In the present work, the lower threshold  $HU_{min}$  was therefore set to  $HU_{min} = 300$  or, in case of even higher attenuation in the blood lumen, to the maximum HU in the blood lumen of the respective AAA plus 10 HU:

$$HU_{min} = \max_{Lum.}(\max\{HU\} + 10, 300). \quad (2.55)$$

For automatization reasons, the maximum HU in the lumen was thereby determined as the maximum HU only along the lumen centerline. An example for the assignment of material properties is shown in Figure 2.19. For this AAA,  $HU_{min}$  was set to 320 HU. Pure calcification was assumed for  $HU > 520$ . In the magnification within Figure 2.19, it can also be recognized that

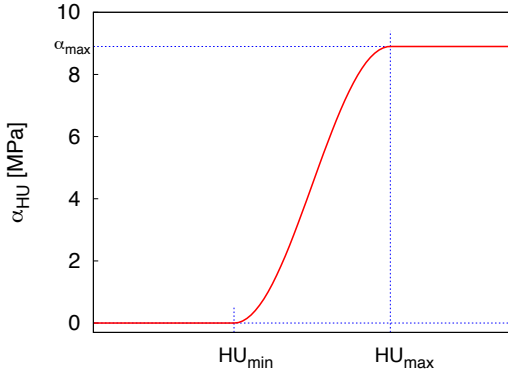


Figure 2.18: Stiffness  $\alpha_{HU}$  as a function of the HU value. The stiffness was set to 0 before the HU reaches a lower threshold. After a transition zone between  $HU_{min}$  and  $HU_{max}$ , pure calcification was assumed for  $HU > HU_{max}$ . Especially the lower threshold  $HU_{min}$  needed to be adapted patient-specifically due to administration of contrast agent during the CT imaging routine with associated high attenuation in the blood lumen.

calcification properties were assigned to the inner layer of AAA wall (e.g. intima/media), but not to the outer two layers of elements which represented the usually non-calcified adventitia.

The method of HU mapping for the incorporation of calcification into FE analysis that was implemented for the current work comes along with some advantages and disadvantages which are summarized briefly:

- + The method does not require any modifications to the segmentation or the meshing. The HUs are mapped to the FE mesh and the decision whether calcification is existent or not is shifted to the element evaluation in the FE solver. This also enables a quick and easy switch between simulations including or neglecting calcifications.
- + The HU mapping automatically captures all calcifications that have at least the size of the mesh size. The same applies to gaps and cracks between calcifications. They can be resolved if they are larger than the mesh size.
- + Calcifications can be modeled within both the ILT and/or the AAA wall. One can freely choose in how many or in which AAA wall layers calcifications should be considered.
- A very accurate segmentation of the AAA geometry is needed, since it determines the relative location of calcifications. If the lumen and the ILT are segmented too small, the calcifications tend to be positioned further outside in the AAA wall. For a too large segmentation of the lumen and the ILT, the calcifications are located deeper within the ILT. Ideally, during segmentation, calcifications should be half-included within the lumen/ILT mask, while the second half is positioned in the domain of the AAA wall.

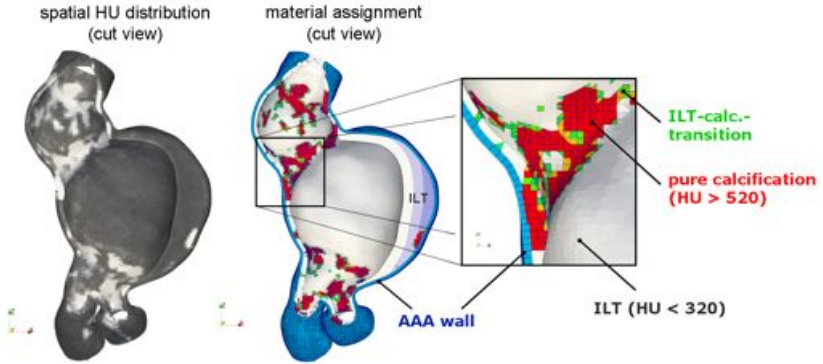


Figure 2.19: HU distribution and material assignment in a cut view for a representative AAA. Material properties for calcifications were assigned to the inner layer of the AAA wall and anywhere within the ILT, where calcification was present ( $HU > 320$ ). Material properties for the outer two layers of elements of the AAA wall remained unchanged. The transition between calcification and AAA wall/ILT was set to  $320 \leq HU \leq 520$  (green to orange color) with material parameters according to Eq. (2.54). Pure calcification (red color) was assumed to be present for  $HU > 520$ .

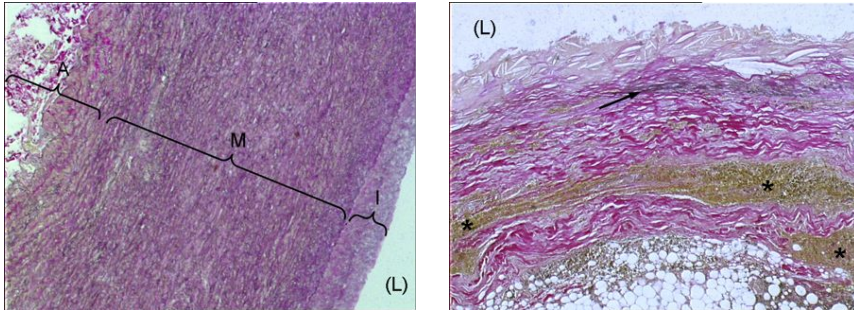
- The  $HU_{min}$  needs to be larger than the maximum HU in the lumen, which needs to be set patient-specifically. Calcifications with low HU might be neglected for the reason of too much contrast agent, while user intervention is impossible.

### 2.5.3 Arterial Wall of AAAs

Rupture of an AAA occurs when stress in the vessel wall exceeds the local strength. The mechanical AAA wall properties are therewith the key factors of AAA rupture which are dealt within this section. The biology of arterial walls and the histopathological changes associated with AAA formation are explained in detail. Contrary to the previous sections dealing with ILT and calcifications, the following literature review on experimental works does not aim to be complete. Some pointless contributions have been omitted on purpose, while it cannot be excluded that a valuable study has been overlooked. The abundant literature on AAA simulations (all of them dealing somehow with AAA wall) is not listed at length in this section. It is referred to the recent review article by Humphrey and Holzapfel [101] for an up-to-date overview on existent computational approaches. The section concludes with the implementation issues for FE simulation.

#### Biology and Histopathology of the AAA Wall

All healthy blood vessels, except the thin-walled capillaries and venules, feature similar fundamental structures. Based on diameter and function, the vessel wall can exhibit characteristic



(a) Healthy aorta: The intima (I) exhibits some age-related thickening. There is a clear boundary to the media (M), which represents the thickest layer. There is no distinct boundary between media and adventitia (A) in this slice. The image appears slightly grayish due to the homogeneously distributed elastin.

(b) Aneurysmatic aorta: There is a marked decrease of elastic fiber content with only fractions of elastin left (indicated by the arrow). Cell infiltrates (e.g. macrophages) are displayed in brown color and are indicated with stars “\*”.

Figure 2.20: Histological slices of healthy aortic wall and AAA wall with Van Gieson’s staining (collagen=violet, elastin=black, nuclei=brown/black). The luminal side of wall is indicated by an (L), respectively. Image courtesy of Christian Reeps.

modifications. In general, a healthy vessel wall features three different layers, which are termed (tunica) *intima*, (tunica) *media* and (tunica) *adventitia* [55, 91, 108]. The intima is the inner boundary of the vessel which consists of one layer of endothelial cells and which is in contact to the blood flow. The endothelial cells have a sensing function (e.g. wall shear stress) and they can absorb and secrete chemical substances. The *stratum subendotheliale* below the endothelial layer can contain delicate connective tissue, fibroblasts and small amounts of SMCs [55]. The *membrana elastica interna* is a thin layer of fenestrated elastic fibers which forms the boundary to the media. In healthy arteries, the media bears most of the forces exerted by blood pressure. It is thinner in veins. It contains SMCs which are mainly oriented along the circumferential direction as well as an extracellular matrix containing elastic and collagenous fibers and proteoglycans [91]. Arteries close to the heart, such as the aorta, feature a higher content of elastic fibers (“elastic” type arteries), while distal arteries feature higher amounts of SMCs (“active” type arteries) [55]. The adventitia consists of connective tissue, mainly collagenous fibers. A slight *membrana elastica externa* can form the border to the media. The *vasa vasorum* enters the adventitia for the blood supply of larger vessels. The adventitia also serves to the fixation of the vessel to its surroundings [108]. This layered structure can also be seen in the histological slice of a healthy aortic wall sample in Figure 2.20 (a).

AAA development is associated with changes of connective tissue and the loss of elastin is often regarded as an initial step of AAA formation [78, 180] as a consequence to genetic predisposition [20] and/or mechanical and chemical mechanisms [167]. The fragmentation of elastic fibers proceeds during AAA growth. This decrease of elastic fiber content is often concomitant with the death of SMCs and increased collagen production [15]. In histological examinations of

AAA wall, He and Roach [78] found volume fractions of elastic fibers and SMCs of  $2.4 \pm 2.2\%$  and  $2.2 \pm 2.0\%$ , respectively. The percentage of collagen fibers was  $95.6 \pm 2.5\%$ . For healthy abdominal aortic wall, volume fractions of the same constituents were  $22.7 \pm 5.7\%$ ,  $22.6 \pm 5.5\%$  and  $54.8 \pm 4.5\%$ , respectively [78]. Especially type I and III collagen production in the adventitia compensates the loss of elastic fibers and SMCs to retain the structural integrity of the AAA wall in the early stages [15]. Probably under the influence of protease overexpression [159] (mostly represented by matrix metalloproteinases, but also cathepsin and serine proteases [167]) and/or inflammatory cells that also infiltrate due to adventitial neovascularization [180], an imbalance between collagen production and structural protein degradation can set in. Proteases feature an elastase activity and are capable of degrading all kinds of extracellular matrix proteins while at the same time inflammation hampers the synthesis of elastic fibers and synthesis of proteinase-inhibitors [167, 180]. This critical wall weakening, together with an increase in mechanical loading due to associated vessel enlargement can eventually lead to the rupture of the AAA wall. A histological slice through an AAA wall sample is given in Figure 2.20 (b).

### Literature Review - Experiments and Strain Energy Functions

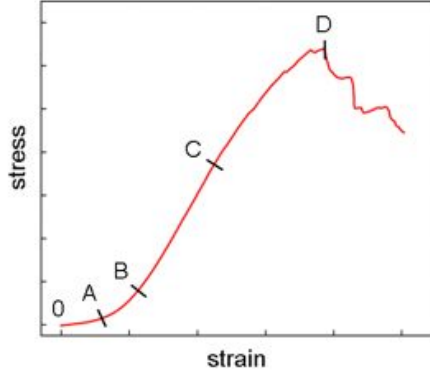
The mechanical properties of AAA wall play a major role in FE simulations and correct constitutive modeling is necessary to get reliable and physiologically reasonable results. They must be derived from mechanical experiments, e.g. uni-axial or biaxial tensile tests. This current section gives a summary of the existent literature on mechanical experiments on AAA tissue. The focus is on AAA wall thickness, elastic properties and failure properties. First of all, however, some aspects of mechanical properties of healthy arterial wall are recapitulated, while only the few fundamental works by Fung, Humphrey or Holzapfel are considered. Much of their ideas can be conveyed to the mechanical testing and the constitutive modeling of AAA wall, which will be dealt with and summarized thereafter.

The basis for the experimental characterization of the mechanical properties of arterial tissues (or more general: soft tissues) in tensile tests was laid by the works of Fung. One of Fung's fundamental works was already published in 1967 [56], which dealt not only with the phenomenological consideration of the nonlinearity, strain-rate dependency, relaxation and failure properties of arteries in tensile tests, but also with the finite strain constitutive modeling of arterial walls. Meanwhile, Fung's findings can also be consulted in more detail in a series of books [57, 58]. With regard to elastic properties of biological soft tissue, Fung probably became most famous for the Fung-type SEF he proposed for the constitutive modeling of the elastic soft tissue response [58]:

$$W = c(e^Q - 1) \quad (2.56)$$

with  $Q = a_1 E_{11}^2 + a_2 E_{22}^2 + a_3 E_{12}^2 + a_3 E_{21}^2 + 2a_4 E_{11} E_{22}$ , while there is also an extension from the 2D to a 3D finite strain constitutive model. Eq. (2.56) is sometimes also termed the *Fung's law*. It is generally known to fit the experimental stress-strain curves of any biological soft tissue quite well (the exponential function is extremely versatile). On the other hand, the exponential function may behave unfavorable in numerical, linearization-based applications. Fung also coined the terms of the "toe"-region and the "elastic stiffness" as characteristics of a stress-strain curve of soft tissue under elongation, see also Figure 2.21. Details on the experimental set-ups for tensile tests or the measuring and modeling of (visco-)elastic properties of arteries, but from a slightly different perspective, can also be found in the works by Humphrey [98, 100].

Figure 2.21: Characteristic stress-strain curve of soft tissue under elongation. Fung termed the region between 0 and B the “toe”. The section between B and C was termed the “elastic stiffness” of the material [58]. Elsewhere, the initial soft behavior between 0 and A is sometimes associated with the elastin response, while the region between A and C is related to the collagen recruitment and the collagen response [165]. The maximum stress is measured at point D during failure of the material.



When it comes to the measuring and modeling of anisotropic mechanical properties of arteries, one has to consider the groundbreaking works by Holzapfel [89, 90, 92, 93, 94]. Holzapfel devoted his research to the investigation of anisotropy in soft tissue and especially within arteries. His works deal with experimental test methods to measure tissue properties, but also with the microstructurally motivated constitutive modeling of arteries. The general formulation of the anisotropic Holzapfel-like SEF for constitutive modeling of arteries which is promoted throughout the just mentioned contributions is given as follows [94]:

$$W(\bar{I}_1, \bar{I}_4, \bar{I}_6) = \frac{k_1}{2k_2} \sum_{i=4,6} \{ \exp\{k_2[(1-\rho)(\bar{I}_i - 3)^2 + \rho(\bar{I}_i - 1)^2]\} - 1 \}, \quad (2.57)$$

where  $k_1$  and  $k_2$  are material parameters,  $\rho$  is a weighting factor between isotropic ( $\rho = 0$ ) and anisotropic behavior ( $\rho = 1$ ) and  $\bar{I}_4$  and  $\bar{I}_6$  denote the fourth and sixth invariant of  $\bar{\mathbf{C}}$ . The anisotropic behavior is thereby introduced through the term  $\frac{k_1}{2k_2} \sum_{i=4,6} \{ \exp\{k_2(\bar{I}_i - 1)^2\} - 1 \}$

which represents the hyperelastic response of two oriented collagen fiber families.  $\bar{I}_4$  and  $\bar{I}_6$  are calculated by

$$\bar{I}_4 = \bar{\mathbf{C}} : \mathbf{M} \otimes \mathbf{M}, \quad \bar{I}_6 = \bar{\mathbf{C}} : \mathbf{M}' \otimes \mathbf{M}', \quad (2.58)$$

where  $\mathbf{M}$  and  $\mathbf{M}'$  are the directions of the two families of collagen fibers.  $\bar{I}_4$  and  $\bar{I}_6$  are consequently the (isochoric) stretches in the two fiber directions.

The probably first uniaxial tensile tests with AAA wall tissue were performed by Raghavan *et al.* in 1996 [165]. A total of 61 AAA wall specimens and 7 healthy aortic wall specimens were investigated and results were described in an uni-dimensional mathematical model, e.g.

$$\sigma = \frac{1}{K + AB^{-1}} \epsilon. \quad (2.59)$$

The mechanical tissue response was also interpreted with respect to the tissue microstructure: The parameter A from Eq. (2.59) was interpreted as the “collagen recruitment” parameter, while combinations of A, B and K were interpreted as stiffness of elastin and collagen. AAA specimens were either tested in longitudinal or circumferential direction, but Raghavan *et al.* did not

find statistically significant differences in mechanical properties for these two directions, nor were the elastic properties of AAA tissue statistically significantly different to elastic properties of normal aortic tissue. However, a significant decrease in strength was stated ( $201 \text{ N/cm}^2$  (Cauchy stress) for normal aortic tissue vs.  $86 \text{ N/cm}^2$  for AAA tissue). Wall thickness measurements were not reported.

Since the proposed uni-dimensional model in [165] could not be used for 3D finite strain FE simulations, Raghavan and Vorp proposed the associated three-dimensional hyperelastic constitutive law four years later [164]. The proposed isotropic, finite strain constitutive model

$$W = \alpha (I_1 - 3) + \beta (I_1 - 3)^2 \quad (2.60)$$

was based on uniaxial tensile test results of freshly excised AAA tissue. In the present work, Eq. (2.60) is sometimes also referred to as the ‘‘Raghavan & Vorp’’ (R&V) material model. The parameters for Eq. (2.60) were given as mean $\pm$ SEM (standard error of the mean) with  $\alpha = 17.4 \pm 1.5 \text{ N/cm}^2$  and  $\beta = 188.1 \pm 37.2 \text{ N/cm}^2$ . With regard to the sample size of  $n=69$ , the standard errors  $sd$  of the parameters  $\alpha$  and  $\beta$  can be calculated as  $sd = SEM \cdot \sqrt{n}$  to  $7.46 \text{ N/cm}^2$  and  $309 \text{ N/cm}^2$ , respectively. This indicates a drastic variation of the material parameters over the AAA sample population. A complementary sensitivity analysis performed in their work [164], however, exhibited that results of FE wall stress analyses were almost independent from the parameter variation. The material parameters also have a physical interpretation:  $6 \cdot \alpha$  is equivalent to the initial stiffness, while  $\beta$  is related to the stiffness in the high strain region (e.g. between B and C in Figure 2.21). Similar to the previous work ([165]), Raghavan and Vorp did not address wall thickness or its variability. The excellent viability of the proposed material model for the modeling of AAA wall tissue was affirmed by Marini *et al.* [137], in the term paper by Christoph Hannich [77] and in the diploma thesis of Ilona Trübswetter [209]. Furthermore, the R&V material model was used in a wide range of computational AAA applications (e.g. [43, 48, 49, 82, 133, 142, 169, 195]). In this regard, the fundamental work by Raghavan and Vorp still sets the reference for AAA wall material modeling.

In 2001, Thubrikar *et al.* [206] were the first who published thickness measurements, besides elastic properties and strength of 47 AAA wall specimens measured in uniaxial tensile tests. Mean AAA wall thickness was found to be  $2.09 \pm 0.59 \text{ mm}$  in the anterior region and  $2.73 \pm 0.46 \text{ mm}$  in the posterior region. A mean yield strength of about  $0.5 \text{ MPa}$  (Cauchy stress) was reported. They also stressed that there was a possible relationship between sample excision site and measured mechanical properties. The experimental data was not fitted to a 3D finite strain material model.

Okamoto *et al.* [154] were the first to investigate the biaxial mechanical properties of aneurysmal tissue, which was harvested from thoracic aortic aneurysms (TAA). They found that TAA wall always featured anisotropic behavior, but they also stated that there was no consistent preferential stiffening direction. Tensile test data was also fitted to the 2D Fung’s law (Eq. (2.56)). Thickness of TAA tissue was reported to  $2.6 \pm 0.5 \text{ mm}$  for the 40 biaxial specimens. They complemented their study of biaxial testing with uniaxial tensile strength data. The mean strength was  $2.045 \pm 0.46 \text{ MPa}$  (Cauchy) at an average failure stretch of  $\lambda = 1.65$  for patients younger than 50 years. Specimens from older patients featured significantly lower strength and failure stretch ( $1.35 \pm 0.37 \text{ MPa}$ ,  $\lambda = 1.51$ ). Individual wall thickness measurements were not reported.

Vallabhaneni *et al.* [215] focused on the investigation of uniaxial tensile strength and related matrix metalloproteinase (MMP 2 and 9) activity. MMP 2 and 9 activities were significantly

lower in AAA specimens compared to nonaneurysmal aorta, while a significant decrease in wall strength from nonaneurysmal to AAA tissue was reported. Contrary to their results they concluded that MMP hyperactivity can lead to spatial heterogeneity of AAA wall strength. In comparison to other literature, strength values measured by Vallabhaneni *et al.* [215] were implausibly low (mean: 0.53 MPa; presumably 1.PK stress). Wall thickness measurements were not reported.

A first approach to not only measure but also model some of the spatial heterogeneity of the material properties of AAA wall was performed by Vande Geest *et al.* [222] in 2006. The contribution dealt with the noninvasive determination of AAA wall strength. Therefore, strength of 83 AAA wall specimens was measured in uniaxial tensile tests. Measurements were correlated to a small set of non-invasively assessable explanatory parameters yielding a stochastic scalar model for the spatial distribution of AAA wall strength (see also Maier *et al.* [133] for a more detailed discussion). The mean strength of the AAA tissue samples was reported with  $0.805 \pm 0.6$  MPa (presumably Cauchy stress - however, this was not stated explicitly in [222]). Vande Geest *et al.* also introduced the *rupture potential index* (“RPI”), defined as the local quotient of wall stress divided by strength. The RPI provided a single measure for the stratification of rupture probability of a patient-specific AAA. The idea of the RPI has meanwhile also been used in a series of subsequent works by other groups, which proved the potential of computational FE analyses in improving AAA rupture risk stratification [62, 104, 133]. However, it should also be noted that the usage of a statistical model for wall strength is limited without detailed knowledge on the distribution of wall thickness. No information on AAA wall thickness was given in [222].

**Excursion - Modeling Issues in Biaxial Tensile Testing** In the same year, Vande Geest *et al.* also published biaxial tensile test data for AAA tissue [220]. A mean thickness of  $1.32 \pm 0.41$  mm was reported for the 26 specimens included in the study. The biaxial test data was fitted to the Fung-like SEF

$$W = b_0 \left( e^{0.5b_1 E_{11}^2} + e^{0.5b_2 E_{22}^2} + e^{b_3 E_{11} E_{22}} - 3 \right), \quad (2.61)$$

where  $b_1$  and  $b_2$  are the stiffness parameters associated with the Green-Lagrange strain in circumferential direction ( $E_{11}$ ) and longitudinal direction ( $E_{22}$ ), respectively.  $b_0$  and  $b_3$  are additional material parameters. The average material parameters for AAA tissue were  $b_0 = 0.33$  kPa,  $b_1 = 1015$ ,  $b_2 = 928$  and  $b_3 = 824$ , indicating a slight stiffening preference of AAA tissue along the circumferential direction. However, regarding individual specimens, 17 specimens featured preferred stiffening into the circumferential direction, while there were 9 specimens featuring the longitudinal axis as principal stiffening direction. Wall thickness measurements were not reported. The major critics especially refer to Figure 6 in this article by Vande Geest *et al.* [220], where the accumulated the strain energy  $W$  in a generic AAA specimen under equibiaxial tension is plotted and compared between the newly proposed anisotropic material law and the previously proposed isotropic R&V material law [164]. Besides, the conclusion drawn from this figure was that the SEF from Eq. (2.61) should be used in order to properly capture the material nonlinearity. Interestingly, however, it was not possible to reproduce the strain energy curve for the isotropic R&V material law shown in this figure. This of course weakens their conclusion drawn from this comparison. Beyond that, things become even more funny if one does not break the strain energy curves at 12 % of equibiaxial Green-Lagrange

strain as done in the aforementioned Figure 6 of [220], but continues to plot the strain energy  $W$  for higher, physiological reasonable strain ranges (e.g. up to 20 % or 30 %). Anyhow, 12 % of equibiaxial strain yields a strain energy  $W \approx 50$  kPa, which is the last data point plotted in Figure 6 of the discussed article. For strains that go beyond 12 %, the strain energy  $W$  for the anisotropic material law increases drastically: For example,  $W$  is  $10^6$  kPa at 18 % of strain,  $10^{12}$  kPa at 24 % of strain and approximately  $10^{20}$  kPa at 30 % of strain. Of course, it is often hard to imagine such large numbers and therefore a maybe little bit too drastic analogy is given in order to illustrate their magnitude: The nuclear weapon "Little Boy" that was detonated above the Japanese city of Hiroshima consisted of uranium-235. Given the density of uranium with  $\rho_{U235} = 19160$  kg/m<sup>3</sup>, the mass defect with  $\Delta m = 0.08$  % and the speed of light with  $c = 3 \cdot 10^8$  m/s, the specific energy of uranium-235 due to nuclear fission can be roughly estimated by  $W_{U235} = \rho_{U235} \cdot \Delta m \cdot c^2$ . The result of  $W_{U235} = 4.6 \cdot 10^{14}$  kPa is exceeded by an AAA tissue sample (which behaves according to Eq. (2.61)) at 26.5 % of strain. This is ridiculous – but of course this example shows that it is not reasonable to chose parameters in the order of 1000 as an argument in an exponential function as it was done in [220].

With regard to these substantial mistakes in this work by Vande Geest *et al.* [220], it is very surprising that the experimental data and/or the proposed SEF has been reused by quite a number of other groups (e.g. [8, 47, 174]). Ferruzzi *et al.* [47], who also gave a more detailed overview of groups re-analyzing the biaxial data by Vande Geest *et al.* [220], used the biaxial data to determine AAA-specific material parameter for a four-fiber-family material model. The four-fiber-family model can thereby be seen as an extension to the two-fiber-family model by Holzapfel [89] as presented in Eq. (2.57). It was probably first presented by Baek *et al.* [5]:

$$W = \frac{c_1}{2}(I_1 - 3) + \sum_{k=1}^4 \frac{c_2^k}{4c_3^k} \{ \exp(c_3^k(\lambda^{k^2} - 1)^2) - 1 \} + K_{act} \left\{ \lambda_\theta + \frac{1}{3} \frac{(\lambda_M - \lambda_\theta)^3}{(\lambda_M - \lambda_0)^2} \right\} \quad (2.62)$$

where  $c_1$  is shear modulus associated with the isotropic contribution of the mechanical response of the material. The material parameters  $c_2^k$  and  $c_3^k$  are associated with the four fiber families (anisotropic response) and  $\lambda^k$  is the stretch of the k-th fiber family, respectively. The last term is associated with muscle activation. Originally, Baek *et al.* [5] fitted the four-fiber-model to the experimentally measured data obtained from quasi-static pressure-diameter and axial force-length tests of rabbit basilar arteries. Ferruzzi *et al.* [47] fitted the parameters of four-fiber-family model to the biaxial tensile test data of AAA tissue provided in [220]. The numerous resultant material parameters are listed in [47]. However, it is notable that the material parameter  $c_1$  associated with the isotropic mechanical response was always close to zero. Ferruzzi *et al.* stated a higher variability in AAA parameters than for normal AA.

In 2011, Raghavan *et al.* [163] performed the so far largest study on wall thickness and wall failure properties including 145 AAA specimens. They harvested complete AAAs from necropsy studies, and investigated the mechanical differences of wall samples from both ruptured ( $n = 4$ ) and non-ruptured ( $n = 9$ ) AAAs. The mean wall thickness measured for ruptured AAAs was  $1.70 \pm 0.4$  mm versus  $1.50 \pm 0.4$  mm for non-ruptured ones. Further, Raghavan *et al.* [163] proposed the *failure tension* as an useful measure for failure properties of AAA wall. The failure tension was thereby defined as the force at break divided by width. As opposed to the failure strength, which was computed as the force at break divided by the cross-sectional area (width multiplied by thickness) of the specimen, the failure tension provided a measure that was

independent of the wall thickness. Measured failure tension was  $1.12 \pm 0.23$  N/mm for ruptured AAAs and  $1.16 \pm 0.36$  N/mm for non-ruptured ones, strength was  $0.95 \pm 0.28$  MPa (ruptured) versus  $0.98 \pm 0.23$  MPa (non-ruptured) [all values in terms of Cauchy stresses]. They concluded that the wall in ruptured AAAs was not globally weaker than the wall of non-ruptured AAAs. This also means that testing results from specimens harvested from non-ruptured AAAs can be assigned to model rupture-prone AAA states.

In 2011, Marini *et al.* [137] performed uniaxial tensile tests and complemented the hyper-elastic material law proposed by Raghavan and Vorp [164] by a continuum damage description, extending the validity of the material law to a stretch range of 50%. Marini *et al.* reported that the average AAA wall specimen behaves elastic up to 17% of strain [137], which was in agreement to earlier studies by Raghavan and Vorp ([164], 17%) or Raghavan *et al.* ([165], 22% in longitudinal direction and 30% in circumferential direction). The parameters of the damage model were fitted to the experimentally measured tensile test data of AAA specimens. As opposed to earlier models (e.g. [225]), it was also possible to consider spatially variable wall strength within the damage model via an additional scalar strength model (e.g. that one proposed in [222]). Based on the tensile test data, Marini *et al.* also claimed that wall strength correlated negatively with wall thickness, which further promoted the idea by Raghavan *et al.* [163] to apply failure tension rather than wall strength for rupture risk assessment. Although the incorporation of the damage model in the material law extended its validity to a strain range of up to 50%, Marini *et al.* noted that a damage model cannot be as accurate as the elastic models. This was also stated previously by Calvo *et al.* [23]. Accordingly, they found a  $R^2$  of 0.995 for the elastic model (for strains up to 17%), while the damage model could only reach  $R^2 = 0.923$  (for strains up to 50%). In the same work, the damage model was also used in a series of AAA FE simulations. Marini *et al.* concluded that the use of the damage model yielded similar good results for status quo AAA rupture risk prediction as the RPI-criterion or the wall stress criterion. The advantage of the damage model was seen in the compatibility to transient growth and remodeling approaches.

A study with a new approach for strength testing was presented by Sugita *et al.* [200]. A “pressure imposed test” was proposed to measure the mechanical properties of TAA wall, especially wall strength, in a multiaxial test setup. The drawback of the so far established biaxial tests rigs of not being capable of measuring strength was circumvented by clamping the sample with a circular die. Quadrilateral specimens of human TAA and porcine aorta were pressurized at the luminal side up to 4500 mmHg or rupture using a balloon. Acting stress in the specimen was calculated as 1.PK stress using the Law of Laplace for spherical bodies. The in-plane strain was determined by optical tracking of markers on the adventitial side. Sugita *et al.* tested 15 specimens excised from 12 patients and 12 control samples from porcine aorta. Cracks in ruptured porcine aortas always initiated from the adventitial side and mostly ran in the circumferential direction. The average thickness of the TAA specimens was reported as  $3.5 \pm 0.9$  mm. Measured strength was  $0.98 \pm 0.39$  MPa (1. PK stress) for specimens which ruptured at the center ( $n=6$ ) and  $1.02 \pm 0.55$  MPa for those which ruptured at the edge ( $n=5$ ). The four specimens which did not rupture featured a strength of at least  $1.56 \pm 0.34$  MPa. The maximum tangential moduli ranged from  $4.9 \pm 2.5$  MPa for center-ruptured specimens to  $13 \pm 3.6$  MPa for non-ruptured specimens. Sugita *et al.* also searched for significant correlations between measured strength and other mechanical parameters. For this, they performed a fit of their experimental data to a

model curve according to

$$TM = C_{\sigma} \{1 - e^{-\frac{\sigma}{\tau_{\sigma}}}\}. \quad (2.63)$$

$TM$  is the tangential elastic modulus,  $C_{\sigma}$  is the asymptotic value of the tangent elastic modulus,  $\sigma$  is the stress acting in the specimen and  $\tau_{\sigma}$  is a parameter responsible for plateauing out. Sugita *et al.* found a significant correlation of the rupture probability of the specimens to the parameter  $\tau_{\sigma}$ . However, it might be doubted that this knowledge is of use for the non-invasive rupture risk prediction, since the plateauing out must have already set in to measure this parameter - which however also means that rupture is already in progress.

### Implementation Issues

As a result of the described microstructural changes in the vessel wall during AAA formation and expansion, mechanical properties are influenced as well. Generally, AAA tissue features significantly reduced strength and failure stretch [165]. Okamoto *et al.* [154] also suggested that this might be an aging-related phenomena. Not a single direct comparison of wall thickness in normal and aneurysmatic aorta could be found in literature. Surprisingly, thickness measurements were only scarcely reported, although these were necessary for the calculation of elastic properties and strength. Although most works reported a large variability of material parameters, a detailed description and modeling of patient-specific material parameters is still lacking. There is only the statistical model for strength distribution by Vande Geest *et al.* [222], which is impractical without detailed knowledge on wall thickness distributions. In consequence, there is a need to address patient-specific variations and distributions of material parameters more accurately. However, more recent works tend to deal especially with more complex material laws (e.g. to model tissue anisotropy), rather than resolving the issue of material parameter variability. In contrary, the choice of patient-specific material parameters is aggravated by the increase in the number of parameters. Thereby, none of the recent works which dealt with the experimental measurement of tissue anisotropy [137, 154, 220] was even successful to determine a preferential stiffening direction of the AAA tissue. Nevertheless, more and more complex material models (up to the four-fiber-family material law) have been developed, while problems with anisotropic models already often start during numerical optimization (curve fitting) of the material parameters: The isotropic contribution often becomes very small (more or less zero). This could be observed in e.g. Ferruzzi *et al.* [47], Xenos *et al.* [236] and in own investigations [209]. However, such a result is not necessarily physically and physiologically reasonable, but is rather attributable to the optimization of an over-determined system (experimental measurements in two directions, but two/four equations for fibers plus isotropic contribution) and the missing of lower bounds for isotropic material parameters. And although it is clear that an anisotropic law can better mimic the material response than an isotropic law in general (isotropy can be seen as special case of anisotropy), already the isotropic R&V material law (Eq. (2.60)) yielded excellent fits of (uniaxial) experimental data ( $R^2 = 0.99$  in [164] or  $R^2 = 0.995$  in [137]). As opposed to this, the proposed anisotropic material laws (Eqs. (2.57), (2.56) or (2.62)) only yielded average coefficients of determination (e.g.  $R^2 = 0.82$  to  $0.97$  for normal AA [219];  $R^2 = 0.9$  for AAA specimens [220]) for fits to biaxial test data. Fits of isotropic material laws to the same biaxial test data were not reported. Moreover, Franck [53] and Trübswetter [209] showed that isotropic material laws only yielded slightly worse fits to biaxial experimental data of porcine aorta than anisotropic material laws. The test protocol was thereby similar to the

protocol in [220] ( $\lambda_\theta:\lambda_L=1:1, 0:1, 1:0, 0.5:1, 1:0.5$  and  $\lambda_{\theta,max} = \lambda_{L,max} = 1.15$ ). With regard to [209], 18 specimens were included in the study. Firstly, the experimental data was fitted to the two fiber family material model by Holzapfel (Eq. (2.57)) yielding a mean coefficient of determination of  $R^2 = 0.9968 \pm 0.0023$  (lowest  $R^2_{min} = 0.9901$ ). Secondly, the same data was fit to the isotropic R&V material model (Eq. (2.60)) which led to a mean  $R^2$  of  $0.9879 \pm 0.0073$  (minimum:  $R^2 = 0.9738$ ). It is therefore questionable if the use of complex anisotropic material laws is reasonable, while there is almost no increase in the quality of the fit. Especially under the considerations of the number of material parameters and that these should be set patient-specifically, the isotropic, two-parametric R&V model has clear advantages [77].

As opposed to ILT and calcifications, the AAA wall could not be reliably segmented from CT or MR images [21]. A practical way to include AAA wall in the FE model was to extrude an idealized AAA wall to the abluminal ILT surface or to the lumen (if no ILT was present) subsequent to the ILT/lumen mesh creation. This was done by a custom-written extrusion algorithm that allows to choose the number of element layers and to adjust wall thickness node-wise (see e.g. Figure 2.4). If not otherwise stated, a spatially uniform thickness of  $t = 1.2$  mm in the prestressed configuration was assumed. The significant variation of elastic material parameters and the inconsistency of the stiffening direction of AAA tissue consequently made it impossible to correctly resolve the tissue anisotropy. This motivated the assumption of a homogeneous and isotropic AAA wall in the present study. Since the viability of the R&V material law (Eq. (2.60)) had already been shown previously, it was adapted to slight compressibility using the isochoric-volumetric split:

$$W_{wall} = W_{wall,iso} + W_{wall,vol} = \alpha (\bar{I}_1 - 3) + \beta (\bar{I}_1 - 3)^2 + \frac{\kappa}{\beta_2} (\beta_2 \ln J + J^{-\beta_2} - 1). \quad (2.64)$$

If not otherwise stated, the elastic parameters  $\alpha$  and  $\beta$  were set to the values proposed in [164].  $\kappa$  was chosen to  $\kappa = \frac{2\alpha}{1-2\nu}$ , with  $\nu = 0.48$ . The parameter  $\beta_2$  was set to  $\beta_2 = -2$ .

Nonetheless, the incorporation of patient-specific wall thickness distribution is seen as a crucial factor in proper AAA risk prediction. Chapter 5 will be devoted to the measuring and modeling of patient-specific material parameters for AAA wall, including wall thickness distribution. It will also deal with patient-specific modeling of the other mechanical properties, such as failure strength, failure tension and elastic properties. Since the emphasis of the current study is to model the patient-specificity, transient phenomena, such as relaxation and viscous effects, were not considered in the AAA wall model for the moment. Chapter 5 will also give a more detailed comparison between mechanical properties of AAA wall tissue and normal aortic wall, which so far has only been poorly covered in literature.

## 2.6 Numerical Solution

### 2.6.1 Boundary Value Problem

Since comparisons of solid state models with fluid-structure interaction models showed that purely structural approaches were feasible to calculate stresses and strains acting in the AAA wall [117, 122], the investigations in the current work were limited to the solution of the boundary value problem of finite deformation elasticity [90]. The strong form of the balance equation for an undeformed structure  $\Omega_0 \subset \mathbb{R}^3$  in the stress-free material configuration yields

$$\text{Div}(\mathbf{FS}) + \mathbf{b}_0 = \mathbf{0} \text{ in } \Omega_0, \quad \mathbf{u} = \mathbf{u}_D^0 \text{ on } \Gamma_D, \quad \mathbf{P} \mathbf{N}_\Gamma = \mathbf{t}_0 \text{ on } \Gamma_N. \quad (2.65)$$

$\mathbf{b}_0$  are body forces in the material configuration.  $\mathbf{u}_D$  and  $\mathbf{t}_0$  are boundary conditions on the Dirichlet ( $\Gamma_D$ ) and Neumann boundary  $\Gamma_N$ , respectively.  $\mathbf{N}_\Gamma$  is the unit outward normal on  $\Gamma_N$  in the material configuration. For all AAA simulations in the present work, the proximal and distal ends of the FE models were chosen as Dirichlet boundaries  $\Gamma_D$  and displacements were constrained to zero. Either the luminal thrombus surface or the luminal AAA wall surface, when no thrombus was present, was chosen as non-zero Neumann boundary. Loading due to blood pressure and flow was modeled as orthogonal pressure onto the deformed spatial configuration of the Neumann boundaries  $\Gamma_N$ . The boundary value problem (Eq. (2.65)) was treated using the FE method under consideration of the kinematic and constitutive equations presented in Sections 2.4.1 through 2.4.3. For a more detailed presentation of the FE method, the reader is referred to [228] or [240]. One peculiarity for AAAs was that geometries derived from CT images showed the vessel under *in vivo* loads. The segmented geometry represented a deformed configuration of the AAA under pressure, which was at least the diastolic pressure. A standard FE simulation, however, starts from an undeformed configuration. Section 2.6.2 below presents the solution to this issue.

### 2.6.2 Prestressing

AAA geometries reconstructed from CT data represented a configuration subjected to *in vivo* blood forces. They were “prestressed”. In order to consider the already acting stresses and strains in the imaged configuration, the FE simulation was split into two parts: Firstly, a *Modified Updated Lagrangean Formulation (MULF)* prestressing method was applied [64, 66, 130] to recover stresses and strains acting in the imaged configuration under the assumption of a certain luminal load present at time of imaging. In a second phase, load was increased to systolic blood pressure using a standard nonlinear FE simulation, while the prestressed state of the model was considered. A detailed explanation of the MULF scheme can be found in [64]. A brief outline is given in the following:

The starting point of the MULF method is a known spatial configuration  $\Omega_t \in \mathbb{R}^3$  obtained from CT images, while the transformation that maps the material configuration to this spatial configuration is unknown.  $\mathbf{x}_t$  is the known corresponding coordinate vector field. The configuration  $\Omega_t$  is subject to an external load  $\mathbf{t}_t \neq \mathbf{0}$  that is assumed to be known and in equilibrium with the stress state of the imaged structure. For ease of notation, body forces  $\mathbf{b}$  are omitted in this discussion. The weak form of the balance equation (Eq. (2.65)) in the material configuration

with respect to  $\Omega_t$  then is

$$\delta\Pi_t = \delta\Pi_t^{int} - \delta\Pi_t^{ext} = \int_{\Omega_t} \delta\mathbf{E} : \mathbf{S} \, d\Omega - \int_{\Gamma_N} \mathbf{t}_t \cdot \delta\mathbf{u} \, d\gamma = 0. \quad (2.66)$$

Equation (2.66) can only be true in the non-trivial case  $\mathbf{S} \neq \mathbf{0}$  if either a deformation gradient  $\mathbf{F} \neq \mathbf{I}$  exists or displacements  $\mathbf{u} \neq \mathbf{0}$  occur that result in a non-trivial deformation gradient. Therefore, the usual incremental load controlled calculation is performed, with the only modification being the incremental summation of displacement increments replaced by an incremental multiplicative update of an independent imprinted deformation gradient. In this incremental prestressing method, the structure does not deform but builds up an imprinted deformation gradient.

For the FE solution, Equation (2.66) has to be discretized by standard finite elements. Accordingly, the discrete configuration  $\mathbf{x}^h$  and displacement field  $\mathbf{u}^h$  are  $\mathbf{x}^h = \sum_{i=1}^{nd} N_i(\boldsymbol{\xi}) \mathbf{x}_i$  and  $\mathbf{u}^h = \sum_{i=1}^{nd} N_i(\boldsymbol{\xi}) \mathbf{u}_i$ , where  $\mathbf{x}_i$  and  $\mathbf{u}_i$  are nodal coordinates and displacements of the  $nd$  nodes adjacent to an element.  $N_i$  are standard finite element shape functions.  $\boldsymbol{\xi} \in \mathbb{R}^3$  is a parametrization of an element in its parameter space with e.g.  $-1 \leq \xi_j \leq 1$ ,  $j = 1, 2, 3$  for a hexahedral shaped element. Then, integration of Eq. (2.66) over the element volume is performed as usual making use of the standard Jacobian mapping

$$\mathbf{J}_t = \frac{\partial \mathbf{x}_t^h}{\partial \boldsymbol{\xi}}, \quad |\mathbf{J}_t| = \det \mathbf{J}_t, \quad \nabla \mathbf{N}_t = \frac{\partial \mathbf{N}}{\partial \mathbf{x}_t^h} = \frac{\partial \mathbf{N}}{\partial \boldsymbol{\xi}} \frac{\partial \boldsymbol{\xi}}{\partial \mathbf{x}_t^h} = \mathbf{N}_{,\boldsymbol{\xi}} \mathbf{J}_t^{-1}. \quad (2.67)$$

Herein,  $\nabla \mathbf{N}_t$  denotes shape function derivatives with respect to known spatial coordinates  $\partial \mathbf{N} / \partial \mathbf{x}_t^h$ . The deformation gradient increment  $\mathbf{F}_{t+1}$  that describes the mapping from an arbitrary configuration  $\mathbf{x}_t^h$  to the following deformed configuration  $\mathbf{x}_{t+1}^h + \Delta \mathbf{x}_{t+1}^h$  is

$$\mathbf{F}_{t+1} = \frac{\partial \mathbf{x}_{t+1}^h}{\partial \mathbf{x}_t^h} = \mathbf{I} + \frac{\partial \Delta \mathbf{x}_{t+1}^h}{\partial \mathbf{x}_t^h} = \mathbf{I} + \mathbf{N}_{,\boldsymbol{\xi}} \mathbf{J}_t^{-1} \Delta \mathbf{x}_{t+1}^h. \quad (2.68)$$

The total deformation gradient  $\mathbf{F}$  can then be calculated by an incremental multiplicative update:

$$\mathbf{F} = \mathbf{F}_{t+1} \tilde{\mathbf{F}}, \quad (2.69)$$

where  $\tilde{\mathbf{F}}$  is the multiplicative deformation gradient history of previous load increments. Note that it is not necessary to know the material configuration  $\mathbf{X}$  to compute either  $\mathbf{F}_{t+1}$ ,  $\tilde{\mathbf{F}}$  or  $\mathbf{F}$ . The unknown in these equations is only the displacement increment  $\Delta \mathbf{x}_{t+1}^h$ . It can be uniquely calculated in an incremental fashion by the discretized, assembled and linearized form of Eq. (2.66):

$$\mathbf{R} = \int_{\Omega_t} \mathbf{B}^T \bar{\mathbf{S}} \, d\Omega - \mathbf{F}^{ext} \approx \int_{\Omega_t} \mathbf{B}^T \bar{\mathbf{S}} \, d\Omega - \mathbf{F}^{ext} + \left( \int_{\Omega_t} \mathbf{B}^T \frac{\partial \bar{\mathbf{S}}}{\partial \mathbf{x}} \, d\Omega + \frac{\partial \mathbf{F}^{ext}}{\partial \mathbf{x}} \right) \Bigg|_{\mathbf{x}_t} \Delta \mathbf{x}_{t+1}^h = \mathbf{0}. \quad (2.70)$$

$\mathbf{B}$  is the nonlinear B-operator,  $\mathbf{F}^{ext}$  are the external loads and  $(\bar{\cdot})$  indicates Voigt notation. Equation (2.70) can be solved by standard Newton-type solution methods yielding a displacement increment  $\Delta \mathbf{x}_{t+1}^h$ , whereas the total deformation gradient from Eq. (2.69) is utilized to compute strains, stresses and the tangent stiffness. Having calculated the displacement increment  $\Delta \mathbf{x}_{t+1}^h$

and the resulting deformation gradient increment  $\mathbf{F}_{t+1}$  from Eq. (2.68), a prestressed/prestrained neighboring configuration  $\Omega_{t+1}$  is uniquely defined in terms of the inverse of the Jacobian mapping  $\mathbf{J}_{t+1}^{-1}$  utilizing Eq. (2.71):

$$\mathbf{J}_{t+1}^{-1} = \mathbf{J}_t^{-1} \mathbf{F}_{t+1}^{-1} \quad (2.71)$$

The geometry displacements  $\mathbf{x}_{t+1}^h$  are *not* updated during the prestressing phase. However, updating  $\mathbf{J}_{t+1}^{-1}$  through Eq. (2.71) performs the corresponding step, but at the level of imprinted quantities. In short, starting with the imaged configuration  $\Omega_t$  in an incremental load increasing scheme, the steps performed to obtain the prestressed configurations  $\Omega_{t+1}, \dots, \Omega_{t+i}, \Omega_{t+i+1}, \dots$  are summarized:

1. Initialize history quantities  $\tilde{\mathbf{F}} = \mathbf{I}$ ,  $\tilde{\mathbf{J}}^{-1} = \mathbf{J}_t^{-1}$ .
2. Repeat for increments  $i$ :
3. Increase external loads  $\mathbf{F}^{ext}$
4. Compute iteratively the nonlinear displacement increment  $\Delta \mathbf{x}_{t+i}^h$  from Eq. (2.70) using the incremental deformation gradient  $\mathbf{F}_{t+i}$  from Eq. (2.68). The total deformation gradient to be used in stress and strain calculation is  $\mathbf{F} = \mathbf{F}_{t+i} \tilde{\mathbf{F}}$ .
5. Compute  $\tilde{\mathbf{J}}_{t+1}^{-1} = \mathbf{J}_t^{-1} \mathbf{F}_{t+i}^{-1}$
6. Update  $\tilde{\mathbf{F}} \leftarrow \mathbf{F}_{t+i} \tilde{\mathbf{F}}$  and  $\tilde{\mathbf{J}}^{-1} \leftarrow \mathbf{J}_{t+i}^{-1}$
7. Repeat from item 2 for next increment  $i \leftarrow i + 1$ .

In all FE simulations of the AAAs included in this study, the MULF prestressing phase was consistently applied until a luminal pressure of  $p = 87$  mmHg was reached. Thereafter, the pressure was incrementally increased up to  $p = 121$  mmHg using a standard nonlinear FE calculation considering the prestressed state through Eq. (2.69). Other methods to take into account the loaded state of the AAA during imaging are the Inverse Design method utilized by Lu *et al.* [128, 129] or the Backward Incremental Method proposed by de Putter *et al.* [38, 196]. For the validation of these prestressing methods, comparisons between *in vivo* AAA wall deformations obtained by dynamic MRI and displacements from FE simulations under consideration of prestress methods were performed in [142].

### 2.6.3 Solution and Performance Details

The system of equations in Eq. (2.65) and consequently also the discretized weak formulation of the problem were inherently nonlinear. The resulting algebraic systems of the FE formulation were hence linearized using Newton's method [116] and iteratively solved until residual and displacement norms were smaller than given tolerances. The linearized system at each iteration step was preconditioned with a *ML* multilevel preconditioner (Sandia National Laboratories, Albuquerque, NM, USA) [67] for symmetrical linear systems and solved with the GMRES iterative solver which is part of the Aztec solver library (Sandia National Laboratories, Albuquerque, NM, USA) [116, 213]. A load control scheme was applied until the required orthogonal pressure was acting on the non-zero Neumann boundary (usually 30 prestressing

steps and 10 subsequent standard forward steps). All simulations were performed within the multiphysics simulation environment BACI [229]. Calculations were performed on 2.0 GHz octocore CPUs (AMD Opteron 6128) with 32 GB shared memory.

The FE mesh of the exemplary AAA shown in Figures 2.22 to 2.24 consisted of 257,305 elements (thereof 185,050 ILT and 72,255 wall elements, respectively) and 184,650 nodes. FE simulations considering the effect of calcifications (according to Section 2.5.2) and neglecting calcifications were performed. Solution time for the simulation considering calcifications was 17660 s (thereof 1110 s element evaluation time, 371 s solver setup time and 12990 s solver time) and 8060 s (thereof 550 s element evaluation time, 332 s solver setup time and 6987 s solver time) for the simulation neglecting calcifications.

## 2.7 Postprocessing

Wall stress, strain and displacement distributions, respectively, were obtained from FE simulation for each AAA. All stress values were processed in terms of von Mises-Cauchy stresses or principal-Cauchy stresses. All strain values were processed in terms of von Mises-Euler-Almansi strains or principal-Euler-Almansi strains. Results were postprocessed using the open source software Paraview (Kitware Inc., Clifton Park, USA), which was used for quantitative analyses of the results and for visualization. Further, a series of AAA specific quantities was computed within the FE framework for each AAA, such as abluminal AAA surface, blood volume, ILT volume, AAA volume (sum of blood and ILT volumes) or the local ILT thickness distribution (calculated as previously presented on page 29, as needed for ILT material parameter calculation), see also Table 2.3.

FE simulation results for an exemplary AAA are shown in Figures 2.22 through 2.24. Some characteristic quantitative FE simulation results for this AAA (e.g. average and maximum values) are also summarized in Table 2.3. In any case (also for the calculation of the geometrical features from Table 2.3), only the sac region of the AAA was considered for the evaluation of the quantities. The sac region of interest was indicated by two planes as demonstrated in Figure 2.23. A pair of planes was saved for each AAA to allow for automated and consistent postprocessing of the results in the further course of this current work (Chapters 4 and 6). Maximum values were calculated as the 99th-percentiles of the respective quantity [197] (this also applies to all the following evaluations within the present work, if not indicated otherwise). Average values were calculated as mean values within the sac region. Only values within the two outer element layers of the AAA wall were considered, since the innermost layer potentially contained calcification.

Table 2.3: Results from computational analysis for the representative AAA shown in Figures 2.22 through 2.24. Besides the results from computational FE analysis (bottom), also a set of geometrical features calculated within the FE framework was obtained (top).

		<b>male, 85y, symptomatic AAA</b>									
		<b>Geometrical features</b>									
		max AAA diameter [mm]	subren. aortic $\phi$ [mm]	related $\phi$ ([194]) [mm]	max ILT thicken. [mm]	abl. AAA surface [cm <sup>2</sup> ]	blood volume [cm <sup>3</sup> ]	ILT volume [cm <sup>3</sup> ]	AAA vol. (blood+ilt) [cm <sup>3</sup> ]		
		63.5	22	21.5	16.9	223	65.1	39.0	104		
		<b>Results from FE analysis</b>									
		max ILT displacement [mm]	max wall displacement [mm]	average von Mises stress [kPa]	max von Mises stress [kPa]	average 1st principal stress [kPa]	max 1st principal stress [kPa]	average von Mises strain [-]	max von Mises strain [-]	average 1st principal strain [-]	max 1st principal strain [-]
<b>calcifications included</b>		0.89	0.60	130.6	310.5	140.3	379.0	0.127	0.200	0.056	0.110
<b>calcifications neglected</b>		0.93	0.70	173.1	352.6	188.2	390.5	0.152	0.207	0.069	0.119

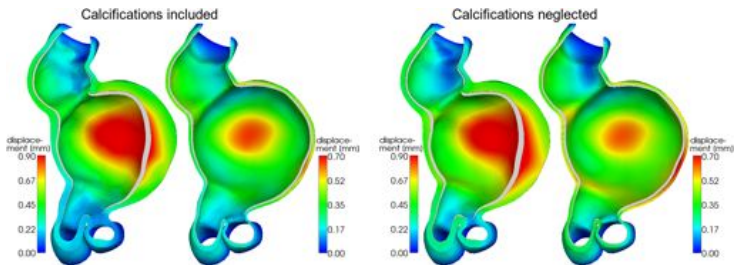


Figure 2.22: Visualization of displacements for an exemplary AAA (cut view) under consideration of calcifications (representations at the left, ILT not visualized in the second representation) and when calcifications were neglected (representations at the right, ILT not visualized in the second representation). Representations show the deformed geometries (displacements three times magnified), while the gray contours indicate the undeformed (prestressed) configurations.

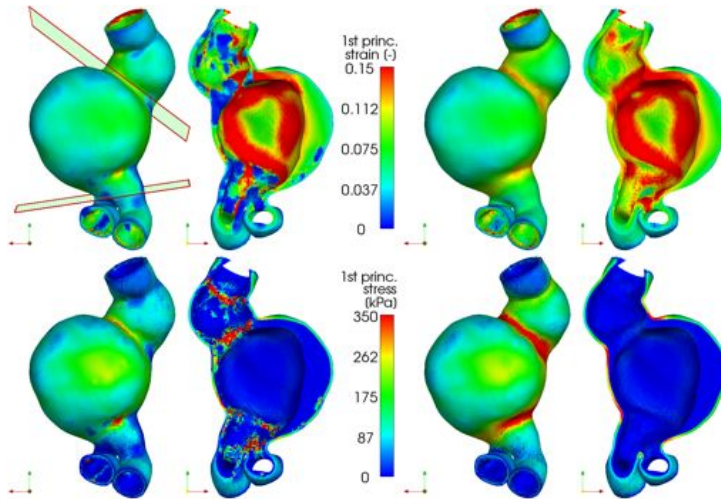


Figure 2.23: 1st principal strain (top row) and stress (bottom row) distributions under consideration of calcifications (representations at the left) and when calcifications were neglected (right). The two planes in the top left picture indicate the sac region of interest for evaluation of average and maximum quantities.

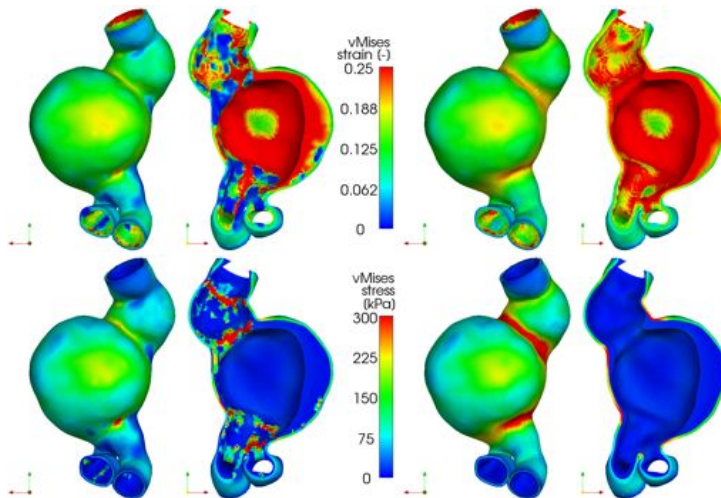


Figure 2.24: Von Mises strain (top row) and stress (bottom row) distributions under consideration of calcifications (left) and when calcifications were neglected (right).



# 3 Some Statistical Methods

This chapter presents statistical methods which will be used later on for the evaluation of simulation results or experimental data, where large data bases will be investigated. It is to note that in statistics, the word *sample* denotes a subset of a population. It is not to be confused with *wall sample* (excised portion of vessel wall), which is also sometimes denoted *sample*, but which exclusively appears in other chapters. In this chapter, the word *sample* is exclusively used in its statistical sense. The current chapter thereby covers two major topics: Section 3.1 deals with hypothesis tests and P-values. The hypothesis tests are mainly used to detect statistically significant differences between two samples - e.g. to show that the maximum wall stress in a set of ruptured AAAs is higher than in a set of non-ruptured AAAs. In the same section, it is also answered what the phrase “statistically significant” actually means. The second major topic is dealt within Section 3.2, which is the identification of correlations between different quantities. It includes regression analysis to create stochastic models, methods to detect and handle outliers and measures to assess the quality of a correlation or a stochastic model. The preliminary work on this topic preformed by Sebastian Schiller [183] is appreciated.

## 3.1 Hypothesis Testing and Statistical Significance

### 3.1.1 Hypothesis Testing

In medicine or biomechanics, a lot of trials are conducted in order to show that one method yields different results than a second method. But there is a need to substantiate the plausibility of results and conclusions drawn from a study. A decision based on the comparison of mean or median values of two samples *A* or *B* is often hard to justify, because of lacking of generally accepted appropriate boundaries for or against a decision or because of the neglect of the fact that differences in the samples can occur by chance. Statistical testing provides a remedy. Such tests are usually hypothesis tests, while the sequence to conduct hypothesis tests is outlined as follows:

1. Specify hypothesis and alternative hypothesis,
2. Decide for a test based on the properties of the sample,
3. Compute the test statistic,
4. Decide for one of the hypotheses.

To conduct a hypothesis test, one has to specify the *null hypothesis*  $H_0$  which is considered to be the truth unless proven otherwise. Usually, the statement of the null hypothesis is that two samples *A* and *B* stem from the same population. The *alternative hypothesis*  $H_1$  is the

hypothesis one usually wants to demonstrate in the study, which comes into effect when the null hypothesis was proven to be incorrect. This can be translated into the formal statement

$$H_0 : A = B, \quad H_1 : A \neq B. \tag{3.1}$$

Hypotheses that do not include any assumption on the direction of the difference between the samples are called *two-sided* ('A is different from B'). Hypotheses specified with regard to a direction of the difference (e.g. 'A is smaller than B') are called *one-sided*. The decision for or against  $H_0$  is dependent on the test statistic, which is calculated from the samples. However, even if two methods are the same, samples in a study are subject to sampling errors which might be misinterpreted as a difference between A and B. If  $H_0$  is true, but one rejects  $H_0$  and decides for  $H_1$ , one commits the so-called  $\alpha$ -error. The  $\alpha$ -error cannot be avoided in general (while it can only occur if  $H_0$  is true) - but it can be controlled. This can be explained by a small example: Let's assume that random samples are taken from a normal distribution  $f(x)$ <sup>1</sup>. If one wants to check retrospectively whether the samples stem from the distribution  $f(x)$  - which is obviously true - one can calculate the test statistic  $t$  of an one-sample t-test (see also Section 3.1.3) for each sample:

$$t = \frac{\bar{x} - \mu_0}{s/\sqrt{n}}, \tag{3.3}$$

with  $\bar{x}$  as the sample mean,  $\mu_0$  as the expectation,  $s$  as the sample standard deviation and  $n$  as the sample size. In this case, the density function of the test statistic  $t$  is a t-distribution<sup>2</sup> with the probability of  $t$  lying within  $[-t_{n-1,1-\alpha/2}; t_{n-1,1-\alpha/2}]$  being exactly  $(1 - \alpha) \cdot 100\%$ . Consequently, an objective selection for the *region of acceptance* of  $H_0$  can be given by  $-t_{n-1,1-\alpha/2} \leq t \leq t_{n-1,1-\alpha/2}$  (two-sided test). The *region of rejection* of  $H_0$  (or *critical region*) is objectively defined by  $|t| > t_{n-1,1-\alpha/2}$ , where  $H_0$  is rejected in favor for  $H_1$ . This is also graphically demonstrated in Figure 3.1. Based on our example, this approach ensures that we come to the correct decision (acceptance of  $H_0$ ) in  $(1 - \alpha) \cdot 100\%$  of all cases, while the risk of committing the  $\alpha$ -error is  $\alpha \cdot 100\%$ .  $\alpha$  is therefore frequently entitled the *significance level*. Its choice is a somewhat arbitrary task, but in most applications a level of  $\alpha = 0.05$  is chosen for no better reason than that it is conventional. Also in the current work and if not otherwise stated,  $\alpha$  is set to 0.05. Hence, the associated risk of a rejection of  $H_0$  by accident is 5%. The other way round, the acceptance of  $H_0$  while  $H_1$  is actually true is denoted  $\beta$ -error. As opposed to the  $\alpha$ -error, the  $\beta$ -error cannot be easily controlled. However, the chance of committing a  $\beta$ -error generally increases for smaller  $\alpha$  [234].

### 3.1.2 Statistical Significance: The P-Value

P-values are an integral part of statistical techniques in medicine, which are often used to measure the strength of a statistical evidence [6]. As already explained before, hypothesis testing

<sup>1</sup>The normal distribution is defined by

$$f(x) = \frac{1}{\sigma \cdot \sqrt{2\pi}} \cdot e^{-\frac{(x-\mu)^2}{2\sigma^2}}, \tag{3.2}$$

with  $\sigma$  as the standard deviation and  $\mu$  as the expectation.

<sup>2</sup>The t-distribution shares some common properties (population mean is 0, symmetry,  $t \in ]-\infty; +\infty[$ ) with the normal distribution. In contrast, the specific form of the t-distribution is dependent on the number of degrees of freedom ( $ndof = n - 1$ , with  $n$  as the sample size), which is not listed explicitly here.

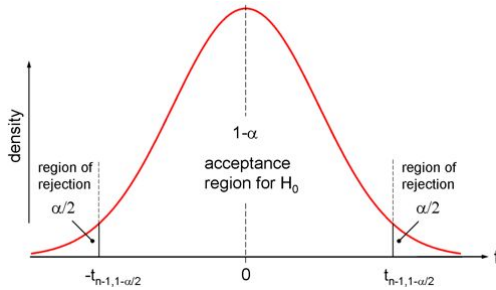


Figure 3.1: t-distribution with acceptance and rejection regions for a two-sided t-test.

is a method to decide or reject for a null hypothesis  $H_0$ , which in the latter case leads to the acceptance of the alternative hypothesis  $H_1$ . The connection between hypothesis testing and the P-value can thereby be best explained by a reformulation of the steps performed during a hypothesis test [6]:

1. Specify null hypothesis  $H_0$  and alternative hypothesis  $H_1$ ,
2. Decide for a test and choose the significance level  $\alpha$ ,
3. Compute the P-value,
4. If the P-value is smaller than  $\alpha$ , reject  $H_0$  in favor of  $H_1$ .

In other words, the use of the P-value is additional to the calculation of the test statistic. Most statistical software packages automatically compute both values. Related to the common choice of  $\alpha = 0.05$ , test results are usually considered as “statistically significant” for  $P < 0.05$ . In contrast to test statistics, the P-value can be interpreted as the probability that the result was obtained by chance. A further advantage of the P-value is that it can be obtained for a great variety of statistical tests. It provides a measure of consistent meaning when test types change and consequently test statistics cannot be compared any more. However, at the same time, reporting only the P-value but not the type of test also enables “cheating”. For example, if one first checks for the direction of the difference using a two-sided test and then performs an one-sided test based on these results, the P-value will be halved in the second run. In the current work, the P-value rather than the test statistic is reported for any hypothesis test. If not otherwise stated, the significance level is set to  $\alpha = 0.05$  which means that significant differences between two samples are stated for  $P < 0.05$ . All P-values reported in the present work refer to two-sided tests.

### 3.1.3 Types of Statistical Tests

#### Parametric Tests

For parametric tests, it is required that the type of the sample distributions is known and fulfills certain conditions. The most popular representatives of parametric tests are the *Student's t-tests*

(or just *t*-tests) [18], which are introduced in the present section. For the application of any *t*-test, the sample must come from a normally distributed population (which can e.g. be checked using the Shapiro-Wilk-Test presented later on as one of the examples for non-parametric tests). If a sample distribution does not follow a normal distribution, a non-parametric test or another suited parametric test has to be applied instead of the *t*-test. For any of the *t*-tests listed below, the region of acceptance of  $H_0$  is defined by  $|t| \leq t_{f,1-\alpha/2}$  (two-sided), where  $f$  is the number of degrees of freedom. Accordingly, the region of rejection of  $H_0$  in favor of  $H_1$  is  $|t| > t_{f,1-\alpha/2}$ . Values  $t_{f,1-\alpha/2}$  are documented in tables or are provided by statistical software.

**One-Sample t-test** With the one-sample *t*-test it can be checked whether the mean of a sample population is equal to a specified value  $\mu_0$ . The formula to compute the test statistic  $t$  is given by Eq. (3.3). In the current work and if not otherwise stated,  $\mu_0$  is set to 0.

**Two-Sample t-test for Paired Samples** The two-sample *t*-test for paired samples is used to check for a difference  $\delta$  in the expectations  $\mu_A$  and  $\mu_B$  of two dependent samples  $A = \{a_1, a_2, \dots, a_n\}$  and  $B = \{b_1, b_2, \dots, b_n\}$ , respectively. An example would be the test for differences in maximum wall stresses for the same set of AAAs under two different modeling assumptions, where each AAAs within the study cohort is simulated twice. The hypotheses for a two-sided test read

$$H_0 : \mu_A - \mu_B = \delta, \quad H_1 : \mu_A - \mu_B \neq \delta. \quad (3.4)$$

The test statistic  $t$  is calculated by

$$t = \frac{\bar{d} - \delta}{\frac{s_D}{\sqrt{n}}}, \quad (3.5)$$

where  $\bar{d}$  is the mean of the differences  $d_i = a_i - b_i$  and  $s_D$  is the standard deviation of  $D = \{d_1, d_2, \dots, d_n\}$  [234]. The number of degrees of freedom is  $f = n - 1$ . It is required that  $D$  (not  $A$  or  $B$ ) follows a normal distribution. In practice,  $\delta$  is often set to 0.

**Two-Sample t-test with Independent Samples** The two-sample *t*-test for independent samples is used to check if the expectations  $\mu_A$  and  $\mu_B$  of two samples  $A = \{a_1, a_2, \dots, a_{n_A}\}$  and  $B = \{b_1, b_2, \dots, b_{n_B}\}$ , respectively, differ by a specified value  $\delta$ :

$$H_0 : \mu_A - \mu_B = \delta, \quad H_1 : \mu_A - \mu_B \neq \delta. \quad (3.6)$$

An example would be to test for differences in maximum wall stresses between  $n_A$  ruptured AAAs and  $n_B$  non-ruptured AAAs. The test statistic  $t$  can be calculated by

$$t = \frac{\bar{a} - \bar{b} - \delta}{s \sqrt{n_A^{-1} + n_B^{-1}}}, \quad (3.7)$$

where  $s$  is calculated from

$$s^2 = \frac{(n_A - 1)s_A^2 + (n_B - 1)s_B^2}{n_A + n_B - 2}. \quad (3.8)$$

The number of degrees of freedom is  $f = n_A + n_B - 2$ . An additional requirement to use the two-sample *t*-test for independent samples is that both samples feature same variances. This can be checked by the F-test [234], where the P-value needs to be larger than  $\alpha$  to confirm equal variances.

**Welch Two-Sample t-test with Independent Samples** The Welch two-sample t-test for independent samples is an alternative to the previous t-test in case of unequal variances, where the formula for the test statistic is slightly modified to

$$t = \frac{\bar{a} - \bar{b} - \delta}{\sqrt{\frac{s_A^2}{n_A} + \frac{s_B^2}{n_B}}}. \quad (3.9)$$

$s_A^2$  and  $s_B^2$  are the sample variances in  $A$  and  $B$ , respectively. The number of degrees of freedom is calculated as

$$f = \text{floor} \left( \frac{(s_A^2/n_A + s_B^2/n_B)^2}{\frac{(s_A^2/n_A)^2}{n_A-1} + \frac{(s_B^2/n_B)^2}{n_B-1}} \right). \quad (3.10)$$

### Non-Parametric Tests

In non-parametric tests, the distribution function of the statistical population is unknown and is therefore part of the test itself. Utilizing non-parametric tests, it can be checked if a sample population follows a certain type of distribution or if two samples originate in the same population. The latter test is thereby analogous to the parametric tests, with the difference that there are weaker requirements on the samples. Due to the multitude of different test statistics, the details on calculations and critical values are omitted for the sake of brevity in this section.

**Shapiro-Wilk Test** Lots of statistical tests have been derived based on the distributional assumptions of normality, such as e.g. the t-test. To check whether a given sample actually comes from a normally distributed population, the *Shapiro-Wilk test* can be used [176, 188]. There are also other more versatile tests, such as e.g. the Kolmogorov-Smirnov test, that check whether the population of a sample follows a particular (not necessarily normal) distribution. The Shapiro-Wilk test, however, might probably be the most widespread and most easy-to-use test to check for normality, which is therefore used in the present work. It is referred to [176, 188] for the formulas used to calculate the test statistics. The null hypothesis  $H_0$  of the Shapiro-Wilk test is that the investigated sample stems from a normally distributed population. Accordingly, the test statistic has to fall below a critical value to reject the normality hypothesis  $H_0$  for a sample [188]. Analogously, the P-value has to be larger than  $\alpha$  to confirm the normality.

**Wilcoxon Rank Sum and Signed Rank Tests** The *Wilcoxon rank sum test*, which is also known as *two-sample Wilcoxon test* or *Mann-Whitney test*, goes back to Wilcoxon [235] and Mann & Whitney [135]. It can be tested if two independent (unpaired) samples are originated in the same population. The samples do not need to be normally distributed, however, they should feature equal variances. The null hypothesis of the two-sample Wilcoxon test is that the location shift between two populations is  $\delta$ . The null hypothesis is rejected if the test statistic exceeds the critical value ( $H_0 : \mu_A - \mu_B = \delta$ ). In practice,  $\delta$  is often set to 0 (=the two samples originate in the same population), where consequently the rejection of the null hypothesis indicates that two samples originate from two different populations. In the *Wilcoxon signed rank test* it is checked if the sample  $A$  stems from a

population with a median  $\mu_A$ , which is equal to a specified value  $\mu_0$  ( $H_0 : \mu_A = \mu_0$ ). The only assumption on this test is that the sample distribution is somehow symmetric. An analogical test can be carried out for paired samples  $A$  and  $B$ , where  $d_i = a_i - b_i$  is used in the evaluation. The null hypothesis is that the medians of the two sample populations are equal ( $H_0 : \mu_A = \mu_B$ ), which is equivalent to  $\mu_D = 0$ . Since  $D$  should follow a symmetric distribution, the requirements on  $A$  and  $B$  are that their distributions are somehow similar. The procedure for carrying out any of these Wilcoxon tests includes sorting of values, the assignment of numerical ranks and some basic arithmetic calculations yielding the test statistic. The test statistic is then compared to critical values which leads to the decision of acceptance or rejection of  $H_0$ .

Rank tests have weaker requirements on the samples than t-tests. However, t-tests have higher *power*, while rank tests are considered to be *conservative* [234]. This means that carrying out a t-test (if the requirements are fulfilled) might lead to the rejection of  $H_0$  and therewith detect significant differences, while the rank tests are more likely to retain the null hypothesis  $H_0$ .

## 3.2 Regression and Outlier Detection

Physical laws allow for an exact determination of the response if the variables on the right hand side of the equation are known. For e.g. Hooke's law, the force of a spring can be exactly predicted if spring stiffness and displacement are known - the variables are related to each other by an exact equation. However, when it comes to biological systems, such as the human body or to the human cardiovascular system, the determination of exact relations is almost impossible. In these cases, stochastic relationships are used, whereas the prediction of unknown quantities is often based on other more easily assessable variables and where the accuracy of predictions is dependent on the available variables and the quality of the stochastic model. In the following, it is discussed how a stochastic model is created from given data using *regression analysis*, how the model quality can be assessed and how obtained models can be protected from contamination in the data set (keywords: *Outlier detection* and *robust regression*). Such regression analyses will be applied later on in Chapter 5 to own experimental data in order to create stochastic models for the preoperative prediction of mechanical AAA wall properties.

### 3.2.1 Regression Analysis

Regression analysis is the most routinely applied statistical tool to fit equations between a dependent variable  $\mathbf{y} = (y_1, \dots, y_n)^T$  (also called *response variable*) and any desired number  $p \geq 1$  of independent variables  $\mathbf{x}_p = (x_1, \dots, x_n)_p^T$  (also *regressors* or *explanatory variable*, where  $n$  is the number of observations (data sets)). Although regression analysis is not restricted to linear models, a linear relationship between  $\mathbf{y}$  and  $\mathbf{x}_p$  can be generally described by the equation [175]

$$\mathbf{y} = \mathbf{X}\boldsymbol{\beta} + \boldsymbol{\epsilon}, \quad (3.11)$$

where  $\mathbf{X}$  denotes the  $n$ -by- $p$  *design matrix* that contains the  $p \geq 1$  different *explanatory variables* for the observations:

$$\mathbf{X} = \begin{bmatrix} x_{11} & x_{12} & \cdots & x_{1p} \\ x_{21} & x_{22} & \cdots & x_{2p} \\ \vdots & \vdots & \ddots & \vdots \\ x_{n1} & x_{n2} & \cdots & x_{np} \end{bmatrix} \quad (3.12)$$

$\boldsymbol{\beta} = (\beta_1, \dots, \beta_p)^T$  is the vector of *regression coefficients* or *parameters*.  $\epsilon$  is the vector of error terms. The ranges of  $\mathbf{X}$  and  $\mathbf{y}$  are often called the  $X$ -space (or parameter space) and the  $Y$ -space, respectively. For  $p = 1$ , the regression analysis is denoted *simple regression*, while an additional constant intercept can be added to the model. For  $p > 1$  the regression analysis is called *multiple regression*. The methods presented in the following work for both simple and multiple regression. The aim of any regression analysis is to find the optimal set of fitted coefficients  $\hat{\boldsymbol{\beta}}$ . Please note that in statistics the notion error  $\epsilon$  is used for a non-observable error between optimally fitted values of a model to the true values. The residual  $\mathbf{r} = (r_1, \dots, r_n)^T$ , on the other hand, is the difference between the observed value  $y_i$  and the value from the fitted (e.g. linear) model  $\hat{y}_i = (\mathbf{X}\hat{\boldsymbol{\beta}})_i$  [175]:

$$r_i = y_i - \hat{y}_i \quad (3.13)$$

The most popular method to fit a linear model is based on minimizing this residual using the least squares (LS) method, which goes back to Gauss and corresponds to

$$\min_{\boldsymbol{\beta}} \|\mathbf{r}\|_2, \quad (3.14)$$

where  $\|\cdot\|_2$  is the L2-norm. The solution of this minimization problem can be easily performed in any statistical software.

### Pearson's Product-Moment Correlation Coefficient

One of the simplest measures for the quality of a linear model is the *Pearson's product-moment correlation coefficient*  $r$  (also denoted *Pearson's  $r$*  or just *correlation coefficient*). For a simple regression model, it is calculated by

$$r = \frac{\sum_{i=1}^n (x_i - \bar{x}) \sum_{i=1}^n (y_i - \bar{y})}{\sqrt{\sum_{i=1}^n (x_i - \bar{x})^2} \sqrt{\sum_{i=1}^n (y_i - \bar{y})^2}}, \quad (3.15)$$

where  $\bar{x}$  and  $\bar{y}$  are the mean values of  $\mathbf{x}$  and  $\mathbf{y}$ , respectively. It is a measure for linear dependence between two variables (here  $\mathbf{x}$  and  $\mathbf{y}$ ), taking values  $r \in [-1; +1]$ . The extrem values  $-1$  and  $+1$  denote a perfectly linear relationship of two variables, while  $r = 0$  means that there is no linear relationship. Since the Eq. (3.15) for the calculation of the correlation coefficient is incapable of identifying nonlinear relationships, it only yields feasible values for the evaluation of linear models. The correlation coefficient  $r$  can also be used to assess the quality of a linear multiple regression model. In this case,  $x_i$  and  $\bar{x}$  in Eq. (3.15) need to be substituted by  $\hat{y}_i$  and

$\bar{y}$ , respectively. It is also possible to check if a correlation coefficient  $r$  is significantly different from 0. The method makes use of the test statistic

$$t = \frac{r}{\sqrt{\frac{1-r^2}{n-2}}}, \quad (3.16)$$

which is related to the t-test (Sec. 3.1.3) and where statistical significance is stated for  $|t| > t_{f,1-\alpha/2}$ . Analogously and as used throughout the present work, a significant difference of  $r$  from 0 can also be shown for  $P < \alpha$ .

### Coefficient of Determination

Another measure for the quality of a model is the *coefficient of determination* [18]. It can be applied for both linear and non-linear models. Eq. (3.13) can be rewritten as

$$(y_i - \bar{y}) = (\hat{y}_i - \bar{y}) + r_i. \quad (3.17)$$

On the right hand side of Eq. (3.17),  $(\hat{y}_i - \bar{y})$  obviously represents the improvement of the prediction due to the previously fitted model, while  $r_i$  represents the variation of  $y_i$  which cannot be explained by the derived model. Squaring of Eq. (3.17) and summation over the  $n$  observations leads to

$$\sum_{i=1}^n (y_i - \bar{y})^2 = \sum_{i=1}^n (\hat{y}_i - \bar{y})^2 + \underbrace{2 \sum_{i=1}^n ((\hat{y}_i - \bar{y}) \cdot r_i)}_{=0 \text{ for LS methods}} + \sum_{i=1}^n r_i^2, \quad (3.18)$$

which is better known under the more established formulation

$$SS_y = SS_{\hat{y}} + SS_r. \quad (3.19)$$

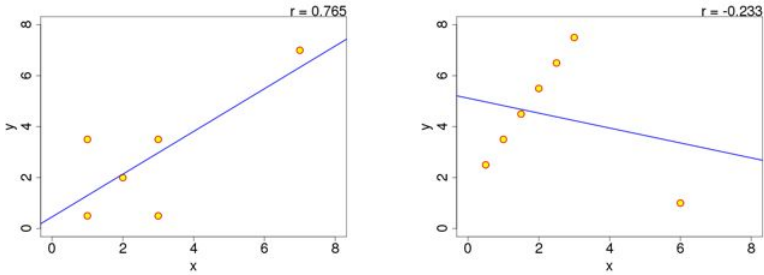
$SS_y$  denotes the total sum of squares or the sample variance.  $SS_{\hat{y}}$  and  $SS_r$  are called the regression sum of squares and the residual sum of squares, respectively. In [18], the coefficient of determination is then defined as

$$R^2 = \frac{SS_{\hat{y}}}{SS_y} = 1 - \frac{SS_r}{SS_y}. \quad (3.20)$$

It provides a measure for the goodness of fit which indicates the percentage of the y-variability that is captured by the fitted model. For linear models, the coefficient of determination can also be calculated from  $R^2 = r^2$ . Hence, it is bounded to the interval  $[0; 1]$ .

### 3.2.2 Outlier Detection

The LS method is optimal to generate regression models if the error distribution for the fitted model follows a normal distribution [175]. Real data does never completely satisfy this assumption. This is why regression models based on the LS method can be easily and wrongly influenced by outliers (see examples in Figure 3.2). Although literature is not consistent in characterization and handling of outliers, the current work distinguishes between leverage points



(a) Example of a “good” leverage point: The leverage point at the top right causes a high correlation, although there is no correlation otherwise.

(b) Example of a “bad” leverage point: The leverage point does not match the pattern of the other points and tilts the regression line.

Figure 3.2: Academic examples of outliers. Outliers have a strong potential to influence regression results.

(=outliers in X-space), outliers in Y-space and in X-Y-space, and regression outliers. For example, the odd point in Figure 3.2 (a) is a potential outlier in X, Y and X-Y-space, but it is not a regression outlier. The odd point in Figure 3.2 (b) is a potential outlier in X-space, but not in Y-space. As seen in these two examples, outliers can both deteriorate or improve the correlation coefficient which is used to assess the quality of a model. However, the main issue with outliers is that they can strongly affect the regression coefficients  $\hat{\beta}$  and therewith lead to a wrong model. A sensible treatment of outliers prior to model generation is consequently essential in order to obtain reliable predictions. Thereby, two different ways are followed in literature. One approach is *robust regression* where outliers are not excluded from the data set, but rather their influence on the results is minimized. Representatives of robust regression methods are e.g. the least median of squares (LMS) method by Rousseeuw [175] or the maximum likelihood type estimates (M-estimates) by Huber [97]. The more classical approach, which will also be followed in the present work, is *outlier diagnostics*. Outlier diagnostics includes identification of outliers and removal of outlying observations from the data set. A problem that comes with outlier identification is that there is no hard mathematical definition of an outlier, but there are rather a lot of different approaches. Further, the measures for outlier detection are often ambiguous and can lead to the detection of different potential outliers, whereas not all of them do necessarily have to be excluded from the analysis. These arguments prevent automated methods for outlier identification or even outlier removal. Consequently, the purpose of outlier diagnostic methods which can be found in statistical software can therefore only be to point out potential outliers. The proper identification of outliers therefore requires a lot of tedious and manual work and, unfortunately, outlier removal remains a very personal and subjective decision. In simple regression, the detection of leverage points or outliers might to some extent be possible by visual observation of the scatter plot (e.g. Figure 3.2). However, such graphical methods do not work any more for multiple regression, where the X-space can have multiple dimensions.

Consequently, there is a need for objective procedures to compute potential outliers. Some of the methods are presented in the following.

### Hat Matrix

The *hat matrix* occurs frequently in classical diagnostics and is defined as [16, 175]

$$\mathbf{H} = \mathbf{X}(\mathbf{X}^T\mathbf{X})^{-1}\mathbf{X}^T. \quad (3.21)$$

It is a symmetric  $n$ -by- $n$  matrix that is called *hat matrix* because it transforms the observed vector  $\mathbf{y}$  into its LS estimate  $\hat{\mathbf{y}} = \mathbf{H}\mathbf{y}$  (it puts a hat on  $\mathbf{y}$ ) [175]. The diagonal elements  $h_{ii}$  of  $\mathbf{H}$  are thereby a measure for the influence of the  $i$ -th observation on the fit and are consequently called the *leverages* [44]. The calculation of the hat matrix includes the  $\mathbf{X}$  matrix, but does not include  $\mathbf{y}$ . For this reason, it can obviously only detect outliers in the  $X$ -space (leverage points). It is recommended that particular attention should be paid to observations with  $h_{ii} > 2\frac{p}{n}$  [10, 16, 175, 222]. But already in [10] it is annotated that this threshold might point out too many leverage points. Consequently, in [175] it is also proposed to use  $h_{ii} > 3\frac{p}{n}$  as an adequate threshold. However, an outlier in  $X$ -space does not necessarily have to be a regression outlier. When it is in very good agreement with the regression model, it can even be beneficial reducing the confidence intervals. [44] therefore deemphasizes the use of the  $h_{ii}$  leverages for outlier detection. In the current work, the critical value for the detection of  $X$ -space outliers was set  $3\frac{p}{n}$ .

### Studentized Residual

A measure for a residual based outlier detection in the  $Y$ -space is the *studentized residual* (sometimes also *externally studentized residual* or *jackknifed residual*) [10, 44, 175]. It is defined as

$$t_i = \frac{r_i}{s_{(i)}\sqrt{1 - h_{ii}}}. \quad (3.22)$$

$s_{(i)}\sqrt{1 - h_{ii}}$  denotes the external standard error of the residual, where  $s_{(i)}$  is the variance of the residual when its calculation is rerun omitting the  $i$ -th observation [44, 175]:

$$s_{(i)} = \sqrt{\frac{1}{n - p - 1} \sum_{j=1, j \neq i}^n r_j^2}. \quad (3.23)$$

The studentized residual can be used for outlier detection on its own (see e.g. the work by Vande Geest *et al.* [222]), although uncommon. If so, observations that lie outside a  $(1 - \alpha) \cdot 100\%$  confidence interval of a  $t$ -distribution are potential outliers. The confidence intervals are calculated by  $[-t_{n-p-1, \alpha/2}, +t_{n-p-1, \alpha/2}]$  [16]. A 95% confidence interval was used e.g. in [222]. The use of a purely residual based outlier detection has a major disadvantage: An initial regression model has to be built which is in turn used to calculate the residuals. If residual outliers are then removed and a second LS fit is performed subsequently, one only ends up with smaller errors and nicer correlation coefficients, while the final regression model is unlikely to change. If for example residual based outlier deletion is applied to the data set in Figure 3.2 (b), the true outlier cannot be identified any more since the regression line has already been substantially tilted before. Rather two correct data points would be removed prior to the true outlier. Usually, the studentized residuals play an important role in other outlier detection methods as presented in the following.

## DFFIT

The former methods were designed to detect cases with either high leverage  $h_{ii}$  or large studentized residual  $t_i$ . However, these two indicators for potential outliers do not necessarily overlap. A measure that combines both possibilities is the DFFIT (sometimes also DFFITS, DFITS or DEFFITS) [16, 17, 175]:

$$DFFIT_i = \sqrt{\frac{h_{ii}}{1-h_{ii}}} \cdot t_i, \quad (3.24)$$

where the term  $\sqrt{\frac{h_{ii}}{1-h_{ii}}}$  takes the largest values for points with greatest leverage in X-space, while the studentized residual  $t_i$  acts as a second factor weighting the outlyingness in Y-space. Observations with  $|DFFIT_i| > 2\left(\frac{p}{n}\right)^{0.5}$  are potential outliers [10, 16]. In [16],  $\sqrt{p}$  is suggested as a cutoff value.

## Cook's Distance

Another method specially designed for outlier detection in X-Y-space is based on the *Cook's Distance* ( $CD$ ). The  $CD$  is defined as [17, 44, 175]

$$CD_i = \frac{h_{ii}}{p(1-h_{ii})} \cdot s_i^2, \quad (3.25)$$

where  $s_i$  is the internally studentized residual

$$s_i = \frac{r_i}{s\sqrt{1-h_{ii}}} \quad (3.26)$$

with  $s$  as the residual mean square (often mean square error - MSE) of the full data set:

$$s = \sqrt{\frac{1}{n-p} \sum_{j=1}^n r_j^2}. \quad (3.27)$$

Thus the  $CD$  is dependent on a part  $\left(\frac{h_{ii}}{p(1-h_{ii})}\right)$  that measures the leverage in X-space and the internally studentized residual  $s_{(i)}$  as a factor that weighs the residual in Y-space. Observations with  $CD_i > \frac{4}{n}$  are potential outliers [17].

Compared to the studentized residual method,  $CD$  and DFFIT put more weight on the leverage. In other words, the studentized residual tends to remove observation with large fitting error (mainly a cleaning of the data set, potentially leading to better correlation coefficients). Whereas  $CD$  and DFFIT try to detect highly influential points, which distort the LS regression results.

In the current work, all statistical analyses were performed with the statistical software R (R Development Core Team, Vienna, Austria) [162].



# 4 Mechanotransduction in Abdominal Aortic Aneurysms

Mechanotransduction is one of the essential processes in mechanobiology. Humphrey and Holzapfel [101] distinguish three fundamental mechanobiological processes:

**Mechanotransduction** the sensing of mechanical stimuli.

**Mechanotranscription** gene expression to govern the response.

**Mechanotranslation** production and rearrangement of functional biomolecules.

Mechanobiology is essential for physiological adaptation processes of the cardiovascular system to its environmental and internal loading conditions. Primarily, the influence of blood pressure and wall shear stress on the endothelium has received much attention in the past: Deviations from the physiological flow conditions can lead to arterial remodeling [36, 99, 121] and pathogenesis of atherosclerosis, atherothrombosis and peripheral occlusive disease [150]. Although histopathological changes in the aortic wall are seen as the major cause for AAA formation [81], it cannot be excluded that mechanotransduction also plays a central role in AAA growth. However, the exact mechanobiological mechanisms, in particular mechanotransduction processes, that lead to dilative angiopathy or aneurysm formation are not clear enough. Nevertheless, it has been assumed that mechanical wall stresses and strains induced by blood pressure [217] and flow [65, 122] can lead to inflammatory and proteolytic AAA wall destabilization [27, 107] which promotes AAA expansion and rupture. Still, a close and causal relationship between these factors has thus far never been demonstrated *in vivo* for methodical reasons. Yet, the mechanical quantities acting in AAA wall on the one side and biological activity within the AAA wall on the other side can be obtained separately, using two independent methods: The FE method and [18F]-fluorodeoxyglucose positron emission tomography/CT (FDG-PET/CT). Details on the FE analysis of AAAs, which enables the prediction of realistic loading of the AAA wall even in complex, patient-specific geometries, have already been described in Chapter 2. FDG-PET/CT is an imaging modality that is used to visualize the metabolic activity in the human body. In the current study, both the FE simulation results and PET/CT images were available for 52 AAAs. The aim of this chapter was to investigate the interplay between mechanical quantities obtained by FE simulation and biological tissue reaction assessed by FDG-PET/CT imaging. It starts with a detailed description of FDG-PET/CT imaging in Section 4.1. Section 4.2 is then devoted to the literature review of already existent FE and FDG-PET/CT based approaches to investigate mechanobiological interaction in AAAs. A profound study on the correlations of mechanical loading to metabolic activity is performed in Section 4.3.

## 4.1 FDG-PET/CT Imaging for Engineers

FDG-PET/CT is a nuclear medicine imaging technique that combines the standard CT with the functional PET imaging. While CT is usually used to assess the morphology of structures within a patient, PET is used to visualize functional processes in the body that cannot be captured with CT or MRI. In case of FDG-PET/CT, a [ $^{18}\text{F}$ ]-fluorodeoxyglucose (FDG) tracer is administered to the patient, which is a radioactive analogue of glucose. The FDG is usually injected 60 minutes prior to scanning, which allows it to circulate within the body and accumulate at locations of increased glucose metabolism. During the subsequent radioactive decay of FDG with a half life of 109 minutes [80], positrons are emitted, which are then absorbed in the nearby tissue resulting in the production of a pair of gamma photons that can leave the body and be detected by the PET scanner. Based on the locations and activity of the decay measured by the scanner, a three-dimensional map of the local FDG-activity/uptake can be visualized. The measured FDG-uptake is representative for the *in vivo* metabolic activity.

In clinical practice, PET scanners are most frequently found in combination with CT scanners (hybrid PET/CT scanner). These machines are capable of performing sequential CT and PET scans within one investigation, whereas different concepts can be applied [80]:

**PET with low-dose CT**, where the low-dose CT is acquired for the attenuation correction of the PET (e.g. contrast-enhanced CT images or diagnostic MRI has already been performed previously), see for example Figure 4.1.

**PET with contrast enhanced CT**, where the contrast-enhanced CT is used for attenuation correction.

**PET with contrast-enhanced CT and low-dose CT**, where a low-dose CT is acquired for attenuation correction in addition to the diagnostic contrast-enhanced CT (these were the standard PET/CT data sets in the current work).

An attenuation correction accounts for the different absorption of gamma photons within different regions of the body. E.g., without attenuation correction, the same FDG-uptake in portions of lung and liver would lead to different measurements of FDG-activity as the gamma photons have to travel through different materials before reaching the detector. The surrounding liver would absorb more of the originating gamma photons than the less dense lung tissue. The attenuation correction of the PET data is usually performed based on the HU of the originating material obtained by low-dose CT (first and third case of the above list) or contrast-enhanced CT (second case). The attenuation corrected PET images are often fused with CT images for diagnostic purposes (Figure 4.1 (d)).

While the original purpose of PET imaging was the detection of cancer metastasis, physicians have also discovered the potential of FDG-PET/CT as a biomarker for non-invasive *in vivo* evaluation of AAAs by assessing the local glucose metabolism within the vessel wall through the FDG-uptake [114, 155, 178, 179]. However, the histopathological changes in AAA wall associated with increased FDG-uptake remain disputed and the role of FDG-PET/CT in the non-invasive evaluation of AAAs still needs to be explored in more detail. Various researchers, including our own group, promote that increased FDG-metabolic activity in the AAA wall is associated with inflammation, increased proteolytic activity and structure-protein-degradation [39, 171, 179, 210] leading to wall instability, rapid expansion and rupture risk [168, 179, 237].

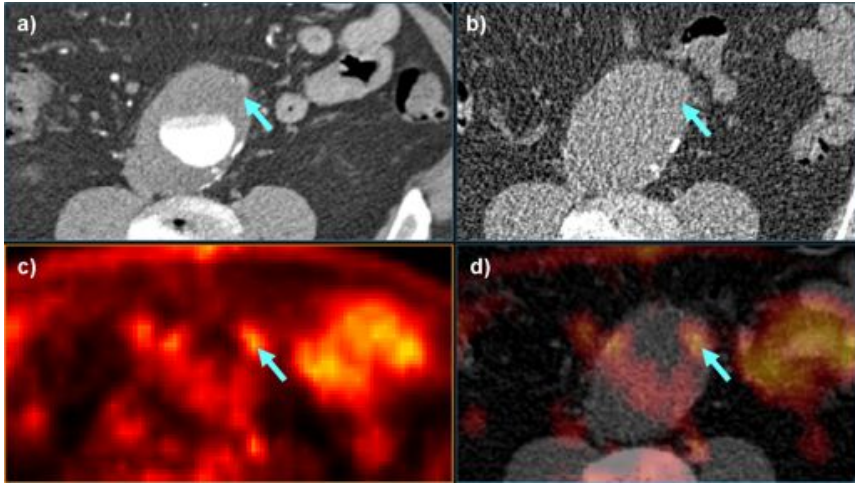


Figure 4.1: Transversal images of a patient with aneurysmatic aorta: The contrast enhanced CT image (a) was acquired in a stand-alone CT scanner. One day later, an additional low-dose CT (b) for attenuation correction and a PET scan (c) were performed using a combined PET/CT scanner. (d) shows the fusion of the low-dose CT and the PET image. Gray values in CT images and in the fused PET/CT image represent the HU. Yellowish red colors in the PET image and in the fused PET/CT image indicate the FDG-activity. The blue arrows are added for orientation purposes and point to the same site of increased FDG-uptake in the AAA wall.

Others, however, support the theory that increased FDG-uptake rather indicates hypoxia but not inflammation [51]. Finally, a recent study by Kotze *et al.* [113] stated a negative relationship between increased FDG-metabolic activity and AAA growth rate, which is in disagreement with previous observations of wall instability and expansion.

## 4.2 Literature Review

Independent of the histopathological changes that are associated with increased FDG-uptake in the AAA wall, which are not covered in the present work, it is an interesting question whether distributions of mechanical quantities are correlated to patterns of FDG-uptake. A close relationship of biomechanical loads and FDG-uptake could even demonstrate the presence of mechanotransduction processes in the AAA wall. A first study that goes into that direction has been presented by our group in 2009 [170]. In this study, it was hypothesized that FDG-uptake might correlate to wall stress levels in AAAs, as found by visual inspections of PET/CT images and wall stress results obtained by FE analyses of 18 AAAs. An example AAA is given in Figure 4.2 exhibiting a convincing correspondence of regions with increased FDG-uptake and wall stress patterns. Xu *et al.* [237] also compared FDG-PET/CT images to FE wall stress results

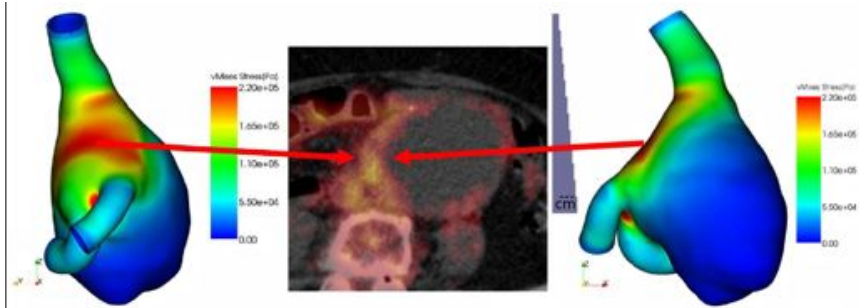


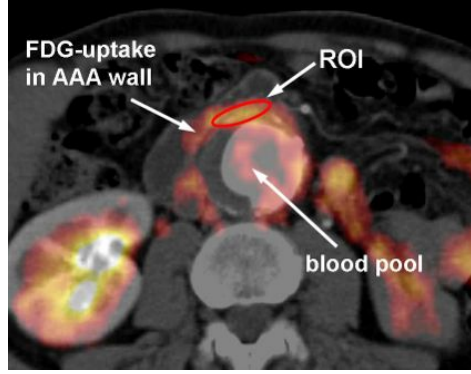
Figure 4.2: Example of the visual comparison of wall stresses obtained by FE analysis (left and right AAA geometries) and FDG-metabolic activity as represented by the fused FDG-PET/CT image in the middle as performed by Reeps *et al.* [170]. Sites of high wall stress show good co-localization to portions of AAA wall with increased metabolic activity. Figure adapted from [170].

in five AAA patients. They found that regions of high wall stress co-localized with regions of positive FDG-uptake. Later on, two of these patients experienced rupture of their AAA and the physicians found that sites of rupture corresponded to previously identified sites of high metabolic activity and high wall stress. Both of these studies [170, 237] had in common that the conclusions arose only from visual observations between two-dimensional PET/CT images and three-dimensional wall stress patterns. The relationships between FDG-metabolic activity and wall stresses were investigated only qualitatively - proper quantifications of the correlations were not possible.

To overcome this drawback of having only a qualitative description of the interplay between FDG-uptake and mechanical loading, a novel approach was proposed by our group in 2011 [130]. Thereby, a method for the three-dimensional visualization of the FDG-uptake in the AAA wall using the FE geometry was presented. This method enabled a quantitative correlation of the spatial FDG-uptake to the wall stress distributions. Two different investigations were performed to quantitatively evaluate the correlations between FDG-uptake in AAA wall and the biomechanical loading: Firstly, a spatial, element-wise correlation of FDG-uptake to wall stresses. Secondly, a comparison of maximum wall stress and strain measured anywhere in the AAA wall to the maximum metabolic activity. The rest of this section is devoted to a more detailed summary of this work by Maier *et al.* [130]:

This study included 18 AAA patients which underwent FDG-PET/CT imaging. The patient age varied from 59 to 85 years with an average of  $71.9 \pm 6.9$  years. Maximum aortic aneurysm diameter ranged from 45 to 82 mm with an average of  $62.2 \pm 9.4$  mm. PET/CT examinations were performed after bolus injection of 370 MBq FDG (uptake time: 90 min), including a low-dose CT scan for attenuation correction of PET emission data, a routine diagnostic contrast-enhanced thoracoabdominal multi-slice CT and PET images acquired for 3 min per scan. PET data was consecutively reconstructed at slice distance  $d = 5$  mm with measured attenuation correction based on the low dose CT transmission data, comparable to the procedure presented

Figure 4.3: Transversal fused FDG-PET/CT image showing an AAA with locally increased FDG-uptake in its wall. For the determination of the maximum Standardized Uptake Value ( $SUV_{max}$ ), an ellipsoid region of interest (ROI) is placed over the wall portion featuring highest focal FDG-uptake. Picture adapted from Maier *et al.* [130].



in Section 4.1 and in Figure 4.1. For quantification of the maximum FDG-uptake of each AAA, the fused FDG-PET/CT scans were conventionally analyzed by a nuclear medicine physician using the scanner specific software TrueD<sup>TM</sup> (Siemens medical solutions, Erlangen, Germany). Thereby, a two-dimensional ellipsoid region of interest (ROI) was placed over the highest focal FDG-uptake of the aortic wall, as shown in Figure 4.3. The maximum Standardized Uptake Value  $SUV_{max}$ , a patient weight and dosage independent quantity for the metabolic activity, was calculated from the maximum FDG-uptake measured within this ROI (*single hot-spot method*) [80]:

$$SUV_{max} [-] = \frac{\max \text{ FDG-uptake } \left[ \frac{\text{MBq}}{\text{g}} \right] \cdot \text{patient weight } [\text{g}]}{\text{injected activity } [\text{MBq}]} \quad (4.1)$$

For the FE model generation, the blood lumen and the ILT of the AAAs were segmented from contrast-enhanced CT images. The AAA wall was assumed to have a uniform thickness of  $t = 1.2$  mm. The reconstructed AAA geometries were meshed with a hexahedral-dominated mesh at a base level size of  $h = 1.0$  mm. Nonlinear FE analysis was performed for each AAA, while special regard was paid to the prestressing of the AAA geometries obtained from *in vivo* CT images, as also described in detail in Section 2.6.2 and in [64, 66]. Calcifications were neglected in this study. The aortic wall was modeled with a Raghavan & Vorp type SEF, see Eq. (2.60) (material parameters from [164]). ILT, if existent, was modeled using a coupled form of the compressible neo-Hookean type material [90] with the SEF  $W_{ILT}(C) = c_1(I_1 - 3) + \frac{c_2}{\beta}(J^{-2\beta} - 1)$  and material parameters  $c_1 = 18.0$  kPa and  $\beta = 4.5$ . The proximal and distal ends of the models were constrained by Dirichlet boundary conditions (all displacements set to zero). The external tissue support and the contact to the spine were neglected applying a zero-pressure Neumann boundary condition to the abluminal AAA surface. The luminal AAA surface was loaded with a hydrostatic pressure of  $p = 121$  mmHg consistently for all AAAs in the study, while the MULF prestressing was applied up to a luminal pressure of  $p = 87$  mmHg. All simulations were performed using the software package BACI [229].

One of the innovative new ideas in the work by Maier *et al.* was to map the FDG-uptake from the unfused PET images to the FE mesh of the AAAs. Thereby, it was first necessary to determine the correct position of CT-based AAA geometry within the PET images, which

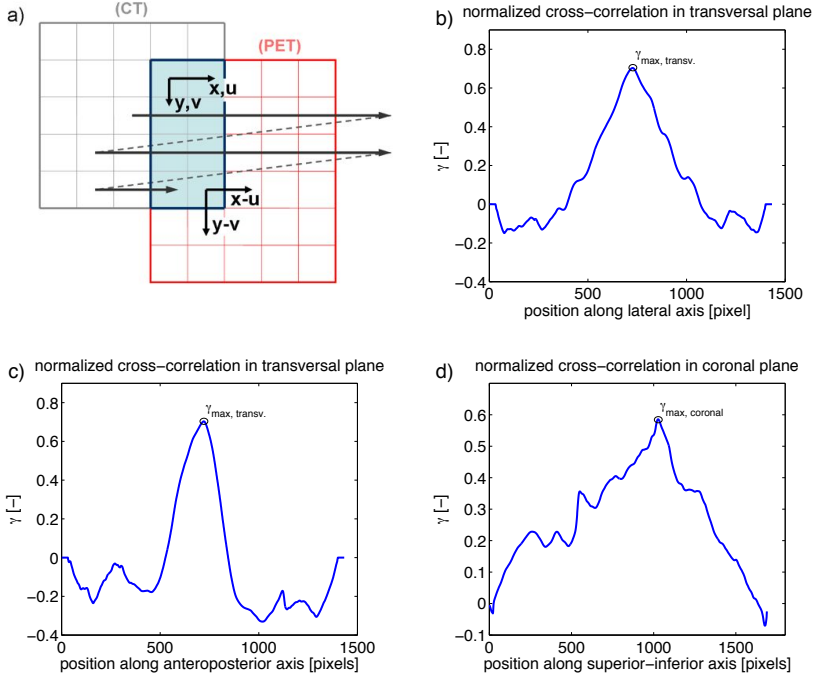


Figure 4.4: (a) Schematic drawing representing the translation  $(u, v)$  of the CT image over the PET image during the cross-correlation process. Normalized cross-correlation value  $\gamma$  along translations in (b) lateral axis, (c) anteroposterior axis and (d) superior-inferior axis of an exemplary AAA. The maximum of  $\gamma$  indicates the best-fit position of the CT image and the AAA geometry to the PET image. Pictures adapted from Maier *et al.* [130].

was performed by normalized cross-correlation between CT and PET images. The normalized cross-correlation value  $\gamma$  for each possible overlap of two images was calculated according to the formula [123, 158]:

$$\gamma(u, v) = \frac{\sum_{x,y} [f(x, y) - \bar{f}_{u,v}] [t(x - u, y - v) - \bar{t}]}{\{\sum_{x,y} [f(x, y) - \bar{f}_{u,v}]^2 \sum [t(x - u, y - v) - \bar{t}]^2\}^{0.5}}, \quad (4.2)$$

where  $f(x, y)$  is the FDG-uptake of the PET data at pixel  $(x, y)$  and  $\bar{f}_{u,v}$  is the mean FDG-uptake in the overlapping area of the CT and PET images (see Figure 4.4 (a)).  $t(x, y)$  is the grayscale value of the CT data at pixel  $(x, y)$  and  $\bar{t}_{u,v}$  is the mean grayscale value in the overlapping area of the two images. The overlap, or simply said the position of the CT image in the PET image, is defined by the pixel-wise translation  $(u, v)$  of the CT image over the PET image. The maximum value of  $\gamma$  among all possible overlaps indicates the best-fit position  $(u, v)$  of the CT images

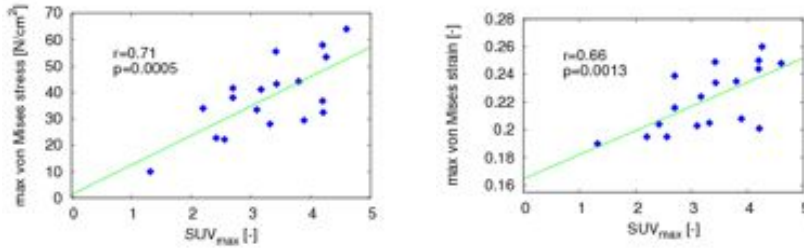


Figure 4.5: Correlation of  $SUV_{max}$  to maximum von Mises wall stresses (left) and von Mises strains (right). Diagrams adapted from Maier *et al.* [130].

within the PET data, while the accuracy is limited to CT data resolution. Curves of the normalized cross-correlation value  $\gamma$  for translations of a CT image along the lateral, anteroposterior and superior-inferior axes of PET data for a typical AAA are shown in Figures 4.4 (b) through (d). A more detailed explanation of the whole process is given in Maier *et al.* [130]. Subsequently, the calculated translation  $(u, v)$  was used to map the FDG-uptake to the FE mesh of the AAA wall. This was performed using a custom algorithm which interpolates the FDG-uptake at the center of gravity of each finite element, similarly to the HU-mapping process explained in detail in Section 2.5.2.

Correlations between metabolic activity and mechanical quantities obtained by FE simulation were evaluated for two different aspects: Firstly, maximum standardized uptake values ( $SUV_{max}$ ) of FDG-uptake obtained by conventional analyses of FDG-PET/CT images in the TrueD software (Figure 4.3) were correlated to the 99th-percentiles (denoted as *maximum* in the following) of mechanical stresses and strains [197] in the sac region using the Pearson product-moment correlation coefficient  $r$ .  $SUV_{max}$  ranged from 1.32 to 4.60 (mean $\pm$ sd:  $3.31 \pm 0.87$ ). Maximum wall stresses obtained by computational FE analyses varied from 10.0 to  $64.0 \text{ N/cm}^2$  with an average of  $38.2 \pm 13.8 \text{ N/cm}^2$ . Maximum strains ranged from 0.190 to 0.260 with an average of  $0.222 \pm 0.023$ .  $SUV_{max}$  was significantly correlated to maximum wall stress and strain ( $SUV_{max}$  to max stress:  $r = 0.71$ ,  $P = 0.0005$ ;  $SUV_{max}$  to max strain:  $r = 0.66$ ,  $P = 0.0013$ ), as also depicted in Figure 4.5. Secondly, the spatial correlation of FDG-uptake to stress distributions was assessed quantitatively. To achieve this, an element-wise correlation of the spatial FDG-uptake to the wall stress was performed (Pearson product-moment correlation coefficient denoted “ $r_{spatial}$ ”). Diagrams of these spatial correlations for all 18 AAAs are shown in Figure 4.6. The  $r_{spatial}$  ranged from  $-0.168$  to  $0.738$  with an average of  $0.372 \pm 0.263$ . Sixteen AAAs had positive correlations, while there were negative correlations of FDG-uptake to wall stress for two AAAs.

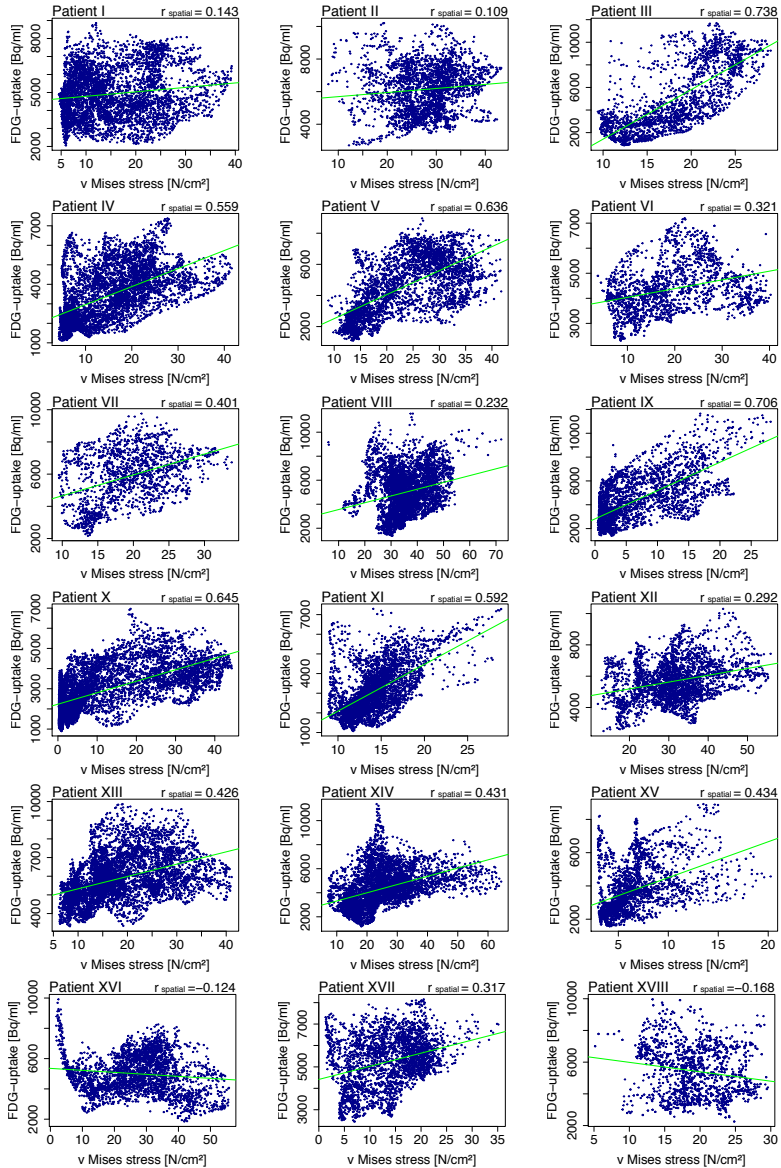


Figure 4.6: Element-wise correlations of FDG-uptake to von Mises stress in the AAA wall. One point in the diagrams represents ten neighboring finite elements. Positive correlations of FDG-uptake to wall stress were obtained for 16 patients. Negative correlations were obtained for patients XVI and XVIII. Diagrams adapted from Maier *et al.* [130].

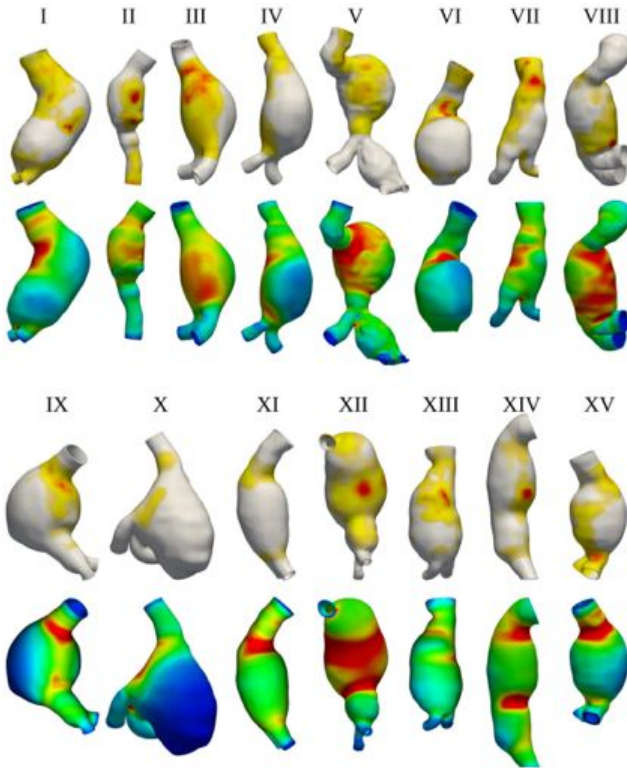


Figure 4.7: AAAs exhibiting good visual correlation of metabolic activity (FDG-uptake, upper rows) to computed wall stress distribution (von Mises stress, bottom rows). AAA sizes are not to scale. Color scales are stretched to the individual patient's data range. Figure adapted from Maier *et al.* [130].

Three-dimensional visualizations of spatial FDG-uptake in AAA wall and stress distributions are shown in Figures 4.7 and 4.8. Fifteen AAAs exhibited good visual correlation of FDG-uptake to computed wall stresses (Figure 4.7). Figure 4.8 shows 3 AAAs which had wall stress independent FDG-uptake.

It was concluded that the results clearly demonstrated a significant quantitative correlation of individually acting stresses and strains with FDG-metabolic activity in the aortic wall. Maier *et al.* further hypothesized that high stress beyond the physiologically healthy range is a mechanotransductive trigger for biological response of the vessel wall leading to elevated FDG-metabolic activity. The mechanobiological mechanisms leading to increased FDG-metabolic activity in AAA wall could not be identified. However, inflammatory and proteolytic activities were listed as the most probable causes [114, 168, 171, 210]. Alternatively, increased mechanical loading

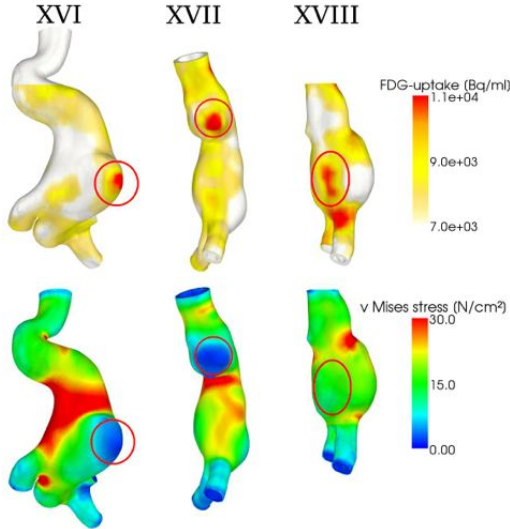


Figure 4.8: AAAs featuring stress independent FDG-uptake in their wall (marked with circles). Colors indicate FDG-uptake (upper row) and von Mises stress (bottom row). For patients XVI and XVII, highest FDG-uptake is located in areas of eccentric ILT-filled bulges. AAA sizes are not to scale. Figure adapted from Maier *et al.* [130].

potentially might initiate regenerative processes, such as compensatory collagen fiber production by SMCs [75], related to increased metabolic activity detected by FDG-PET/CT. This might also explain inverse trends between FDG-uptake and AAA expansion, which have been reported in [113]. For the stress independent FDG-uptake that was observed in three cases (Figure 4.8), Maier *et al.* named potential reasons for two of these patients. In these cases, areas with high stress and strain independent FDG-uptake were located at unusual eccentric bulges of AAA morphology with a large ILT burden (Figure 4.8). This might lead to hypoxia in AAA wall beneath the internal ILT [226], leading to neovascularization. Alternatively, autoimmunological inflammatory processes in the AAA wall were also conceivable [107], resulting in initial destabilization of vessel wall followed by eccentric AAA growth and secondary ILT deposition.

In summary, existent literature ([130, 170, 237]) pointed out that the FDG-glucose metabolism detected by FDG-PET/CT might be co-localized to high mechanical loads in the AAA wall as assessed by FE analyses. Especially the study by Maier *et al.* [130] had the advantage that the FDG-uptake in the AAA wall could be visualized three-dimensionally on the AAA geometry such that quantitative, observer-independent correlations could be obtained. Nevertheless, the study performed by Maier *et al.* had some drawbacks. First of all, the spatial correlations were performed by an element-wise comparison of the local FDG-uptake to the acting stresses. The local FDG-uptake, however, is a quantity that is influenced by the amount of FDG administered and the patient weight, as opposed to the SUV which is normalized with respect to the latter two quantities [80]. Further, also the quality of the FE models was hampered by the choice of an obsolete ILT model and by the neglect of calcifications.

## 4.3 Correlation of Metabolic Activity to Biomechanical Loading

The study in this section aims at overcoming the aforementioned limitations and at verifying the preliminary results from [130, 170, 237] by performing a more profound investigation of the mechanobiological interactions in a statistical meaningful study cohort of 50 AAA patients. Thereby, the observer-independent registration and mapping of PET data to the reconstructed AAA geometry by the algorithm proposed in [130] is maintained and optimized with one detail: Instead of the FDG-uptake, the dimensionless SUV is mapped to the AAA geometry. The use of the SUV enables a consistent comparison of metabolic activity not only within one AAA, but also between different patients. As opposed to the preceding study, the nonlinear FE simulations are performed with the up-to-date ILT material model proposed by Gasser *et al.* [63] (as introduced in Section 2.5.1) and consider the effect of calcifications (as presented in Section 2.5.2).

Objective element-wise correlations of local mechanical quantities with values and distributions of mural aortic FDG-metabolism are enabled. In addition, clinical or mechanical patient-specific quantities which are not related to a spatial distribution (e.g. age, maximum wall stress or maximum AAA diameter) can be correlated to maximum SUV and average SUV in the AAA wall. This might lead to the identification of further parameters that have a bearing on the FDG-metabolism.

### 4.3.1 Methods

#### Study Population

Data sets of 52 AAA patients which underwent PET/CT imaging over a 5-year-period were analyzed retrospectively. Two patients had an inflammatory AAA and were therefore excluded from statistical analyses. The main study cohort comprised 50 (9 female, 41 male) patients with non-ruptured, non-inflammatory AAA. Patient age of this group ranged from 48 to 85 years, with an average of  $69 \pm 8.25$  years (median: 69 years). At time of imaging maximum perpendicular infrarenal AAA diameter ranged from 38 to 89 mm with an average of  $58.0 \pm 13.0$  mm (median: 54.55 mm). All patients were scheduled for surgical repair. Informed consent was obtained from the patients before participation in the study. The study was conducted after approval by the ethics committee of the university hospital Rechts der Isar, Technische Universität München, Germany.

#### FDG-PET/CT Imaging

Patients with contraindications for PET/CT such as chronic renal failure (serum creatinine  $> 1.6$  mg/dl), congestive heart failure, elevated blood glucose levels (blood glucose  $> 130$  mg/dl) or known intolerance against iodinated contrast media were excluded from the study. Combined FDG-PET/CT data sets of the patients were acquired in the Klinikum rechts der Isar, university hospital of the Technische Universität München. Patients were instructed to fast for at least 6 hours before PET/CT examination. After bolus injection of 370 MBq FDG (uptake time: 90 min), a low-dose CT scan (Siemens Biograph Sensation 64, Erlangen, Germany; 120 kV,

20 mAs) was obtained for attenuation correction of PET emission data, followed by routine diagnostic contrast enhanced thoracoabdominal multi-slice CT (100 ml contrast medium Imeron 300). Data was processed on a Volume Wizard workstation (Siemens medical solutions) and slices were indexed at 5 mm. Immediately after CT scanning, PET images were acquired for 3 min per scan in bed position. PET data was consecutively reconstructed with measured attenuation correction based on the low dose CT transmission data. Anonymized image data was then transferred to the Institute of Computational Mechanics, Technische Universität München. PET images were used for evaluation of the FDG-metabolic activity, while CT images were used for the reconstruction of the individual AAA geometry for further computational FE analyses.

### AAA Geometry Reconstruction and FE Analysis

Contrast enhanced CT images (3 mm reformatted slice distance) were imported into the commercial image processing software Mimics 13.0. Lumen and, if existent, ILT were segmented and three-dimensionally reconstructed as previously described in Section 2.2. Hexahedral-dominated FE meshes of the AAA geometries were created using the commercial software Harpoon as described in Section 2.3. An idealized AAA wall with spatially uniform thickness of  $t = 1.2$  mm was consistently added to each AAA. The meshed AAA geometries were used for sophisticated nonlinear FE analyses, which were described by our group in [133, 137, 169]. FE calculations were performed utilizing adequate hyperelastic material models for the different constituents of the AAA:

**AAA wall** A hyperelastic, isotropic, almost incompressible material model described by the SEF

$$W_{wall} = W_{iso}(\bar{C}) + W_{vol}(J) = \alpha (\bar{I}_1 - 3) + \beta (\bar{I}_1 - 3)^2 + \frac{\kappa}{\eta^2} (\eta \ln J + J^{-\eta} - 1) \quad (4.3)$$

was used to model the AAA wall in simulations as already described in Section 2.5.3 (Eqs. (2.47) and (2.60)). The isochoric contribution  $W_{iso}$  and the volumetric part  $W_{vol}$  were chosen according to Raghavan and Vorp [164] and Ogden [152], respectively. The material parameters were set to  $\alpha = 0.174$  MPa,  $\beta = 1.88$  MPa,  $\kappa = 8.7$  MPa (resembling a Poisson's ratio of  $\nu = 0.48$ ) and  $\eta = -2$ .

**Intraluminal thrombus** ILT was modeled using an Ogden-type SEF

$$W_{iso} = c(\bar{I}_1^2 - 2\bar{I}_2 - 3) + \frac{\kappa}{\eta^2} (\eta \ln J + J^{-\eta} - 1). \quad (4.4)$$

The isochoric contribution of this SEF was proposed by Gasser *et al.* [63]. The implementation of this material incorporates a variable ILT stiffness, which decreases from the luminal ( $c = 2.62$  kPa) to the abluminal layer ( $c = 1.73$  kPa) (see also Section 2.5.1, as well as Eq. (2.45) and Figure 2.8). The bulk modulus  $\kappa$  was adapted to the isochoric stiffness parameter  $c$  of each element using the formula  $\kappa = 8 \frac{c}{1-2\nu}$ , such that a spatially constant Poisson's ratio  $\nu = 0.48$  was obtained

**Calcification** Calcifications in the AAA wall or within the ILT were automatically identified using the HU mapping method presented in Section 2.5.2 (see also Figures 2.17

through 2.19). If the HU of a finite element exceeded a lower threshold of  $HU = 300$ , an additional strain energy contribution  $W_{calc}$  was added to the SEF of the wall or the ILT:

$$W_{calcified\_wall/ILT} = W_{wall/ILT} + W_{calc.}, \quad (4.5)$$

$$\text{with } W_{calc.} = \alpha_{HU}(\bar{I}_1 - 3) + \frac{\kappa}{\beta^2}(\beta \ln J + J^{-\beta} - 1). \quad (4.6)$$

The correlation function for the material parameter  $\alpha_{HU}$  of calcified elements was chosen identically to Eq. (2.54), which describes a sinusoidal increase from  $\alpha_{HU} = 0$  at  $HU_{min} = 300$  to  $\alpha_{HU} = \alpha_{HU,max} = 8.929$  MPa at  $HU_{max}$ . For the calculations in this chapter,  $HU_{max}$  was set to 600. The bulk modulus  $\kappa$  was adapted to the material parameter  $\alpha_{HU}$  of each element to retain a spatially constant Poisson's ratio of  $\nu = 0.48$ .

Finite strain theory and geometrical nonlinear model assumptions for the deforming AAA wall and the ILT were applied in the FE calculations. The displacements of the proximal and distal ends of the models were constrained to zero. Hemodynamic forces were modeled as orthogonal pressure to the deformed configuration of the luminal ILT surface or the ILT-free luminal surface of the AAA wall. In addition, the prestressed state of the AAA models (reconstructed from CT images that show the AAA under *in vivo* loading) was taken into account by applying the MULF prestressing algorithm (Section 2.6.2; [64, 66, 130]). Thereby, a diastolic pressure of  $p = 87$  mmHg was assumed for all patients to act in the imaged AAA configuration for the recovery of the prestress. A standard forward nonlinear FE simulation was applied for the increase in pressure from  $p = 87$  mmHg to  $p = 121$  mmHg in all patients. All calculations were performed using the non-commercial FE solver BACI [229].

### Visualization of the Metabolic Activity in the AAA

In order to enable consistent comparisons between results of FE calculations and metabolic activity in the AAA wall, the two-dimensional data from PET/CT images were transformed into three-dimensional visualizations of the spatial FDG-uptake (SUV) using the geometry of the FE models. For that purpose, the three-dimensional FE models reconstructed from CT data were registered and matched to the attenuation corrected PET data as previously described in Section 4.2 and in [130]. The contours of a typical AAA geometry relative to the PET data after this registration procedure are shown in Figure 4.9 (left), which demonstrates the correct fitting of the AAA geometry to the PET data. The FDG-uptake at the center of gravity of each finite element of the FE model was then trilinearly interpolated from the PET image data, which was then used for the calculation of the SUV according to Eq. (4.7):

$$SUV [-] = \frac{FDG\text{-uptake} \left[ \frac{\text{MBq}}{\text{g}} \right] \cdot \text{patient weight} [\text{g}]}{\text{injected activity} [\text{MBq}]} \quad (4.7)$$

The administered dosage and the patient weight needed in this calculation were obtained from the DICOM meta data of each patient. The spatial SUV distribution in the AAA wall was then visualized in the open source software Paraview using the geometry of the FE model, as displayed in Figure 4.9 (right).

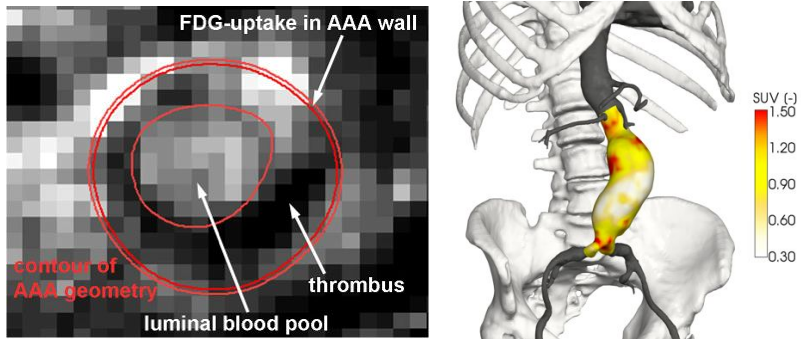


Figure 4.9: (a) Extract of PET image with contours of a patient-specific AAA geometry after registration of the CT data to the PET data. Bright pixels indicate increased FDG-uptake and metabolic activity in the AAA wall. The exact position of the AAA geometry within the PET data has been determined by a normalized cross-correlations and visual comparison. (b) Three-dimensional visualization of an AAA showing the SUV mapped from the PET data to the FE mesh. SUV (yellow to red color) ranges from 0.3 to 1.5  $[-]$ . The visualization was created using the software Paraview.

### Statistical Evaluation of FDG-uptake and Correlation to Clinical, Mechanical and Geometrical AAA Properties

Only aneurysmatic aortic segments in between the renal artery bifurcation and the aortic bifurcation were considered for evaluation. FDG-uptake at side branches (e.g. lumbar and lower mesenteric arteries) was excluded from analyses. Two types of evaluations were performed: Firstly, maximum SUV (assessed as 99.95th-percentile and denoted as "SUVmax" in the following) and the average SUV (denoted as "SUVavg") were correlated to constant, location-independent patient-specific quantities. More precisely, SUVmax and SUVavg were correlated to clinical quantities (patient age and sex), mechanical quantities (maximum wall displacement, average and maximum von Mises wall stresses, average and maximum von Mises wall strains) and geometrical quantities (maximum AAA diameter, abluminal AAA surface, ILT volume). Maximum mechanical and maximum geometrical quantities were assessed as the 99th-percentiles of their respective spatial distributions. Information on the individual patient's medical history (hypertension, diabetes mellitus, laboratory parameters, the patient's smoking habits, etc.) was not consistently available for the patients included in this study and was therefore not considered in the evaluation. The Pearson product-moment correlation coefficient  $r$  was applied for statistical evaluation. Secondly, quantities that featured a spatial distribution, such as e.g. local diameter or wall stress distributions, were subjected to spatial element-wise correlations with the SUV distributions. Element-wise correlations were performed for the SUV distributions to wall stress, wall strain, displacement, local radius/diameter and ILT thickness distributions, respectively. The Pearson product-moment correlation coefficient  $r$  was used for quantitative evaluations of spatial correlations. The statistical significance level was set to  $\alpha = 0.05$  for all evaluations. All

Table 4.1: Correlation of mural AAA FDG-metabolism (SUVmax and SUVavg) to clinical, mechanical and geometrical quantities. Statistically significant correlations ( $P < 0.05$ ) are printed in bold:

	Correlations of SUVmax to ...		Correlations of SUVavg to ...	
	r-value	P-value	r-value	P-value
... patient sex	-0.123	0.393	<b>-0.352</b>	<b>0.012</b>
... patient age	-0.035	0.810	0.055	0.705
... maximum wall displacement	<b>0.490</b>	<b>3E-4</b>	-0.099	0.493
... average vM wall stress	<b>0.449</b>	<b>0.001</b>	-0.062	0.670
... maximum vM wall stress	<b>0.576</b>	<b>2E-5</b>	0.090	0.533
... average vM wall strain	<b>0.365</b>	<b>0.009</b>	-0.123	0.396
... maximum vM wall strain	<b>0.550</b>	<b>4E-5</b>	0.000	1.000
... maximum AAA diameter	<b>0.344</b>	<b>0.014</b>	-0.116	0.423
... abluminal AAA surface	<b>0.358</b>	<b>0.011</b>	-0.040	0.781
... ILT volume	0.118	0.415	-0.132	0.362

statistical analyses were performed with the statistical software R (R Development Core Team, Vienna, Austria).

### 4.3.2 Results

#### Statistical Evaluation

The main study cohort comprised of 50 patients with non-ruptured, non-inflammatory AAA. SUVmax in the AAA sac region ranged from 1.151 to 2.061 with a mean±sd of  $1.573 \pm 0.195$  and a median of 1.574. SUVavg in the AAA sac region ranged from 0.529 to 0.955 with a mean±sd of  $0.756 \pm 0.088$  and a median of 0.744. Maximum diastolic to systolic wall displacements as obtained by FE simulations ranged from 0.41 to 1.42 mm and had a mean±sd of  $0.79 \pm 0.25$  mm and a median of 0.76 mm. Maximum wall stresses varied from 146 to 542 kPa with a mean±sd of  $310 \pm 83$  kPa and a median of 306 kPa. Average wall stresses ranged from 69 to 328 kPa with a mean±sd of  $170 \pm 58$  kPa and a median of 166 kPa. Maximum wall strains ranged from 0.132 to 0.239 with a mean±sd of  $0.194 \pm 0.024$  and a median of 0.193. Average wall strains varied from 0.078 to 0.214 and had a mean±sd of  $0.145 \pm 0.032$  and a median of 0.145. The abluminal AAA wall surface (sac area only) ranged from 100 to 805 cm<sup>2</sup> with a mean±sd of  $336 \pm 165$  cm<sup>2</sup> and a median of 296 cm<sup>2</sup>. The ILT volume ranged from 0 to 351 cm<sup>3</sup> and had a mean±sd of  $88 \pm 93$  cm<sup>3</sup> and a median of 50 cm<sup>3</sup>. Three patients had an AAA without ILT. These results as well as the data for the individual patients are also listed in detail in Table B.1 in the Appendix B.

In correlation analyses of SUVmax and SUVavg to clinical, mechanical and geometrical quantities, the strongest relationship was found between SUVmax and maximum wall stresses ( $r = 0.576$ ,  $P = 0.00002$ ; Table 4.1, Figure 4.10). With regard to clinical quantities, a significant correlation was obtained between SUVavg and patient sex, demonstrating a higher av-

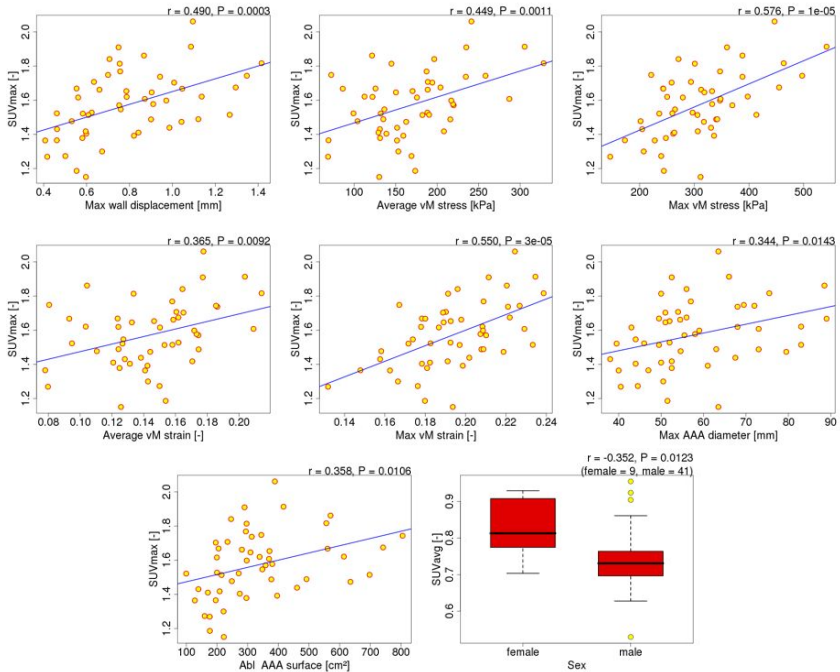


Figure 4.10: Diagrams showing the significant correlations of SUVmax and SUVavg to mechanical, clinical and geometrical quantities. The blue line in each diagram is the best fit line obtained by linear regression.

erage FDG-uptake in the AAA wall of female patients ( $r = -0.352$ ,  $P = 0.012$ ). Further, SUVmax had significant correlations with the following mechanical quantities: Average wall stress ( $r = 0.449$ ,  $P = 0.001$ ), average and maximum wall strains ( $r = 0.365$ ,  $P = 0.009$  and  $r = 0.550$ ,  $P = 0.00004$ ) and maximum wall displacements ( $r = 0.490$ ,  $P = 0.0003$ ). With regard to geometrical quantities, SUVmax was positively correlated to the patient’s maximum AAA diameter ( $r = 0.344$ ,  $P = 0.014$ ) and the abluminal AAA surface ( $r = 0.358$ ,  $P = 0.011$ ). All analyzed correlations, including also those ones not reaching significance, are summarized in Table 4.1. Diagrams for all the significant correlations are given in Figure 4.10.

The spatial co-localizations of SUV patterns to distributions of mechanical and geometrical quantities were investigated by means of element-wise correlations. Best spatial correlations were obtained between the SUV distributions and the local displacements of the AAA wall. Thereby, high SUV was associated with smaller displacements ( $r_{spatial} = -0.148 \pm 0.202$  (mean $\pm$ sd)). Negative spatial correlations between SUV and displacement patterns were obtained for 39 patients, positive correlations were obtained in 11 patients. Correlation coefficients

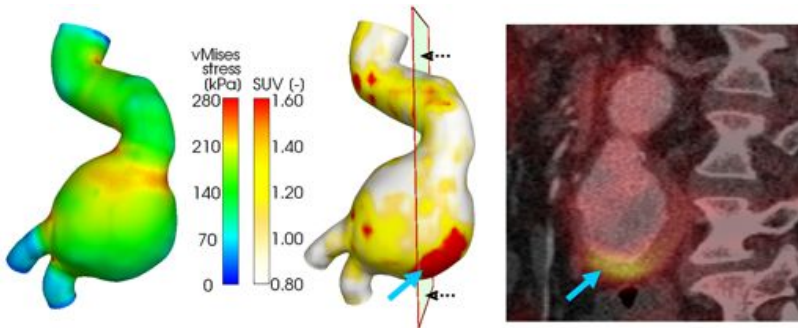


Figure 4.11: Wall stress distribution, SUV distribution and fused PET/CT image (sagittal view) for an inflammatory AAA ( $SUV_{max}=3.027$ ,  $SUV_{avg}=1.126$ ; patient not included for statistical evaluation) with stress-independent FDG-uptake (blue arrows). The plane in the 3D representation indicates the position of the fused PET/CT image and the dotted black arrows indicate the view direction in the CT image.

for the individual patients ranged from  $-0.587$  to  $0.37$  and had a median of  $-0.152$ . The second best spatial correlations were obtained between the SUV distributions and wall stress distributions: Positive correlations were obtained in 36 patients, while negative correlations were stated for 14 patients. The spatial correlations of the SUV to AAA wall stress varied from  $-0.282$  to  $0.389$  with a  $mean \pm sd$  of  $0.088 \pm 0.186$  and a median of  $0.091$ . Spatial correlations of SUV to wall strain distributions were slightly worse than correlations to wall stress distributions. Spatial correlations of local FDG-metabolism to local AAA diameter or local ILT thickness were subject to large variations. This means that regions with increased SUV were as likely to be found at large diameters and behind thick ILT burden as well as at less dilated regions with low or no ILT burden. A detailed overview of the spatial correlations for all patients and quantities, as well as some descriptive statistics are documented in Table B.2 in Appendix B.

### Individual Case Assessment – Peculiarities

As explained before, the two inflammatory AAAs had been excluded from the statistical analyses. However, it is worth mentioning that these AAAs featured the highest  $SUV_{max}$  and  $SUV_{avg}$  values measured in this study ( $SUV_{max}=3.027$  and  $2.517$ ,  $SUV_{avg}=1.126$  and  $1.027$ ). The 3D visualization of the SUV for one of these inflammatory AAAs is given in Figure 4.11. The SUV distributions did not match any of the distributions of mechanical or geometrical quantities. The reader is referred to [171] for a more detailed investigation on this topic.

For the majority of the other patients, a moderate visual co-localization of regions with increased SUV to areas with high wall stress was found, while areas of low wall stress often showed low SUV. Two examples of AAAs where the shape of the SUV distributions was in fair agreement to the shape of the wall stress distribution are shown in Figure 4.12. The scatter plots for the spatial element-wise correlation of local SUV to local wall stress are shown in the same figure. Despite the good visual match of SUV and wall stress patterns and the clear tendency to

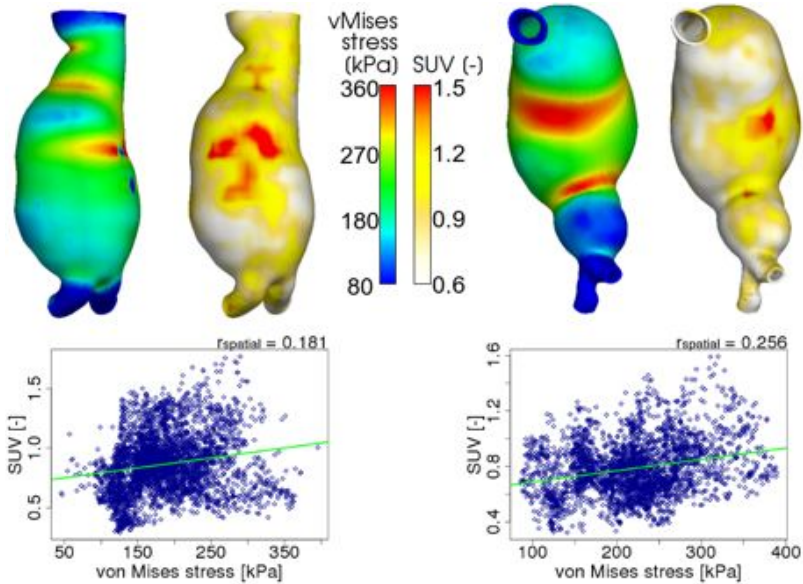


Figure 4.12: Wall stress and SUV distributions in the AAA wall for two patients (Left: Patient 27; Right: Patient 20). Regions with increased SUV were close to regions with increased wall stress, while areas with low wall stress showed low SUV. Scatter plots for element-wise correlation of SUV to von Mises wall stress confirm weak but highly significant spatial correlations of the SUV to the mechanical loading ( $P < 1E - 05$  for both cases).

increased SUV with increasing wall stress, the spatial correlation coefficients ( $r_{spatial} = 0.181$  and  $r_{spatial} = 0.256$ , Figure 4.12) only reached moderate values.

However, there were also AAAs which revealed a clear mismatch between regional SUV patterns and wall stress patterns. Three AAAs featured drastically increased SUV at the tips of unusual eccentric bulges in the AAA wall, while the mechanical stresses and strains were very low at such sites. The example AAA shown in Figure 4.13 (Patient 3;  $SUV_{max}=2.061$ ) featured the highest  $SUV_{max}$  within the main cohort of 50 patients selected for statistical evaluation.

Furthermore, five patients had AAAs that featured focal FDG-uptake behind thick layers of ILT, as for example shown in Figure 4.14. In turn, the thick ILT burden caused the wall stresses to remain at a low level. Moreover, we found AAAs with increased SUV at regions that were in contact to other body parts, mainly to the spine (Figure 4.15 (a)). The FDG-uptake at all such sites was not necessarily in mismatch to the mechanical loading as obtained from computational analyses. It was also noticeable that most AAAs featured slightly increased FDG-uptake in their shoulder regions matching the increased wall stress at such sites. Examples are given in Figure 4.12 (Patient 27 at the left) or in Figure 4.15 (b). The SUV in both contact and shoulder

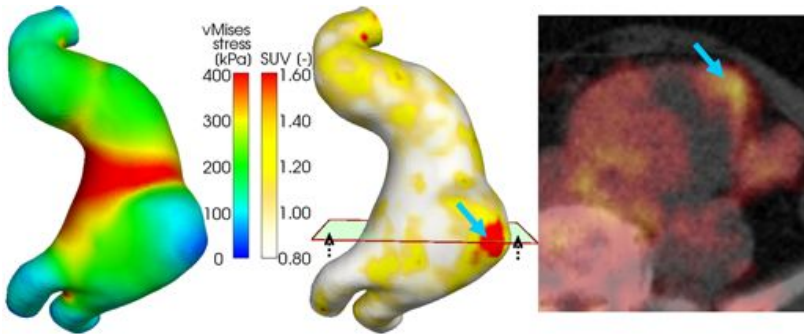


Figure 4.13: Wall stress and SUV distributions for an AAA (Patient 3:  $SUV_{max}=2.061$ ) with stress-independent, focal FDG-uptake at eccentric, ILT-filled bulges (blue arrows). The fused PET/CT image (transversal view) corresponds to the position indicated by the plane in the 3D representation. Dotted black arrows indicate the view direction in the CT image.

regions was bounded to moderate values, such that these regions were usually not the locations of maximum metabolic activity in the AAA wall.

### 4.3.3 Discussion

Arterial dilation and remodeling as a response to altered flow and pressure conditions have been well investigated [36, 99] and can be induced experimentally in animal models [140]. However, mechanisms of shear stress induced arterial dilation and remodeling applicable to small arteries cannot be applied to the pathogenesis of AAA, where internal thrombus lining and endothelial loss prevent a shear stress induced liberation of nitric oxide pathways [35, 223] and where blood pressure induced biomechanical loading is of major importance. In AAA pathogenesis, inflammatory and proteolytic processes are the key factors which lead to wall degradation and aneurysm formation. In this study, it was therefore analyzed if there is an interplay between biomechanical loads exerted by blood pressure and inflammatory/proteolytic processes. Loading in the wall of patient-specific AAA geometries was calculated by means of most up-to-date FE simulations, while the FDG-uptake measured by PET/CT was used for the quantification of *in vivo* metabolic activity in the AAA wall. Thereby the use of the same geometry (FE mesh) for the visualization and evaluation of the mechanical quantities and the FDG-uptake (SUV), respectively, enabled a consistent investigation of the mechanobiological interplay in the AAA wall of 50 patients.

Despite the enhanced methods concerning material models in the present study (more sophisticated ILT model, inclusion of calcification) the promising numbers from our earlier study (Maier *et al.* [130]) could not be completely confirmed. Too many AAAs featured FDG-uptake that was in mismatch to the distribution of mechanical quantities (Figures 4.11, 4.13 and 4.14). Earlier, Xu *et al.* [237] had stated a perfect match between locations of increased wall stress and FDG-uptake for the small study cohort of 5 patients. With regard to the current findings, it might be assumed that these patients were selected and special cases. Nonetheless, the present results

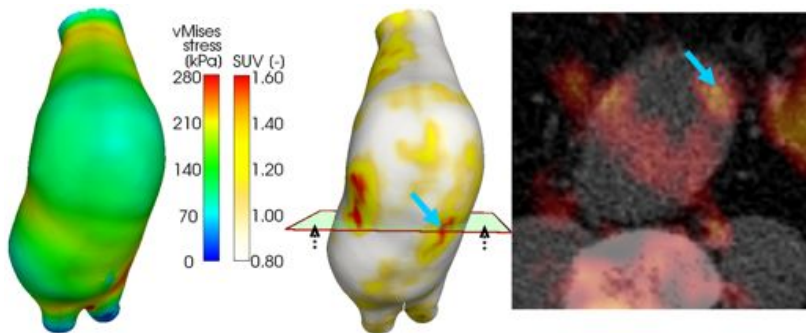


Figure 4.14: Wall stress and SUV distributions for an AAA (Patient 13:  $SUV_{max}=1.653$ ) exhibiting high focal SUV behind thick layers of ILT (blue arrows), while same locations feature comparably low wall stress. The fused PET/CT image (transversal view) corresponds to the position indicated by the plane in the 3D representation. The dotted black arrows indicate the view direction in the CT image.

point out that unphysiologically increased wall stress might be one of the possible triggers for increased FDG-uptake. A good correlation was obtained between  $SUV_{max}$  and maximum wall stress ( $r = 0.576$ ,  $P = 0.00002$ ; Table 4.1), supporting the findings of earlier studies, which reported that unphysiologically increased wall stress might induce increased FDG-uptake in AAA wall [130, 170, 237]. On the other hand, only moderate correlations were obtained for the spatial comparisons between wall stress distribution and SUV distribution. In this regard, however, it seems particularly noteworthy that especially the increased FDG-uptake in the shoulder regions of AAAs was in good agreement with regions of high wall stress for several patients (see e.g. Figure 4.15). This matches the observations by Li *et al.* [124] stating the shoulder region as the main AAA expansion zone with consequent high biological activity. Interestingly, there was also a highly significant correlation of  $SUV_{max}$  to maximum wall displacement during simulation, while the majority of AAAs exhibited a negative spatial correlation of local displacement to local SUV. The reservation must be made, however, that the displacements in the sac region were influenced by the zero displacement DBCs at the distal and proximal model ends of the AAA models [148]. Furthermore, there was a significant increase of  $SUV_{max}$  with increasing maximum AAA diameter and increasing AAA surface (Table 4.1). Of course, this might be explained by the fact that increased FDG-uptake is just to be more likely to occur with increasing AAA size. While on the other side, the relationship between AAA size and mechanical loading was not explicitly investigated. Generally, of course, size is one of the factors governing the mechanical loading and vice versa.

However, SUV distributions and patterns of mechanical loading did not match in all regions and all patients, indicating that there were also other triggers for increased metabolic activity. In the present study, these mismatches were investigated in detail. For example, the role of ILT on FDG-uptake was inconsistent. For the majority of AAAs, low FDG-uptake was found in the wall behind thick ILT burden. In some cases, however, focally high FDG-uptake was

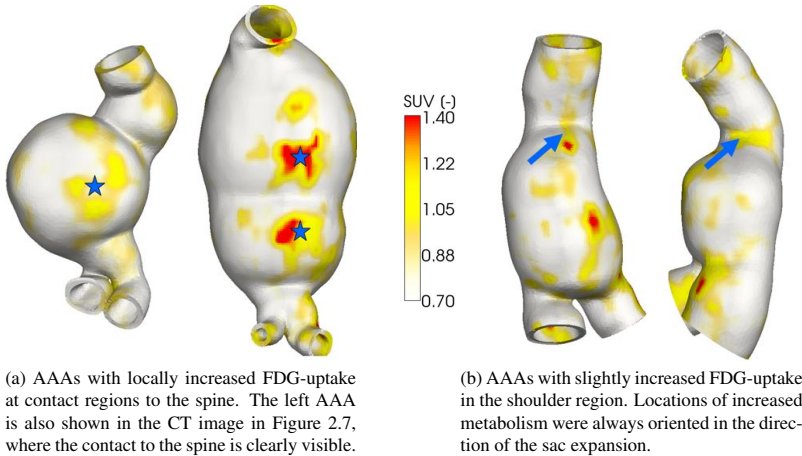


Figure 4.15: Examples of AAAs exhibiting increased SUV at wall portions that were in contact to the spine (a)(indicated by stars) and at the shoulder regions of the AAA (b)(indicated by arrows).

found behind thick ILT burden (Figure 4.14), sometimes even at sites with eccentric bulges in the AAA wall showing very low wall stress (Figure 4.13). This may be explained by hypoxia in the AAA wall beneath ILT as previously hypothesized [51, 226]. Hypoxia may lead to mural neovascularization and inflammatory-proteolytic reactions with presumably increased FDG-uptake. Concerning the sites of eccentric bulges in AAA wall, it could also be hypothesized that the expansion was initiated by a tear in the atherosclerotic layer of the AAA wall. The remaining medial-adventitial wall might subsequently have undergone eccentric expansion with secondary ILT deposition. The highest SUVmax in this study was measured for an AAA with such an eccentric bulge (Figure 4.13). Finally, slightly increased FDG-uptake was observed at sites where the AAA wall was in contact with the spine (Figure 4.15) for a large set of AAAs. Concerning this last point, coarse PET resolution complicated the attribution of the FDG-uptake to the actual source of radiation. Conceivably, the increased FDG-uptake could stem from the affected AAA wall. On the other side, the good blood-supply of the neighboring spine associated with increased FDG-uptake might have caused spill-over effects, which were misinterpreted as metabolic activity in the AAA wall. But also the good correlation between SUVmax and the maximum displacements obtained from FE analyses (Table 4.1) might indicate that movement and rubbing of the AAA wall along the spine, could be the cause for the FDG-uptake at such sites.

Alternatively, spatial and quantitative miscorrelations of FDG-uptake and biomechanical quantities may be explained by technical limitations during PET imaging or computational FE analyses. Despite registration of PET data, accuracy of FDG mapping to the FE mesh may be hampered by small respiratory or body movements during PET imaging. Moreover, FDG-uptake in AAA wall was potentially over- and underestimated due to luminal or tissue spill-over effects

caused by the 5 mm resolution of state-of-the-art PET scanners. More rapid PET/CT scanners with higher resolution and appropriate software tools for partial volume correction will help to improve the accuracy of FDG-uptake and to reduce movement artifacts. Furthermore, although most state-of-the-art FE models and methods were utilized in this study, there may be incongruities between the real mechanical AAA conditions and the quantities predicted by computational FE analyses. Especially unknown wall thickness distribution, varying material properties of AAA wall, modeling of load-reduction effects caused by ILT or neglect of surrounding tissue [145] are sources of model errors and represent topics for future mechanical AAA research. Consequently, these aspects can lead to quantitative and regional misjudgments of *in vivo* mechanical loading and subsequently to miscorrelations with detected FDG-uptake. Taking into account all the aforementioned effects, the correlation of  $r = 0.576$  obtained between SUVmax and maximum wall stress has to be highlighted once more, indicating a strong interaction between mechanical loading to biological tissue reaction in the AAA wall. In turn, increased FDG-uptake, measured by FDG-PET/CT is an indicator for either unphysiologically high wall stress or otherwise inflammatory, hypoxic or frictional and contact related processes that necessitate a closer clinical investigation.

The biological and biochemical mechanisms leading to increased AAA FDG-metabolism due to high biomechanical stress and strain still have to be elucidated in detail. It can be hypothesized that cyclic stresses and strains exerted by blood pressure acting in AAA wall may cause pro-inflammatory cytokine liberation by SMCs in aortic wall media [13, 73], followed by macrophage infiltration with increased FDG metabolism. Alternatively, high cyclic loading may lead to fatigue disruption of elastic or collagenous fibers. Fiber fragments may consecutively work as adequate agents and stimuli for macrophage infiltration and subsequent inflammatory and proteolytic cascades as previously suggested [27]. As an aside, the association of elevated FDG-uptake with inflammation is also valid for other cardiovascular diseases, such as atherosclerosis [70, 177] and aortic dissection [109, 173]. Lastly, regenerative processes, such as compensatory collagen fiber production as the response of SMCs to increased biomechanical loads [22, 115], might also be relevant for increased glucose metabolism detected by FDG-PET/CT. This argument has recently been backed by the findings by Kotze *et al.* [113] who stated a negative correlation between FDG-uptake and future AAA growth.

## 4.4 Conclusion - Mechanotransduction in AAA

PET/CT imaging is a non-invasive imaging method that can visualize the glucose metabolism in the human body and e.g. the AAA wall. So far, increased FDG-uptake in the AAA wall as assessed by FDG-PET/CT has been regarded as unspecific, while it was often associated with acute symptoms and rupture risk [168, 178]. Together with the earlier studies by Reeps *et al.* [170], Xu *et al.* [237] and Maier *et al.* [130], the present study could show that mechanical loading in the AAA wall is one of the triggers of FDG-metabolism - even though some of the promising results of earlier studies [130, 170, 237] could not be confirmed. Nevertheless, the results of the present study are an evidence of mechanotransduction and other mechanobiological processes during AAA development and expansion.

Since detailed molecular mechanotransduction mechanisms in AAA wall still have to be elucidated, future work should include histopathological analyses of paired tissue samples from

low and high FDG-uptake sites to identify the histopathological changes that are associated with FDG-uptake. Mechanical tests of wall samples from sites of low and high FDG-uptake will be dealt within the next chapter. Moreover, the examination of the development of the FDG-uptake in AAA wall over time and also comparisons of FDG-uptake in AAAs to FDG-uptake in the normal aorta will be needed to finally evaluate the meaning of PET and FDG-metabolism for the non-invasive evaluation of AAAs.



# 5 Mechanical Testing of AAA Wall

It is generally agreed that rupture of an AAA occurs when the stress in the AAA wall exceeds the local wall strength [62, 103, 133, 137, 164, 222]. In consequence, the clinically well established diameter criterion, based on the law of Laplace and on the assumptions of uniform wall thickness and strength, sometimes fails to predict AAA rupture. As shown in Section 2.5.3 and the literature review therein, this might be attributable to the significant variation of mechanical AAA wall properties between patients or even locally within an AAA, which is not captured by the diameter criterion. Further, also in FE based rupture risk prediction, detailed knowledge about wall thickness distribution and spatial variations of elastic properties would contribute to more reliable and realistic wall stress calculations. Methods for the preoperative assessment of non-uniform mechanical AAA wall properties, whether wall thickness, elastic properties or failure properties, would therefore be an essential improvement to both risk assessment using the diameter criterion and FE based rupture risk assessment.

Although the ranges for AAA wall thickness, elastic parameters or failure properties have already been well described in the current literature (see Section 2.5.3) and also large variations of these mechanical properties have been revealed, the proper assessment of the patient-specific variations is still a lacking. A first approach to assess and model such variations was proposed by Vande Geest *et al.* [222]. They developed a statistical model for the non-invasive estimation of AAA wall strength, however, as already mentioned in Chapter 2, the use of a wall strength model is limited without detailed knowledge on the patient-specific wall thickness distribution. Nevertheless, the methodology suggested in the work by Vande Geest *et al.* [222] was novel and practicable and will therefore be adapted for the development of own statistical models as described later on in this chapter. An approach for the non-invasive wall thickness reconstruction was presented in [139, 189]. However, the implementation of the methods proposed therein remained elusive. In consequence, there are currently no established methods which could provide reliable estimations of patient-specific distributions of mechanical properties based on clinical and preoperatively available data.

The aim of the study presented in this chapter was therefore to measure thickness, elastic properties and failure properties of AAA wall samples and to create models for the non-invasive estimation of these properties for future preoperative use. In short, AAA wall samples were harvested during open AAA repair and experimentally investigated in uniaxial tensile tests. In addition, a set of non-invasively measurable explanatory variables that could potentially have a correlation to mechanical testing results was assessed for each specimen. This set of non-invasively measurable quantities also included the information of local metabolic activity assessed by PET/CT imaging, as already presented in Chapter 4. In this regard, this current study might also help to answer the question for the role of PET/CT imaging in the non-invasive evaluation of the AAA.

A detailed description of the mechanical testing of AAA wall specimens and the assessment of non-invasive explanatory variables can be found in Section 5.1. General testing results were

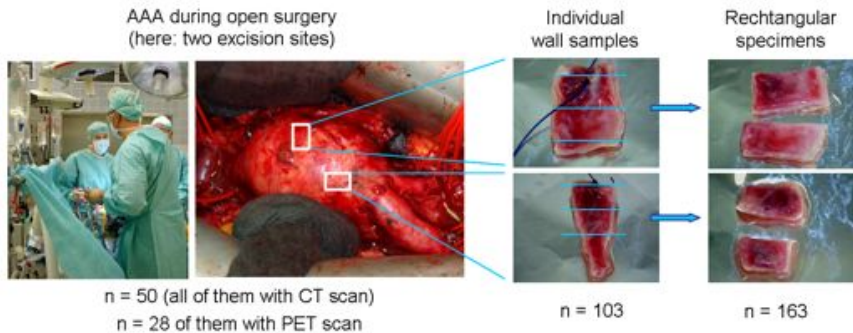


Figure 5.1: Samples were excised during open surgery (left). Proximal ends of samples were marked with a thread (middle) and exact excision sites were recorded. Samples were cut into smaller rectangular specimens suitable for uniaxial tensile testing (right, also indicated by blue lines in middle pictures). Number of patients participating in this study, number of samples and specimens are indicated below the respective pictures.

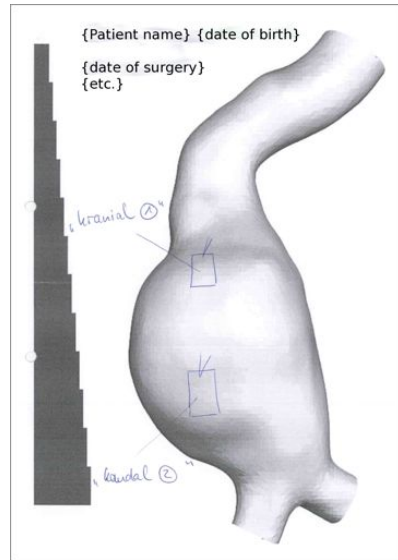
then summarized in Section 5.2. In subsequence, testing results of the individual specimens were correlated to the potential explanatory variables and significant explanatory variables were identified. The results of these simple regression analyses are presented in Section 5.3. In what follows, a detailed comparison between testing results of AAA specimens and specimens harvested from normal abdominal aortic wall was conducted in Section 5.4. Finally, multiple regression analyses were carried out for the different mechanical AAA wall properties in Section 5.5. In this way, most accurate statistical models for the prediction of the patient-specific variation of mechanical AAA wall properties were obtained, while the models were only based on non-invasively available data and mutual dependence of different explanatory variables was considered. The new models allow future preoperative prediction of patient-specific variations in mechanical AAA wall properties and can be used to improve both purely CT-morphologically based rupture risk prediction (e.g. maximum diameter criterion) and sophisticated patient-specific FE analysis.

## 5.1 Methods

### 5.1.1 Study Population and Tissue Sampling

The study included 50 patients over a 30-month period, who presented with infrarenal AAA and different AAA morphologies. All patients underwent CT imaging as part of elective or emergency evaluation. 28 of the patients with elective evaluation underwent additional 18F-FDG-PET/CT. Further patient characteristics are summarized in Table 5.1. CT images were immediately forwarded to create a 3D reconstruction of the AAA geometry following the elaborated segmentation protocol presented in Chapter 2. A hard copy of the resulting 3D reconstruction was handed to the surgeon before surgery. All patients underwent open AAA repair

Figure 5.2: Hard copy of a 3D reconstruction of a patient-specific AAA geometry with cm-scale to its left. This sheet was filled by the surgeon immediately after sample excision indicating the exact excision sites for the two samples harvested from this AAA (denoted “kranial 1” and “kaudal 2”). The recordings were later used for assessment of non-invasively available explanatory variables at the excision sites.



based on the recommendations of the vascular board for different indications. Blood sampling was performed prior to surgical intervention by vein puncture. One to four AAA wall samples from different sites of the AAA were harvested from each patient depending on the surgical situation (Figure 5.1). Exact sample excision sites and orientations were recorded in the hard copy (Figure 5.2). Samples were stored in lactated Ringer’s solution (130 mmol sodium chloride, 5 mmol potassium chloride, 2 mmol calcium chloride, 3 mmol sodium lactate) at 4 °C and underwent mechanical testing within 24 hours after equalizing to room temperature. In total, samples from 103 different excision sites were obtained. In addition, small portions of 2–3 mm were prepared from each tissue sample, transferred into 4% formalin and embedded in paraffin to assess tissue morphology and AAA wall integrity in histological investigations. However, since patient-specific histology is only invasively available, histological results are not considered in this study.

Additionally, the study included 10 organ donors (3 woman, 2 men, 5 unknown) with non-dilated, healthy abdominal aorta (AA). During kidney harvest from organ donors (kidneys are usually harvested together with renal arteries and a small portion of AA), exactly one sample of normal AA wall was excised from each patient. Exact excision sites of normal AA wall samples were not recorded, but it was clear that all samples were harvested close to the bifurcations of the renal arteries. The AA samples were similarly processed as previously explained for AAA wall samples. Patient characteristics of the organ donors are summarized in Table 5.4 on page 125. The study was approved by the ethics committee of the university hospital Rechts der Isar, Technische Universität München, Germany.

Table 5.1: Patient characteristics for AAA patients with sample donor

	From	To	Mean±sd	Median
Age	48	90	68.5±8.0	69
Max. AAA diameter	33	89	59.8±12.3	56
Max. ILT thickness*	0	45.6	22.5±9.0	23.1
Subrenal aortic diameter	14	26	21.2±2.8	21

\* 47 AAAs had ILT

Medical history	Yes	No	Unknown
Ruptured AAA	5	45	-
Chronic kidney disease (CKD)	14	35	1
Coronary heart disease (CHD)	18	29	3
Diabetes mellitus (DM)	10	38	2
Hypercholesterolemia	4	43	3
Hyperlipidemia	23	24	3
Hypertension	31	17	2
Marphan	0	50	-
PVD	6	41	3
Smoking status	28	22	-

Drug use	Yes	No	Unknown
ASA, Clopid	32	15	3
Beta Blocker**	25	22	3
ACE inhibitors**	16	31	3
Statins	23	24	3
Diuretics	12	35	3

\*\* 12 of the patients took both Beta Blocker and ACE inhibitors

## 5.1.2 Mechanical Testing

Mechanical testing was performed to investigate AAA wall thickness, elastic properties, and failure load. Since different AAA wall layers cannot be resolved with a common medical imaging modality and moreover the assumption of a three-layered structure is not valid any more for AAA wall [181], mechanical tests on the complete wall compound were performed, rather than separating the layers for testing, as exemplarily presented in [94]. Samples were cleaned from loosely adherent thrombus deposition, if applicable, and then cut into individual rectangular specimens suitable for uniaxial tensile testing (typically 20 mm x 8 mm, see also Figure 5.1). Specimens were visually checked for calcification and attention was paid to detect hard, calcified tissue constituents during cutting. Consequently, the specimens were categorized into 'no calcification', 'slight calcification' and 'severe calcification' for later statistical analysis. Specimen orientation was deduced from the sample marking and documented. If possible, circumferential orientation was preferred to longitudinal orientation, since highest principal stresses in the AAA wall are usually oriented in circumferential direction. Specimen width was mea-

sured using digital calipers. Specimen thickness was averaged from five measuring points on the specimen surface using a Mitutoyo “Quick-Mini Series 700” digital thickness gauge (Mitutoyo, Kawasaki, Japan. Part-No. 700-118. Constant measure force = 0.5 N, measuring anvil diameter = 5 mm, accuracy=20  $\mu$ m). The intra-operator and the inter-operator independence were checked, though preparation and testing of all specimens were carried out by the same operator. In total, 163 specimens were obtained from the wall samples harvested during open surgery. Elastic properties and failure load were investigated with uniaxial tensile tests using an ElectroForce 3100 tensile test machine (Bose Corporation, Eden Prairie, USA). The machine featured a maximum tensile force of 22 N and a maximum clamp displacement of 5 mm. The resolutions were 1 mN and 1  $\mu$ m, respectively. Specimens were clamped at an initial clamp distance of 7.3 mm. For the measurement of elastic properties at a physiological stress-stretch range, the specimens were exposed to cyclic sinusoidal loading at frequency of  $f = 0.5$  Hz and up to a stress of approximately  $P = 0.20$  MPa (depending on specimen thickness). 19 cycles were used for preconditioning [56, 58, 98, 137, 193], data from the 20th cycle was used for evaluation. Applied force and clamp displacement were continuously recorded at a sampling rate of 200 Hz. Subsequent to cyclic testing, specimens underwent destructive testing in order to measure their failure load. Therefore, the clamps were moved to their maximum displacement at a speed of 0.2 mm/s. Applied force and clamp displacement were recorded at a sampling rate of 40 Hz. Failure load was assessed as the maximum tensile force measured in this experiment. Specimens that slipped from the clamps during testing were excluded from the study. Specimens that ruptured close to the clamps were not excluded from the study since their failure loads were higher than average.

### 5.1.3 Assessment of Testing Results

Experimentally assessed clamp displacements and measured forces were converted into suitable stretch and stress measures: Stretch was calculated as

$$\lambda = \frac{\Delta x + l_0}{l_0} = \frac{x + l_{x=0}}{x_0 + l_{x=0}}, \quad (5.1)$$

with  $\Delta x$  as the clamp displacement and  $l_0$  the initial clamp distance. Stress was calculated in terms of the First Piola-Kirchhoff (1.PK) stress in testing direction:

$$P_{11} = \frac{F}{A_0}, \quad (5.2)$$

with  $F$  as measured force and  $A_0$  as initial cross-sectional area of the specimen. Examples of resulting stretch-stress curves for a cyclic and a destructive test are shown in Figure 5.3. Biological tissues feature a nonlinear stress-stretch behavior with an initially soft response followed by stiffening of the material. To account for this material-nonlinearity, the obtained stretch-stress curves from cyclic testing were used to fit a hyperelastic, incompressible, isotropic material model described by the SEF

$$W = \frac{\alpha}{6} (I_1 - 3) + \beta (I_1 - 3)^2, \quad (5.3)$$

while the only difference to the R&V model (Eq. (2.60), [164]) is the use of  $\frac{\alpha}{6}$  instead of  $\alpha$ . In this way,  $\alpha$  can be interpreted as the initial stiffness of the specimen (at the load-free state).  $\beta$

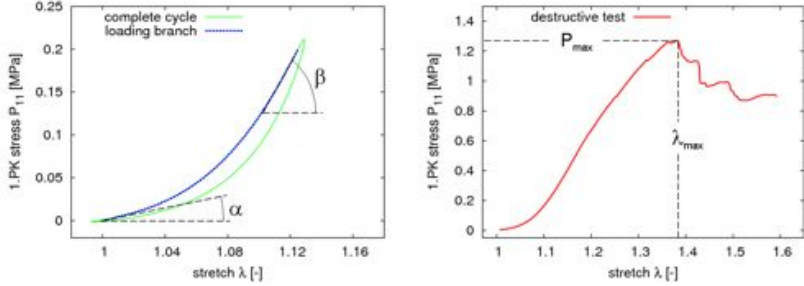


Figure 5.3: Experimental stress-stretch curves of an AAA wall specimen obtained from tensile testing. Left: The solid curve represents the complete 20th cycle, including hysteresis between the loading and unloading branches. The dashed curve represents the loading branch used for assessment of elastic material parameters. It features characteristic nonlinear stress-stretch behavior with initial soft response (alpha stiffness), followed by stiffening in the high stretch region (beta stiffness). Right: Curve obtained from destructive tensile testing. The wall strength is defined as the maximum stress. Visually noticeable damage to the specimen was first observed at this point during the experiments.

represents the stiffness measured in the high stretch region after the stiffening of the material (e.g. under physiological prestretch due to diastolic blood pressure), see also Figure 5.3.  $\alpha$  and  $\beta$  are the sought material parameters for the individual specimen, denoted alpha stiffness and beta stiffness for the remaining of this chapter. Following differentiation and under the assumption of an uniaxial stress state during testing, Eq. (5.3) can be transformed to a relation between  $P_{11}$  and  $\lambda$ :

$$P_{11} = \left( \frac{\alpha}{3} + 4\beta(\lambda^2 + 2\lambda^{-1} - 3) \right) (\lambda - \lambda^{-2}) \quad (5.4)$$

Using this formula, alpha and beta stiffness were then determined from the experimental data of each specimen utilizing a Levenberg-Marquardt curve fitting algorithm [166].

Two failure measures, the strength and the failure tension, were derived from destructive testing. Specimen strength was assessed as maximum stress during the destructive test.  $P_{max}$  denotes the strength in terms of 1.PK stresses:

$$P_{max} = \frac{F_{max}}{A_0}, \quad (5.5)$$

with  $F_{max}$  as the maximum force and  $A_0$  the initial cross-sectional area of the specimen. As already mentioned previously, the use of a strength formula for AAA rupture risk prediction is only reasonable if the actual wall thickness of a specific AAA is known. If wall thickness is unknown, e.g. the AAA geometry is obtained from CT images, a strength measure that is independent of the actual wall thickness has to be used. Such a measure, the failure tension, has been proposed by Raghavan *et al.* [163]. Failure tension in terms of 1.PK stresses is denoted by  $T_{max}$ :

$$T_{max} = \frac{F_{max}}{\text{specimen width}} \quad (5.6)$$

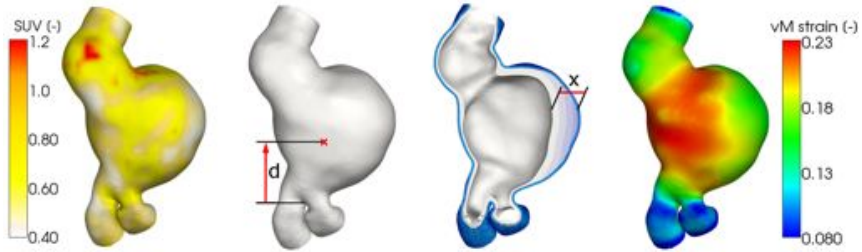


Figure 5.4: Reconstructed AAA model showing spatial SUV distribution (Standardized Uptake Value, obtained from FDG-PET/CT imaging) (left), distance of sample excision site to bifurcation “d” (middle-left), local thrombus thickness “x” at sample excision site (middle-right) and Euler-Almansi-Von Mises strain distribution in the AAA wall (right). All PET data, geometrical information and FE results at sample excision sites were automatically assessed using Paraview.

The failure tension states the maximum force that can be born by a wall portion of generic width, independent of its thickness. The stretch associated with  $P_{max}$  and  $T_{max}$  was considered as failure stretch  $\lambda_{max}$ , see also Figure 5.3. Accordingly, strength ( $\sigma_{max}$ ) and failure tension ( $T_{max,Cauchy}$ ) in terms of Cauchy stresses, respectively, were obtained by

$$\sigma_{max} = P_{max} \cdot \lambda_{max}, \quad T_{max,Cauchy} = T_{max} \cdot \sqrt{\lambda_{max}}. \quad (5.7)$$

#### 5.1.4 Non-invasively Assessable Explanatory Variables

In order to enable future preoperative estimations of patient-specific AAA wall properties, we chose a set of 49 relatively non-invasively assessable explanatory variables, which might potentially be related to the mechanical AAA wall properties. Explanatory variables can be either a characteristic without spatial distribution (e.g. age, sex, ...) or a local quantity at the sample excision site. They are grouped in *patient characteristics*, *patient’s medical history*, *specimen-specific data*, *AAA geometry*, *medication*, *geometrical data at excision site*, *results from FE analysis at excision site*, *PET imaging* and *biochemical blood analysis*. Below, all the explanatory variables are listed together with annotations in brackets, giving either the unit or the statistical binary coding (e.g. “no= 0; yes= 1”) for the individual parameter:

##### Patient characteristics

sex	female= 0; male= 1
age	[years]
AAA-status	elective= 0; ruptured= 1

##### Patient’s medical history

chronic kidney disease (CKD)	no= 0; yes= 1
coronary heart disease (CHD)	no= 0; yes= 1
diabetes mellitus (DM)	no= 0; yes= 1

hypercholesterolemia	no= 0; yes= 1
hyperlipidemia	no= 0; yes= 1
hypertension	no= 0; yes= 1
peripheral vascular disease (PVD)	no= 0; yes= 1
smoking status	no= 0; yes= 1

Grouping for CKD was based on an estimated glomerular filtration rate according to the Kidney Disease Improving Global Outcomes (KDIGO) [28]: Patients with eGFR < 60ml/min (stage 3, 4 and 5) were considered as patients with CKD [207]. Hypertension was defined as systolic blood pressure > 140 mmHg and diastolic pressure > 90 mmHg [74]. Patients suffering from DM were defined by a fasting plasma glucose > 126 mg/dl, or use of oral hypoglycemic agents or insulin [2]. Patients were considered as smokers if they were active smokers or stopped smoking less than ten years ago [52]. Information on CHD, hypercholesterolemia (cholesterol in blood > 240 mg/dl), hyperlipidemia and peripheral vascular disease (PVD) was taken from the patient charts.

**Specimen-specific data**

testing direction	long.= -0.5; unkn.= 0; circ.= 0.5
calcification	none= -0.5; slight= 0; severe= 0.5
specimen thickness	[mm]

**AAA geometry**

maximum AAA diameter	[mm]
maximum AAA thrombus thickness	[mm]
subrenal aortic diameter (if the aneurysm reached the renal arteries, the aortic diameter between celiac and superior mesenteric artery minus 2.5 mm was used instead)	[mm]

**Medication**

acetylsalicylic acid (ASA), clopid	no= 0; yes= 1
beta blocker	no= 0; yes= 1
angiotensin-converting-enzyme (ACE) inhibitors	no= 0; yes= 1
statins	no= 0; yes= 1
diuretics	no= 0; yes= 1

Medication details were obtained from the patient charts. Information on the duration of the medication was not available on the charts.

**Geometrical data at excision site**

distance of excision site to bifurcation	[mm] (see Figure 5.4)
relative z-position (distance to bifurcation divided by the length of the AAA)	[-]
local thrombus thickness at excision site	[mm] (see Figure 5.4)
relative thrombus thickness (local thrombus thickness divided by max AAA thrombus thickness)	[-]
local radius at excision site	[mm]
local normalized diameter “NORD” (two times local radius divided by subrenal aortic diameter)	[-]

All values at sample excision sites were fully automatically assessed from 3D reconstructed AAA geometries using Paraview (Kitware Inc., Clifton Park, USA). To account for segmentation inaccuracies or imprecise location of the sample excision site, the quantities were averaged within the AAA wall over a radius of 6 mm around the marked excision site.

### Results from FE analysis at excision site

1st principal stress (Cauchy)	[kPa]
2nd principal stress	[kPa]
von Mises stress	[kPa]
difference between 1st and 2nd principal stress	[kPa]
sum of 1st and 2nd principal stress	[kPa]
1st principal strain (Euler-Almansi)	[-]
2nd principal strain	[-]
von Mises strain	[-] (see Figure 5.4)

FE simulations have been performed as described in Chapter 2 under the assumptions of spatially constant wall thickness ( $t = 1.2$  mm) and constant material parameters for the AAA wall (Eq. (2.60)). Calcifications were not considered in these simulations. All calculations were performed using the non-commercial FE solver BACI [229].

### PET imaging

SUV at sample excision site	[-] (see Figure 5.4)
-----------------------------	----------------------

The SUV at the sample excision site was automatically assessed using Paraview, after mapping of the PET information to the FE model as presented in Chapter 4.

### Biochemical blood analysis

		(Phys. reference range)
calcium	[mmol/l]	(2.2-2.65 [105])
creatinine (values from patients on dialysis (stage 5, eGFR < 15 ml/min) were excluded)	[mg/dl]	(0.5-1.1 [59], for population $\geq 50$ years)
creatinkinase	[U/l]	(<170 [105])
high-sensitivity C-reactive protein (hsCRP)	[mg/l]	(<5 [105])
erythrocytes	[Mio/ $\mu$ l]	(4.1-5.9 [205])
fibrinogen	[mg/dl]	(180-350 [105])
hematocrit	[%]	(39-49 [105])
hemoglobin	[g/dl]	(12.3-17.5 [205])
leukocytes	[1000/ $\mu$ l]	(4-10 [105])
potassium	[mmol/l]	(3.6-5.2 [105])
sodium	[mmol/l]	(135-145 [105])
thrombocytes	[1000/ $\mu$ l]	(140-360 [205])
blood urea	[mg/dl]	(8.4-29.4 [59], for population $\geq 50$ years)

Experimentally measured mechanical wall properties (thickness, alpha and beta stiffness, failure tension and wall strength) were first correlated to the above mentioned explanatory variables using simple linear regression. The correlations were evaluated using the Pearson product-moment correlation coefficient  $r$ . Correlations with P-values < 0.05 were considered as statis-

tically significant. The equations for the obtained simple regression models are printed on top of each diagram. Results from multiple regression analysis will be presented in Section 5.5.

## 5.2 Tensile Test Results

In total, 163 AAA wall specimens from 103 different excision sites and 50 patients were investigated. Wall thickness was measured for all specimens. Some specimens were excluded from the tensile testing because of inadequate sample dimensions ( $n = 3$ ), presence of branching arteries ( $n = 2$ ) or damage to the specimen during preparation ( $n = 4$ ). Tensile test results of  $n = 3$  specimens were discarded after testing, because of extended calcification covering the complete length of the specimens, yielding up to 1000-fold increased stiffness values. Other missing values were attributable to maloperation of the tensile test machine or its software or deficient clamping of the specimens.

Experimental results are summarized in the box and whisker plots in Figure 5.5. Wall thickness ranged from 0.85 mm to 3.20 mm with a median of 1.57 mm and a mean of  $1.67 \pm 0.49$  mm. Measured alpha stiffness ranged from 0.012 MPa to 1.068 MPa with a median of 0.314 MPa and a mean of  $0.339 \pm 0.229$  MPa. Beta stiffness varied from 0.224 MPa to 22.26 MPa with a median of 3.112 MPa and a mean of  $4.329 \pm 3.971$  MPa. Failure stretch ranged from 1.057 to 2.528 with a median of 1.446 and a mean of  $1.482 \pm 0.191$ . Failure tension in terms of 1.PK stresses varied from 0.541 N/mm to 4.13 N/mm with a median of 1.423 N/mm and a mean of  $1.523 \pm 0.556$  N/mm. For Cauchy stresses, failure tension ranged from 0.652 N/mm to 4.738 N/mm with a median of 1.780 N/mm and had a mean of  $1.838 \pm 0.628$  N/mm. Wall strength in terms of 1.PK stresses ranged from 0.36 MPa to 3.197 MPa, with a median of 0.952 MPa and a mean of  $1.063 \pm 0.49$  MPa. In terms of Cauchy stresses, wall strength varied from 0.491 MPa to 4.349 MPa with a median of 1.443 MPa and a mean of  $1.554 \pm 0.691$  MPa.

Mean and median stress-stretch curves for the AAA wall specimens under longitudinal ( $n = 49$ ) and circumferential ( $n = 74$ ) elongation, respectively, are given in Figure 5.6. The mean stress-stretch behavior was almost similar for both testing directions. Median curves were almost identical up to a stretch of  $\lambda = 1.1$ . The interquartile stress ranges for longitudinally and circumferentially tested AAA wall specimens were comparable. A model curve according to Eq. (5.3) with the median material parameters from Figure 5.5 was added for comparison.

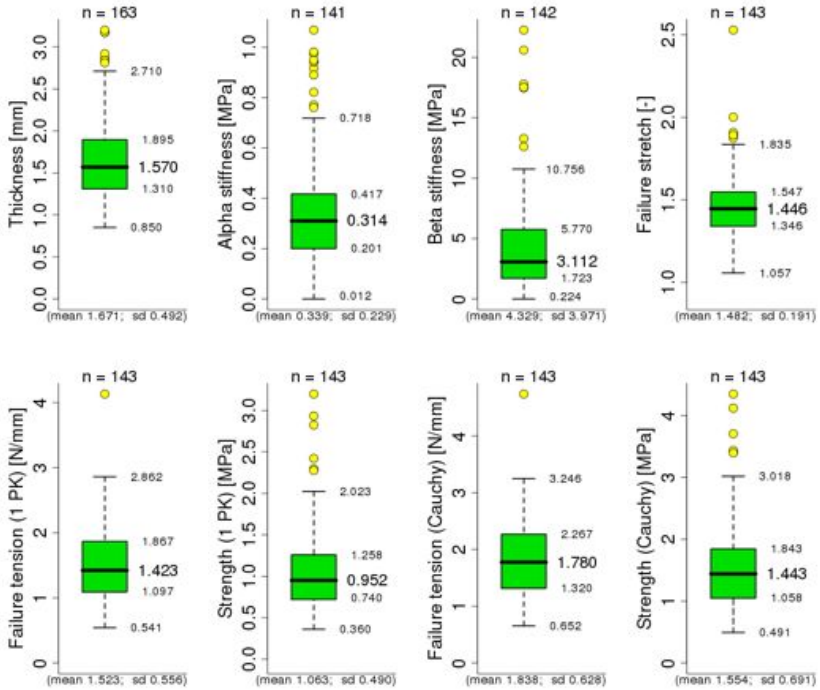


Figure 5.5: Box and whisker plots summarizing experimentally measured wall thickness, alpha stiffness, beta stiffness, failure stretch, failure tension and wall strength in terms of 1.PK stresses and failure tension and wall strength in terms of Cauchy stresses . Median values, 25th and 75th-percentiles and extreme values within the interquartile range are printed next to the respective lines. Mean value and standard deviation (sd) are given in brackets below each diagram. The number of specimens is printed on top of each diagram.

## 5.3 Simple Regression

Altogether, 49 different patient and specimen-specific explanatory variables were correlated to the experimental results using simple linear regression. Additionally, alpha and beta stiffness, failure stretch, failure tension and strength were correlated to the measured wall thickness. The correlations with associated  $r$  and  $P$ -values were documented in Tables 5.2 and 5.3. Strain measures (1st principal strain, 2nd principal strain and von Mises strain at the sample excision site) did not yield any better correlations than the respective stress measures. They were therefore omitted in the two tables. Further, hsCRP, fibrinogen and creatinkinase values were only avail-

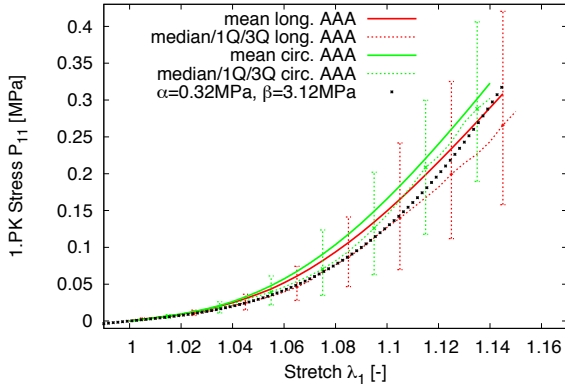


Figure 5.6: AAA wall under uniaxial tension: Stress-stretch curves (loading branch only) for longitudinal (red) and circumferential (green) testing directions. Solid lines are calculated as the mean curves from experimentally obtained stress-stretch curves. The dashed curves indicate the experimentally measured medians (median stress at any given stretch). The whiskers branching off the medians indicate the first (1Q) and third quartiles (3Q) of stresses at the given stretches. The dotted black line indicates the model behavior for a material following the SEF presented in Eq. (5.3) with the median material parameters from Figure 5.5.

able for about half of the patients and correlations for these values were also not listed in the tables. There were no correlations of experimental results to hsCRP, fibrinogen and creatin kinase values for the subgroup of patients for whose this data was available.

### 5.3.1 Regression Results

#### Wall Thickness

Experimentally measured wall thickness was most significantly correlated to the metabolic activity at the sample excision site assessed by the SUV ( $r = 0.601$ ,  $P < 1E - 09$ ). Moreover, wall thickness was dependent on the patient's medical history: Smokers ( $r = 0.199$ ,  $P = 0.011$ ) and patients suffering from DM ( $r = 0.309$ ,  $P = 0.0001$ ) or hypercholesterolemia ( $r = 0.184$ ,  $P = 0.022$ ) had increased AAA wall thickness. It was decreased for patients suffering from CKD ( $r = -0.274$ ,  $P = 0.0004$ ). Patients receiving ACE inhibitors had a significantly increased wall thickness ( $r = 0.165$ ,  $P = 0.040$ ). In addition, wall thickness increased with increasing distance of the excision site to the bifurcation ( $r = 0.186$ ,  $P = 0.017$ ), but decreased with local thrombus thickness ( $r = -0.176$ ,  $P = 0.025$ ). Significant correlations were detected between wall thickness and creatinine ( $r = -0.168$ ,  $P = 0.039$ ), erythrocytes ( $r = 0.186$ ,  $P = 0.021$ ), hemoglobin ( $r = 0.183$ ,  $P = 0.020$ ), sodium ( $r = -0.226$ ,  $P = 0.004$ ) and thrombocytes ( $r = 0.455$ ,  $P < 1E - 08$ ). No significant correlations were observed for patient sex, age, AAA-status, the maximum AAA diameter or acting strains and stresses at the sample excision

sites.  $r$  and  $P$ -values for all analyzed correlations are also summarized in Tables 5.2 and 5.3. Plots for all significant correlations are shown in Figure 5.7.

### Alpha Stiffness

The experimentally measured alpha stiffness had significant correlations to the existence of calcification within the specimen ( $r = 0.308$ ,  $P = 0.0002$ ), the subrenal aortic diameter ( $r = 0.250$ ,  $P = 0.003$ ), the SUV ( $r = -0.275$ ,  $P = 0.014$ ) and urea ( $r = -0.214$ ,  $P = 0.016$ ). There were no correlations to the testing direction of the specimens, to local ILT thickness and radius or any variable of the patient's medical history.  $r$  and  $P$ -values for all analyzed correlations are also summarized in Tables 5.2 and 5.3. Diagrams for the significant correlations are shown in Figure 5.8.

### Beta Stiffness

Significant correlations were found for beta stiffness to sex ( $r = 0.166$ ,  $P = 0.048$ ), CKD ( $r = 0.174$ ,  $P = 0.040$ ), wall thickness ( $r = -0.241$ ,  $P = 0.004$ ), maximum AAA thrombus thickness ( $r = 0.175$ ,  $P = 0.037$ ), patients receiving beta blockers ( $r = -0.177$ ,  $P = 0.041$ ), SUV ( $r = -0.385$ ,  $P = 0.0004$ ) and urea ( $r = -0.207$ ,  $P = 0.020$ ). Further, the local (absolute) thrombus thickness ( $r = 0.254$ ,  $P = 0.002$ ) had a better correlation to beta stiffness than the relative thrombus thickness ( $r = 0.200$ ,  $P = 0.020$ ). Analogously, the subrenal aortic diameter ( $r = 0.251$ ,  $P = 0.003$ ) had a better correlation to beta stiffness than NORD ( $r = -0.177$ ,  $P = 0.035$ ). There was no correlation of beta stiffness to the testing direction.  $r$  and  $P$ -values for all analyzed correlations are also summarized in Tables 5.2 and 5.3. Plots for all significant correlations, except for NORD and the relative thrombus thickness, are shown in Figure 5.9.

### Failure Stretch

The failure stretch was significantly correlated to the patient's age ( $r = 0.167$ ,  $P = 0.046$ ), CHD ( $r = 0.192$ ,  $P = 0.026$ ), the testing direction ( $r = -0.250$ ,  $P = 0.003$ ) (lower failure stretch in circumferential direction) and the maximum AAA diameter ( $r = -0.218$ ,  $P = 0.009$ ). Further, failure stretch was correlated to the stress measures 1st principal stress ( $r = -0.196$ ,  $P = 0.019$ ), 2nd principal stress ( $r = -0.217$ ,  $P = 0.009$ ), von Mises stress ( $r = -0.198$ ,  $P = 0.018$ ) and sum of 1st and 2nd principal stress ( $r = -0.212$ ,  $P = 0.011$ ).  $r$  and  $P$ -values for all analyzed correlations are also summarized in Tables 5.2 and 5.3. Plots for significant correlations are shown in Figure 5.10. Diagrams for the 1st principal stress and the von Mises stress are omitted to avoid redundancy.

### Failure Tension

Failure tension in terms of 1.PK stresses was significantly correlated to 1st principal stress ( $r = 0.190$ ,  $P = 0.023$ ), 2nd principal stress ( $r = 0.181$ ,  $P = 0.031$ ), von Mises stress ( $r = 0.184$ ,  $P = 0.028$ ) and sum of 1st and 2nd principal stress ( $r = -0.194$ ,  $P = 0.020$ ), whereas failure tension in terms of Cauchy stresses was not. In the following cases, the failure tensions in terms of 1.PK and Cauchy stresses shared significant correlations to the same explanatory variables, whereas  $r$  and  $P$ -values given in the subsequent relate to 1.PK stresses: Positive correlation was

detected for failure tension to wall thickness ( $r = 0.258$ ,  $P = 0.002$ ) and patients exposed to beta blockers ( $r = 0.227$ ,  $P = 0.008$ ). However, failure tension was reduced for patients suffering from CKD ( $r = -0.194$ ,  $P = 0.021$ ), hypercholesterolemia ( $r = -0.184$ ,  $P = 0.033$ ) and with high blood-values of potassium ( $r = -0.243$ ,  $P = 0.004$ ) and urea ( $r = -0.207$ ,  $P = 0.020$ ). The positive correlations of failure tension to maximum AAA diameter and to the distance of the excision site to the bifurcation ( $r = 0.159$ ,  $P = 0.058$  and  $r = 0.160$ ,  $P = 0.056$ , respectively) were close to statistical significance.  $r$  and  $P$ -values for correlations of failure tension in terms of Cauchy stresses and can be found in Tables 5.2 and 5.3. Plots for significant correlations of failure tension are shown in Figure 5.11 (1.PK stress only). Diagrams for 2nd principal stress and von Mises stress are omitted to avoid redundancy.

### Wall Strength

Wall strength in terms of 1.PK stresses and Cauchy stresses had significant correlations to the same explanatory variables, except for creatinine, which was only correlated to strength in terms of Cauchy stresses ( $r = 0.187$ ,  $P = 0.033$ ). The following  $r$  and  $P$ -values are given for wall strength in terms of 1.PK stresses: Wall strength had significant correlations to patient age ( $r = 0.171$ ,  $P = 0.041$ ) and to the following diseases in the patient's medical history: CKD ( $r = 0.184$ ,  $P = 0.029$ ), CHD ( $r = 0.174$ ,  $P = 0.045$ ), DM ( $r = -0.230$ ,  $P = 0.007$ ) and hypercholesterolemia ( $r = -0.182$ ,  $P = 0.036$ ). Further, wall strength was significantly correlated to calcification ( $r = -0.212$ ,  $P = 0.011$ ), wall thickness ( $r = -0.348$ ,  $P = 0.00002$ ), ACE inhibitors ( $r = -0.248$ ,  $P = 0.004$ ) and SUV ( $r = -0.236$ ,  $P = 0.037$ ).  $r$  and  $P$ -values for correlations of wall strength in terms of Cauchy stresses can be found in Tables 5.2 and 5.3. Plots for significant correlations are shown in Figure 5.12 (1.PK stress only).

### Notes

No significant correlations were found for any of the experimental results to the AAA-status (ruptured, elective). Further, no significant correlations were observed to hyperlipidemia, hypertension or PVD from patient's medical history and for ASA/clopid, statins or diuretics from the patients' medication. None of the mechanical properties was correlated to hsCRP, fibrinogen, creatin kinase, calcium, hematocrit or leukocytes obtained from biochemical blood analysis. No significant correlation was found for local radius/diameter or the difference between the 1st and 2nd principal stress acting at the sample excision site. Moreover, relative quantities (relative z-position, relative ILT thickness at sample excision site) did not yield better  $r$ -values or smaller  $P$ -values than the associated absolute values (distance to bifurcation, ILT thickness). Also the normalized diameter "NORD" did not yield better  $r$ -values or smaller  $P$ -values to any of the experimental results than its determinants, the local diameter and the subrenal aortic diameter.

Table 5.2: r-values and P-values for simple regressions. Statistically significant correlations are printed in bold.

		Patient characteristics			Patient's medical history							
		Sex	Age	Ruptured	CKD	CHD	DM	Hyperchol.	Hyperlipidemia	Hypertonia	PVD	Smoking status
Thickness	r	-0.019	-0.079	-0.127	<b>-0.274</b>	-0.033	<b>0.309</b>	<b>0.184</b>	0.079	-0.002	-0.031	<b>0.198</b>
	P	0.811	0.318	0.107	<b>0.0004</b>	0.682	<b>9E-5</b>	<b>0.023</b>	0.331	0.984	0.703	<b>0.011</b>
Alpha stiffness	r	0.075	-0.027	-0.034	-0.090	-0.154	-0.016	-0.008	0.016	0.027	-0.078	-0.123
	P	0.374	0.747	0.690	0.289	0.077	0.858	0.925	0.851	0.756	0.370	0.143
Beta stiffness	r	<b>0.166</b>	0.027	-0.030	<b>0.174</b>	0.050	-0.150	-0.011	-0.023	0.093	-0.053	-0.065
	P	<b>0.048</b>	0.753	0.722	<b>0.040</b>	0.571	0.082	0.899	0.797	0.285	0.548	0.444
Failure stretch	r	-0.055	<b>0.167</b>	-0.090	-0.007	<b>0.193</b>	-0.032	0.113	0.021	-0.116	-0.009	-0.113
	P	0.512	<b>0.046</b>	0.283	0.937	<b>0.026</b>	0.714	0.192	0.813	0.177	0.918	0.178
Failure tension (1.PK)	r	0.074	0.080	0.038	<b>-0.194</b>	0.017	0.006	<b>-0.184</b>	0.113	0.063	-0.034	0.047
	P	0.382	0.342	0.648	<b>0.021</b>	0.849	0.947	<b>0.033</b>	0.194	0.470	0.693	0.578
Strength (1.PK)	r	0.092	<b>0.171</b>	0.007	<b>0.184</b>	<b>0.174</b>	<b>-0.230</b>	<b>-0.198</b>	-0.133	0.035	0.094	-0.072
	P	0.274	<b>0.041</b>	0.933	<b>0.029</b>	<b>0.045</b>	<b>0.007</b>	<b>0.022</b>	0.125	0.685	0.282	0.393
Failure tension (Cauchy)	r	0.067	0.105	0.019	<b>-0.202</b>	0.057	0.003	<b>-0.174</b>	0.123	0.048	-0.037	0.033
	P	0.426	0.214	0.648	<b>0.016</b>	0.516	0.974	<b>0.044</b>	0.157	0.579	0.670	0.697
Strength (Cauchy)	r	0.075	<b>0.210</b>	-0.018	<b>0.185</b>	<b>0.225</b>	<b>-0.235</b>	<b>-0.182</b>	-0.127	0.006	0.109	-0.115
	P	0.374	<b>0.012</b>	0.835	<b>0.028</b>	<b>0.009</b>	<b>0.006</b>	<b>0.036</b>	0.144	0.946	0.209	0.173

		Specimen-specific data			AAA geometry			Medication				
		Direction	Calcification	Thickness	Max AAA $\varnothing$	Max ILT thick.	Subrenal a. $\varnothing$	ASA, Clopid	Beta blocker	ACE inh.	Statins	Diuretics
Thickness	r	<b>-0.252</b>	0.046	<b>1.000</b>	0.054	0.089	-0.015	0.099	-0.059	<b>0.165</b>	0.055	0.027
	P	<b>0.001</b>	0.557	<b>0.000</b>	0.490	0.261	0.853	0.220	0.467	<b>0.040</b>	0.500	0.738
Alpha stiffness	r	0.028	<b>0.308</b>	0.103	-0.001	0.083	<b>0.250</b>	0.077	-0.017	0.065	0.050	-0.177
	P	0.737	<b>0.0002</b>	0.224	0.990	0.324	<b>0.003</b>	0.380	0.850	0.460	0.566	0.041
Beta stiffness	r	0.125	0.153	<b>-0.241</b>	-0.069	<b>0.175</b>	<b>0.251</b>	0.114	<b>0.177</b>	-0.134	0.103	-0.044
	P	0.139	0.070	<b>0.004</b>	0.415	<b>0.037</b>	<b>0.003</b>	0.192	<b>0.041</b>	0.123	0.237	0.618
Failure stretch	r	<b>-0.250</b>	-0.055	0.092	<b>-0.218</b>	-0.007	0.035	-0.023	0.065	0.080	-0.056	0.023
	P	<b>0.003</b>	0.515	0.277	<b>0.009</b>	0.936	0.680	0.796	0.453	0.359	0.524	0.794
Failure tension (1.PK)	r	-0.014	-0.050	<b>0.258</b>	0.159	0.118	0.140	0.136	<b>0.227</b>	-0.020	-0.039	0.059
	P	0.870	0.551	<b>0.002</b>	0.058	0.160	0.096	0.116	<b>0.008</b>	0.819	0.651	0.496
Strength (1.PK)	r	0.074	<b>-0.212</b>	<b>-0.348</b>	-0.078	-0.052	-0.010	0.032	0.123	<b>-0.250</b>	0.027	0.050
	P	0.382	<b>0.011</b>	<b>2E-5</b>	0.353	0.537	0.901	0.712	0.158	<b>0.004</b>	0.754	0.567
Failure tension (Cauchy)	r	-0.048	-0.061	<b>0.272</b>	0.125	0.118	0.143	0.132	<b>0.244</b>	-0.010	-0.058	0.069
	P	0.569	0.467	<b>0.001</b>	0.136	0.160	0.089	0.130	<b>0.004</b>	0.911	0.508	0.427
Strength (Cauchy)	r	0.038	<b>-0.232</b>	<b>-0.361</b>	-0.127	-0.057	-0.016	0.022	0.123	<b>-0.248</b>	0.003	0.052
	P	0.654	<b>0.005</b>	<b>9E-6</b>	0.131	0.499	0.852	0.797	0.156	<b>0.004</b>	0.973	0.548

Table 5.3: Continuation: r-values and P-values for simple regressions. Statistically significant correlations are printed in bold.

		Local geometrical data/results from FE analysis at excision site										
		Distance to bifurcation	Relative z-position	Thrombus thickness	Relative ILT thick.	Radius	NORD	2nd principal stress	1st principal stress	Von Mises stress	1st+2nd princ. stress	1st-2nd princ. stress
Thickness	r	<b>0.186</b>	0.102	<b>-0.176</b>	-0.146	0.020	0.009	0.137	0.088	0.092	0.111	0.005
	P	<b>0.017</b>	0.196	<b>0.025</b>	0.068	0.803	0.911	0.082	0.262	0.243	0.158	0.954
Alpha stiffness	r	-0.028	-0.050	0.071	0.097	-0.026	-0.148	0.008	0.023	0.022	0.018	0.033
	P	0.738	0.554	0.402	0.260	0.762	0.079	0.924	0.782	0.792	0.830	0.701
Beta stiffness	r	0.027	0.038	<b>0.254</b>	<b>0.200</b>	-0.067	<b>-0.177</b>	-0.143	-0.132	-0.140	-0.141	-0.075
	P	0.752	0.656	<b>0.002</b>	<b>0.020</b>	0.428	<b>0.035</b>	0.089	0.117	0.097	0.094	0.376
Failure stretch	r	-0.146	-0.113	0.090	0.135	-0.084	-0.079	<b>-0.217</b>	<b>-0.196</b>	<b>-0.198</b>	<b>-0.212</b>	-0.105
	P	0.082	0.181	0.288	0.115	0.319	0.350	<b>0.009</b>	<b>0.019</b>	<b>0.018</b>	<b>0.011</b>	0.211
Failure tension (1.PK)	r	0.160	0.094	-0.095	-0.119	0.035	-0.037	<b>0.181</b>	<b>0.190</b>	<b>0.184</b>	<b>0.194</b>	0.134
	P	0.056	0.264	0.259	0.166	0.682	0.664	<b>0.031</b>	<b>0.023</b>	<b>0.028</b>	<b>0.020</b>	0.110
Strength (1.PK)	r	-0.039	0.025	0.013	0.007	-0.105	-0.085	-0.003	0.034	0.026	0.020	0.062
	P	0.641	0.768	0.882	0.931	0.211	0.312	0.968	0.688	0.754	0.810	0.459
Failure tension (Cauchy)	r	0.140	0.079	-0.083	-0.101	0.021	-0.049	0.148	0.162	0.155	0.163	0.120
	P	0.095	0.346	0.322	0.238	0.805	0.562	0.077	0.053	0.064	0.052	0.152
Strength (Cauchy)	r	-0.073	0.007	0.016	0.020	-0.128	-0.100	-0.048	-0.003	-0.011	-0.021	0.047
	P	0.389	0.938	0.846	0.813	0.129	0.237	0.567	0.970	0.895	0.801	0.579

		PET	Biochemical blood analysis									
		SUV	Calcium	Creatinine	Erythrocytes	Hematocrit	Hemoglobin	Leukocytes	Potassium	Sodium	Thrombocytes	Urea
Thickness	r	<b>0.601</b>	-0.077	<b>-0.168</b>	<b>0.186</b>	0.147	<b>0.183</b>	-0.022	0.058	<b>-0.226</b>	<b>0.455</b>	-0.131
	P	<b>2E-10</b>	0.551	<b>0.039</b>	<b>0.021</b>	0.069	<b>0.020</b>	0.781	0.465	<b>0.004</b>	<b>1E-9</b>	0.115
Alpha stiffness	r	<b>-0.275</b>	0.077	-0.025	0.101	0.104	0.131	-0.071	0.009	-0.009	0.107	<b>-0.214</b>
	P	<b>0.014</b>	0.568	0.779	0.246	0.231	0.122	0.404	0.917	0.917	0.207	<b>0.016</b>
Beta stiffness	r	<b>-0.385</b>	0.083	0.093	0.022	0.048	0.096	-0.101	-0.152	0.148	-0.083	<b>-0.207</b>
	P	<b>0.0004</b>	0.539	0.290	0.804	0.585	0.260	0.234	0.075	0.083	0.331	<b>0.020</b>
Failure stretch	r	0.069	0.158	0.026	0.073	0.030	0.037	-0.140	0.076	-0.142	0.113	0.070
	P	0.548	0.227	0.771	0.402	0.730	0.659	0.097	0.373	0.096	0.180	0.438
Failure tension (1.PK)	r	0.044	-0.071	-0.143	0.087	0.107	0.132	0.038	<b>-0.243</b>	-0.076	0.108	<b>-0.207</b>
	P	0.702	0.588	0.102	0.316	0.219	0.120	0.654	<b>0.004</b>	0.372	0.203	<b>0.020</b>
Strength (1.PK)	r	<b>-0.236</b>	0.173	0.170	-0.013	0.014	0.016	-0.022	-0.149	0.049	-0.081	-0.059
	P	<b>0.037</b>	0.185	0.052	0.881	0.872	0.854	0.797	0.080	0.569	0.337	0.509
Failure tension (Cauchy)	r	0.060	-0.049	-0.139	0.102	0.117	0.144	0.010	<b>-0.242</b>	-0.102	0.125	<b>-0.201</b>
	P	0.602	0.711	0.114	0.239	0.177	0.088	0.906	<b>0.004</b>	0.231	0.141	<b>0.024</b>
Strength (Cauchy)	r	<b>-0.237</b>	0.215	<b>0.187</b>	-0.008	0.013	0.018	-0.063	-0.136	0.006	-0.075	-0.035
	P	<b>0.037</b>	0.100	<b>0.033</b>	0.923	0.883	0.834	0.458	0.110	0.947	0.376	0.697

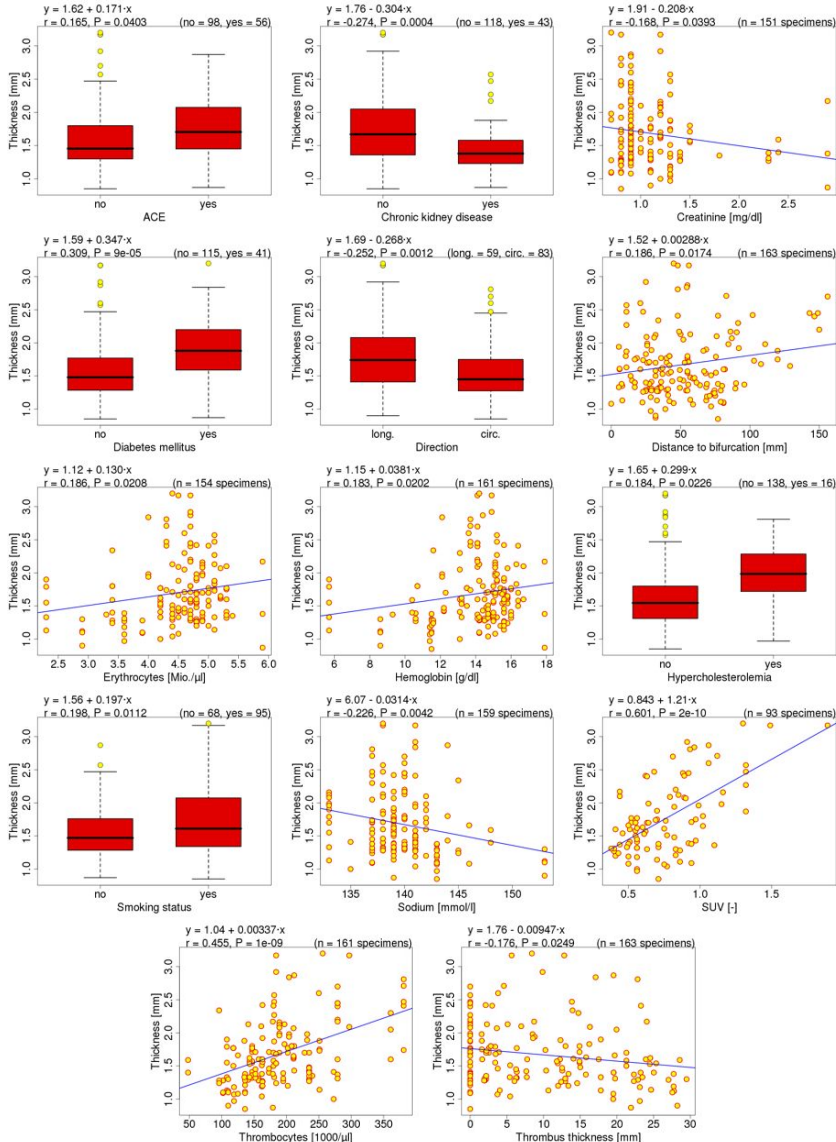


Figure 5.7: Box and whisker plots and scatter plots for experimentally measured AAA wall thickness over explanatory variables (only significant correlations, in alphabetical order). Equations for the simple regression variables,  $r$  and  $P$ -values are given on top of each diagram. Best correlations were found for AAA wall thickness to SUV, thrombocytes and DM. For specimen counts differing from  $n = 163$ , information on the respective explanatory variable was unavailable for the missing number of specimens.

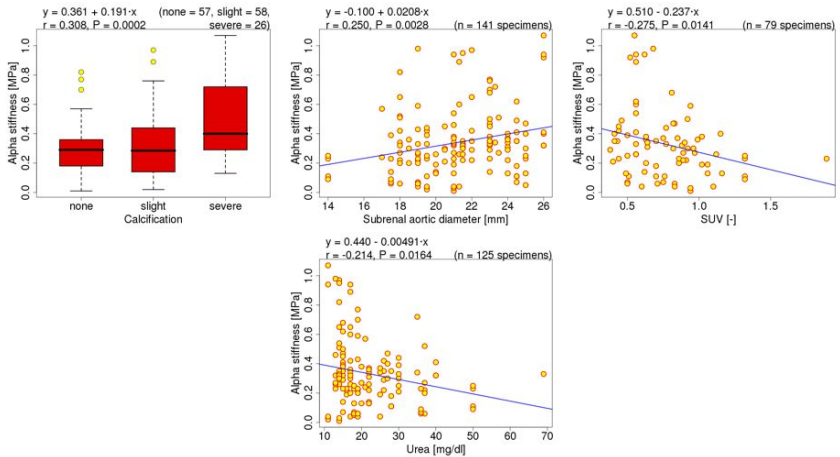


Figure 5.8: Box and whisker plots and scatter plots for experimentally measured alpha stiffness over calcification, subrenal aortic diameter, SUV and urea. Equations for the simple regression models,  $r$  and  $P$ -values, as well as number of specimens considered in the correlations are given on top of each diagram. Best correlations were found for alpha stiffness to calcification, subrenal aortic diameter and SUV. For specimen counts differing from  $n = 141$ , information on the respective explanatory variable was unavailable for the missing number of specimens.

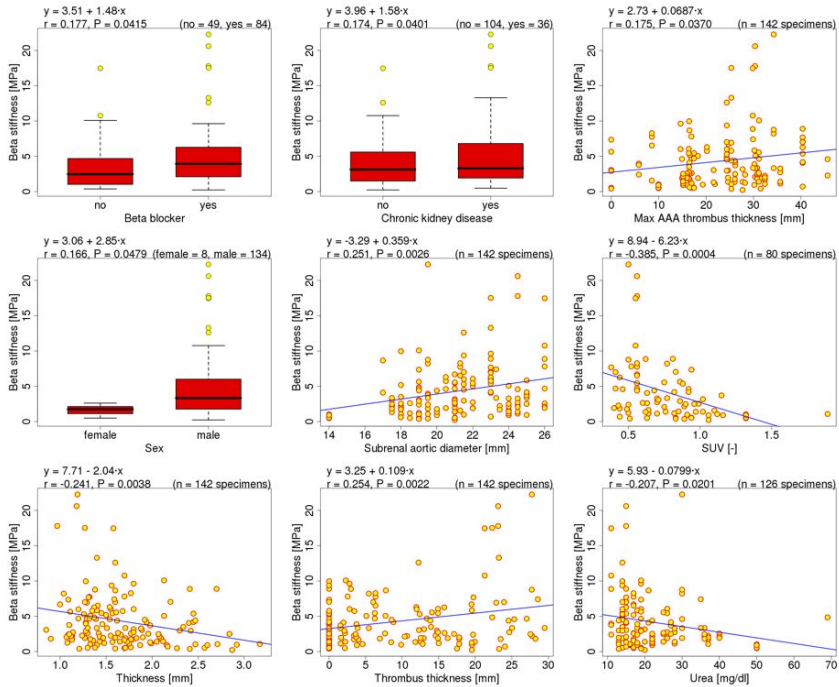


Figure 5.9: Box and whisker plots and scatter plots for experimentally measured beta stiffness over explanatory variables (for significant correlations, in alphabetical order). Equations for the simple regression models,  $r$  and  $P$ -values, as well as number of specimens considered in the correlations are given on top of each diagram. Best correlations were found for AAA wall thickness to SUV, thrombus thickness at sample excision site and subrenal aortic diameter. For specimen counts differing from  $n=142$ , information on the respective explanatory variable was unavailable for the missing number of specimens.

## 5 Mechanical Testing of AAA Wall

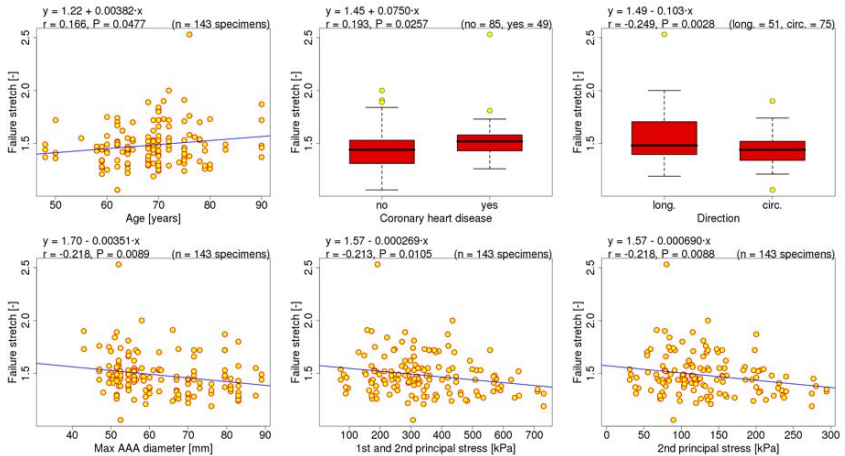


Figure 5.10: Box and whisker plots and scatter plots for experimentally measured failure stretch over patient age, CHD, testing direction, maximum AAA diameter, the sum of 1st and second principal stress and the 2nd principal stress. Equations for the simple regression models,  $r$  and  $P$ -values, as well as number of specimens considered in the correlations are given on top of each diagram. Best correlations were found for failure stretch to testing direction, maximum AAA diameter and the 2nd principal stress. For specimen counts differing from  $n = 143$ , information on the respective explanatory variable was unavailable for the missing number of specimens.

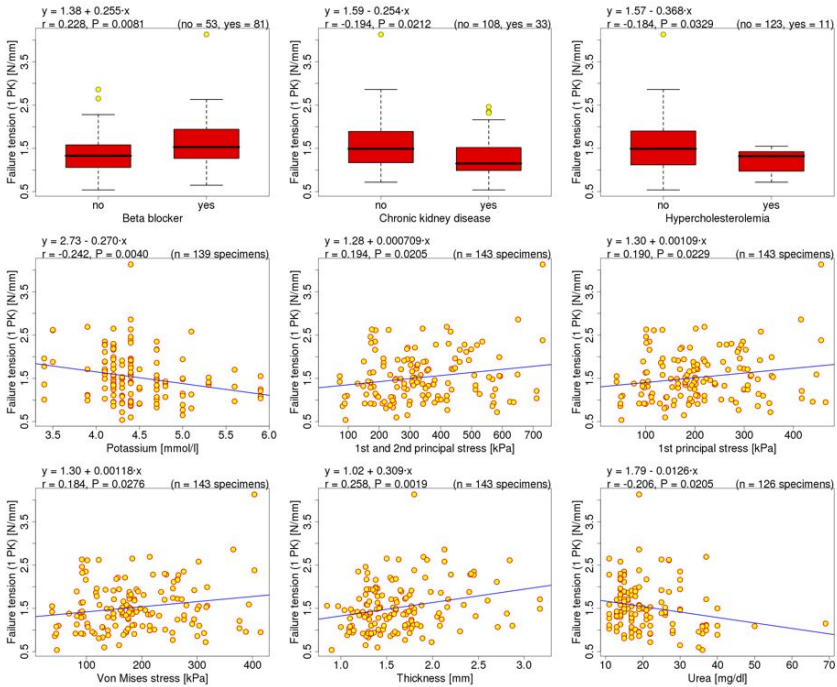


Figure 5.11: Box and whisker plots and scatter plots for significant correlations of experimentally measured failure tension (only for failure tension in terms of 1.PK stress), in alphabetical order. Equations for the simple regression models,  $r$  and P-values, as well as number of specimens considered in the correlations are given on top of each diagram. Best correlations were found for failure tension to wall thickness, blood potassium and beta blocker. For specimen counts differing from  $n = 143$ , information on the respective explanatory variable was unavailable for the missing number of specimens.

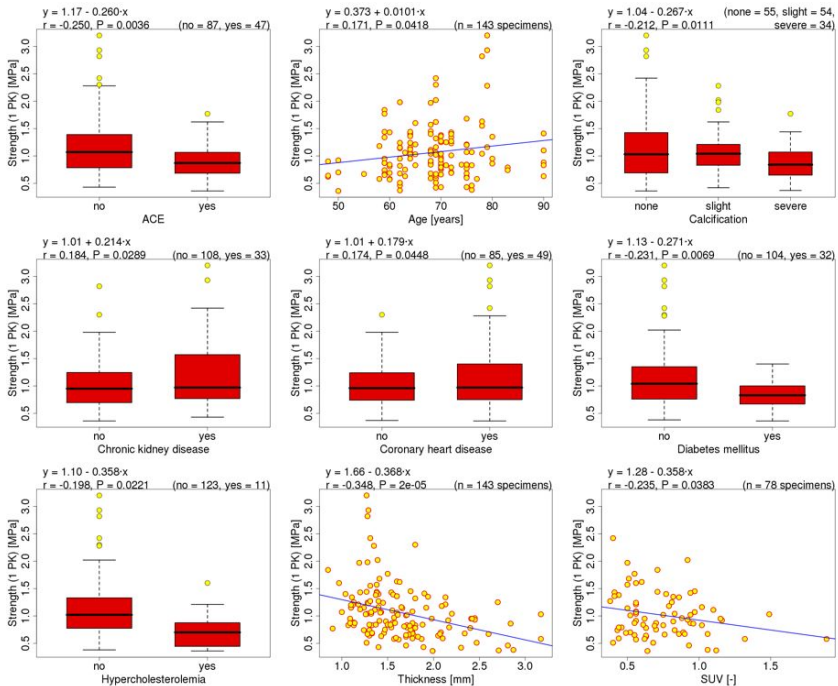


Figure 5.12: Box and whisker plots and scatter plots for experimentally measured AAA wall strength (in terms of 1.PK stresses only) over significantly correlated explanatory variables. Equations for the simple regression models,  $r$  and  $P$ -values, as well as number of specimens considered in the correlations are given on top of each diagram. Best correlations were found for AAA wall strength to wall thickness, ACE inhibitors, DM and SUV. For specimen counts differing from  $n = 143$ , information on the respective explanatory variable was unavailable for the missing number of specimens.

### 5.3.2 Interpretation and Discussion of the Results

All values and correlations for failure tension and wall strength listed in this section refer to quantities in terms of 1.PK stresses, if not stated otherwise.

The SUV as the quantitative measure for local metabolic activity obtained by FDG-PET/CT has shown to bear great potential for non-invasive estimation of AAA wall properties. Correlations of the SUV to experimentally measured AAA wall properties yielded the best correlations in the current study. For instance, the wall thickness of samples from sites with increased SUV was significantly higher than for samples excised from sites with low metabolic activity ( $r = 0.601$ ,  $P < 1E-09$ ). As hypothesized by various groups [39, 168, 171, 210], this increase in wall thickness might be caused by local inflammatory processes and macrophage

infiltration, among other possible causes [51, 113]. The findings that strength decreases with increasing SUV ( $r = -0.236$ ,  $P = 0.037$ ) but failure tension is independent of the SUV ( $r = 0.044$ ,  $P = 0.702$ ) further substantiates the hypothesis that wall thickening is rather mediated by accumulation of non load-bearing components than by production of collagenous fibers and/or SMCs. Analogously, the decrease of stiffness values with increasing metabolic activity was consistent with this hypothesis (SUV to alpha stiffness:  $r = -0.275$ ,  $P = 0.014$ ; SUV to beta stiffness:  $r = -0.385$ ,  $P = 0.0004$ ). With regard to clinical practice, rupture risk of AAAs with increased metabolic activity remains unaffected, since failure tension was independent of the SUV. However, for AAAs with increased metabolic activity, it cannot be excluded that rapid AAA expansion over short time, together with the markedly changed mechanical AAA wall properties might lead to a rupture prone state as reported in [168, 171, 179].

One of the most crucial findings might be the identification of CKD and its corresponding laboratory parameters (e.g. increased creatinine, potassium and urea levels) as important clinical parameters for AAA rupture risk stratification. Interestingly, failure tension was significantly decreased in patients suffering from CKD. Failure tension medians were 1.15 N/mm for patients suffering from CKD and 1.48 N/mm for patients without CKD (Figure 5.11 (top middle),  $r = -0.194$ ;  $P = 0.021$ ). The reduction in failure tension may be explained by the dominant decrease in wall thickness despite the slight increase in wall strength. This may be attributable to a reduced content of collagenous fibers, which has already been demonstrated for atherosclerotic lesions in CKD patients in the context of other cardiovascular diseases [156, 157]. Histological investigations of AAA tissue samples are needed to confirm this hypothesis. For clinical practice, the reduction in failure tension implies that a 4.3 cm AAA in a patient suffering from CKD and a 5.5 cm AAA in a patient without CKD feature equivalent rupture risk, thus indicating a drastically increased rupture risk in patients with CKD. So far, this predisposition has not yet been associated with AAA progression or rupture [27, 204]. With respect to these findings, it is recommended that CKD should be included in future studies on risk factors of AAA rupture.

Apart from CKD, a significant influence of smoking and DM on AAA wall properties was found. Positive smoking status or DM were associated with significantly increased wall thickness, while beta stiffness and wall strength were significantly decreased. In contrast to CKD, the combination of these parameters did not lead to reduced failure tension. The experiments further revealed that patients suffering from hypercholesterolemia, which is a risk factor for the formation of AAA and for cardiovascular diseases in general [52], featured an increased AAA wall thickness, whereas both failure tension and wall strength were significantly decreased. This finding, however, has to be treated with care, since the percentage of patients suffering from hypercholesterolemia seems disproportionately low. A revisit of this data was not possible, since cholesterol levels in blood had not been tested by default in the hospital. In patients exposed to ACE inhibitors, wall thickness was increased and wall strength was reduced, resulting in unaffected failure tension. For patients receiving beta blockers, however, wall thickness and strength remained unaffected, while failure tension was increased. Notably, these medication effects diverged although 12 of the 16 patients exposed to ACE inhibitors additionally took beta blockers (Table 5.1). Anyways, correlations between experimental testing results and medication should be treated with care, since the patient charts did not provide any information on dose or duration of medications.

Neither measured elastic properties, failure tension nor wall strength correlated to the testing direction of the specimens. Although earlier studies actually stated anisotropy for both healthy

[93] and aneurysmatic aortic wall [154, 222], there is no contradiction to the present results: The present findings rather indicate that there are more substantial factors than anisotropy that govern the mechanical properties of AAA wall. Besides e.g. the SUV, as discussed above, a more important explanatory variable than tissue anisotropy was the existence of calcification. Calcification had influence on alpha stiffness ( $r = 0.308$ ,  $P = 0.0002$ ) and wall strength ( $r = -0.212$ ,  $P = 0.011$ ). However, there was no correlation between existent calcification and failure tension ( $r = -0.050$ ,  $P = 0.551$ ). Especially with respect to FE analysis of AAAs, these findings indicate that the modeling of inflammatory processes and existent calcification, respectively, are more essential for a correct wall stress calculation than modeling tissue anisotropy. The increase in failure tension for specimens from excision sites exposed to high *in vivo* loading (failure tension vs. 1st principal stress:  $r = 0.190$ ,  $P = 0.023$ ) is in agreement with theories of mechanobiological tissue response [98, 99, 101].

### Comparison to Literature

The experimentally measured data in this work is in reasonable agreement with other studies. Compared to the largest study so far (145 specimens) performed by Raghavan *et al.* [163], mean wall thickness in our study (163 specimens,  $1.67 \pm 0.49$  mm) is in excellent match with their data ( $1.70 \pm 0.4$  mm for ruptured AAAs,  $1.50 \pm 0.4$  mm for non-ruptured AAAs). Thubrikar *et al.* [206] investigated 47 AAA wall specimens and found a mean wall thickness of  $2.09 \pm 0.59$  mm in the anterior region and  $2.73 \pm 0.46$  mm in the posterior region. Both of these values are slightly higher than the results from our study. We could only harvest few samples from the posterior AAA region and could not examine this relationship in the present study. Vande Geest *et al.* [220] investigated 26 specimens and found a sample thickness of  $1.32 \pm 0.41$  mm.

A comparison of elastic properties is hardly possible because of the different choices and meanings of stiffness measures in literature. In the present study, elastic parameters were chosen with respect to a SEF comparable to that one proposed by Raghavan and Vorp [164]. Consequently, a straightforward comparison can only be performed to the stiffness values presented in their work. In the present study, alpha stiffness was  $0.339 \pm 0.229$  MPa and beta stiffness was  $4.329 \pm 3.971$  MPa. Raghavan and Vorp [164] found an alpha stiffness of  $1.044 \pm 0.746$  MPa and a beta stiffness of  $1.88 \pm 3.09$  MPa. Hence, the present findings indicate a more distinct non-linear elastic behavior for AAA wall than previously reported. A similar tendency to a stronger nonlinearity was found by Vande Geest *et al.* [220]. They hypothesized that the increase in nonlinearity was caused by their biaxial tensile testing. In consequence, they concluded that biaxial testing must be used to measure the correct nonlinearity. This is in disagreement with the present results where the marked nonlinearity could also be measured in uniaxial tensile tests. Further, the major limitations of the study by Vande Geest have already been argued in Section 2.5.3. It might be supposed that discrepancies between the current results and the results by Raghavan and Vorp [164] stem from the determination of the load-free specimen state, the measurement resolution and/or other variations in the experimental set-up or test protocol.

Mean failure tension (1.PK stress) in the present study was  $1.523 \pm 0.566$  N/mm and mean wall strength (1.PK stress) was  $1.063 \pm 0.490$  MPa. Both values are at the upper range of reported experiments thus far: Failure tension in Raghavan *et al.* [163] was  $1.12 \pm 0.23$  N/mm for specimens from ruptured AAAs and  $1.16 \pm 0.36$  N/mm for specimens from non-ruptured AAAs, wall strength was  $0.95 \pm 0.28$  MPa for ruptured AAAs  $0.98 \pm 0.23$  MPa for non-ruptured

ones (Cauchy stresses). Okamoto *et al.* [154] found a strength of  $1.35 \pm 0.37$  MPa (Cauchy) for patients older than 50 years. Vande Geest *et al.* [222] found a strength of  $0.805 \pm 0.6$  MPa (presumably Cauchy). Thubrikar *et al.* [206] reported a yield strength of about 0.5 MPa (Cauchy). Yield strength is about 50 % of ultimate strength for AAA wall samples as shown by Marini *et al.* [137]. Therefore, yield strength values have to be multiplied by a factor of two in order to compare them to the ultimate strength values, whereupon the results by Thubrikar *et al.* match the values of other studies. Strength values reported by Sugita *et al.* [200] ( $0.98 \pm 0.39$  MPa to  $1.56 \pm 0.34$  MPa, 1.PK stress), were higher than strength measured in the present study. The reasons for the variations in reported failure tension and wall strength values seem to be hardly distinguishable. One reason might be the higher reported thickness in Thubrikar *et al.* [206] which by implication brings about lower strength. Another reason for some nonconformity might e.g. be the use of tissue obtained from necropsy in Raghavan *et al.* [163], whereas freshly harvested tissue was used in the present study. Nevertheless, based on the current findings, the main statement by Raghavan *et al.* [163] that the wall of ruptured aneurysms is not globally weaker than that of non-ruptured ones can be agreed on.

Predictions of AAA wall properties by non-invasively assessable parameters are scarce in literature. The only study that included few explanatory variables has been performed by Vande Geest *et al.* [222]. They found correlations of wall strength to local normalized diameter, maximum AAA diameter, local thrombus thickness, sex and family history of AAA. They found no correlations between wall strength and patient age or smoking status. Interestingly, in the current study, there was no correlation of wall strength to any of these explanatory variables. Hence, the formula provided by Vande Geest *et al.* [222] is highly disputable and should be treated with caution. Additionally, it is worth mentioning that a detailed description of wall strength, such as provided in [222], is impractical without detailed knowledge on real *in vivo* wall thickness or, at least, usage of a wall thickness model at the same time. In consequence, there is a pressing need for a statistical wall thickness model and also for a new statistical strength model. Both will be presented in Section 5.5. Although the strength model by Vande Geest *et al.* [222] could not be validated at all, there are other studies, including the works of our own group, that actually show an improvement of FE based rupture risk prediction due to usage of this strength model. The explanation might be an incorrect incorporation of the ILT in the FE models [133, 147]. Therein, ILT is often modeled as a blood proof AAA constituent and blood forces are modeled onto its luminal surface. This method assigns a major cushioning effect to the thrombus - which does not reflect the *in vivo* experimental results by Schurink *et al.* [185]. They actually found that thrombus does not reduce the pressure acting onto the AAA wall and therefore the cushioning effect of thrombus might not be as large as obtained in FE simulations so far shown in literature. On the other hand, ILT plays a major role in the strength model reducing the strength of the adjacent wall drastically. In this way, the strength model proposed by Vande Geest *et al.* [222] might counteract the modeling error in the wall stress calculation. A better way, however, for genuine FE modeling is definitely the physically correct inclusion of thrombus effects leading to more realistic wall stress, combined with a correct model for AAA wall strength.

## Limitations

This study used samples from patients undergoing elective or emergency AAA repair. Sample dimensions were therefore often limited to a size that was legitimate with the surgery process

and resulting specimens were often smaller than 20 mm. Subtracting the clamping regions at both ends of a specimen, a maximum free specimen length (=distance between the two clamps) that was consistently available for all tested specimens was 7.3 mm. Considering that average sample width already was 8 mm, it becomes clear that the assumption of an uniaxial stress state might not have been completely fulfilled during mechanical testing. These circumstances probably influenced the accuracy and reliability of alpha-stiffness and beta-stiffness measurements.

In the current study, it was found that most reliable prediction of mechanical AAA wall properties was based on PET/CT imaging. This imaging routine, however, is not the clinical standard procedure for AAA patients and therefore was only available for a small number of patients. Other explanatory variables yielded correlations that only had a low  $r$ -value (often close to  $r = 0.2$ ). Firstly, some of the low  $r$ -values may be caused by the parametrization of some explanatory variables using only discrete values (“yes/no” or “1/0”). In such cases, more detailed data was not consistently available for all patients. Secondly, due to the huge number of significant explanatory variables, provided that these variables are not inter-dependent, it becomes clear that the individual correlations must be bounded to low  $r$ -values. To overcome this limitation, multiple linear regression models for the prediction of mechanical properties will be created, which can reach better correlation coefficients (Section 5.5). Thereby, it is considered that PET imaging is not routinely available and models that spare PET data will also be presented.

Some results may also be hampered by the small number of female patients ( $n = 3$ ; 9 specimens), patients suffering from hypercholesterolemia ( $n = 4$ ; 16 specimens) or patients with ruptured AAA ( $n = 5$ ; 15 specimens) (Table 5.1). Further, the patients’ medication also poses some problems, since firstly, the medication dose and duration were not available from the patient charts. Secondly, it cannot be stated whether the changes in experimental results were mediated by the medication or rather by the disease which should be treated by the medication. And third, the medication can also influence the blood values measured in the biochemical blood analysis. Moreover, a statistically significant correlation was obtained between wall thickness and specimen orientation during tensile testing (thickness vs. circumferential orientation:  $r = -0.252$ ,  $P = 0.0012$ ), which obviously makes no sense. This is an accidental result, which might be attributed to the fact that the surgeons tended to excise samples with longitudinal orientation when surgery was complicated. Nevertheless, these circumstances did not detrimentally influence the measured tissue anisotropy: Due to the finding that thinner specimens generally featured higher beta-stiffness ( $r = -0.241$ ,  $P = 0.0038$ ) and strength ( $r = -0.348$ ,  $P = 2E - 05$ ), circumferential specimen orientation could have boosted higher beta-stiffness and strength values. This effect, however, was not seen in the current study (circumferential orientation vs. beta stiffness:  $r = 0.125$ ,  $P = 0.1390$ ; circumferential orientation vs. strength:  $r = 0.074$ ,  $P = 0.3817$ ). Still, biaxial tension test results in combination with detailed information on explanatory variables might be applied to finally answer this question. Lastly, the finding that failure stretch increases with increasing patient age (Table 5.2) seems implausible and should be handled carefully.

Table 5.4: Patient characteristics for normal AA wall donors and patient-averaged testing results (number of specimens for each patient is given in brackets behind the respective patient Id). Failure tension ( $T_{max}$ ) and strength ( $P_{max}$ ) are given in terms of 1.PK stresses, respectively. “Larger than”-values (e.g. “>2.22”) indicate that the tensile test machine specifications were insufficient to appropriately damage at least one specimen from this patient during destructive testing. Mean $\pm$ sd values for failure tension, strength and failure stretch ( $\lambda_{max}$ ) were calculated independent of the fact that some specimens could actually bear higher loads or stretch before failure. (Dir.=testing direction; Calc.=calcification)

Pat. Id (no. specs.)	Age [y.]	Sex	Dir.	Calc.	t [mm]	$\alpha$ [MPa]	$\beta$ [MPa]	$T_{max}$ [ $\frac{N}{mm}$ ]	$P_{max}$ [MPa]	$\lambda_{max}$ [-]
1 (1)	32	fem.	circ.	no	1.27	0.641	2.031	>2.22	>1.75	>1.37
2 (1)	45	male	long.	no	0.89	0.012	0.154	too distensible		>1.44
3 (8)	77	unkn	both	no	0.65	0.121	9.271	>2.05	>3.36	>1.36
4 (3)	63	fem.	both	no	1.39	0.123	1.508	1.32	0.95	1.65
5 (1)	52	fem.	circ.	no	1.48	0.149	0.753	1.54	1.04	1.71
6 (2)	40	male	long.	no	1.38	0.064	0.053	>2.17	>1.75	>1.87
7 (1)	32	unkn	unkn	no	1.2	0.199	0.515	not tested		
8 (1)	21	unkn	unkn	no	0.77	0.058	0.053	too distensible		>2.03
9 (2)	74	unkn	long.	yes	1.85	0.450	2.491	1.21	0.94	1.36
10 (3)	33	unkn	both	no	1.35	0.030	0.056	too distensible		>1.88
<b>mean</b>	46.9				1.22	0.185	1.689	>1.75	>1.63	>1.62
<b><math>\pm</math>sd:</b>	$\pm$ 19.1				$\pm$ 0.36	$\pm$ 0.203	$\pm$ 2.087	$\pm$ 0.45	$\pm$ 0.93	$\pm$ 0.27

## 5.4 Normal Abdominal Aortic (AA) Wall

### 5.4.1 Tensile Test Results for Normal AA Wall

The ten samples of normal AA wall were similarly processed as the AAA samples and a total of 23 specimens suitable for uniaxial tensile testing could be obtained. The mechanical testing and the assessment of the testing results were identical to the procedures described in Sections 5.1.2 and 5.1.3. Especially for the normal AA specimens, the tensile test machine specifications were often insufficient for the successful destructive testing of these specimens: In 7 cases, the specimens were too distensible such that the available machine clamp displacement of 5 mm was not sufficient to appropriately load the specimens and initiate damage. Failure tension and strength values for these specimens were discarded. Stretches that were obtained for these specimens at the maximum clamp displacement were documented but tagged with a “larger than” sign (e.g. “>1.44”), indicating that damage has not been initiated at this stretch. Further, the maximum machine tensile force of 22 N was reached during destructive testing of 8 specimens (without damage initiation in 7 specimens). Measured values for specimen tension, stress and stretch, respectively, when the maximum machine force has been exceeded were documented but also tagged with a “larger than” sign (e.g. “>2.2 N/mm”). One specimen slipped from the clamps during destructive testing. The measurements for this specimen were discarded. Characteristics and testing results of the normal AA specimens are given in Table 5.4. Testing results were

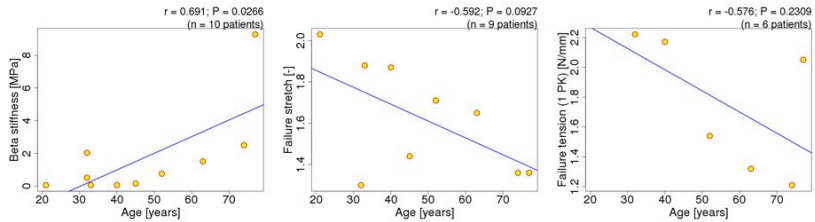


Figure 5.13: Normal AA wall: Scatter plots for beta stiffness, failure stretch and failure tension over patient age, respectively. The blue line in each diagram is the best fit line obtained by linear regression (LS fit). Only the correlation of beta stiffness to patient age reached statistical significance.

averaged for each patient, in order to avoid unfavorable influence due to the heavily varying number of specimens per patient.

Normal AA wall thickness ranged from 0.65 mm to 1.85 mm with a median of 1.37 mm and a mean of  $1.22 \pm 0.36$  mm. Alpha stiffness of AA wall ranged from 0.012 MPa to 0.641 MPa with a median of 0.122 MPa and a mean of  $0.185 \pm 0.203$  MPa. Beta stiffness varied from 0.053 MPa to 9.271 MPa with a median of 0.634 MPa and a mean of  $1.689 \pm 2.087$  MPa. Failure stretch ranged from 1.30 to 2.03 with a median of 1.68 and a mean of  $1.62 \pm 0.27$ . Failure tension of AA wall in terms of 1.PK stresses varied from 1.21 N/mm to 2.17 N/mm with a median of 1.65 N/mm and a mean of  $1.75 \pm 0.45$  N/mm. AA wall strength in terms of 1.PK stresses ranged from 0.94 MPa to 3.36 MPa, with a median of 1.34 MPa and a mean of  $1.63 \pm 0.93$  MPa, as also summarized in Table 5.4.

While a huge amount of non-invasively assessable data was available for the AAA wall samples, there were only very few explanatory variables available for normal AA wall samples, such as patient age and sex. Correlation analyses were performed to investigate the relationship between these two explanatory variables and the patient-averaged testing results. There was a significant correlation between patient age and beta stiffness ( $r = 0.691$ ,  $P = 0.0266$ ). Further, there were good, but non-significant correlations between patient age and failure tension ( $r = -0.592$ ,  $P = 0.0927$ ), as well as between patient age and failure stretch ( $r = -0.576$ ,  $P = 0.2309$ ). Diagrams for these three correlations are given in Figure 5.13. There was no significant correlation of any of the experimental results to patient sex.

An explanatory variable that was frequently available for normal AA wall samples was the sample orientation (=testing direction). For each patient, the mean values of elastic properties and failure properties in longitudinal and in circumferential testing direction, respectively, were calculated. For some patients (Id: 1, 2, 5, 6 and 9) results were available for only one testing direction. Sample/specimen orientations were not known for patients 7 and 8. Evaluation of the testing results showed that mean alpha stiffness and mean beta stiffness for circumferentially tested specimens ( $\alpha = 0.228$  MPa,  $\beta = 3.493$  MPa) were approximately twice as high as for longitudinally tested specimens ( $\alpha = 0.120$  MPa,  $\beta = 1.332$  MPa). However, differences were not statistically significant ( $\alpha$ :  $P = 0.178$ ;  $\beta$ :  $P = 0.792$ ). Both mean failure tension and mean failure stretch were slightly but non-significantly increased for circumferentially tested specimens (failure tension: 1.62 N/mm (long.) vs. 1.91 N/mm (circ.),  $P = 0.393$ ; failure

Table 5.5: Normal AA wall: Elastic and failure properties with respect to testing directions. Results were averaged over the number of equally oriented specimens for each patient. None of the differences between longitudinally and circumferentially tested specimens were significant.

	Patient Id	$\alpha$ [MPa]	$\beta$ [MPa]	$T_{max}$ [ $\frac{N}{mm}$ ]	$P_{max}$ [MPa]	$\lambda_{max}$ [-]
longitudinally tested specimens	2	0.012	0.154	-	-	>1.44
	3	0.063	4.100	>2.00	>3.84	>1.28
	4	0.108	1.120	1.08	0.77	1.57
	6	0.064	0.053	>2.17	>1.75	>1.87
	9	0.450	2.491	1.21	0.94	1.36
	10	0.025	0.073	-	-	>1.70
	<b>mean</b>	0.120	1.332	>1.62	>1.83	>1.54
<b><math>\pm</math>sd:</b>	$\pm 0.175$	$\pm 1.732$	$\pm 0.55$	$\pm 1.41$	$\pm 0.24$	
circumferentially tested specimens	1	0.641	2.031	>2.22	>1.75	>1.37
	3	0.155	12.370	>2.08	>3.13	>1.37
	4	0.151	2.286	1.80	1.30	1.81
	5	0.149	0.753	1.54	1.04	1.71
	10	0.042	0.023	-	-	>2.24
	<b>mean</b>	0.228	3.493	>1.91	>1.81	>1.70
	<b><math>\pm</math>sd:</b>	$\pm 0.236$	$\pm 5.048$	$\pm 0.30$	$\pm 0.93$	$\pm 0.36$

stretch: 1.54 (long.) vs. 1.70 (circ.),  $P = 0.410$ ). In Table 5.5, testing results are summarized with respect to specimen orientation.

Characteristic stress-stretch curves for normal AA wall under longitudinal or circumferential elongation are given in Figure 5.14 (as obtained from the tests of individual specimens - not from patient-averaged curves). These curves exhibit a markedly increased stiffness of normal AA wall in circumferential direction or rather a very soft behavior of longitudinally tested specimens.

## 5.4.2 Comparison between AAA Wall and Normal AA Wall

In order to perform a consistent comparison between AAA wall and healthy AA wall, patient-averaged values were calculated for all AAA patients. Subsequently, differences in mechanical properties between AAA wall and AA wall were investigated (all values as mean $\pm$ sd; relative differences are given with respect to properties of normal AA wall): AAA wall was 39 % thicker than healthy AA wall (AAA:  $1.70 \pm 0.47$  mm vs. AA:  $1.22 \pm 0.36$  mm;  $P = 0.003$ ). Alpha and beta stiffness of AAA specimens were increased by 102 % and 150 %, respectively (AAA:  $\alpha = 0.374 \pm 0.249$  MPa,  $\beta = 4.221 \pm 3.092$  MPa vs. AA:  $\alpha = 0.185 \pm 0.203$  MPa,  $\beta = 1.689 \pm 2.078$  MPa;  $P_{(\alpha)} = 0.0051$ ,  $P_{(\beta)} = 0.0012$ ). The average AAA wall specimen failed at 15 % lower tension than the average normal AA wall specimen (AAA:  $1.48 \pm 0.47$  N/mm vs. AA:  $> 1.75 \pm 0.45$  N/mm;  $P = 0.137$ ). AAA wall strength was reduced by 38 % (AAA:  $1.01 \pm 0.39$  MPa vs. AA:  $> 1.63 \pm 0.93$  MPa;  $P = 0.089$ ). The average failure stretch of AAA

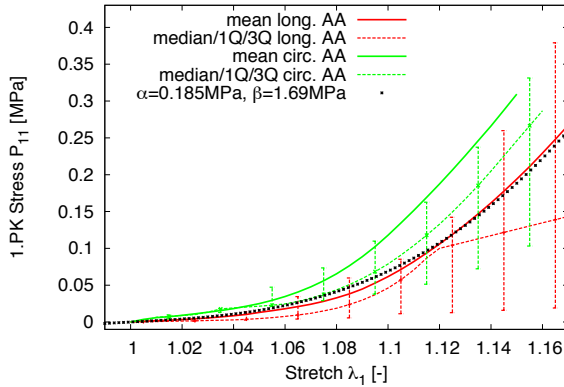


Figure 5.14: Normal AA wall under uniaxial tension: Stress-stretch curves (loading branch only) for longitudinal (red) and circumferential (green) testing directions. Solid lines are calculated as the mean curves from experimentally obtained stress-stretch curves. The dashed J-shape curves indicate the experimentally measured medians (median stress at any given stretch). The whiskers branching off the medians indicate the first (1Q) and third quartiles (3Q) of stresses at the given stretches. The dotted line indicates the model behavior for a R&V type SEF with the mean material parameters from Table 5.4.

specimens was 19% lower than for normal AA wall (AAA:  $1.50 \pm 0.14$  vs. AA:  $> 1.62 \pm 0.27$ ;  $P = 0.229$ ). This comparison is also summarized in Table 5.6. A graphical comparison of the patient-averaged mechanical properties between normal AA wall and AAA wall is given in Figure 5.15.

While there was a significant difference in elastic properties between circumferentially and longitudinally tested normal AA specimens (Table 5.4), this statement cannot be maintained for AAA wall specimens (Table 5.2). This can also be observed graphically in Figures 5.6 and 5.14. A comparison between the stress-stretch behavior of AAA wall and normal AA wall independent of the testing direction is given in Figure 5.16. This figure shows characteristic stress-stretch curves, which were calculated from the complete data set of experimental curves independently of testing directions. Specimens with unknown testing orientation were included. Mean curves for AAA wall and normal AA wall demonstrate an overall stiffer behavior of AAA tissue. The same tendency is given by the median curves. In the stretch range  $\lambda > 1.12$ , there was a marked stiffening of the 3Q-curve of normal AA wall. At the same time, the very low 1Q-curve indicates that there was also a considerable number of normal AA wall specimens that still featured a very soft mechanical response in this stretch region.

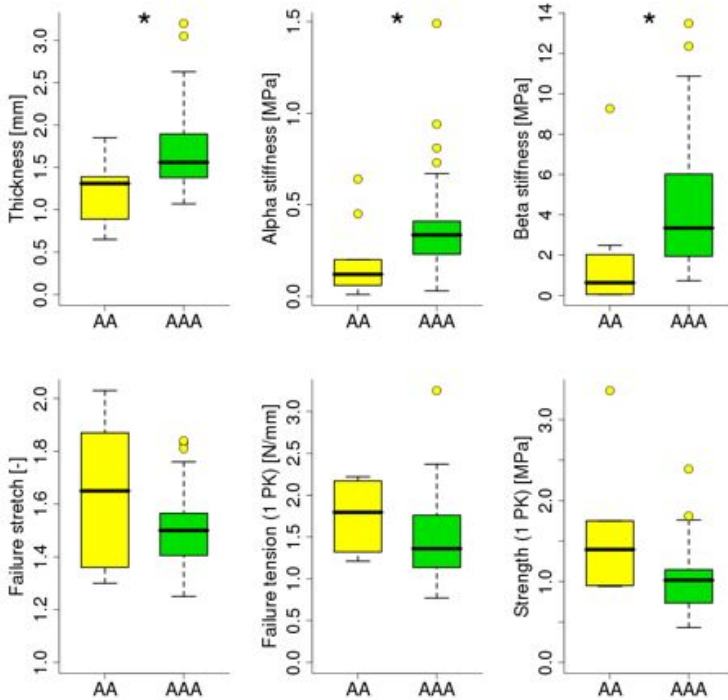


Figure 5.15: Comparison of mechanical properties between normal AA wall and AAA wall (patient-averaged values). Box and whisker plots show experimentally measured wall thickness, alpha stiffness, beta stiffness, failure tension in terms of 1.PK stresses and wall strength in terms of 1.PK stresses for normal AA wall (yellow) and AAA wall (green), respectively. Statistically significant differences between normal AA wall and AAA wall are indicated with a star “\*”.

Table 5.6: Comparison of mechanical properties between normal AA wall and AAA wall: Patient-averaged values for thickness, elastic properties and failure properties.  $\Delta$  denotes the relative difference between properties of normal AA wall and AAA wall (with respect to normal AA wall).

		<b>t</b> [mm]	<b><math>\alpha</math></b> [MPa]	<b><math>\beta</math></b> [MPa]	<b><math>T_{max}</math></b> [ $\frac{N}{mm}$ ]	<b><math>P_{max}</math></b> [MPa]	<b><math>\lambda_{max}</math></b> [-]
<b>normal AA wall (10 pat.)</b>	mean	1.22	0.185	1.689	>1.75	>1.63	>1.62
	$\pm$ sd:	$\pm$ 0.36	$\pm$ 0.203	$\pm$ 2.087	$\pm$ 0.45	$\pm$ 0.93	$\pm$ 0.27
<b>AAA wall (50 patients)</b>	mean	1.70	0.374	4.221	1.48	1.01	1.50
	$\pm$ sd:	$\pm$ 0.47	$\pm$ 0.249	$\pm$ 3.092	$\pm$ 0.47	$\pm$ 0.39	$\pm$ 0.14
$\Delta$ [%]		+39.3	+102.2	+149.9	-15.4	-38.0	-19.4
<b>P-value</b>		0.0030	0.0051	0.0012	0.1367	0.0893	0.2288

### 5.4.3 Interpretation and Discussion

Extensive literature is existent on both normal AA wall and AAA wall. However, comparisons between mechanical properties of normal AA tissue and AAA tissue based on this literature are hampered by different testing methods (e.g. sample preparation, tensile test machine, etc.) and different evaluation of the results (e.g. different SEFs, stress measures, etc.) in the independent studies. Only few contributions included investigations of normal AA tissue and AAA tissue performed with the same experimental set-up. Raghavan *et al.* [165] investigated the difference in elastic and failure properties. They stated significantly decreased strength for AAA samples. They also found a stiffer behavior of AAA wall samples. However, the differences to the elastic properties of normal AA samples did not reach statistical significance. Differences in elastic properties between normal AA samples and AAA samples were also investigated in biaxial tensile tests by Vande Geest *et al.* [220]. This data was later also reanalyzed by Ferruzzi *et al.* [47], who stated a stiffening and a loss of extensibility with both age and development of AAA. Wall thickness was not reported in any of these studies.

The comparison of mechanical properties of normal AA tissue and AAA tissue in the present study included the so far largest specimen population. Thereby, the present study also considers comparisons of wall thickness, which have so far been cut out in the literature. In this first “complete” comparison of its kind, it could be shown that AAA wall was significantly thicker and also significantly stiffer than normal AA wall. Further, AAA wall failed at lower stretch, tension and stress, respectively, whereas these differences did not reach statistical significance. However, especially the comparison of failure properties between AAA wall and normal AA wall may be hampered by the fact that normal AA wall could often not be appropriately damaged during tensile testing due to insufficient machine specifications. In many cases normal AA wall could actually have undergone even higher stretch, tension and stress, respectively. Analogously, the actual differences in failure properties between AAA wall and normal AA wall might be larger than currently indicated in Table 5.6 and Figure 5.15. This might also explain why e.g. Raghavan *et al.* [165] reached statistical significance for the differences in failure properties between normal AA tissue and AAA tissue, while the present study could not state significance.

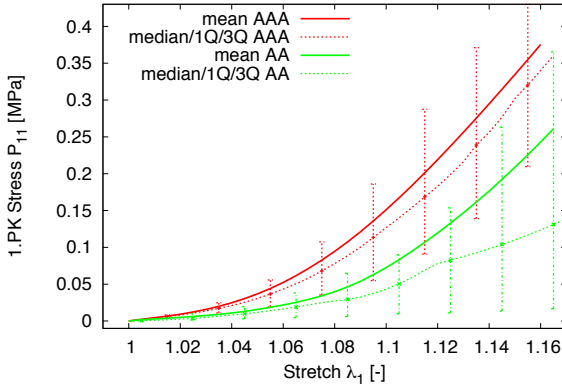


Figure 5.16: Comparison of stress-stretch curves for AAA wall (red) and normal AA wall (green). The solid lines represent the mean stress-stretch response from all experimentally investigated AAA or normal AA specimens, respectively. The dashed J-shape curves indicate the overall measured medians for AAA specimens and normal AA specimens, respectively. The whiskers branching off the medians indicate the first (1Q) and third quartiles (3Q) of stresses at the given stretches.

The correlations of experimentally measured mechanical properties of normal AA specimens with the patient age (Figure 5.13) indicated that there is a significant increase of beta stiffness with increasing age, while at the same time failure stretch and failure tension are reduced in older people. These findings and also the result of increased stiffness of AAA wall specimens (Table 5.6 and Figures 5.15 to 5.16) are in perfect agreement with the above mentioned statements by Ferruzzi *et al.* [47].

Lastly, the investigation could also demonstrate that AAA tissue behaves almost isotropic (Table 5.2 and Figure 5.6), while normal AA wall features marked, but non-significant anisotropy with stiffer behavior, higher strength and failure stretch in circumferential direction, respectively (Table 5.5 and Figure 5.14). The poor P-values related to direction dependencies in normal AA tissue were attributable to the non-Gaussian distributions of the values and also to the even more drastic variation of mechanical properties in normal AA tissue compared to AAA tissue. As a concluding remark, these results validate retrospectively the choice of the isotropic hyperelastic material law for the modeling of AAA wall as presented in Chapter 2.

## 5.5 Multiple Regression

As seen in Section 5.3, there were a multitude of explanatory variables which were significantly correlated to the experimentally measured AAA wall properties. The large number of significant explanatory variables, provided that they are not inter-dependent, implied small  $r$ -values for the individual correlations. The prediction of material properties should therefore not be based on a simple regression model. To account for the concurrent effect of the large number of explanatory variables and to obtain more reliable equations for the prediction of material properties, multiple regression analyses had to be performed. Since best correlations in simple regression were obtained with the local SUV assessed by PET/CT, but knowing that this imaging modality is not routinely applied for AAA patients in clinical practice, two different regression models were created for each mechanical AAA wall property: One model including the SUV and all other explanatory variables, and one model including all explanatory variables except the SUV.

### 5.5.1 Methods

For the development of any multiple regression model it was first necessary to select a subset of potentially significant explanatory variables. Thereby, explanatory variables with  $P < 0.1$  ( $P < 0.05$  for wall thickness) from the associated simple linear regression were considered as potentially significant and were included in the initial data set. Continuous variables were centered with respect to their overall mean. The binary coding for non-continuous explanatory variables remained the same as in Section 5.1.4. Hypercholesterolemia was excluded as explanatory variable due to the small number of affected patients. Further, explanatory variables related to medication were excluded since medication doses and durations were not known. To avoid colinearities between explanatory variables, only one stress measure with the highest significance from simple regression was included in a multiple regression analysis. Since Cauchy stresses are a more common output quantity of FE programs rather than 1.PK stresses, multiple regression models for failure tension and wall strength were created in terms of Cauchy stresses. This also allows for a consistent comparison between acting stresses and strength/tension during post-processing. Multiple regression models for 1.PK failure tension and wall strength were not created. Backward multiple regression analyses were then performed for wall thickness ( $t$ ), alpha stiffness ( $\alpha$ ), beta stiffness ( $\beta$ ), failure tension ( $T_{max,Cauchy}$ ) and wall strength ( $\sigma_{max}$ ), respectively, according to the following scheme:

1. Perform a backward multiple linear regression with the initial data set (remove explanatory variables one to one until there are no more non-significant ones left ( $\alpha = 0.05$ )), in order to get a first set of significant explanatory variables.
2. Limit the data set to the significant explanatory variables from Step 1 and perform an outlier detection for the X-space using the hat matrix (see Section 3.2.2).
3. Perform an outlier detection for the X-Y-space using the Cook's Distance (complemented by the Studentized Residual and the DFFITS) (see Section 3.2.2).
4. Remove outliers, if applicable.

5. Check for suppressors [18, 29] and co-collinearities between the explanatory variables. Remove the explanatory variable from the data set, if applicable.
6. Update the initial data set (remove outliers and negative suppressors) and rerun the multiple linear regression with the updated initial data set.
7. Check for changes in the set of significant explanatory variables. If there are changes go back to Step 2. Otherwise evaluate the final regression model.

## 5.5.2 Results

### Wall Thickness - Including SUV

The data set was limited to the 93 observations from 28 patients for which PET/CT images were available. Further, the initial set of explanatory variables was reduced to the quantities which were significantly correlated to experimentally measured wall thickness. These were the distance to bifurcation, DM, smoking status, CKD, creatinine, erythrocytes, thrombocytes, hemoglobin, sodium, SUV and ILT thickness.

A backward multiple linear regression was performed to get a first guess of the stochastic model (Step 1). The software output using R [162] was:

```
Residuals:
    Min       1Q   Median       3Q      Max
-0.69347 -0.23561 -0.03243  0.20570  0.90748

Coefficients:
            Estimate Std. Error t value Pr(>|t|)
(Intercept)  1.8380792   0.0416383   44.144 < 2e-16 ***
CKD          -0.2924461   0.0905669   -3.229 0.001753 **
Erythrocytes -0.3585281   0.1448159   -2.476 0.015233 *
Thrombocytes  0.0032140   0.0005864    5.481 4.07e-07 ***
Hemoglobin   0.1380433   0.0396489    3.482 0.000782 ***
SUV          1.1743848   0.1348315    8.710 1.76e-13 ***
---
Signif. codes:  0 '***' 0.001 '**' 0.01 '*' 0.05 '.' 0.1 ' ' 1

Residual standard error: 0.3498 on 87 degrees of freedom
Multiple R-squared:  0.6328,    Adjusted R-squared:  0.6117
F-statistic: 29.99 on 5 and 87 DF,  p-value: < 2.2e-16

Centers:
Erythrocytes   Thrombocytes   Hemoglobin      SUV
  4.6569767    204.2258065    14.2666667     0.7674194
```

This will be briefly explained: Starting with the middle section with the heading “Coefficients”, the output lists the significant explanatory variables, in this case the intercept, CKD, erythrocytes, thrombocytes, hemoglobin and the SUV. The fitted coefficients  $\hat{\beta}_i$  for the respective explanatory variable are listed in the second column with the heading “Estimate”. These values

can be explained as the mean influence of the explanatory variables - e.g. if one plots the wall thickness over an explanatory variable, this is the slope of the line in the diagram. The next column "Std. Error" gives the standard error for the fitted coefficients. The last two columns "t value" and "Pr(>|t|)" (P-value) are redundant, since the P-values can be calculated from the t-values and the degrees of freedom. The P-value represents the probability of the true mean influence being 0 (no correlation) or less. The centers at the bottom of the output are the mean values of the explanatory variables included in the stochastic model. The stochastic equation for the prediction of the wall thickness  $t$  based on that output would then read as follows:

$$\begin{aligned}
 t [\text{mm}] = & 1.84 \text{ mm} - 0.292 \cdot CKD [0/1] - 0.359 \frac{\text{mm } \mu\text{l}}{\text{Mio}} \cdot (\text{erythrocytes} - 4.66 \frac{\text{Mio}}{\mu\text{l}}) \quad (5.8) \\
 & + 0.00321 \frac{\text{mm } \mu\text{l}}{1000} \cdot (\text{thrombocytes} - 204 \frac{1000}{\mu\text{l}}) \\
 & + 0.138 \frac{\text{mm dl}}{\text{g}} \cdot (\text{hemoglobin} - 14.3 \frac{\text{g}}{\text{dl}}) + 1.17 \text{ mm} \cdot (\text{SUV} - 0.767)
 \end{aligned}$$

The "residual standard error" is then the expected deviation of the predicted value from the actually measured value. The "Min" residual at the top denotes the minimum residual obtained for Equation (5.8) ( $= \min(r_i) = \min(y_i - \hat{y}_i)$ ), accordingly "Max" for the maximum residual. "1Q" and "3Q" denote the first and third quartiles of the residuals (=the 25th and the 75th-percentiles), respectively. In the following, all this information will accompany the multiple regression models and stochastic equations in form of condensed tables.

In subsequence to this initial guess for the multiple regression model, the data set was limited to the five significant explanatory variables included in Eq. (5.8) and an outlier detection was performed. Using the standard cutoff value  $h_{max} = 2 \frac{p}{n}$  [10, 16] for hat matrix based outlier detection, 18(!) potential outliers were marked. As a logical consequence, the cutoff value was increased to  $h_{max} = 3 \frac{p}{n}$  [175], yielding one outlier in X-space. Without further reference,  $h_{ii} > 3 \frac{p}{n}$  is used for all hat matrix based outlier detections in the subsequent regression models. The DFFITS method for outlier detection in X-Y-space brought about 9 potential outliers, which was also unduly high. The Cook's Distance method with the cutoff value  $CD_{max} = \frac{4}{n}$  pointed out 6 potential outliers. To further reduce the number of potential outliers in X-Y-space the cutoff value for the Cook's Distance method was increased to  $CD_{max} = \frac{5}{n}$ . This is still in agreement with [17] which states  $CD_{max} < 1$  as feasible cutoff values. Using the new cutoff value, the Cook's Distance method pointed out the 3 most influential X-Y-space outliers. These 3 cases were also included in the 9 potential outliers of the DFFITS method. The Y-space outlier detection method based on studentized residuals brought about 6 observations with too large residual for the 95% confidence interval and 4 observations for the 97.5% confidence interval. However, only 2 of the 3 X-Y-space outliers, which were consistently identified by the Cook's Distance and the DFFITS methods, could be detected based on studentized residuals. Since consequently the studentized residual was not capable of reliably identifying the overly influential points and the DFFITS method tended to point out too many potential outliers, mainly the Cook's Distance and the hat matrix results will be used in the following to detect a reasonable number of outliers. Consequently, one X-space outlier and three X-Y-space outliers were removed from the initial data set. On another note, it was noticed that the prediction of wall thickness decreased ( $\hat{\beta}_{\text{erythrocytes}} = -0.359$ , see model above) as the erythrocytes increased. This was counter to the simple regression results, where a clearly positive correlation between

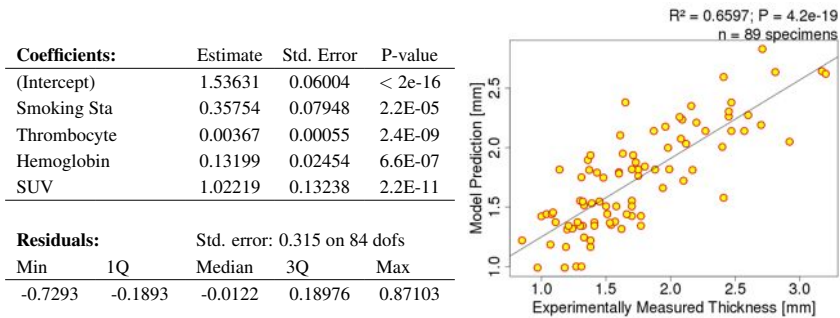


Figure 5.17: Regression model for wall thickness including smoking status, hemoglobin, thrombocytes and the SUV as explanatory variables (Equation (5.9)). Left: Summary of coefficients and residuals. Right: Predicted beta stiffness versus experimentally measured beta stiffness.

erythrocytes and wall thickness was found (see e.g. Figure 5.7 in Section 5.3.1). In this case, the erythrocytes variable acted as a *suppressor* [18, 29]. Performing a multicollinearity analysis, it was found that erythrocytes and hemoglobin were overly correlated ( $r = 0.925$ ). To remove this source of collinearity, the erythrocytes were removed from the data set since it was the less significant variable ( $P_{erythrocytes} = 0.015233$  vs.  $P_{hemoglobin} = 0.000782$ ). The second run of the backward multiple linear regression with the updated data set then brought about a new regression model including smoking Status, thrombocytes, hemoglobin and the SUV as significant explanatory variables. Another check for outliers using the hat matrix and the Cook's Distance revealed no change in the outliers. The final stochastic equation for the prediction of the wall thickness  $t$  including PET/CT data therefore reads:

$$\begin{aligned}
 t \text{ [mm]} = & 1.54 \text{ mm} + 0.358 \text{ mm} \cdot \text{smoking status} [0/1] \\
 & + 0.00367 \frac{\text{mm } \mu\text{l}}{1000} \cdot (\text{thrombocytes} - 204 \frac{1000}{\mu\text{l}}) \\
 & + 0.132 \frac{\text{mm dl}}{\text{g}} \cdot (\text{hemoglobin} - 14.3 \frac{\text{g}}{\text{dl}}) + 1.02 \text{ mm} \cdot (\text{SUV} - 0.767)
 \end{aligned} \tag{5.9}$$

Significant regression coefficients and residual information are also summarized in Figure 5.17. The coefficient of determination between the experimentally measured values and the stochastic model was  $R^2 = 0.6597$ . A diagram in which predicted values according to Eq. (5.9) were compared to experimentally measured wall thickness is printed in Figure 5.17.

### Wall Thickness - Without SUV

In order to create a stochastic wall thickness model that does not require PET/CT data, a second multiple linear regression was performed. This time, the SUV was excluded from the initial set of explanatory variables. All 163 observations were included in the analysis. The initial set of explanatory variables was reduced to the quantities which were significantly correlated to experimentally measured wall thickness. These were distance to bifurcation, DM, smoking

status, CKD, creatinine, erythrocytes, thrombocytes, hemoglobin, sodium, and local thrombus thickness. A first run of the multiple linear regression without previous outlier detection brought about a model that only included DM, CKD and thrombocytes. The outlier detection based on these explanatory variables revealed 4 hat matrix outliers (2 patients). The calculation of the Cook's Distance exposed 9 X-Y-space outliers, whereas one of them had already been detected before using the hat matrix. In total, 12 observations were removed from the data set. The updated and final regression model resulted into a four-parametric regression model, including DM, CKD, thrombocytes and spatially variable ILT thickness:

$$t \text{ [mm]} = 1.63 \text{ mm} + 0.175 \text{ mm} \cdot DM [0/1] - 0.235 \text{ mm} \cdot CKD [0/1] \quad (5.10)$$

$$+ 0.00311 \frac{\text{mm } \mu\text{l}}{1000} \cdot (\text{thrombocytes} - 188 \frac{1000}{\mu\text{l}})$$

$$- 0.00764 \frac{\text{mm}}{\text{mm}} \cdot (\text{ILT thickness} - 9.66 \text{ mm})$$

Regression coefficients for the significant explanatory variables and information on residuals are given in Figure 5.18. The coefficient of determination between experimentally measured thickness and the stochastic model was  $R^2 = 0.4265$ . The diagram showing predicted versus measured wall thickness for the stochastic Eq. (5.10) is given in Figure 5.18.

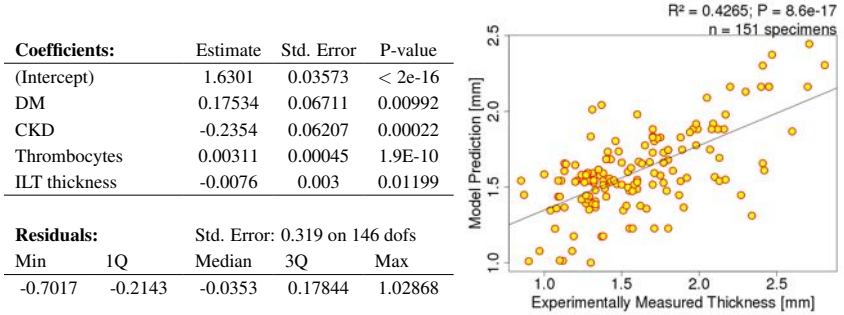


Figure 5.18: Regression model for wall thickness without the SUV. It includes DM, CKD, thrombocytes and ILT thickness (Equation (5.10)).

With the removal of two further outliers pointed out by the studentized residual method for a 95 % confidence interval and lowering the significance level  $\alpha$  to 0.1 (explanatory variables remain in the model for  $P < 0.1$ ), one ends up with a five-parametric regression model. The stochastic equation for the wall thickness prediction with a  $R^2 = 0.4761$  then reads:

$$t \text{ [mm]} = 1.61 \text{ mm} + 0.00171 \frac{\text{mm}}{\text{mm}} \cdot (\text{distance to bifurcation} - 51.7 \text{ mm}) \quad (5.11)$$

$$+ 0.181 \text{ mm} \cdot DM [0/1] - 0.249 \text{ mm} \cdot CKD [0/1]$$

$$+ 0.00289 \frac{\text{mm } \mu\text{l}}{1000} \cdot (\text{thrombocytes} - 188 \frac{1000}{\mu\text{l}})$$

$$- 0.00505 \frac{\text{mm}}{\text{mm}} \cdot (\text{ILT thickness} - 9.66 \text{ mm})$$

The newly included explanatory variable is the distance to the bifurcation. The increase of the  $R^2$  to 0.4761 is thereby also mediated by the removal of the two Y-space outliers using the studentized residuals, and is not only attributable to the additional explanatory variable. A diagram for predicted wall thickness over experimentally measured thickness for the stochastic Equation (5.11) can be found in Figures 5.19.

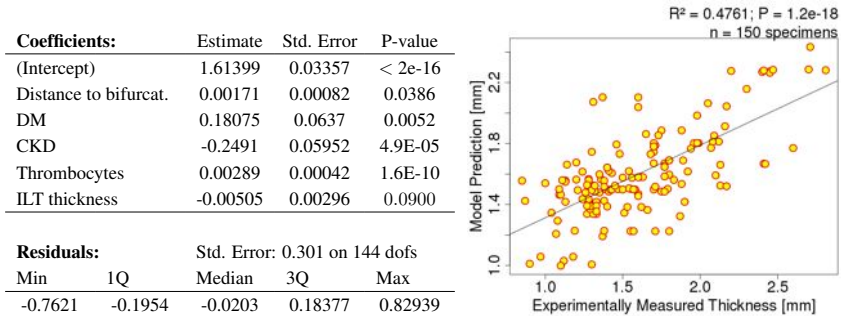


Figure 5.19: Regression model for wall thickness with lowered significance level to enforce a five-parametric model. It additionally includes the distance to the bifurcation (Equation (5.11)).

## Discussion of the Wall Thickness Models

The multiple regression models created in the preceding section show the influence of the most significant individual explanatory variables on wall thickness distribution, with their mutual influence being eliminated. The most reliable wall thickness prediction was obtained when PET/CT imaging of the AAA has been performed (Eq. (5.9),  $R^2 = 0.6597$ ), where the SUV turned out to be the most significant explanatory variable ( $P = 2.2 \cdot 10^{-11}$ ). The stochastic equations can be easily interpreted. Eq. (5.9) states that an increase in the SUV by 1.0 was related to an increase in wall thickness by 1.022 mm. In the current study the SUV at the excision sites ranged from 0.382 to 1.891, which was associated with a change in wall thickness by 1.542 mm. Eq. (5.9) further states that AAA wall was 0.358 mm thicker in smokers, while changes of the laboratory blood parameters over the physiological thrombocyte range ( $140 \frac{1000}{\mu\text{l}}$  to  $360 \frac{1000}{\mu\text{l}}$ , see page 107) and over the physiological hemoglobin range (12.3 g/dl to 17.5 g/dl) were associated with wall thickening by 0.81 mm and 0.686 mm, respectively.

But also without knowledge on the spatial SUV distribution, it was possible to generate stochastic wall thickness models with reasonable predictive capability. Coefficients of determination for the wall thickness models excluding PET data were  $R^2 = 0.4265$  (Eq. (5.10)) and  $R^2 = 0.4761$  (Eq. (5.11)). These models identified DM (AAA wall was thicker by 0.175 mm (Eq. (5.10)) / 0.181 mm (Eq. (5.11)) in DM patients), CKD (thinner by 0.235 mm / 0.249 mm in CKD patients), thrombocytes, ILT thickness (thinner by 0.0505 mm / 0.076 mm per 1 cm ILT) and the distance to the bifurcation (wall thickness increased by 0.171 mm per 10 cm) to be significant. They did not include smoking status and hemoglobin. On the one side, the change in

significant explanatory variables is an undesired result, because of loss of consistency. On the other side, it may be speculated that the SUV does well incorporate the effects of DM and CKD on wall thickness, while it is not capable of accommodating the smoking related wall thickening. The explanatory variable that was included in all models without exception was the thrombocyte count. The suspicion that the increase in wall thickness with the increase in thrombocyte count might be caused by insufficient ILT removal from specimens is disproved by the significant negative correlation between local ILT thickness and measured wall thickness. In general, the obtained models are plausible. For example, a wall thinning behind ILT has already been stated by Kazi *et al.* [110]. Further, smoking and DM is often concomitant with atherosclerosis and related wall thickening [134]. Lastly, also the increase in wall thickness with decreasing distance to the heart (= with increasing distance to the bifurcation) is credible. The benefit of the present work is that these effects can now be precisely quantified.

Interestingly, few specimens were extremely thick (more than 3 mm). This could be partly captured by the model including the PET data, but not at all by the models excluding the PET data. This is a clear advantage of the model including PET data in the explanatory variables. At the same time, this might also explain the increase in number of outliers from Eq. (5.9) (4 outliers) to Eq. (5.11) (14 outliers).

### Alpha Stiffness

The initial data set was limited to the 93 observations from 28 patients for which PET/CT images were available. Further, 14 observations were removed from the data set, because alpha stiffness was not measured in tensile tests. This means both PET information and alpha stiffness measures were only available for 79 cases. The initial set of explanatory variables consisted of calcification, subrenal diameter, thrombocytes, SUV and urea. The explanatory variables from the patients medical history were also included in the initial data set, although in simple regression analyses these quantities reached P-values slightly higher than  $P = 0.10$ . After iterating over Steps 2 to 7 of the multiple regression scheme presented in Section 5.5.1, four hat matrix outliers and 4 Cook's Distance outliers were removed for the final regression model. The stochastic equation for the alpha stiffness prediction ( $R^2 = 0.304$ ,  $P = 6.0 \cdot 10^{-5}$ ) included four explanatory variables (calcification, subrenal diameter, smoking status and urea), but did not contain the SUV. The preceding limitation to observations containing the SUV did not comply with the obtained stochastic model. Consequently, the limitation to observations with SUV information was undone and the complete observations were included for the analysis. In this run, 22 specimens had to be removed from the data set, because of missing measurements of alpha stiffness. Two hat matrix outliers and 7 Cook's Distance outliers were removed from the data set. The obtained stochastic model was:

$$\begin{aligned} \alpha \text{ [MPa]} = & 0.409 \text{ MPa} + 0.115 \text{ MPa} \cdot \text{calcification} [-0.5/0/0.5] \\ & + 0.0296 \frac{\text{MPa}}{\text{mm}} \cdot (\text{subrenal diameter} - 21.16 \text{ mm}) \\ & - 0.0794 \text{ MPa} \cdot \text{smoking status} [0/1] - 0.0932 \text{ MPa} \cdot \text{CHD} [0/1] \end{aligned} \quad (5.12)$$

The coefficient of determination obtained for this model was  $R^2 = 0.2319$ . More detailed information on the model (Eq. (5.12)) and a diagram with predicted alpha stiffness values versus measured alpha stiffness values are shown in Figure 5.20.

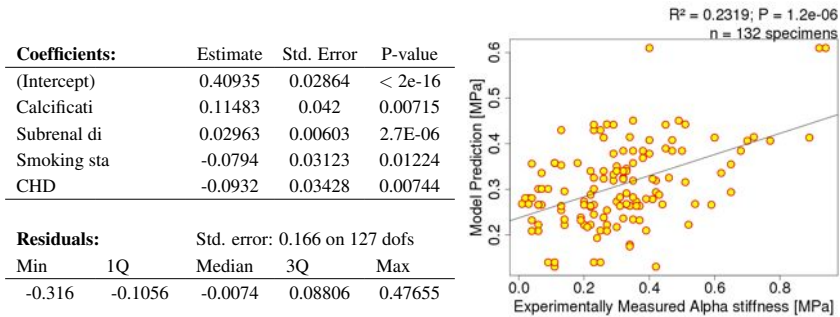


Figure 5.20: Regression model for alpha stiffness according to the stochastic Equation (5.12). It includes calcification, subrenal diameter, smoking status, CHD.

As already mentioned in Section 2.5.2, calcifications might already be considered explicitly in the model as separate AAA constituents. In this case, the regression model to predict the material parameters for AAA wall should not include the explanatory variable calcifications a second time. For this reason, a second multiple regression analysis was performed, excluding the explanatory variable calcification from the initial data set. Four hat matrix outliers and 5 Cook's distance outliers were detected and removed from the data set. The regression model excluding the explanatory variable calcification yielded

$$\alpha \text{ [MPa]} = 0.329 \text{ MPa} + 0.0221 \frac{\text{MPa}}{\text{mm}} \cdot (\text{subrenal diameter} - 21.16 \text{ mm}) - 0.0675 \text{ MPa} \cdot \text{CHD} [0/1] \quad (5.13)$$

Table 5.11: Coefficients and residuals for Eq. (5.13)

<b>Coefficients:</b>			
	Estimate	Std. Error	P-value
(Intercept)	0.32927	0.02064	< 2e-16
Subrenal di	0.02212	0.00622	0.00052
CHD	-0.0675	0.0353	0.058

<b>Residuals:</b>				
Std. error: 0.169 on 129 dofs				
Min	1Q	Median	3Q	Max
-0.3157	-0.1055	-0.0139	0.08096	0.55767

The coefficient of determination resulted in  $R^2 = 0.0898$ . The patient's smoking status turned out to be not significant any more. Residual information and more detailed information on the resulting stochastic equation (Eq. (5.13)) are documented in Table 5.11.

### Beta Stiffness - Including SUV

First, only observations with PET information available were included for the creation of a stochastic model for beta stiffness prediction. The explanatory variables patient sex, testing di-

rection (although  $P > 0.1$  in simple linear regression), calcification, max ILT thickness, subrenal aortic diameter, SUV, local thrombus thickness, first principal stress (since close to  $P = 0.1$ ), CKD, DM, potassium, sodium and urea were considered in the analysis. Thirteen specimens were excluded because of missing beta stiffness measurements (80 remaining observations). After two iterations over Steps 2 to 7 of the scheme presented Section 5.5.1, three hat matrix outliers and 5 Cook's Distance outliers were removed from the data set. The regression analysis yielded a two-parametric model:

$$\beta \text{ [MPa]} = 4.05 \text{ MPa} + 3.67 \text{ MPa} \cdot \text{calcification} [-0.5/0/0.5] - 2.96 \text{ MPa} \cdot (\text{SUV} - 0.765) \quad (5.14)$$

The coefficient of determination was  $R^2 = 0.400$ . Residual information and more detailed information on the significant explanatory variables are summarized in Figure 5.21. Predicted values versus measured values of beta stiffness are plotted in a diagram in Figure 5.21.

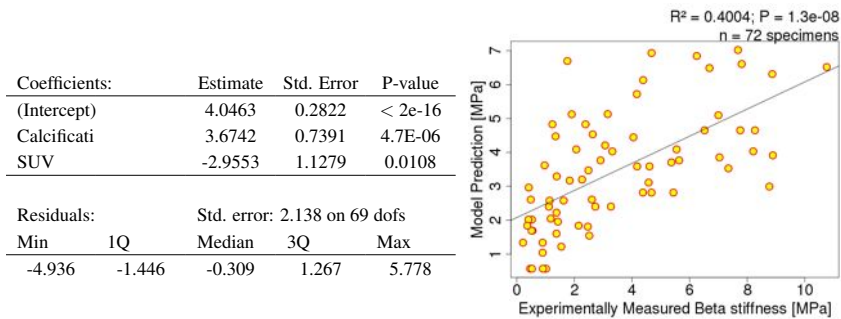


Figure 5.21: Regression model for beta stiffness including calcification and the SUV as explanatory variables (Equation (5.14)).

In the same way as done before for the alpha stiffness, calcification was removed from the initial set of explanatory variables and the regression analysis was repeated. This time, 8 hat matrix outliers and 5 Cook's distance outliers (1 overlap) were excluded from the final model:

$$\beta \text{ [MPa]} = 2.31 \text{ MPa} + 3.67 \text{ MPa} \cdot CKD [0/1] - 0.200 \frac{\text{MPa dl}}{\text{mg}} \cdot (\text{urea} - 21.3 \frac{\text{mg}}{\text{dl}}) - 3.98 \frac{\text{MPa l}}{\text{mmol}} \cdot (\text{potassium} - 4.43 \frac{\text{mmol}}{\text{l}}) - 4.27 \text{ MPa} \cdot (\text{SUV} - 0.765) \quad (5.15)$$

The coefficient of determination was  $R^2 = 0.2854$ . Residuals and coefficient information are summarized in Figure 5.22. A diagram for the model (equations (5.15)) is given in Figure 5.22.

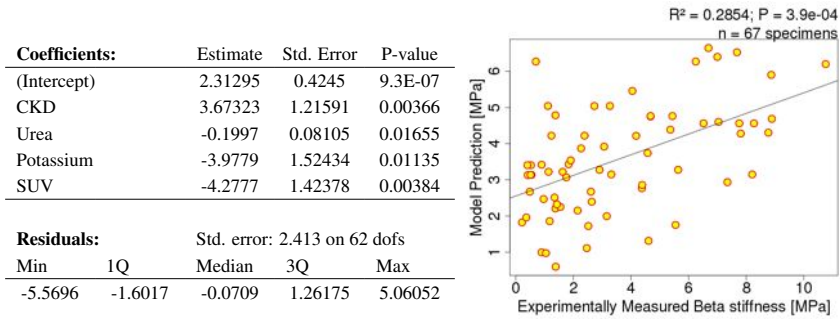


Figure 5.22: Regression model for beta stiffness excluding calcifications. It includes CKD, urea, potassium and the SUV. (Equation (5.15)).

### Beta Stiffness - Without SUV

In order to create models that do not require PET imaging information, the SUV was removed from the initial set of explanatory variables and all specimens were included in the analysis. Since beta stiffness could not be successfully measured for 21 specimens, the initial data set consisted of 142 observations. The regression model was obtained after only one iteration. However, 9 hat matrix outliers and 8 Cook's Distance outliers (2 overlap) had to be removed before. Calcification turned out not to be significant for this final model. The stochastic equation reads

$$\begin{aligned}
 \beta \text{ [MPa]} = & 3.42 \text{ MPa} + 0.208 \frac{\text{MPa}}{\text{mm}} \cdot (\text{subrenal diameter} - 21.2 \text{ mm}) \\
 & - 1.98 \text{ MPa} \cdot DM [0/1] - 0.174 \frac{\text{MPa dl}}{\text{mg}} \cdot (\text{urea} - 22.1 \frac{\text{mg}}{\text{dl}}) \\
 & + 2.96 \text{ MPa} \cdot CKD [0/1] - 2.22 \frac{\text{MPa l}}{\text{mmol}} \cdot (\text{potassium} - 4.49 \frac{\text{mmol}}{\text{l}})
 \end{aligned} \quad (5.16)$$

More detailed information on the significant explanatory variables and residuals are summarized in Figure 5.23. The coefficient of determination for this model was  $R^2 = 0.2061$ . A diagram showing predicted beta stiffness over experimentally measured beta stiffness is given in Figure 5.23.

### Discussion of the Stochastic Models for Alpha and Beta Stiffness

Existent calcifications and the subrenal aortic diameter emerged as dominant factors for the determination of elastic AAA wall properties. In accordance to the presented approach of explicit modeling of calcifications (Section 2.5.2), also stochastic models that excluded calcification from the explanatory variables were created. In doing so, the coefficient of determination for alpha stiffness prediction was reduced from  $R^2 = 0.2319$  (Eq. (5.12)) to  $R^2 = 0.0898$  (Eq. (5.13)).

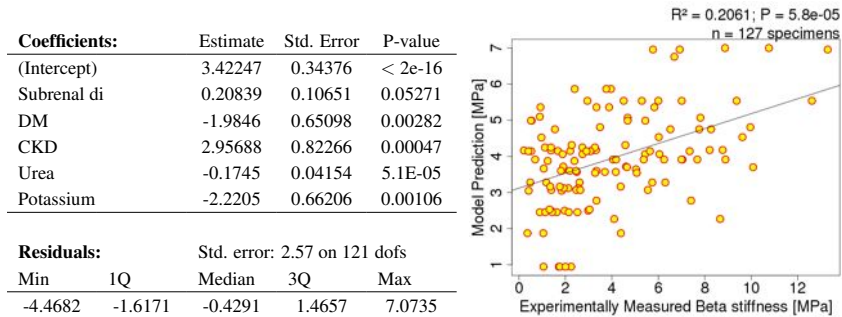


Figure 5.23: Regression model for beta stiffness excluding the SUV. It includes the subrenal diameter, CKD, DM, urea, and potassium (Equation (5.16)).

Firstly, this means that a reliable preoperative prediction of local alpha stiffness is almost impossible, especially if calcifications are excluded from the model. Secondly, it is to note that in the latter case, Eq. (5.13) only yields spatially constant values for the prediction of alpha stiffness. Nevertheless, it could be seen that besides existent calcifications, mainly the subrenal diameter was an indicator for the elastic behavior of the AAA wall specimens. This may be explained by the hypothesis that a large subrenal diameter is an indicator of dilatative angiopathy with stiffening of the aorta in general. The decrease in alpha stiffness for smokers might be mediated by the increased wall thickness as previously stated for this patient group. CHD was a persistent significant explanatory variable for alpha stiffness prediction, while the reason for this relationship remains unanswered. Due to the very low  $R^2$ -values, the use of the stochastic models to estimate the *in vivo* alpha stiffness of AAA wall by means of the investigated non-invasively assessable explanatory variables cannot be recommended.

For the prediction of beta stiffness, already the use of the two explanatory variables SUV and calcification brought about a very useful model (Eq. (5.14),  $R^2 = 0.4004$  - which is of similar quality to the strength model by Vande Geest *et al.* [222] with  $R^2$  ranging from 0.36 to 0.476). When calcification was excluded from the stochastic models, especially CKD, urea and potassium were much in evidence. The observed increase in beta stiffness for patients suffering from CKD thereby is in agreement with carotid-femoral pulse wave velocity measurements, as e.g. performed by Guérin *et al.* [72], revealing increased aortic stiffness in these patients. Although patient sex was detected as a factor leading to lower beta stiffness values in simple regression analyses, it turned out not to be significant in the multiple regression models. However, the gender aspect might be incorporated by the explanatory variables SUV and subrenal diameter: Eq. (5.14) stated a strong negative correlation of the local SUV on beta stiffness, while concurrently a higher average SUV in the AAA wall of female patients has already been discovered in Section 4.3.2. Eq. (5.16) states an increase of beta stiffness with increasing subrenal aortic diameter, while the existence of smaller subrenal aortic diameters in female patients was already demonstrated in [194].

Although the testing direction was deliberately included in the multiple linear regression analyses, it did not have significant influence on either alpha stiffness or beta stiffness in any of the

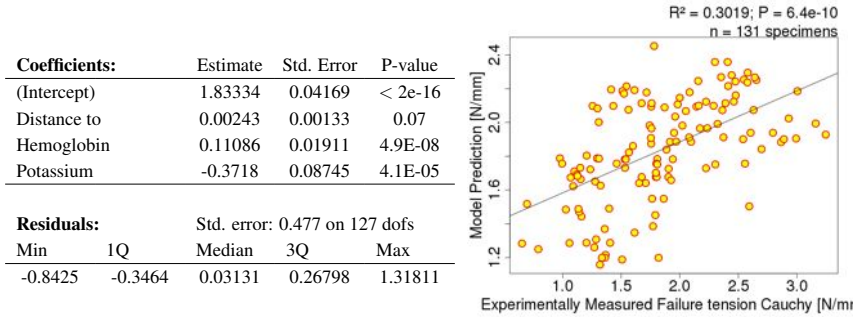


Figure 5.24: Regression model for failure tension with distance to bifurcation, hemoglobin and potassium as explanatory variables (Equation (5.17)).

created models. This deemphasizes the use of anisotropic material models in FE simulations of AAAs.

## Failure Tension

Simple regression analyses could not reveal a correlation between failure tension ( $T_{max,Cauchy}$ ) and the SUV at the sample excision site. It was therefore not necessary to perform a multiple linear regression including the SUV as explanatory variable. Failure tension measurements were available for 143 observations. The initial set of explanatory variables included CKD, subrenal aortic diameter, distance to bifurcation, sum of 1st and 2nd principal stress, hemoglobin, potassium and urea. Iterations over Steps 2 to 7 of the scheme presented in Section 5.5.1, revealed 8 hat matrix outliers and 5 Cook's Distance outliers (1 overlap) which were removed. A three-parametric stochastic equation was obtained:

$$\begin{aligned}
 T_{max,Cauchy} \left[ \frac{\text{N}}{\text{mm}} \right] = & 1.83 \frac{\text{N}}{\text{mm}} + 0.111 \frac{\text{N dl}}{\text{mm g}} \cdot \left( \text{hemoglobin} - 13.6 \frac{\text{g}}{\text{dl}} \right) \\
 & + 0.00243 \frac{\text{N}}{\text{mm}^2} \cdot \left( \text{distance to bifurcation} - 53.9 \text{ mm} \right) \\
 & - 0.372 \frac{\text{N l}}{\text{mm mmol}} \cdot \left( \text{potassium} - 4.47 \frac{\text{mmol}}{\text{l}} \right)
 \end{aligned} \quad (5.17)$$

The correlation coefficient for this model was  $R^2 = 0.3019$ . Some more information on the explanatory variables and on the residuals is documented in Figure 5.24. This figure also includes a diagram showing predicted failure tension over experimentally measured failure tension.

## Discussion of the Stochastic Model for Failure Tension

The model in Eq. (5.17) revealed that there was limited contribution of spatially varying explanatory variables on the failure tension of AAA wall. The only spatially distributed significant explanatory variable was the distance to the bifurcation. Thereby higher failure tension was

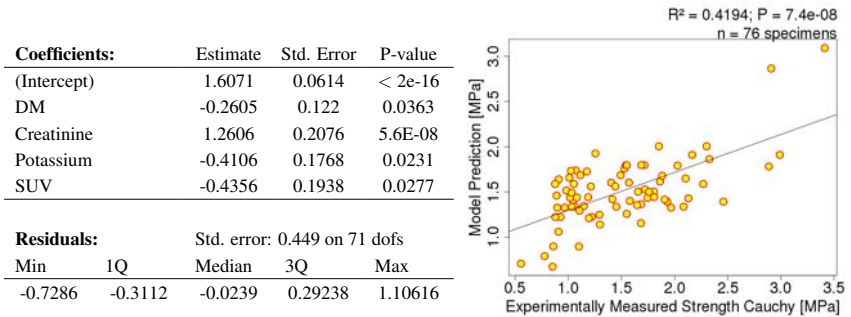


Figure 5.25: Regression model for wall strength including DM, creatinine, potassium and the SUV as explanatory variables (Equation (5.18)).

measured for specimens that were harvested with increasing distance to the bifurcation (= closer to the heart). For example, in a typical AAA with a sac length of 12 cm, the difference in failure tension between a wall portion at the proximal neck and a wall portion close to the bifurcation would be 0.292 N/mm. The final model did not include CKD, although the decrease in failure tension in CKD patients was one of the crucial findings obtained by the simple linear regression analyses. However, a comparable effect might be induced by the negative correlation between predicted failure tension and the potassium value assessed by biochemical blood analysis, since at the same time high potassium values do also indicate kidney malfunction. According to Eq. (5.17), an increase of the potassium values from 3.6 mmol/l to 5.2 mmol/l (=physiological range, page 107) would be related to a decrease in failure tension by 0.595 N/mm. The increase in failure tension with increased hemoglobin levels might be related to the significant thickening of AAA wall, which had previously been associated with high hemoglobin levels (Eq. (5.9)).

### Wall Strength - Including SUV

The SUV was available for 93 specimens, with wall strength measurements for 78 out of them. The initial set of explanatory variables included age, CKD, CHD, DM, calcification, SUV, calcium, creatinine and potassium. During the iterations over Steps 2 to 7 of the scheme presented in Section 5.5.1 one hat matrix outlier and one Cook’s Distance outlier was removed from the data set. The final regression model included four explanatory variables: DM, creatinine, potassium and SUV. No patient was on dialysis therapy and creatinine values considered in this regression analysis ranged from 0.8 mg/dl to 2.3 mg/dl.

The stochastic equation for the prediction of Cauchy wall strength  $\sigma_{max}$  was:

$$\begin{aligned}
 \sigma_{max} [\text{MPa}] = & 1.61 \text{ MPa} - 0.261 \text{ MPa} \cdot \text{DM} [0/1] \\
 & + 1.26 \frac{\text{MPa dl}}{\text{mg}} \cdot (\text{creatinine} - 1.04 \frac{\text{mg}}{\text{dl}}) \\
 & - 0.411 \frac{\text{MPa l}}{\text{mmol}} \cdot (\text{potassium} - 4.39 \frac{\text{mmol}}{\text{l}}) - 0.436 \text{ MPa} \cdot (\text{SUV} - 0.741)
 \end{aligned}
 \tag{5.18}$$

The correlation coefficient for this model was  $R^2 = 0.4194$ . More detailed information on the residuals and explanatory variables is given in Figure 5.25. A diagram showing predicted wall strength over experimentally measured wall strength is given in Figure 5.25.

### Wall Strength - Without SUV

A second multiple regression was performed to create a stochastic model for wall strength prediction that does not require PET data. Accordingly, the SUV was removed from the set of initial explanatory variables and all 143 observations with strength measurements available were included in the regression analysis. During the iterations over Steps 2 and 7 of the scheme presented in Section 5.5.1, four hat matrix outliers and 5 Cook's Distance outliers (2 overlap) were identified and removed from the data set. The final regression model included DM, CKD and potassium as explanatory variables.

$$\begin{aligned} \sigma_{max} [\text{MPa}] = & 1.48 \text{ MPa} - 0.335 \text{ MPa} \cdot \text{DM} [0/1] + 0.403 \frac{\text{MPa dl}}{\text{mg}} \cdot (\text{CKD} [0/1]) \\ & - 0.425 \frac{\text{MPa l}}{\text{mmol}} \cdot (\text{potassium} - 4.47 \frac{\text{mmol}}{\text{l}}) \end{aligned} \quad (5.19)$$

The coefficient of determination for this model was  $R^2 = 0.1876$ . Regression coefficients and residual information, as well as a diagram showing predicted wall strength over experimentally measured wall strength are given in Figure 5.26.

### Discussion of the Stochastic Models for Wall Strength

Simple regression results had already shown that wall strength was negatively correlated to wall thickness ( $r = -0.348$ ,  $P = 2.0 \cdot 10^{-5}$ ). Not surprisingly, wall strength as obtained by multiple regression analyses was negatively correlated to explanatory variables which had previously exhibited positive correlations to wall thickness: These explanatory variables were DM and the SUV. Positive correlations were found between wall strength and the explanatory variables creatinine and CKD, respectively. Both of these explanatory variables had previously been related to significant thinning of the AAA wall. The only explanatory variable from Equations (5.18) and (5.19), which was not correlated to experimentally measured wall thickness in simple regression analyses was potassium as obtained from biochemical blood analysis. Thereby, an increase of potassium over its physiological range (3.6 mmol/l to 5.2 mmol/l) was related to a decrease in wall strength by 0.6570 MPa (Eq. (5.18)) / 0.6797 MPa (Eq. (5.19)). In Eq. (5.18), the only spatial contribution on wall strength was exerted by the SUV assessed by FDG-PET/CT. The coefficient of determination of  $R^2 = 0.4194$  for this model was similar to values which Vande Geest *et al.* obtained for their strength model (0.36 to 0.476, [222]). Equation (5.19) did not feature any spatial contribution. The set of significant explanatory variables obtained in the present models (CKD, creatinine, DM, potassium, SUV) was not even close to the set of significant variables in the stochastic strength model proposed by Vande Geest *et al.* (patient sex, AAA family history, ILT thickness, NORD). Especially in the case when PET/CT images were not available, the prediction of (spatially constant) wall strength was imprecise ( $R^2 = 0.1876$ ). Further, the increase in strength for patients suffering from CKD might be misleading, since failure tension of specimens from this patient group was actually significantly decreased. This

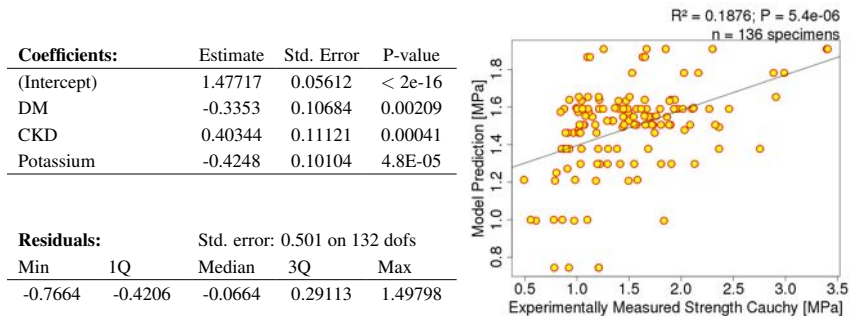


Figure 5.26: Regression model for wall strength excluding SUV as explanatory variable. The model includes DM, CKD and potassium (Equation (5.19)).

formula (Eq. (5.19)) should only be used in combination with wall thickness models that capture the decrease in wall thickness for CKD patients (e.g. Eqs. (5.10) and (5.11)).

### 5.5.3 General Discussion of Multiple Linear Regression Models

Sophisticated FE based rupture risk prediction has to consider patient-specific variations in mechanical properties of AAA wall. Multiple regression models for patient-specific wall thickness distributions have been created in the preceding section. These stochastic models only include the most significant explanatory variables, while potential mutual influence of the sometimes larger number of explanatory variables has been reduced. On the one side, it is to note that a large number of significant explanatory variables have been identified by simple regression which are not included in the final multiple regression models any more. Examples are patient age and sex, laboratory parameters such as erythrocytes and sodium, as well as results from preoperative FE analyses under the assumption of spatially constant material parameters. The advantage of the stochastic models not including any measure from FE results is that the FE analysis does not become implicit. On the other side, a set of explanatory variables was reoccurring in the different stochastic models, emerging as essential parameters for the non-invasive preoperative estimation of mechanical AAA wall properties. This set of explanatory variables includes several quantities from the patient’s medical history such as CKD, DM and the smoking status. The individual patient’s medical history therefore plays a major role in the assessment of AAA rupture risk. Besides these factors, also laboratory parameters obtained by biochemical blood analysis were reoccurring explanatory variables - most of all hemoglobin, thrombocytes, urea and potassium. Since the main task of any vessel is to transport blood, functional relationships between blood component concentrations and mechanical vessel wall properties are plausible. In simple regression analyses, correlations of mechanical AAA wall properties were detected to erythrocytes (red blood cells), which represent up to 49% of the human blood volume [205], and to hemoglobin (the most important functional component of erythrocytes). The latter was also identified to play an important role in multiple linear regression models. Thrombocytes are further cellular components of blood, which were included as variable in the final

regression models for wall thickness determination. Lastly, besides the mentioned main components of blood, also “transported” components were reoccurring explanatory variables: Urea and potassium. Reoccurring geometrical quantities were the subrenal aortic diameter, the local ILT thickness and the distance to the bifurcation. The SUV as a measure of the local metabolic activity in the AAA wall had significant influence on the wall thickness distribution and the wall strength distribution. Increased SUV was thereby associated with increased wall thickness and decreased strength. As a consequence of this interplay, the SUV was not a significant explanatory variable for the determination of failure tension. This fact actually votes in favor of constant wall thickness models in combination with a failure tension model, especially when PET data is not available and accurate prediction of wall thickness and strength is aggravated.

As a general comment to the procedure, it was remarkable that resulting models (even the final explanatory variables in the model) were dependent on the choice of the initial data set. It was experienced that the removal of only one or two outliers could drastically change the regression model. Also the change in the initial set of explanatory variables often implied a different outcome (since explanatory variables, even if they do not turn up in the final model, are considered in the outlier detection). In order to counteract such undesired effects, the protocol as presented in Section 5.5.1 has been developed and applied. Additionally, different scenarios for outlier removal (and different initial sets of explanatory variables) have been investigated in order to detect explanatory variables which were consistently and most often included in the individual stochastic models. Care has been taken that these explanatory variables were included in the final models. Nevertheless, it was not possible to avoid ambiguities in the models. For example, in Eq. (5.9) the smoking status had significant influence on the wall thickness prediction. To create the models described by Eqs. (5.10) and (5.11), the smoking status was removed (besides the SUV and hemoglobin) and DM, CKD, ILT thickness and distance to the bifurcation were added to the models. However, it is unlikely that the patient’s smoking status could be adequately represented by DM, CKD, ILT thickness and distance to the bifurcation. On the other hand, it is implausible that the influence of the smoking status on mechanical AAA wall properties has completely vanished in Eqs. (5.10) and (5.11). Moreover, simple regression analyses revealed a significant increase in wall thickness in patients with positive smoking status, while failure tension and wall strength remained unaffected. If Eq. (5.9) is used to model the spatial wall thickness distribution, one ends up with an increase in wall thickness for smokers. None of the strength models, however, incorporates a decrease in wall strength for this patient group, which in sum leads to an increase in failure tension. This outcome is in contrast to the results obtained by simple regression. This issue should be addressed in future work.

Lastly, it would have been desirable to have less influence of laboratory parameters from biochemical blood analysis in the final models. Laboratory parameters are susceptible to daily changes, which is unlikely to happen for the mechanical AAA wall properties. More influence of local AAA geometry, as a more persistent measure, would have contributed to a more robust modeling of mechanical AAA wall properties.

## 5.6 Conclusion

Advanced approaches in rupture risk prediction should consider patient-specific variations in AAA wall thickness, elastic properties and failure properties. Large variations in these quantities

are stated in literature, but models to capture them are still lacking. In consequence, thickness, elastic properties and failure properties of AAA wall were measured in the current study and results were described in unprecedented detail. Thereby it is only a side note that AAA wall is thicker, stiffer, less anisotropic, less distensible and less strong than wall from healthy abdominal aorta. The benefit of the current study is that experimental testing results were correlated to non-invasively assessable explanatory variables to detect reasons for the variation of mechanical properties and to find easily assessable quantities that can be used to preoperatively predict AAA wall properties in the future. Simple regression models and multiple linear regression models have been created to allow for such preoperative estimations of thickness, elastic properties and failure properties of AAA wall.

One of the crucial findings of the current study was that AAA wall failure tension was significantly decreased for patients suffering from CKD. Similar tendencies were obtained for increased blood-values of creatinine, potassium and urea, all of which are related to kidney malfunction. According to these findings, AAAs in patients with CKD or kidney malfunction are more likely to rupture than AAAs of same size in patients with other medical history. This relation between CKD and decreased failure tension has so far not been considered in literature. It is suggested to include CKD in future investigations on baseline risk factors associated with AAA rupture. Moreover, rupture risk prediction based on the diameter criterion should include patient-specific variations in AAA wall failure tension. In this context, it is straightforward to take into account the decrease in failure tension for patients suffering from CKD.

Besides CKD and the other parameters from the patient's medical history, especially the local metabolic activity measured by FDG-PET/CT and quantified using the SUV provides valuable information on the distribution of mechanical properties. During multiple linear regression analysis, the SUV was included as a significant explanatory variable in all models, except for the prediction of alpha stiffness and failure tension, respectively. Since FDG-PET/CT imaging is not the clinical standard procedure for AAA patients, also multiple regression models without the use of PET data have been created for all mechanical quantities.

FE based rupture risk prediction should include patient-specific variations in mechanical AAA wall properties. In the next chapter it will be investigated whether the use of both wall thickness and wall strength models is superior to the model assumption of uniform wall thickness in combination with a failure tension model only. In any case, histological investigations are needed to give reasons for the described changes in mechanical properties. The results thereof will be dealt within subsequent works by Reeps *et al.* [172] and Grabher-Meier *et al.* [69].

# 6 Incorporating Testing Results into FE Analysis of Patient-Specific AAAs

Approaches to model patient-specific variations in mechanical AAA wall properties have so far been barely reported in literature [222]. Multiple regression models for the different mechanical properties were therefore created in the previous chapter to remedy this issue. In the current chapter, some of these models are tested for their predictive capabilities. One way to perform such a test is to apply these models to FE simulations of AAAs and to check whether their application yields better distinctions between non-ruptured and ruptured AAAs as e.g. obtained by the diameter criterion or by the FE simulations under the assumption of uniform mechanical properties [48, 62, 133, 211, 218]. In the current chapter, stochastic models for wall thickness, failure tension and strength prediction have been implemented, respectively, and applied in simulation of 100 AAAs (20 ruptured AAAs and 80 electively repaired AAAs). Maximum wall stresses and rupture risk indices (defined as stress divided by the appropriate failure measure) are calculated with respect to 4 different modeling variants for each AAA. The predictive capabilities of the mechanics based indices are evaluated by mutual comparison. Differences to the maximum diameter criterion are elaborated upon. The decision for the best method to identify rupture-prone AAAs is based on how reliable the different modeling variants distinguish between non-ruptured and ruptured AAAs.

## 6.1 Methods

### 6.1.1 Study Population

Data sets of 100 AAA patients (82 male, 18 female) who had underwent elective or emergency resection of their infrarenal AAA at the hospital Rechts der Isar, Technische Universität München, Munich, Germany, were analyzed retrospectively. 20 patients had a ruptured AAA, 80 patients had an asymptomatic or symptomatic, non-ruptured AAA. At time of imaging, maximum AAA diameter ranged from 33 to 97 mm with an average of  $60.6 \pm 14.8$  mm (median: 56.25 mm). Patient age ranged from 48 to 93 years and had a mean of  $70.4 \pm 9.0$  years (median: 70 years). More detailed patient characteristics are given in Table 6.1. CT images were available for 96 patients. MR images were provided for 4 patients. No patient from the group of patients with ruptured AAA underwent PET imaging.

Table 6.1: Patient characteristics for AAA patients included in the study (symptomatic AAAs were categorized as non-ruptured AAAs):

	Total	Non-rupt.	Ruptured
n	100	80	20
Male/female	82/18	67/13	15/5
Max AAA $\phi$ [mm]	60.60 $\pm$ 14.81	57.47 $\pm$ 13.45	73.10 $\pm$ 13.64
Age [years]	70.4 $\pm$ 9.0	68.4 $\pm$ 7.5	78.1 $\pm$ 10.4
CKD	28 (3 unkn)	20 (1 unkn.)	8 (2 unkn.)
DM	21 (6 unkn.)	17 (1 unkn.)	4 (5 unkn.)
CHD	33 (7 unkn.)	29 (1 unkn.)	4 (6 unkn.)
Creatinine [mg/dl]	1.20 $\pm$ 0.84	1.19 $\pm$ 0.90	1.24 $\pm$ 0.49
Erythrocytes [Mio/ $\mu$ l]	4.37 $\pm$ 0.71	4.58 $\pm$ 0.54	3.49 $\pm$ 0.68
Hemoglobin [g/dl]	13.49 $\pm$ 2.32	14.15 $\pm$ 1.71	10.6 $\pm$ 2.46
Potassium [mmol/l]	4.51 $\pm$ 0.51	4.54 $\pm$ 0.53	4.42 $\pm$ 0.42
Thrombocytes [100/ $\mu$ l]	206 $\pm$ 69	207 $\pm$ 56	201 $\pm$ 110
Urea [mg/dl]	21.9 $\pm$ 9.5	20.7 $\pm$ 9.6	26.8 $\pm$ 7.5

### 6.1.2 AAA Geometry Reconstruction, Model Variations and FE Analysis

AAA geometries and FE meshes of lumen and thrombus were created as described in Chapter 2. In order to be able to rate the influence of patient-specific wall thickness on AAA rupture risk prediction, two FE models with different assumptions on wall thickness were created for each AAA: One model with spatially constant wall thickness  $t = 1.57$  mm (median thickness measured for the 163 specimens in Section 5.2) and one model with patient-specific, spatially variable wall thickness according to Eq. (5.11). It was not possible to apply Eq. (5.9) for the wall thickness prediction in this current study, since PET imaging was not available for any patient with ruptured AAA. The hyperelastic AAA wall was modeled using the SEF proposed in Eq. (2.64), however, the isochoric contribution was modified to

$$W_{wall,iso} = \frac{\alpha}{6} (\bar{I}_1 - 3) + \beta (\bar{I}_1 - 3)^2, \quad (6.1)$$

such that it was in concordance with the SEF used for the fitting of the material parameters in Section 5.1. For all patients, the material parameters in Eq. (6.1) were consistently set to the median values ( $\alpha = 0.314$  MPa,  $\beta = 3.12$  MPa) from Section 5.2. Each FE model was simulated twice - once considering the effect of calcification on wall stress results and once neglecting calcification in the simulation. A rupture risk index (RRI) distribution was calculated for each AAA. For models with spatially constant wall thickness, the RRI was calculated as the quotient of von Mises stress divided by failure tension, where Equation (5.17) was used to predict failure tension. For models with patient-specific, spatially variable wall thickness, the RRI was calculated as the quotient of von Mises stress divided by wall strength. In this case, Equation (5.19) was used to predict wall strength.

The four different model assumptions (Methods 1 to 4) for each AAA are briefly summarized:

**Method 1** The model was created as described in Sections 2.2 and 2.3. In contrast to the workflow described therein, a spatially constant wall thickness of  $t = 1.57$  mm (median thickness measured for the 163 specimens in Section 5.2) was consistently used for all AAAs. Calcifications were neglected in the simulation. A spatial distribution of the RRI was calculated by

$$RRI(\mathbf{x}) = \frac{\sigma_{von\ Mises}(\mathbf{x})}{T_{max,Cauchy}(\mathbf{x})}, \quad (6.2)$$

where patient-specific failure tension  $T_{max,Cauchy}(\mathbf{x})$  was calculated according to Eq (5.17).

**Method 2** The model was processed similarly to Method 1, with the only difference that calcifications were considered in the simulations according to Eqs. (2.51) through (2.55). Lower and upper thresholds for the consideration of calcification in Eq. (2.54) were set to  $HU_{min} = 300$  and  $HU_{max} = 600$ .  $\alpha_{HU,max}$  was set to 8.929 MPa. The AAA models of the 4 patients who underwent MR imaging were not considered for this method.

**Method 3** The model was created under consideration of a spatially variable distribution of patient-specific wall thickness according to Eq. (5.11). Calcifications were neglected in the simulation. The RRI for Method 3 was calculated as the quotient of local wall stress divided by local wall strength:

$$RRI(\mathbf{x}) = \frac{\sigma_{von\ Mises}(\mathbf{x})}{\sigma_{max}(\mathbf{x})}, \quad (6.3)$$

where the patient-specific (but spatially constant) wall strength  $\sigma_{max}(\mathbf{x})$  was modeled according to Eq. (5.19).

**Method 4** The model was processed similarly to Method 3, but with the difference that calcifications were included in the simulations according to Eqs. (2.51) through (2.55). The AAA models of the 4 patients who underwent MR imaging were not considered for this method.

A total of 392 nonlinear FE simulations were performed under application of appropriate boundary conditions and under consideration of the prestressed state of the AAA models as described in Section 2.6. All simulations were performed using the FE solver BACI [229].

### 6.1.3 Statistical Evaluation

Only aneurysmatic aortic segments in between the renal artery bifurcation and the aortic bifurcation were considered for evaluation. Maximum von Mises wall stress and maximum RRI were assessed as the 99th-percentiles of the respective values within these segments [197]. Wilcoxon rank sum tests were performed to test for statistically significant differences in these maximum values between non-ruptured and ruptured AAAs. Mean $\pm$ sd were calculated for all combinations of quantities and patient groups with respect to the 4 methods described. Relative differences  $\delta$  in maximum diameter, maximum wall stress and maximum RRI between the groups of non-ruptured and ruptured AAAs were calculated with respect to the non-ruptured group. In

Table 6.2: Maximum diameter, maximum von Mises wall stress and maximum RRI for the groups of non-ruptured and ruptured AAAs as obtained for Methods 1 through 4. Colors are related to the diagrams in Figure 6.1:

	Method 1				Method 3			
	ele./symp.	rpt.	$\delta(\%)$	P	ele./symp.	rpt.	$\delta(\%)$	P
Max $\phi$ [mm]	57.5±13.4	73.1±13.6	27.2	3E-5	57.5±13.4	73.1±13.6	27.2	3E-5
Max stress [kPa]	241±68	319±90	32.1	2E-4	230±69	317±93	37.7	2E-4
Max RRI [-]	0.132±.042	0.216±0.08	63.7	2E-6	0.160±.068	0.202±.069	25.9	0.003
	Method 2				Method 4			
	ele./symp.	rpt.	$\delta(\%)$	P	ele./symp.	rpt.	$\delta(\%)$	P
Max $\phi^*$ [mm]	57.3±13.2	73.1±13.6	27.5	2E-5	57.3±13.2	73.1±13.64	27.5	2E-5
Max stress* [kPa]	242±68	317±90	31.1	2E-4	229±69	316±94	38.0	3E-4
Max RRI* [-]	0.131±.041	0.214±.084	63.8	2E-6	0.159±.068	0.201±.069	26.2	0.003

\* (without 4 MRI patients)

box and whisker plots, boxes were drawn from the 25th to the 75th-percentiles, with a line at the median. Whiskers were drawn from the box to the highest and lowest values that were within  $1.5 \times$  the interquartile range. Values more extreme than this were plotted individually.

## 6.2 Results

The maximum AAA diameter of non-ruptured and ruptured AAAs differed significantly ( $P = 3E - 5$ ). It was larger in ruptured AAAs by  $\delta = 27.2\%$  in average. Maximum wall stress in ruptured AAAs was  $32.1\%$  ( $P = 2E - 4$ ) (Method 1) and  $31.1\%$  ( $P = 2E - 4$ ) (Method 2) higher than in electively repaired or symptomatic AAAs. Under consideration of patient-specific wall thickness distributions, the difference in maximum wall stress between the non-ruptured and the ruptured group increased to  $37.7\%$  ( $P = 2E - 4$ ) (Method 3) and  $38.0\%$  ( $P = 2E - 4$ ) (Method 4), respectively. The relative difference in the maximum RRI was  $63.7\%$  ( $P = 2E - 6$ ) (Method 1) and  $63.8\%$  ( $P = 2E - 6$ ) (Method 2). The maximum RRI in Method 3 ( $\delta = 25.9\%$ ,  $P = 0.003$ ) and Method 4 ( $\delta = 26.2\%$ ,  $P = 0.003$ ) failed to provide a better distinction between non-ruptured and ruptured AAAs than the maximum diameter criterion. More detailed results are summarized in Table 6.2. Box and whisker plots for the different quantities and methods are given in Figure 6.1.

## 6.3 Discussion

### 6.3.1 Interpretation of the Results

Models for patient-specific wall thickness, failure tension and wall strength distributions were implemented and tested in FE simulations of 100 AAAs. The rupture risk index RRI was proposed as the quotient of locally acting wall stress divided by local failure tension (for constant

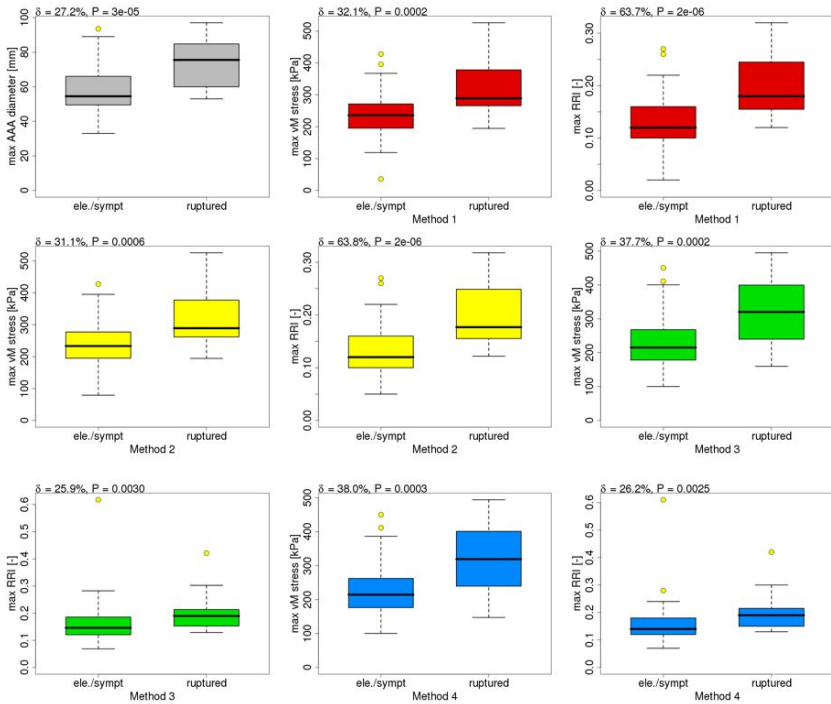


Figure 6.1: Maximum AAA diameter (gray), maximum von Mises wall stress and maximum RRI for non-ruptured and ruptured AAA patients according to Methods 1 (red), 2 (yellow), 3 (green) and 4 (blue), respectively.

wall thickness models) or as the quotient of locally acting wall strength divided by patient-specific wall strength (for models with spatially variable wall thickness). Maximum diameter, maximum wall stress and maximum RRI were evaluated for each AAA with respect to 4 different modeling methods. The best distinction between the 80 electively repaired/symptomatic AAAs and the 20 ruptured AAAs was thereby obtained for the RRI, under the assumption of constant wall thickness in combination with the failure tension model (Eq. (6.2), Methods 1 and 2). Results were thereby almost independent of the neglect (Method 1,  $\delta = 63.7\%$ ,  $P = 2E-6$ ) or consideration of calcifications (Method 2,  $\delta = 63.8\%$ ,  $P = 2E-6$ ) (Table 6.2). Although calcifications were previously shown to alter the stress distribution within one AAA markedly (Chapter 2), there were no implications that the consideration of calcifications actually leads to a more distinct differentiation between non-ruptured and ruptured AAAs within the investigated patient population. Interestingly, the maximum RRI according to Methods 1 and 2 did not yield

any outliers with too low maximum RRI in the group of ruptured AAAs. In contrast, the outliers with too high RRI in the group of non-ruptured AAAs are tolerable, since these might actually indicate rupture-prone or symptomatic AAAs, which were electively treated just in time prior to a potential incident.

When patient-specific wall thickness was applied (Methods 3 and 4), the maximum wall stress criterion featured slightly better predictive capabilities ( $\delta = 37.7\%$  to  $38.0\%$  than the maximum diameter criterion ( $\delta = 27.2\%$  to  $27.5\%$ ). The RRI with respect to the wall strength model (Eq. (6.3), Methods 3 and 4) failed to outnumber rupture risk prediction by the maximum diameter criterion. The outcome for the RRI in Methods 3 and 4 was probably attributable to the increase in the strength prediction with patients suffering from CKD (Eq. (5.19)), which led to a decrease in the RRI for these patients. This tendency, however, is contrary to the results from Section 5.3.1 that clearly indicted a higher risk of rupture for this patient group. Moreover, the situation might further be aggravated by the disproportionately high number of CKD patients within the group of patients with ruptured AAA (Table 6.1). In contrast, in the model for wall thickness prediction (Eq. (5.11)) CKD had a negative contribution on the prediction, promoting AAA rupture.

### 6.3.2 Limitations

One limitation in this study was that PET images were not available for any of the patients with ruptured AAA. This prevented the application of the most sophisticated wall thickness and wall strength models (Eqs. (5.9) and (5.18)) that require the local SUV as an input variable.

Further, patient-specific variations of material parameters for the hyperelastic material model in Eq. (6.1) were not considered in this evaluation. Although, earlier observations by Raghavan & Vorp revealed only a minor influence of variations in material parameters on wall stress [164], a comprehensive investigation on this topic should be conducted based on the data and stochastic models from the current work (Eqs. (5.12) to (5.16)).

The failure tension model in Eq. (5.17), which was used for the calculation of the RRI in the FE models with constant wall thickness (Eq. (6.2)), was dependent on the hemoglobin levels from laboratory blood analyses. Thereby, the prediction of failure tension decreased for lower hemoglobin levels. Especially for the group of patients with ruptured AAA, where blood sampling was often performed after AAA rupture but prior to surgery, the hemoglobin levels might already have been reduced in consequence to internal bleeding. Where possible, laboratory blood test results from dates prior to rupture were preferably applied in the current investigation. Such data, however, was not consistently available for all patients from the group of patients with ruptured AAA, which might have distorted the results for the RRI in Methods 1 and 2. The creation of a multiple regression model that excludes hemoglobin from the set of explanatory variables is a necessary future step.

Under the assumption that rupture occurs at  $RRI = 1$ , the average maximum RRIs of about 0.215 for the patients with ruptured AAAs were comparably low. Firstly, this might be attributed to the fact that a luminal pressure of  $p = 121$  mmHg was consistently applied to all patients. Especially in case of physical exertion, the actual blood pressure might be higher, whereupon the wall stresses and RRIs would increase. The blood pressure of the individual patient at the time AAA rupture, however, was unknown. Secondly, it was remarkable that the ILT-free AAAs featured disproportionately high wall stresses and RRIs. There was one ILT-free AAA within

the group of ruptured AAAs. Interestingly, this AAA featured the highest maximum RRI and the second highest maximum wall stress within its group throughout the 4 different methods. This might indicate a too dominant cushioning effect of the ILT in the FE simulations. This hypothesis is actually supported by the findings in [185], where no pressure reduction on the AAA wall could be observed despite the presence of ILT. From this perspective, a reconsideration of the modeling assumptions for ILT seems necessary.

## 6.4 Conclusion

The rupture risk index as calculated from FE simulations with constant wall thickness and the stochastic failure tension model proposed in Eq. (5.17) has great potential to improve AAA rupture risk prediction. Also the evaluation of maximum wall stresses obtained from FE simulations incorporating patient-specific wall thickness distributions seems to be a feasible approach. No improvement in rupture risk prediction was seen for the application of the stochastic wall strength model. The disproportionately high number of CKD patients within the group of patients with ruptured AAA is a further evidence that CKD should be considered as risk factor for AAA rupture in the future.



## 7 Conclusion and Outlook

In the presented work, a workflow was implemented that enabled sophisticated FE simulations of AAAs. The individual steps which were necessary to perform such FE simulations were automated as far as possible, whilst only minimally affecting the patient-specific characteristics. During the course of the presented work, a continuously growing AAA data base was created, which by the end of the work already contained more than 100 patients. The data base was set up in such a way that all the FE models could be continuously adapted to every step of progress in terms of modeling assumptions and techniques. Need for methodical improvement is seen with regards to auto-segmentation methods and automatization of meshing procedures.

Furthermore, mechanobiological interactions between mechanical quantities acting in the AAA wall as assessed by FE simulations and biological tissue response as measured by FDG-PET/CT imaging were investigated in detail. It can be stated that unphysiologically high wall stress is one possible trigger for increased mural FDG-metabolism, amongst other possible causes, which were discussed in detail. Although the results from this study demonstrated the role of mechanical stresses in mechanotransduction processes in the AAA wall, the following investigations will be beneficial for a more complete understanding of these processes: First of all, the FDG-uptake in the AAA wall should be quantitatively compared to the FDG-uptake in healthy AA wall. This would clarify whether the FDG-metabolic activity in the AAA wall is actually relatively higher or lower for healthy AA. Another maybe even more important investigation would be the assessment of the FDG-metabolism over time as the aneurysm grows. Such an investigation would be able to shed light on whether FDG-metabolism is related to rapid expansion or rather to negative growth, as it was discussed in the literature.

The experimental study performed for the presented work allowed for an adequate investigation of the influence of FDG-metabolism on the mechanical properties of AAA wall. Increased metabolism at specimen excision site was shown to correlate with the AAA wall thickness. However, since wall thickness and increased FDG-metabolism were at the same time negatively correlated to wall strength, it was not possible to conclude whether increased FDG-metabolism promotes or counteracts AAA rupture. Consequently, an useful quantity that was introduced for the evaluation of experimentally measured failure properties was the failure tension. It is an alternative to the separate estimations of both wall thickness and strength. The potential of the failure tension as a measure to improve AAA rupture risk stratification was observed, since it was not possible to derive actual patient-specific wall thickness distributions using standard imaging technologies. Thereby, one of the key findings of the presented experimental study was that failure tension was significantly decreased in patients suffering from CKD. Furthermore, it was observed that failure tension was decreased in patients with increased blood levels of creatinine, potassium and urea - all of which are associated with kidney malfunction. These findings can be easily conveyed into clinical practice and used in combination with the maximum diameter criterion, since it simply implies a higher AAA rupture risk for patient with CKD at a comparably smaller AAA diameter. The open question is what histopathological changes

in the AAA wall are associated with CKD. Fortunately, small wall portions were cut from each experimentally investigated specimen and adequately stored for later histological evaluation. Efforts in this direction, which are currently in progress, are seen as an important step to obtain a comprehensive conclusion on this issue. A larger clinical study should follow to investigate rupture risk of AAAs in patient groups with and without CKD.

The patient-specific variations in mechanical AAA wall properties, which were identified as the bottleneck for the improvement of AAA risk stratification, could be partly captured using multiple regression models. Especially the elaborated stochastic models for preoperative prediction of wall thickness and failure tension were shown to bear potential for a more reliable risk prediction. Based on the stochastic model for failure tension, the proposed risk index differed by more than 63 % between groups of ruptured and electively treated AAAs. Nevertheless, the stochastic models were also hampered by the inclusion of explanatory parameters, such as hemoglobin values from laboratory blood tests, which are susceptible to changes brought on by AAA rupture. This prevents a proper validation of the models based on comparison of risk indices between patients with non-ruptured AAA and ruptured AAA. A reconsideration of the multiple regression modeling is recommended, which should also take nonlinear contributions of explanatory variables into account.

It was observed throughout the performed simulations that ILT exerted a major cushioning effect on the AAA wall. Considering that ILT is deposited under physiologic luminal pressure and existent prestress in the AAA wall, it is likely that the assumption of existent prestress in ILT at the time of CT imaging does not actually meet reality. It is conceivable that the MULF prestressing can be modified such that a stress-free ILT deposition under physiological loading conditions can be modeled, while the prestress in the AAA wall is maintained. Alternatively, the modeling of ILT as a poro-elastic material seems to be in accordance to *in vivo* pressure measurements reported in literature. Moreover, *in vivo* measurements on the pressure transmission in ILT seem to be one of the rare methods to actually validate simulation results. Nevertheless, as soon as the actual physiological behavior of ILT can be sufficiently resolved and mimicked by the FE models, simulations on all models within the created AAA data base can simply be repeated in the presented semi-automatic processes after incorporating the more sophisticated modeling assumptions.

Some additional investigations that would be interesting, but outside the scope of the presented work, include the consideration of axial prestretch in the AAA or the modeling of potentially existent residual stresses within the AAA wall. Also the identification of *in vivo* material parameters based on motion MRI, registration of physiological deformations and inverse FE analysis can be seen as methods for both further improvement of FE models or the validation of current modeling techniques.

Finally, a continued expansion of the AAA data base is recommended. Especially data on small ruptured AAAs, of which only very little data are available, would contribute to make the data base even more diagnostically conclusive. On the other hand, the current AAA data base is probably one of the most detailed collection of patient-specific AAA data world-wide, combining standard clinical data from patient charts and CT imaging with computational FE modeling, PET imaging data, results from experimental mechanical tests and histology. In the future, this focus needs to be maintained, in order to keep providing a fundamental structure for top-level research.

# A Appendix: Segmentation

The large database of AAAs that is investigated in the present work requires methods that ensure consistent and high model quality and that allow for the automatization of preprocessing, solution and postprocessing. Firstly, this necessitates the organization of the AAA data in a well defined file structure. The description of the file structure of the data base is therefore the first point in this chapter. As a second point, an elaborated segmentation protocol for consistent AAA segmentation and 3D geometry reconstruction from medical imaging data is presented. The last section covers the meshing protocol.

In this chapter, *text in italics* refers to software functions. Typewriter font refers to the file structure of the AAA data base.

## A.1 Structure of the AAA Data Base

The file structure is briefly depicted in Figure A.1. The patient case is saved in a folder according to the patient type (e.g. `prospektiv/` (patients with sample donation), `rupturiert/` (patients with ruptured AAA), ...), whereas the patient folder itself is named after the patient (e.g. “fall01/”). In the patient folder, there are an input (`i/`) and an output folder (`o/`), respectively. The input folder contains the anonymized CT images used for segmentation, the segmentation files and files that are created during and FE model generation. If PET/CT imaging has been performed for that patient, the unfused, attenuation-corrected PET images are saved in the input folder. All simulation results are saved in the output folder.

## A.2 Segmentation Protocol

Since all AAAs within the present work have been segmented and reconstructed using the commercial software Mimics (Materialise, Leuven, Belgium), Mimics-specific parameters and peculiarities, which have been omitted in the main part (Section 2.2) for the purpose of conciseness, are elucidated here. Nevertheless, the protocol is not restricted to application in Mimics, but can likewise be conveyed to other image segmentation software.

### A.2.1 Image Import

Transversal planes must be chosen as the principal working planes (consistent orientation of the model in the xyz-space with all other FE models, best segmentation results). Ideally, sequences with a slice distance of  $\leq 3$  mm and pixel sizes  $< 1$  mm are chosen for segmentation. Slice distance and pixel size can be assessed from the DICOM meta data of the image sequence.

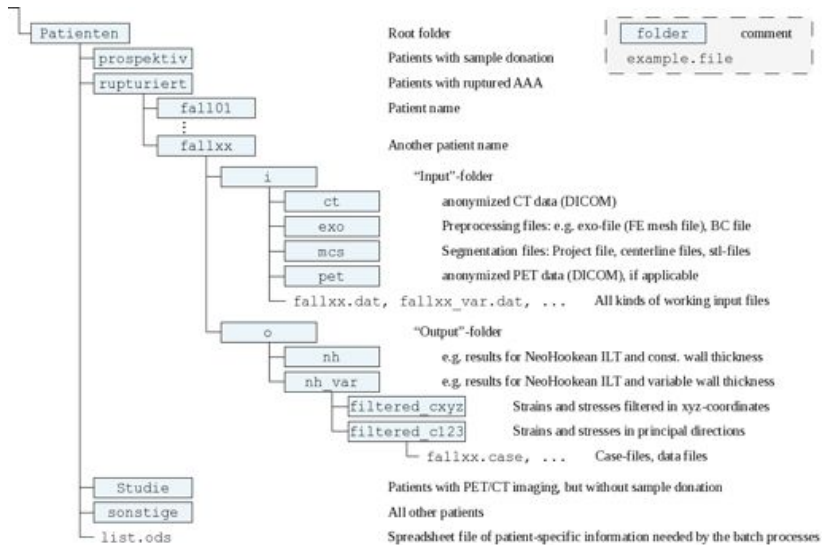


Figure A.1: File structure of the AAA data base.

## A.2.2 Lumen

The lumen can be quickly and reliably segmented using standard software functions. The workflow is outlined by the following steps:

1. *Threshold* the blood lumen (selects all voxels within a certain HU range and groups them in one mask). The correct choice of the upper and lower bounds for thresholding is thereby dependent on the amount of contrast agent in the blood lumen. A rule of thumb is to set the lower bound as high as possible but such that all pixels inside the lumen are selected, and the upper bound such that only single pixels are noticeably missing.
2. *Crop Mask* (Cut the mask proximal to the celiac artery bifurcation and close to the common iliac arteries bifurcations).
3. *Morphology Operations*  $\rightarrow$  *Erode* (1 Pixel) (shrinks the mask by 1 pixel (8-connectivity in transversal planes)).
4. Cut off the renal arteries and the inferior mesenteric artery (using *Edit Masks*).
5. Perform a *Region Grow* (selects only regions of the active mask which are still connected to the lumen).
6. Manual repair (using *Edit Masks*) (only remove spikes or islands - typically around calcifications, see Figure A.2).

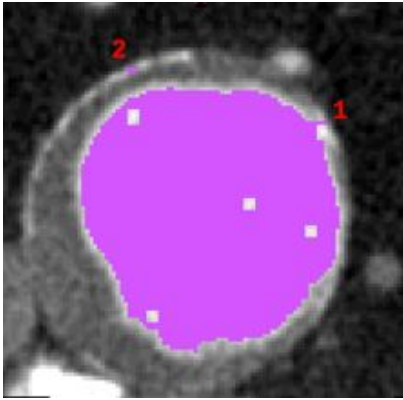


Figure A.2: Manual repair: Only remove sharp spikes (1) or islands (2). Holes within the lumen do not need to be treated.

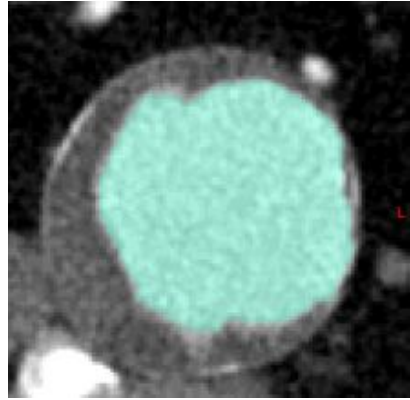


Figure A.3: Example of a final lumen mask (turquoise color).

7. *Morphology Operations*  $\rightarrow$  *Dilate* (1 Pixel)

8. *Morphology Operations*  $\rightarrow$  *Close* (1 Pixel)

9. Check contour and manually repair inaccuracies.

The final lumen mask should then look like Figure A.3.

### A.2.3 Intraluminal Thrombus (ILT)

The 3D ILT geometry will be created by 3D Boolean subtraction of the lumen from the complete 3D geometry (including both lumen and thrombus). A very practical way to get the required mask of the complete AAA geometry is to add the ILT to the lumen mask slice-by-slice. The steps are:

1. Copy the lumen mask.
2. Add ILT to this mask (in Mimics: Use *Multiple Slice Edit*).
3. Check and repair the mask, if applicable.

If calcifications exist, their inner half should be included in the mask and their outer half excluded. In order to avoid stability issues in later FE simulations, lumen mask and the mask of the complete geometry should bifurcate in the same transversal slice as demonstrated in Figure A.4. It should further be verified that ILT beads do not jut into the blood lumen exceedingly. Such situations could lead to numerical instabilities during the FE simulation. This might especially happen at kinks of the aorta or at the AAA shoulder, where the aorta can be tilted towards the AAA sac. The final mask of the complete AAA geometry (lumen and ILT) should look like the example in Figure A.5.

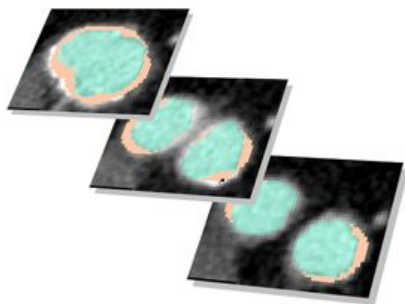


Figure A.4: Lumen and complete geometry masks bifurcate in the same transversal slice.

Table A.1: Calculate 3D settings:

Interpolation Method: Accuracy + Contour
XY-Resolution: 2
<input checked="" type="checkbox"/> Smoothing: Iterations: 3; Factor: 0.7
<input checked="" type="checkbox"/> Shell Reduction: Largest shells: 1
<input checked="" type="checkbox"/> Compensate Shrinkage
<input type="checkbox"/> no Triangle Reduction

Table A.2: Smoothing settings:

(-A-) Smooth:	(-B-) Qual. Pres. Reduce Tris:	(-C-) Remesh → Smooth:
Iterations: 3	Entity: Part	Iterations: 1
Factor: 0.7	Shape quality threshold: 0.5	Factor: 0.7
Use compensation: <input checked="" type="checkbox"/>	Max geometrical error: 0.4	Use compensation: <input type="checkbox"/>
Advanced Options: <input checked="" type="checkbox"/>	Control tri. edge len.: <input checked="" type="checkbox"/>	Advanced Options: <input type="checkbox"/>
Pres. sharp edges: <input type="checkbox"/>	Max edge length: 3.5	Preserve sharp edges: <input type="checkbox"/>
Flip thresh. angle: 30	Iterations: 3	Flip threshold angle: 30
Preserve bad edges: <input type="checkbox"/>	Skip bad edges: <input type="checkbox"/>	Preserve bad edges: <input type="checkbox"/>
	Preserve surface contours: <input type="checkbox"/>	

## A.2.4 3D Reconstruction

When the masks of both lumen and complete AAA geometry are available, one needs to generate the 3D reconstructions. This is done using the Mimics *Calculate 3D* function. The settings for this function are listed in Table A.1. After the 3D reconstruction, the resulting 3D objects have to be checked. If applicable, non-conforming holes or juts can be edited in the masks, whereupon the 3D objects have to be recalculated. The smoothing of the 3D lumen is then performed using the steps (-A-) - (-B-) - (-C-) from Table A.2 and a *Wrap* (Table A.4). After switching off the visibility of the wrapped lumen, the unwrapped lumen is finalized using the steps (-A-) - (-B-) - (-Y-) - (-C-) - (-A-) - (-Z-) (Tables A.2 and A.3). For the complete AAA geometry, the steps (-A-) - (-B-) - (-C-) from Table A.2 are performed. The complete AAA geometry is then unified with the wrapped lumen using the *3D Boolean Union* and finalized using the steps (-A-) - (-B-) - (-Y-) - (-C-) - (-A-) - (-Z-). The contour lines of the final geometries should be checked for accuracy (contour lines should cut the calcifications into halves). After that the 3D geometries should then look like in Figure A.6.

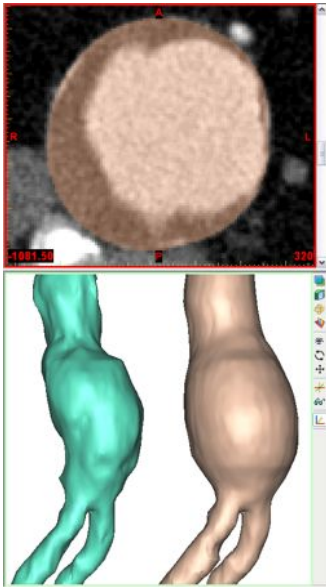


Figure A.5: Top: Mask of complete AAA geometry (lumen and ILT). Bottom: 3D reconstructions of lumen (turquoise) and complete geometry (bronze) before smoothing.

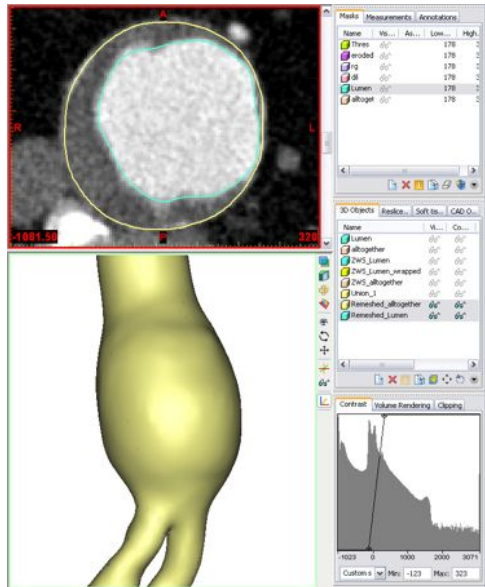


Figure A.6: Top: Contour lines of smoothed lumen and ILT in CT image. Bottom: Final 3D reconstruction of the AAA after application of smoothing algorithms.

### A.2.5 Centerline Calculation, Cutting of the Geometry

Centerlines for both lumen and complete AAA geometry have to be calculated for each AAA (*Fit centerline*  $\rightarrow$  *Resolving Resolution*: 2.0; *Number of Iterations*: 3; *Distance betw. Control Points*: 2.0). The complete AAA geometry is then cut orthogonally at the branching of the renal arteries using the *Cut Centerline Ending*-function and at the common iliac arteries approximately 2 cm distal to the bifurcation. The lumen has to be cut in the same way, but has to stick out at all ends. The ILT geometry is then calculated by a *3D Boolean Subtraction* of the lumen from the complete AAA geometry. To avoid issues during meshing, one should load the ILT into the Mimics Remesh function, separate the inlets and outlets of the ILT to new surfaces and perform step (-Z-) from Table A.3 (it needs to be verified that inlets and outlets did not collapse!). The inlets and outlets should then be flattened using the *Project Mesh*-function. Finally, the 3D geometries of the ILT, lumen and complete geometry have to be exported as binary stl-files (stereolithography format) to the `mcs/`-folder (Figure A.1). Centerlines have to

Table A.3: Fixing settings:

(-Y-) Fixing → Subdivide:		(-Z-) Fixing → Filter Sharp Triangles:	
Entities:	the respective part	Entities:	the respective part
Number of Iterations:	1	Filter distance:	0.5
Large triangles only	<input type="checkbox"/>	Threshold angle:	10
		Filter mode:	Collapse

Table A.4: Wrap settings:

<i>Fixing → Wrap:</i>	
Gap closing distance:	0.3
Smallest detail:	1.5
Protect thin walls	<input type="checkbox"/>
Resulting offset:	0.9
Reduce	<input checked="" type="checkbox"/>
Preserve sharp features	<input type="checkbox"/>
Preserve surface structure	<input type="checkbox"/>

be saved as plain text files without any additional information in the `mcs/`-folder. The raw CT images used for segmentation have to be copied to the `ct/`-folder (Figure A.1).

### A.3 Meshing Protocol

In order to generate FE models of the patient-specific AAAs, the reconstructed geometries have to be meshed. In the current work, the mesh generation is performed using the commercial software Harpoon (Sharc Ltd, Manchester, UK). This software is capable of generating hexahedron-dominant meshes even for irregular geometries. The meshing protocol is outlined in the following:

1. Load the stl-file of the ILT into Harpoon and split the geometry (*Geometry → Separate.. → by Feature*). This should result into exactly five surfaces (four in case of plain lumen). These should be named “TA” (Thrombus Außen), “TI” (Thrombus Innen), “IN”, “OUT1” and “OUT2” (*Geometry → Rename Part*). If there were more or less than five surfaces, the surfaces should be merged again (*Geometry → Merge Parts*). After changing the *Separation Angle* and the *Extraction Angle* in *Preferences → Geometry Preferences...*, the splitting should be repeated until there are exactly five surfaces.
2. Split the lines using *Lines → Separate.. → Line by Region* and delete all lines which do not belong to inlet or outlets. Lines do not need to be renamed.
3. Sort the surface list alphanumerically by clicking on *→ Sort type → alphanumeric* at the bottom-left. (This enables the later usage of a standard boundary condition file and avoids additional user intervention.)

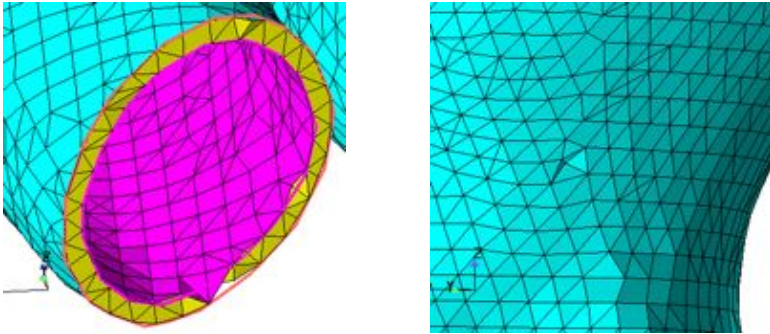


Figure A.7: Small nicks close to the inlet or the outlets are tolerable, as long as there are no gaps. Indentations within ILT regions are also okay.

4. Adjust the mesh settings to:

in <i>Mesh</i> :	
Base Level Size:	0.95 - 1.05
Surface Size:	Level 1
Max Vol Size:	Base Level
Mesh Type:	Hex Dominant
Mesh:	Internal
Expansion:	Fast
Remove Hanging Nodes	<input checked="" type="checkbox"/>

Do not set boundary layers or local refinements. Firstly, try to mesh with *Base Level Size*: 1.0 and check for obvious meshing errors. If there are gaps at the inlet, the outlets, the bifurcation or in areas of thin ILT, the *Base Level Size* can be reduced slightly and the mesh can be recalculated using *Create Mesh* again. Mesh with different *Base Level Sizes* and quickly check for the setting with the best meshing results. This *Base Level Size* should then be used during the next steps. Nicks in the inlet or the outlets and indentations within ILT regions (as shown in Figure A.7) are tolerable.

5. If the mesh has sharp edges at the bifurcation, the stl-geometry (not the mesh!) in this region can be rounded using *Move Nodes*. The geometry in the bifurcation should then look like in Figure A.8. After this it is necessary to recalculate the mesh.
6. Voids at the abluminal surface of the ILT mesh can be fixed by means of *Fix Mesh Cells* → *Add/Del Cells* → *Add Cell (Type: Tet)* (most frequently tetrahedral elements are missing at such sites, see e.g. Figure A.9). This function has to be finalized with *Update Mesh*.
7. The Harpoon-file and the mesh (in Fluent-file format, including surface and volume elements) should be saved in the `mcs/-` folder.
8. Open the Fluent-mesh in Ansys ICEM CFD (ANSYS Inc., Canonsburg, PA, USA). Any tilted surface element of the “TA” next to the inlet or the outlets should be deleted using

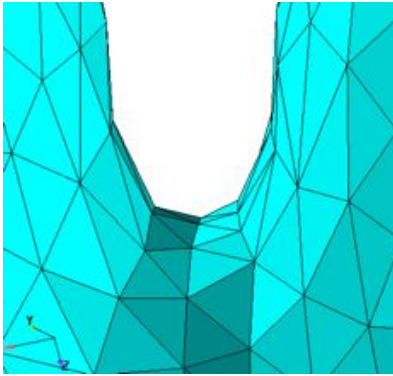


Figure A.8: The stl-triangles in the bifurcation can be arranged using *Move Nodes*. Bad edges should be fixed, while the angle between triangles should be as large as possible.

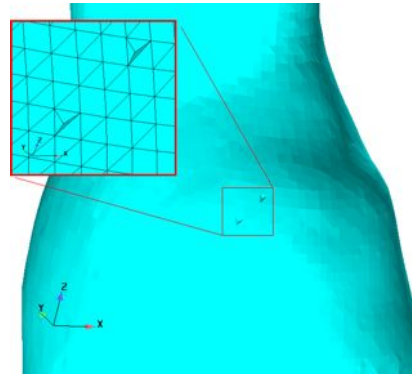


Figure A.9: Missing tetrahedral elements: Such voids can be fixed by means of *Add Cell*.

*Edit Mesh* → *Delete Elements* (Figure A.10). Otherwise, the later wall extrusion onto the “TA” can crash.

9. Define node sets for boundary conditions: *Output* → *Boundary Conditions* → *Exodus-II* → *Surfaces* → *One-sided* → *TA/II/IN/OUT1/OUT2* (repeat for all surfaces) → *Create new* → *Node Set* .
10. Export the mesh as Exodus-file to the `exo/`-folder: *Export Mesh* → *To Exodus* → *Write Exodus input file* → `patientname.prj` → `patientname.uns` → *Output file*: `../exo/patientname` .

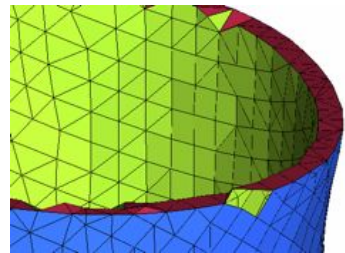
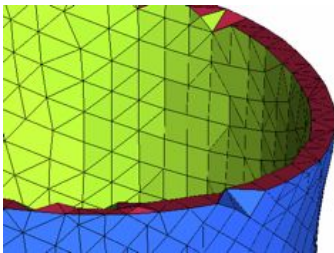


Figure A.10: Tilted surface elements of the “TA” next to the inlet and the outlets have to be deleted without substitution.



# B Appendix: Biomechanics and PET/CT

Table B.1: Clinical patient characteristics, geometrical AAA properties, results from computational analyses and average and maximum SUV (SUVavg and SUVmax) in the sac region for 50 patients with PET/CT scan. Minimum, maximum, mean and sd, and median values are documented at the bottom.

Patient ID	Sex	Age [y]	Max AAA diameter [mm]	Abl_AAA surface [cm <sup>2</sup> ]	Thrombus volume [cm <sup>3</sup> ]	Max wall displacement [mm]	Max vM stress [kPa]	Average vM stress [kPa]	Max vM strain [-]	Average vM strain [-]	SUVavg [-]	SUVmax [-]
1	f	70	68	314	45	0.94	388	235	0.221	0.186	0.821	1.737
2	m	73	54	234	32	0.63	294	189	0.190	0.161	0.698	1.707
3	f	61	63.5	389	46	1.10	447	241	0.224	0.178	0.908	2.061
4	f	84	88.5	570	322	0.87	388	122	0.220	0.104	0.916	1.861
5	m	71	51	196	28	1.01	259	194	0.189	0.165	0.725	1.703
6	f	75	44	275	52	0.60	261	139	0.178	0.131	0.752	1.404
7	m	69	61	396	127	0.82	336	159	0.199	0.142	0.644	1.392
8	m	76	44	348	38	0.76	265	136	0.174	0.127	0.850	1.546
9	f	74	69.5	345	127	0.70	221	72	0.167	0.081	0.731	1.748
10	m	69	68	339	156	0.79	250	122	0.178	0.124	0.736	1.620
11	m	64	46	271	20	0.46	260	99	0.183	0.095	0.924	1.523
12	m	78	43	200	17	0.56	279	176	0.187	0.150	0.825	1.616
13	m	76	52	371	80	0.79	333	170	0.193	0.147	0.812	1.653
14	m	70	52.5	290	7	0.75	360	235	0.211	0.177	0.955	1.909
15	f	60	38	140	17	0.46	205	131	0.158	0.128	0.929	1.431
16	m	62	73	377	137	0.90	340	216	0.208	0.175	0.719	1.488
17	m	68	75.5	557	78	1.42	464	328	0.239	0.214	0.795	1.816
18	f	77	83	614	257	1.14	398	113	0.208	0.104	0.775	1.621
19	m	67	40	128	0	0.41	228	152	0.163	0.141	0.842	1.364
20	f	77	55.5	359	0	0.75	370	220	0.210	0.174	0.774	1.570
21	m	85	63.5	222	39	0.60	311	130	0.194	0.126	0.700	1.151
22	m	59	72	805	233	1.35	497	258	0.227	0.186	0.676	1.743
23	m	76	66	417	0	1.09	542	305	0.235	0.204	0.758	1.913
24	m	56	52.5	209	26	0.60	306	208	0.191	0.171	0.763	1.418
25	m	85	39.5	100	3	0.58	236	132	0.172	0.127	0.704	1.522
26	f	72	40.5	176	41	0.42	146	69	0.132	0.080	0.813	1.269
27	m	65	57	294	69	0.76	347	187	0.209	0.158	0.861	1.768
28	m	69	50.5	222	60	0.67	208	153	0.166	0.143	0.529	1.300
29	f	48	54.5	281	49	0.66	313	189	0.198	0.159	0.703	1.662
30	m	71	58	380	71	0.91	333	219	0.207	0.173	0.627	1.578
31	m	77	52	200	20	0.62	297	188	0.193	0.162	0.761	1.528
32	m	75	50	297	69	0.75	301	145	0.191	0.134	0.680	1.814
33	m	68	51.5	177	17	0.55	244	174	0.180	0.154	0.662	1.187
34	m	68	52.5	296	99	0.58	248	131	0.181	0.125	0.742	1.379
35	m	70	79.5	635	299	1.04	318	163	0.219	0.144	0.724	1.473
36	m	65	47	196	58	0.46	173	69	0.148	0.078	0.696	1.366
37	m	62	50	170	44	0.84	264	129	0.182	0.121	0.698	1.411
38	m	59	59	297	81	0.97	347	217	0.209	0.172	0.673	1.598
39	m	64	56	246	46	0.71	271	197	0.196	0.164	0.709	1.841
40	m	80	67.5	461	171	0.99	331	152	0.202	0.138	0.747	1.439
41	m	70	83	698	335	1.27	414	190	0.233	0.158	0.660	1.514
42	m	69	56	742	191	1.30	455	204	0.222	0.162	0.754	1.675
43	m	60	49.5	295	57	0.55	243	126	0.178	0.124	0.724	1.668
44	m	62	54.6	249	78	0.53	202	104	0.158	0.111	0.812	1.477
45	m	61	63	492	179	1.12	342	135	0.209	0.124	0.758	1.489
46	m	66	51	309	22	0.90	318	150	0.189	0.133	0.904	1.646
47	m	65	49.5	215	29	0.61	306	182	0.197	0.153	0.764	1.513
48	m	83	89	561	351	1.05	243	86	0.180	0.093	0.737	1.667
49	m	72	44.5	160	18	0.50	239	169	0.176	0.150	0.668	1.273
50	m	50	73	370	48	0.87	348	287	0.229	0.209	0.667	1.608
Min		48	38.0	100	0	0.41	146	69	0.132	0.078	0.529	1.151
Max		85	89.0	805	351	1.42	542	328	0.239	0.214	0.955	2.061
Mean		69.1	58.0	336	88	0.79	310	170	0.194	0.145	0.756	1.573
SD		8.25	13.0	165	93	0.25	83	58	0.024	0.032	0.088	0.905
Median		69	54.6	296	50	0.76	306	166	0.193	0.145	0.744	1.574

Table B.2: Overview of spatial correlations of SUV distribution to wall stress, wall strain, displacement, local diameter and local thrombus thickness distribution, respectively. The numbers of positive and negative correlations for each spatially distributed quantity, as well as minimum, maximum, mean and sd, and median values are documented at the bottom.

Patient ID	SUV vs. wall stress distribution	SUV vs. wall strain distribution	SUV vs. displacement distribution	SUV vs. local diameter	SUV vs. local thrombus thickness
1	0.278	0.391	-0.110	-0.102	-0.420
2	0.303	0.294	-0.397	-0.134	-0.456
3	-0.282	-0.302	0.043	0.203	0.392
4	0.389	0.419	-0.071	-0.383	-0.434
5	-0.232	-0.351	-0.200	-0.146	0.351
6	0.195	0.172	-0.150	-0.197	-0.186
7	0.018	-0.010	-0.226	-0.040	-0.095
8	-0.102	-0.170	-0.447	0.083	0.240
9	0.252	0.131	-0.466	0.204	-0.042
10	0.159	0.179	-0.077	0.097	0.170
11	0.258	0.269	0.370	0.226	-0.189
12	0.069	0.062	-0.055	0.039	-0.456
13	-0.248	-0.240	0.051	0.015	0.237
14	0.047	0.095	0.116	0.115	0.237
15	-0.160	-0.102	0.062	0.040	-0.062
16	-0.067	-0.036	0.209	-0.004	0.140
17	-0.117	-0.084	-0.169	-0.250	-0.127
18	0.113	0.057	-0.099	-0.102	-0.136
19	-0.059	-0.047	0.076	0.129	-
20	0.256	0.202	0.185	0.156	-
21	0.166	0.184	0.023	-0.105	-0.066
22	0.154	0.006	-0.169	-0.109	-0.082
23	0.007	-0.189	-0.189	-0.286	-
24	-0.132	-0.092	-0.148	0.077	0.185
25	0.123	0.112	-0.054	-0.022	-0.030
26	0.351	0.339	-0.130	0.012	-0.453
27	0.181	0.205	0.195	0.098	-0.031
28	0.008	-0.109	-0.500	-0.112	0.052
29	0.332	0.270	-0.224	-0.177	-0.389
30	0.035	-0.056	-0.587	-0.266	-0.227
31	0.195	0.045	-0.255	-0.292	-0.369
32	0.051	-0.025	-0.504	-0.209	-0.259
33	0.039	-0.072	-0.340	-0.091	-0.110
34	0.327	0.329	-0.059	0.057	-0.203
35	-0.136	-0.124	-0.154	0.024	0.112
36	0.052	-0.018	-0.084	0.205	0.276
37	-0.198	-0.189	-0.352	-0.027	0.206
38	0.293	0.278	-0.346	-0.116	-0.278
39	-0.044	-0.069	-0.227	-0.081	0.098
40	0.216	0.239	-0.012	0.088	-0.137
41	-0.057	-0.031	-0.173	-0.106	-0.069
42	0.215	0.171	-0.242	-0.198	-0.136
43	0.372	0.351	-0.239	-0.015	-0.283
44	-0.279	-0.292	-0.210	0.060	0.215
45	0.245	0.116	-0.520	-0.026	-0.059
46	0.362	0.367	-0.157	-0.145	-0.283
47	0.203	0.154	-0.138	-0.070	-0.055
48	0.057	0.089	-0.087	0.017	0.046
49	0.199	0.159	0.012	-0.028	-0.253
50	0.015	-0.024	-0.185	-0.089	-0.082
Patients with ...					
... positive correlation.	36	29	11	20	15
... negative correlation.	14	21	39	30	32
Min	-0.282	-0.351	-0.587	-0.383	-0.456
Max	0.389	0.419	0.370	0.226	0.392
Mean	0.088	0.062	-0.148	-0.040	-0.074
SD	0.186	0.193	0.202	0.141	0.228
Median	0.091	0.060	-0.152	-0.028	-0.082



# Bibliography

- [1] M. ABEDIN, Y. TINTUT, L.L. DEMER, *Vascular calcification*, *Arterioscler., Thromb., Vasc. Biol.* **24** (2004) 1161–1170.
- [2] K.G.M.M. ALBERTI, P.Z. ZIMMET, *Definition, diagnosis and classification of diabetes mellitus and its complications. Part 1: Diagnosis and classification of diabetes mellitus. Provisional report of a WHO consultation*, *Diabet. Med.* **15** (1998) 539–553.
- [3] J.H. ASHTON, J.P. VANDE GEEST, B.R. SIMON, D.G. HASKETT, *Compressive mechanical properties of the intraluminal thrombus in abdominal aortic aneurysms and fibrin-based thrombus mimics*, *J. Biomech.* **42** (2009) 197–201.
- [4] M. AUER, T.C. GASSER, *Reconstruction and finite element mesh generation of abdominal aortic aneurysms from computerized tomography angiography data with minimal user interactions*, *IEEE T. Med. Imaging.* **29** (2010) 1022–1028.
- [5] S. BAEK, R.L. GLEASON, K.R. RAJAGOPAL, J.D. HUMPHREY, *Theory of small on large: Potential utility in computations of fluid-solid interactions in arteries*, *Comput. Meth. Appl. Mech. Eng.* **196** (2007) 3070–3078.
- [6] J. BAILAR, D. HOAGLIN, *Medical Uses of Statistics*, John Wiley & Sons, 2012.
- [7] D. BALZANI, *Polyconvex anisotropic energies and modeling of damage applied to arterial walls*, Ph.D. thesis, Technische Universität Darmstadt (2006).
- [8] C.A. BASCIANO, C. KLEINSTREUER, *Invariant-based anisotropic constitutive models of the healthy and aneurysmal abdominal aortic wall*, *J. Biomech. Eng.* **131** (2009) 021009–11.
- [9] D. BEATTIE, C. XU, R. VITO, S. GLAGOV, M.C. WHANG, *Mechanical analysis of heterogeneous, atherosclerotic human aorta*, *J. Biomech. Eng.* **120** (1998) 602–607.
- [10] D.A. BELSLEY, E. KUH, R.E. WELSCH, *Regression diagnostics: Identifying influential data and sources of collinearity*, Wiley, 2004.
- [11] V. BHATTACHARYA, G. STANSBY, *Postgraduate Vascular Surgery: The Candidate's Guide to the FRCS*, Cambridge University Press, 2011.
- [12] J. BIASETTI, F. HUSSAIN, T.C. GASSER, *Blood flow and coherent vortices in the normal and aneurysmal aortas: A fluid dynamical approach to intra-luminal thrombus formation*, *J. R. Soc. Interface* **8** (2011) 1449–1461.
- [13] K.G. BIRUKOV, *Cyclic stretch, reactive oxygen species, and vascular remodeling*, *Antioxid. Redox. Signal.* **11** (2009) 1651–1667.
- [14] J. BOBEL, *Medizintechnik - Verfahren, Systeme, Informationsverarbeitung*, chap. Computertomographie (CT), Springer, Berlin, 2002, pp. 234–254.
- [15] M.K. BODE, Y. SOINI, J. MELKKO, J. SATTA, L. RISTELI, J. RISTELI, *Increased amount of type III pN-collagen in human abdominal aortic aneurysms: Evidence for impaired type III collagen fibrillogenesis*, *J. Vasc. Surg.* **32** (2000) 1201–1207.
- [16] K.A. BOLLEN, R.W. JACKMAN, *Regression diagnostics*, *Sociol. Methods Res.* **13** (1985) 510–542.
- [17] K.A. BOLLEN, R.W. JACKMAN, *Modern methods of data analysis*, vol. 13, chap. Regression diagnostics: An expository treatment of outliers and influential cases, Sage Publications, 1990, pp. 257–291.

- [18] J. BORTZ, C. SCHUSTER, *Statistik für Human- und Sozialwissenschaftler*, Springer-Verlag Berlin Heidelberg New York, 2010.
- [19] K. BOSTRÖM, K.E. WATSON, S. HORN, C. WORTHAM, I.M. HERMAN, L.L. DEMER, *Bone morphogenetic protein expression in human atherosclerotic lesions.*, *J. Clin. Invest.* **91** (1993) 1800–1809.
- [20] M.J. BOWN, G.T. JONES, S. HARRISON, *et al.*, *Abdominal aortic aneurysm is associated with a variant in low-density lipoprotein receptor-related protein 1*, *Am. J. Hum. Gen.* **89** (2011) 619–627.
- [21] M. BREEUWER, S. DE PUTTER, U. KOSE, L. SPEELMAN, K. VISSER, F. GERRITSEN, R. HOOGEVEEN, R. KRAMS, H. VAN DEN BOSCH, J. BUTH, T. GUNTHER, B. WOLTERS, E. VAN DAM, F. VAN DE VOSSE, *Towards patient-specific risk assessment of abdominal aortic aneurysm*, *Med Biol Eng Comp* **46** (2008) 1085–1095.
- [22] J.T. BUTCHER, B.C. BARRETT, R.M. NEREM, *Equibiaxial strain stimulates fibroblastic phenotype shift in smooth muscle cells in an engineered tissue model of the aortic wall*, *Biomaterials* **27** (2006) 5252–5258.
- [23] B. CALVO, E. PEÑA, P. MARTINS, T. MASCARENHAS, M. DOBLARÉ, R.M. NATAL JORGE, A. FERREIRA, *On modelling damage process in vaginal tissue*, *J. Biomech.* **42** (2009) 642–651.
- [24] M. CARMO, L. COLOMBO, A. BRUNO, F.R.M. CORSI, L. RONCORONI, M.S. CUTTIN, F. RADICE, E. MUSSINI, P.G. SETTEMBRINI, *Alteration of elastin, collagen and their cross-links in abdominal aortic aneurysms*, *Eur. J. Vasc. Endovasc. Surg.* **23** (2002) 543–549.
- [25] J. CERVANTES, *Reflections on the 50th anniversary of the first abdominal aortic aneurysm resection*, *World J. Surg.* **27** (2003) 246–248.
- [26] A.H. CHAU, R.C. CHAN, M. SHISHKOV, B. MACNEILL, N. IFTIMIA, G.J. TEARNEY, R.D. KAMM, B.E. BOUMA, M.R. KAAZEMPUR-MOFRAD, *Mechanical analysis of atherosclerotic plaques based on optical coherence tomography*, *Ann. Biomed. Eng.* **32** (2004) 1494–1503.
- [27] E. CHOKE, G. COCKERILL, W.R.W. WILSON, S. SAYED, J. DAWSON, I. LOFTUS, M.M. THOMPSON, *A review of biological factors implicated in abdominal aortic aneurysm rupture*, *Eur. J. Vasc. Endovasc. Surg.* **30** (2005) 227–244.
- [28] CKD-MBD WORK GROUP, *KDIGO clinical practice guideline for the diagnosis, evaluation, prevention, and treatment of chronic kidney disease-mineral and bone disorder (CKD-MBD)*, *Kidney Disease: Improving Global Outcomes (kdigo) CKD-MBD work group.*, *Kidney Int. Suppl.* **113** (2009) 1–130.
- [29] J. COHEN, *Applied multiple regression – correlation analysis for the behavioral sciences*, No. Bd. 1, L. Erlbaum Associates, 2003.
- [30] J.R. COHEN, L.M. GRAVER, *The ruptured abdominal aortic aneurysm of Albert Einstein*, *Surg. Gynecol. Obstet.* **170** (1990) 455–458.
- [31] P.A. COSFORD, G.C. LENG, *Screening for abdominal aortic aneurysm*, *Cochrane Db. Syst. Rev.*
- [32] E.S. CRAWFORD, *The diagnosis and management of aortic dissection*, *JAMA* **264** (1990) 2537–2541.
- [33] K.S. CUNNINGHAM, A.I. GOTLIEB, *The role of shear stress in the pathogenesis of atherosclerosis*, *Lab. Invest.* **85** (2004) 9–23.
- [34] R.C. DARLING, C.R. MESSINA, D.C. BREWSTER, L.W. OTTINGER, *Autopsy study of unoperated abdominal aortic aneurysms*, *Circulation* **54** (1977) 161–164.
- [35] P.F. DAVIES, *Hemodynamic shear stress and the endothelium in cardiovascular pathophysiology*, *Nat. Clin. Pract. Cardiovasc. Med.* **6** (2009) 16–26.
- [36] P.F. DAVIES, J. SPAAN, R. KRAMS, *Shear stress biology of the endothelium*, *Ann. Biomed. Eng.* **33** (2005) 1714–1718–1718.
- [37] S. DE PUTTER, F.N. VAN DE VOSSE, M. BREEUWER, F.A. GERRITSEN, *Local influence of calcifications on the wall mechanics of abdominal aortic aneurysm*, in: *Proc. SPIE*, vol. 6143, SPIE, San Diego, CA, USA, 2006.

- [38] S. DE PUTTER, B.J.B.M. WOLTERS, M.C.M. RUTTEN, M. BREEUWER, F.A. GERRITSEN, F.N. VAN DE VOSSE, *Patient-specific initial wall stress in abdominal aortic aneurysms with a backward incremental method*, J. Biomech. **40** (2007) 1081–1090.
- [39] O.D. DEFAWE, R. HUSTINX, J.O. DEFRAIGNE, R. LIMET, N. SAKALIHASAN, *Distribution of F-18 fluorodeoxyglucose (F-18 FDG) in abdominal aortic aneurysm: High accumulation in macrophages seen on PET imaging and immunohistology*, Clin. Nucl. Med. **30** (2005) 340–341.
- [40] M. DESTRADE, M.D. GILCHRIST, J. MOTHERWAY, J.G. MURPHY, *Slight compressibility and sensitivity to changes in Poisson's ratio*, Int. J. Numer. Meth. Engng **90** (2012) 403–411.
- [41] E. DI MARTINO, S. MANTERO, F. INZOLI, G. MELISSANO, D. ASTORE, R. CHIESA, R. FUMERO, *Biomechanics of abdominal aortic aneurysm in the presence of endoluminal thrombus: Experimental characterisation and structural static computational analysis*, Eur. J. Vasc. Endovasc. Surg. **15** (1998) 290–299.
- [42] S. DOLL, K. SCHWEIZERHOF, *On the development of volumetric strain energy functions*, J. Appl. Mech. **67** (2000) 17–21.
- [43] B.J. DOYLE, A. CALLANAN, T.M. MCGLOUGHLIN, *A comparison of modelling techniques for computing wall stress in abdominal aortic aneurysms*, Biomed. Eng. Online **6** (2007) 38.
- [44] N.R. DRAPER, H. SMITH, *Applied regression analysis*, Wiley, 1998.
- [45] H.H. ECKSTEIN, D. BÖCKLER, I. FLESSENKÄMPER, T. SCHMITZ-RIXEN, S. DEBUS, W. LANG, *Ultrasonographic screening for the detection of abdominal aortic aneurysms*, Dtsch. Arztebl. Int. **106** (2009) 657–663.
- [46] H.H. ECKSTEIN, E. KNIPFER, *Status quo der Gefaesschirurgie*, Der Chirurg **78** (2007) 583–592.
- [47] J. FERRUZZI, D.A. VORP, J.D. HUMPHREY, *On constitutive descriptors of the biaxial mechanical behaviour of human abdominal aorta and aneurysms*, J. R. Soc. Interface **8** (2011) 435–450.
- [48] M.F. FILLINGER, S.P. MARRA, M.L. RAGHAVAN, F.E. KENNEDY, *Prediction of rupture risk in abdominal aortic aneurysm during observation: Wall stress versus diameter*, J. Vasc. Surg. **37** (2003) 724–732.
- [49] M.F. FILLINGER, M.L. RAGHAVAN, S.P. MARRA, J.L. CRONENWETT, F.E. KENNEDY, *In vivo analysis of mechanical wall stress and abdominal aortic aneurysm rupture risk*, J. Vasc. Surg. **36** (2002) 589–597.
- [50] P.J. FLORY, *Thermodynamic relations for high elastic materials*, Trans. Faraday Soc. **57** (1961) 829–838.
- [51] E.J. FOLCO, Y. SHEIKINE, V.Z. ROCHA, T. CHRISTEN, E. SHVARTZ, G.K. SUKHOVA, M.F. DI CARLI, P. LIBBY, *Hypoxia but not inflammation augments glucose uptake in human macrophages: Implications for imaging atherosclerosis with 18fluorine-labeled 2-deoxy-d-glucose positron emission tomography*, J. Am. Coll. Cardiol. **58** (2011) 603–614.
- [52] S.H. FORSDAHL, K. SINGH, S. SOLBERG, B.K. JACOBSEN, *Risk factors for abdominal aortic aneurysms*, Circulation **119** (2009) 2202–2208.
- [53] I. FRANCK, *Biaxiale Messung und Modellierung des anisotropen mechanischen Verhaltens der Aortenwand vom Schwein*, Semesterarbeit, Lehrstuhl für Numerische Mechanik, Technische Universität München (2010).
- [54] R. FRINK, HEART RESEARCH FOUNDATION, *Inflammatory atherosclerosis: Characteristics of the injurious agent*, Heart Research Foundation, 2002.
- [55] H. FRITSCH, W. KUEHNEL, *Taschenatlas der Anatomie, Band 2: Innere Organe*, 9th ed., Georg Thieme Verlag Stuttgart, 2005.
- [56] Y.C. FUNG, *Elasticity of soft tissues in simple elongation*, Am. J. Physiol. **213** (1967) 1532–1544.
- [57] Y.C. FUNG, *Biomechanics – Motion, Flow, Stress, and Growth*, Springer New York Berlin Heidelberg, 1990.
- [58] Y.C. FUNG, *Biomechanics – Mechanical Properties of Living Tissues*, second edition ed., Springer-Verlag New York Berlin Heidelberg, 1993.

- [59] M.D. GARDNER, R. SCOTT, *Age- and sex-related reference ranges for eight plasma constituents derived from randomly selected adults in a Scottish new town.*, J. Clin. Pathol. **33** (1980) 380–385.
- [60] M.D. GASBARRO, K. SHIMADA, E.S. DI MARTINO, *Explicit finite element method for in-vivo mechanics of abdominal aortic aneurysm*, Eur. J. Comput. Mech. **16** (2007) 337–363.
- [61] T. GASSER, G. MARTUFI, M. AUER, M. FOLKESSON, J. SWEDENBORG, *Micromechanical characterization of intra-luminal thrombus tissue from abdominal aortic aneurysms*, Ann. Biomed. Eng. **38** (2010) 371–379.
- [62] T.C. GASSER, M. AUER, F. LABRUTO, J. SWEDENBORG, J. ROY, *Biomechanical rupture risk assessment of abdominal aortic aneurysms: Model complexity versus predictability of finite element simulations*, Eur. J. Vasc. Endovasc. Surg. **40** (2010) 176–185.
- [63] T.C. GASSER, G. GÖRGÜLÜ, M. FOLKESSON, J. SWEDENBORG, *Failure properties of intraluminal thrombus in abdominal aortic aneurysm under static and pulsating mechanical loads*, J. Vasc. Surg. **48** (2008) 179–188.
- [64] M.W. GEE, C. FÖRSTER, W.A. WALL, *A computational strategy for prestressing patient specific biomechanical problems under finite deformation*, Int. J. Numer. Meth. Biomed. Engng. **26** (2010) 52–72.
- [65] M.W. GEE, U. KÜTTLER, W.A. WALL, *Truly monolithic algebraic multigrid for fluid–structure interaction*, Int. J. Numer. Meth. Engng. **85** (2011) 987–1016.
- [66] M.W. GEE, C. REEPS, H.H. ECKSTEIN, W.A. WALL, *Prestressing in finite deformation abdominal aortic aneurysm simulation*, J. Biomech. **42** (2009) 1732–1739.
- [67] M.W. GEE, C.H. SIEFERT, J.J. HU, R.S. TUMINARO, M.G. SALA, *ML 5.0 Smoothed Aggregation User's Guide*, Sandia National Laboratories, Albuquerque, NM (Feb 2007).
- [68] M. GÖTTLINGER, *Implementierung einer inhomogenen hyperelastischen Konstitutivbeziehung zur Druck-analyse im intraluminalen Thrombus des abdominalen Aortenaneurysmas*, Master's thesis, Lehrstuhl für Numerische Mechanik, Technische Universität München (2010).
- [69] V. GRABHER-MEIER, J. PELISEK, A. MAIER, F. HÄRTL, M. WILHELM, J. BIEHLER, S. KEHL, E. MAT-  
EVOSSIAN, M.W. GEE, W.A. WALL, H.H. ECKSTEIN, C. REEPS, *Genexpression und mechanische  
Materialeigenschaften der Aneurysmawand beim AAA*, in: submitted to 28. Jahrestagung der Deutschen  
Gesellschaft für Gefäßchirurgie und Gefäßmedizin, 2012.
- [70] M. GRÆBE, S.F. PEDERSEN, L. BORGWARDT, L. HØJGAARD, H. SILLESEN, A. KJÆR, *Molecular  
pathology in vulnerable carotid plaques: Correlation with [18F]-fluorodeoxyglucose positron emission to-  
mography (FDG-PET)*, Eur. J. Vasc. Endovasc. Surg. **37** (2009) 714–721.
- [71] R.M. GREENHALGH, *Comparison of endovascular aneurysm repair with open repair in patients with ab-  
dominal aortic aneurysm (EVAR trial 1), 30-day operative mortality results: Randomised controlled trial*,  
The Lancet **364** (2004) 843–848.
- [72] A.P. GUÉRIN, B. PANNIER, F. MÉTIVIER, S.J. MARCHAIS, G.M. LONDON, *Assessment and significance  
of arterial stiffness in patients with chronic kidney disease*, Curr. Opin. Nephrol. Hy. **17** (2008) 635–641.
- [73] T.M. GUEST, G. VLASTOS, F.M.F. ALAMEDDINE, W.R. TAYLOR, *Mechanoregulation of monocyte  
chemoattractant protein-1 expression in rat vascular smooth muscle cells*, Antioxid. Redox. Signal. **8** (2006)  
1461–1471.
- [74] GUIDELINES SUBCOMMITTEE, *1999 World Health Organization-International Society of Hypertension  
guidelines for the management of hypertension*, J. Hypertens. **17** (1999) 151–183.
- [75] V. GUPTA, K.J. GRANDE-ALLEN, *Effects of static and cyclic loading in regulating extracellular matrix  
synthesis by cardiovascular cells*, Cardiovasc. Res. **72** (2006) 375–383.
- [76] J.D. HAMILTON, M. KUMARAVEL, M.L. CENSULLO, A.M. COHEN, D.S. KIEVLAN, O.C. WEST, *Mul-  
tidetector CT evaluation of active extravasation in blunt abdominal and pelvic trauma patients*, Radiograph-  
ics **28** (2008) 1603–1616.

- [77] C. HANNICH, *Automatisierte inverse Finite Element Analyse zur Materialparameterbestimmung von aneurysmatischen Aortenwandproben im einachsigen Zugversuch*, Semesterarbeit, Lehrstuhl für Numerische Mechanik, Technische Universität München (2011).
- [78] C.M. HE, M.R. ROACH, *The composition and mechanical properties of abdominal aortic aneurysms*, *J. Vasc. Surg.* **20** (1994) 6–13.
- [79] P. HEIDER, O. WOLF, C. REEPS, M. HANKE, A. ZIMMERMANN, H. BERGER, H.H. ECKSTEIN, *Aneurysmen und Dissektionen der thorakalen und abdominellen Aorta*, *Der Chirurg* **78** (2007) 600–610.
- [80] W. HEINDEL, O. SCHOBER, *PET-CT Hybrid Imaging*, Georg Thieme Verlag Stuttgart New York, 2010.
- [81] F.A.M.V.I. HELLENTHAL, W.A. BUURMAN, W.K.W.H. WODZIG, G.W.H. SCHURINK, *Biomarkers of AAA progression. Part 1: Extracellular matrix degeneration*, *Nat. Rev. Cardiol.* **6** (2009) 464–474.
- [82] M.S. HENG, M.J. FAGAN, J.W. COLLIER, G. DESAI, P.T. MCCOLLUM, I.C. CHETTER, *Peak wall stress measurement in elective and acute abdominal aortic aneurysms*, *J. Vasc. Surg.* **47** (2008) 17–22.
- [83] J.W. HINNEN, O.H.J. KONING, M.J.T. VISSER, H.J. VAN BOCKEL, *Effect of intraluminal thrombus on pressure transmission in the abdominal aortic aneurysm*, *J. Vasc. Surg.* **42** (2005) 1176–1182.
- [84] J.W. HINNEN, O.H.J. KONING, E. VLAANDEREN, J.H. VAN BOCKEL, J.F. HAMMING, *Aneurysm sac pressure monitoring: Effect of pulsatile motion of the pressure sensor on the interpretation of measurements*, *J. Endovasc. Ther.* **13** (2006) 145–151.
- [85] J.W. HINNEN, D.J. RIXEN, O.H. KONING, H.J. VAN BOCKEL, J.F. HAMMING, *Aneurysm sac pressure monitoring: Does the direction of pressure measurement matter in fibrinous thrombus?*, *J. Vasc. Surg.* **45** (2007) 812–816.
- [86] J.W. HINNEN, D.J. RIXEN, O.H.J. KONING, J.H. VAN BOCKEL, J.F. HAMMING, *Development of fibrinous thrombus analogue for in-vitro abdominal aortic aneurysm studies*, *J. Biomech.* **40** (2007) 289–295.
- [87] J.W. HINNEN, M.J.T. VISSER, J.H. VAN BOCKEL, *Aneurysm sac pressure monitoring: Effect of technique on interpretation of measurements*, *Eur. J. Vasc. Endovasc. Surg.* **29** (2005) 233–238.
- [88] M. HIRSCHVOGEL, *Implementierung hyperelastischer Konstitutivbeziehungen zur Modellierung heterogen verteilter Kalzifizierungen im abdominellen Aortenaneurysma*, Semesterarbeit, Lehrstuhl für Numerische Mechanik, Technische Universität München (2011).
- [89] G. HOLZAPFEL, T. GASSER, R. OGDEN, *A new constitutive framework for arterial wall mechanics and a comparative study of material models*, *J. Elasticity* **61** (2000) 1–48.
- [90] G.A. HOLZAPFEL, *Nonlinear solid mechanics: A continuum approach for engineering*, John Wiley & Sons, Ltd, Chichester, 2000.
- [91] G.A. HOLZAPFEL, *Collagen: Structure and Mechanics*, chap. Collagen in Arterial Walls: Biomechanical Aspects, Springer New York, 2008, pp. 285–324.
- [92] G.A. HOLZAPFEL, R.W. OGDEN, *On planar biaxial tests for anisotropic nonlinearly elastic solids. a continuum mechanical framework*, *Math. Mech. Solids* **14** (2009) 474–489.
- [93] G.A. HOLZAPFEL, R.W. OGDEN, *Constitutive modelling of arteries*, *Proc. R. Soc. A* **466** (2010) 1551–1597.
- [94] G.A. HOLZAPFEL, G. SOMMER, C.T. GASSER, P. REGITNIG, *Determination of layer-specific mechanical properties of human coronary arteries with nonatherosclerotic intimal thickening and related constitutive modeling*, *Am. J. Physiol. Heart. Circ. Physiol.* **289** (2005) H2048–2058.
- [95] G.A. HOLZAPFEL, G. SOMMER, P. REGITNIG, *Anisotropic mechanical properties of tissue components in human atherosclerotic plaques*, *J. Biomech. Eng.* **126** (2004) 657–665.
- [96] H. HUANG, R. VIRMANI, H. YOUNIS, A.P. BURKE, R.D. KAMM, R.T. LEE, *The impact of calcification on the biomechanical stability of atherosclerotic plaques*, *Circulation* **103** (2001) 1051–1056.
- [97] P.J. HUBER, *Robust statistics*, Wiley-Interscience, 2004.

- [98] J.D. HUMPHREY, *Cardiovascular Solid Mechanics – Cells, Tissues, and Organs*, Springer Verlag New York Berlin Heidelberg, 2002.
- [99] J.D. HUMPHREY, *Mechanisms of arterial remodeling in hypertension: Coupled roles of wall shear and intramural stress*, *Hypertension* **52** (2008) 195–200.
- [100] J.D. HUMPHREY, S.L. DELANGE, *An Introduction to Biomechanics: Solids and Fluids, Analysis and Design*, Springer, 2004.
- [101] J.D. HUMPHREY, G.A. HOLZAPFEL, *Mechanics, mechanobiology, and modeling of human abdominal aorta and aneurysms*, *J. Biomech.* **45** (2012) 805–814.
- [102] J.D. HUMPHREY, K.R. RAJAGOPAL, *A constrained mixture model for arterial adaptations to a sustained step change in blood flow*, *Biomech. Model. Mechanobiol.* **2** (2003) 109–126.
- [103] J.D. HUMPHREY, C.A. TAYLOR, *Intracranial and abdominal aortic aneurysms: Similarities, differences, and need for a new class of computational models*, *Annu. Rev. Biomed. Eng.* **10** (2008) 221–246.
- [104] A. HYHLIK-DÜRR, T. KRIEGER, P. GEISBÜSCH, D. KOTELIS, T. ABLE, D. BÖCKLER, *Reproducibility of deriving parameters of AAA rupture risk from patient-specific 3D finite element models*, *J. Endovasc. Ther.* **18** (2011) 289–298.
- [105] Institut für medizinische und pharmazeutische Prüfungsfragen, Mainz, Germany, *Laborparameter-Tabellen mit Referenzbereichen* (2010).
- [106] F. INZOLI, F. BOSCHETTI, M. ZAPPA, T. LONGO, R. FUMERO, *Biomechanical factors in abdominal aortic aneurysm rupture*, *Eur. J. Vasc. Surg.* **7** (1993) 667–674.
- [107] V.P. JAGADESHAM, D.J.A. SCOTT, S.R. CARDING, *Abdominal aortic aneurysms: An autoimmune disease?*, *Trends Mol. Med.* **14** (2008) 522–529.
- [108] L.C.U. JUNQUEIRA, J. CARNEIRO, *Histologie*, 6th ed., Springer Medizin Verlag Heidelberg, 2005.
- [109] K. KATO, A. NISHIO, N. KATO, H. USAMI, T. FUJIMAKI, T. MUROHARA, *Uptake of 18F-FDG in acute aortic dissection: A determinant of unfavorable outcome*, *J. Nucl. Med.* **51** (2010) 674–681.
- [110] M. KAZI, J. THYBERG, P. RELIGA, J. ROY, P. ERIKSSON, U. HEDIN, J. SWEDENBORG, *Influence of intraluminal thrombus on structural and cellular composition of abdominal aortic aneurysm wall*, *J. Vasc. Surg.* **38** (2003) 1283–1292.
- [111] S. KEHL, *Finite Elemente basierte Fluid-Struktur-Interaktions Simulation einer Aortendissektion*, Master's thesis, Lehrstuhl für Numerische Mechanik, Technische Universität München (2011).
- [112] M. KJAER, S.P. MAGNUSSON, *Collagen: Structure and Mechanics*, chap. Mechanical Adaption and Tissue Remodeling, Springer New York, 2008, pp. 249–268.
- [113] C. KOTZE, A. GROVES, L. MENEZES, R. HARVEY, R. ENDOZO, I. KAYANI, P. ELL, S. YUSUF, *What is the relationship between 18F-FDG aortic aneurysm uptake on PET/CT and future growth rate?*, *Eur. J. Nucl. Med. Mol. Imaging* **38** (2011) 1493–1499.
- [114] C.W. KOTZE, L.J. MENEZES, R. ENDOZO, A.M. GROVES, P.J. ELL, S.W. YUSUF, *Increased metabolic activity in abdominal aortic aneurysm detected by 18F-fluorodeoxyglucose (18F-FDG) positron emission tomography/computed tomography (PET/CT)*, *Eur. J. Vasc. Endovasc. Surg.* **38** (2009) 93–99.
- [115] K. KURPINSKI, J. PARK, R.G. THAKAR, S. LI, *Regulation of vascular smooth muscle cells and mesenchymal stem cells by mechanical strain.*, *Mol. Cell. Biomech.* **3** (2006) 21–34.
- [116] U. KÜTTLER, *Effiziente Lösungsverfahren für Fluid-Struktur-Interaktions-Probleme*, Ph.D. thesis, Technische Universität München (2009).
- [117] U. KÜTTLER, M. GEE, C. FÖRSTER, A. COMERFORD, W.A. WALL, *Coupling strategies for biomedical fluid-structure interaction problems*, *Int. J. Numer. Meth. Biomed. Engng.* **26** (2010) 305–321.

- [118] E. LARSSON, F. LABRUTO, T.C. GASSER, J. SWEDENBORG, R. HULTGREN, *Analysis of aortic wall stress and rupture risk in patients with abdominal aortic aneurysm with a gender perspective*, J. Vasc. Surg. **54** (2011) 295–299.
- [119] S. LAUTERBACH, *Simulation eines abdominalen Aortenaneurysmas unter Einbezug der Körperumgebung*, Semesterarbeit, Lehrstuhl für Numerische Mechanik, Technische Universität München (2010).
- [120] R.T. LEE, A.J. GRODZINSKY, E.H. FRANK, R.D. KAMM, F.J. SCHOEN, *Structure-dependent dynamic mechanical behavior of fibrous caps from human atherosclerotic plaques*, Circulation **83** (1991) 1764–1770.
- [121] S. LEHOUX, F. TRONC, A. TEDGUI, *Mechanisms of blood flow-induced vascular enlargement*, Biorheology **39** (2002) 319–324.
- [122] J. LEUNG, A. WRIGHT, N. CHESHIRE, J. CRANE, S. THOM, A. HUGHES, Y. XU, *Fluid structure interaction of patient specific abdominal aortic aneurysms: A comparison with solid stress models*, Biomed. Eng. Online **5** (2006) 33.
- [123] J.P. LEWIS, *Fast template matching*, in: Vision Interface, 1995.
- [124] Z.Y. LI, U. SADAT, J. U-KING-IM, T.Y. TANG, D.J. BOWDEN, P.D. HAYES, J.H. GILLARD, *Association between aneurysm shoulder stress and abdominal aortic aneurysm expansion / clinical perspective*, Circulation **122** (2010) 1815–1822.
- [125] Z.Y. LI, J. U-KING-IM, T.Y. TANG, E. SOH, T.C. SEE, J.H. GILLARD, *Impact of calcification and intraluminal thrombus on the computed wall stresses of abdominal aortic aneurysm*, J. Vasc. Surg. **47** (2008) 928–935.
- [126] J.S. LINDHOLT, S. VAMMEN, S. JUUL, E.W. HENNEBERG, H. FASTING, *The validity of ultrasonographic scanning as screening method for abdominal aortic aneurysm*, Eur. J. Vasc. Endovasc. Surg. **17** (1999) 472–475.
- [127] H.M. LOREE, A.J. GRODZINSKY, S.Y. PARK, L.J. GIBSON, R.T. LEE, *Static circumferential tangential modulus of human atherosclerotic tissue*, J. Biomech. **27** (1994) 195–204.
- [128] J. LU, X. ZHOU, M. RAGHAVAN, *Inverse method of stress analysis for cerebral aneurysms*, Biomech. Model. Mechanobiol. **7** (2008) 477–486.
- [129] J. LU, X. ZHOU, M.L. RAGHAVAN, *Inverse elastostatic stress analysis in pre-deformed biological structures: Demonstration using abdominal aortic aneurysms*, J. Biomech. **40** (2007) 693–696.
- [130] A. MAIER, M. ESSLER, M.W. GEE, H.H. ECKSTEIN, W.A. WALL, C. REEPS, *Correlation of biomechanics to tissue reaction in aortic aneurysms assessed by finite elements and [18F]-fluorodeoxyglucose-PET/CT*, Int. J. Numer. Meth. Biomed. Engng. **28** (2012) 456–471.
- [131] A. MAIER, M.W. GEE, C. REEPS, H.H. ECKSTEIN, W.A. WALL, *Impact of model complexity on patient specific wall stress analyses of abdominal aortic aneurysms*, in: O. DÖSSEL, W.C. SCHLEGEL (eds.), World Congress on Medical Physics and Biomedical Engineering, September 7–12, 2009, Munich, Germany, vol. 25/IV of IFMBE Proceedings, Springer, 2009.
- [132] A. MAIER, M.W. GEE, C. REEPS, H.H. ECKSTEIN, W.A. WALL, *Impact of calcifications on patient-specific wall stress analysis of abdominal aortic aneurysms*, Biomech. Model. Mechanobiol. **9** (2010) 511–521.
- [133] A. MAIER, M.W. GEE, C. REEPS, J. PONGRATZ, H.H. ECKSTEIN, W.A. WALL, *A comparison of diameter, wall stress, and rupture potential index for abdominal aortic aneurysm rupture risk prediction*, Ann. Biomed. Eng. **38** (2010) 3124–3134.
- [134] A.M. MALEK, S.L. ALPER, S. IZUMO, *Hemodynamic shear stress and its role in atherosclerosis*, JAMA **282** (1999) 2035–2042.
- [135] H.B. MANN, D.R. WHITNEY, *On a test of whether one of two random variables is stochastically larger than the other*, Ann. Math. Statist. **18** (1947) 50–60.

- [136] B.J. MANNING, T. KRISTMUNDSSON, B. SONESSON, T. RESCH, *Abdominal aortic aneurysm diameter: A comparison of ultrasound measurements with those from standard and three-dimensional computed tomography reconstruction*, *J. Vasc. Surg.* **50** (2009) 263–268.
- [137] G. MARINI, A. MAIER, C. REEPS, H.H. ECKSTEIN, W.A. WALL, M.W. GEE, *A continuum description of the damage process in the arterial wall of abdominal aortic aneurysms*, *Int. J. Numer. Meth. Biomed. Engng.* **28** (2012) 87–99.
- [138] S.P. MARRA, C.P. DAGHLIAN, M.F. FILLINGER, F.E. KENNEDY, *Elemental composition, morphology and mechanical properties of calcified deposits obtained from abdominal aortic aneurysms*, *Acta Biomaterialia* **2** (2006) 515–520.
- [139] G. MARTUFI, E.S. DI MARTINO, C.H. AMON, S.C. MULUK, E.A. FINOL, *Three-dimensional geometrical characterization of abdominal aortic aneurysms: Image-based wall thickness distribution*, *J. Biomech. Eng.* **131** (2009) 061015–11.
- [140] H. MASUDA, K. KAWAMURA, T. SUGIYAMA, A. KAMIYA, *Effects of endothelial denudation in flow-induced arterial dilatation.*, *Front. Med. Biol. Eng.* **5** (1993) 57–62.
- [141] M. MATSUSHITA, N. NISHIKIMI, T. SAKURAI, Y. NIMURA, *Relationship between aortic calcification and atherosclerotic disease in patients with abdominal aortic aneurysm.*, *Int. Angiol.* **19** (2000) 276–279.
- [142] M.A.G. MERKX, M. VAN 'T VEER, L. SPEELMAN, M. BREEUWER, J. BUTH, F.N. VAN DE VOSSE, *Importance of initial stress for abdominal aortic aneurysm wall motion: Dynamic MRI validated finite element analysis*, *J. Biomech.* **42** (2009) 2369–2373.
- [143] C.A. MEYER, C. GUIVIER-CURIEN, J.E. MOORE, JR., *Trans-thrombus blood pressure effects in abdominal aortic aneurysms*, *J. Biomech. Eng.* **132** (2010) 071005–7.
- [144] C. MIEHE, *Aspects of the formulation and finite element implementation of large strain isotropic elasticity*, *Int. J. Numer. Meth. Engng.* **37** (1994) 1981–2004.
- [145] P. MOIREAU, N. XIAO, M. ASTORINO, C. FIGUEROA, D. CHAPPELLE, C. TAYLOR, J.F. GERBEAU, *External tissue support and fluid–structure simulation in blood flows*, *Biomech. Model. Mechanobiol.* **11** (2012) 1–18.
- [146] H. MONSTADT, N. KRASOKHA, F. DORN, S. REESE, W. THEISEN, P. MORDASINI, C. BRECKENFELD, J. GRALLA, J. SLOTBOOM, T. LIEBIG, G. SCHROTH, *Mechanical properties of blood clots - a new test method*, in: O. DÖSSEL, W.C. SCHLEGEL (eds.), *World Congress on Medical Physics and Biomedical Engineering*, September 7 - 12, 2009, Munich, Germany, vol. 25/4 of IFMBE Proceedings, Springer Berlin Heidelberg, 2009.
- [147] W.R. MOWER, W.J. QUINONES, S.S. GAMBHIR, *Effect of intraluminal thrombus on abdominal aortic aneurysm wall stress*, *J. Vasc. Surg.* **26** (1997) 602–608.
- [148] K.W. MÜLLER, *Randbedingungen in komplexen hämodynamischen Systemen*, Master's thesis, Lehrstuhl für Numerische Mechanik, Technische Universität München (2009).
- [149] M. MÜLLER, *Chirurgie für Studium un Praxis*, chap. Gefäßchirurgie - arterielle Aneurysmen, Medizinische Verlags- und Informationsdienste, Breisach, 2004/05, pp. 58–61.
- [150] M.I.M. NOBLE, A.J. DRAKE-HOLLAND, H. VINK, *Hypothesis: Arterial glycocalyx dysfunction is the first step in the atherothrombotic process*, *QJM* **101** (2008) 513–518.
- [151] S. OCKERT, D. BOECKLER, J. ALLENBERG, H. SCHUMACHER, *Rupturiertes abdominelles Aortenaneurysma*, *Gefaesschirurgie* **12** (2007) 379–391.
- [152] R.W. OGDEN, *Large deformation isotropic elasticity: On the correlation of theory and experiment for compressible rubberlike solids*, *P. Roy. Soc. Lond. A Mat.* **328** (1972) 567–583.
- [153] R.W. OGDEN, *Elements of the theory of finite elasticity*, in: *Nonlinear Elasticity - Theory and Applications*, Cambridge University Press, 2001.

- [154] R. OKAMOTO, J. WAGENSEIL, W. DELONG, S. PETERSON, N. KOUCHOUKOS, T. SUNDT, *Mechanical properties of dilated human ascending aorta*, Ann. Biomed. Eng. **30** (2002) 624–635.
- [155] E.A. OSBORN, F.A. JAFFER, *The year in molecular imaging*, J. Am. Coll. Cardiol. Img. **2** (2009) 97–113.
- [156] J. PELISEK, A. ASSADIAN, O. SARKAR, H. ECKSTEIN, H. FRANK, *Carotid plaque composition in chronic kidney disease: A retrospective analysis of patients undergoing carotid endarterectomy*, Eur. J. Vasc. Endovasc. Surg. **39** (2010) 11–16.
- [157] J. PELISEK, I.N. HAHNTOW, H.H. ECKSTEIN, S. OCKERT, C. REEPS, P. HEIDER, P.B. LUPPA, H. FRANK, *Impact of chronic kidney disease on carotid plaque vulnerability*, J. Vasc. Surg. **54** (2011) 1643–1649.
- [158] G.P. PENNEY, J. WEESE, J.A. LITTLE, P. DESMEDT, D.L.G. HILL, D.J. HAWKES, *A comparison of similarity measures for use in 2-D-3-D medical image registration*, IEEE T. Med. Imaging. **17** (1998) 586–595.
- [159] J.A. PHILLIPPI, S. PASTA, D.A. VORP, *Biomechanics and Mechanobiology of Aneurysms*, vol. 7, chap. Biomechanics and Pathobiology of Aortic Aneurysms, Springer Berlin Heidelberg, 2011, pp. 67–118.
- [160] S. POLZER, T. GASSER, J. SWEDENBORG, J. BURSA, *The impact of intraluminal thrombus failure on the mechanical stress in the wall of abdominal aortic aneurysms*, Eur. J. Vasc. Endovasc. Surg. **41** (2011) 467–473.
- [161] D. PROUDFOOT, C.M. SHANAHAN, *Biology of calcification in vascular cells: Intima versus media*, Herz **26** (2001) 245–251.
- [162] R DEVELOPMENT CORE TEAM, *R: A Language and Environment for Statistical Computing*, R Foundation for Statistical Computing, Vienna, Austria (2008).
- [163] M.L. RAGHAVAN, M.M. HANAOKA, J.A. KRATZBERG, M.D.L. HIGUCHI, E.S. DA SILVA, *Biomechanical failure properties and microstructural content of ruptured and unruptured abdominal aortic aneurysms*, J. Biomech. **44** (2011) 2501–2507.
- [164] M.L. RAGHAVAN, D.A. VORP, *Toward a biomechanical tool to evaluate rupture potential of abdominal aortic aneurysm: Identification of a finite strain constitutive model and evaluation of its applicability*, J. Biomech. **33** (2000) 475–482.
- [165] M.L. RAGHAVAN, M.W. WEBSTER, D.A. VORP, *Ex vivo biomechanical behavior of abdominal aortic aneurysm: Assessment using a new mathematical model*, Ann. Biomed. Eng. **24** (1996) 573–582.
- [166] S.M.K. RAUSCH, C. MARTIN, P.B. BORNEMANN, S. UHLIG, W.A. WALL, *Material model of lung parenchyma based on living precision-cut lung slice testing*, J. Mech. Behav. Biomed. Mater. **4** (2011) 583–592.
- [167] C. REEPS, *Nicht-invasive Evaluation des Aortenaneurysmas*, Habilitationsschrift, Technische Universität München (2011).
- [168] C. REEPS, M. ESSLER, J. PELISEK, S. SEIDL, H.H. ECKSTEIN, B.J. KRAUSE, *Increased 18F-fluorodeoxyglucose uptake in abdominal aortic aneurysms in positron emission/computed tomography is associated with inflammation, aortic wall instability, and acute symptoms*, J. Vasc. Surg. **48** (2008) 417–423.
- [169] C. REEPS, M. GEE, A. MAIER, M. GURDAN, H.H. ECKSTEIN, W.A. WALL, *The impact of model assumptions on results of computational mechanics in abdominal aortic aneurysm*, J. Vasc. Surg. **51** (2010) 679–688.
- [170] C. REEPS, M. GEE, J. PELISEK, A. MAIER, M. GURDAN, W. WALL, M. SCHWAIGER, M. ESSLER, H.H. ECKSTEIN, *Interaction of biomechanics and metabolic activity in abdominal aortic aneurysm wall*, in: O. DÖSSEL, W.C. SCHLEGEL (eds.), World Congress on Medical Physics and Biomedical Engineering, September 7 - 12, 2009, Munich, Germany, vol. 25/IV of IFMBE Proceedings, Springer, 2009.

- [171] C. REEPS, M.W. GEE, A. MAIER, J. PELISEK, M. GURDAN, W.A. WALL, J. MARISS, H.H. ECKSTEIN, M. ESSLER, *Glucose metabolism in the vessel wall correlates with mechanical instability and inflammatory changes in a patient with a growing aneurysm of the abdominal aorta*, *Circ. Cardiovasc. Imaging* **2** (2009) 507–509.
- [172] C. REEPS, V. GRABHER-MEIER, A. MAIER, J. PELISEK, J. BIEHLER, S. KEHL, M.W. GEE, W.A. WALL, H.H. ECKSTEIN, *Biomechanische und CT-morphologische Einflussfaktoren auf den Strukturproteingehalt der Aortenwand beim AAA*, in: *submitted to 28. Jahrestagung der Deutschen Gesellschaft für Gefäßchirurgie und Gefäßmedizin*, 2012.
- [173] C. REEPS, J. PELISEK, R.A. BUNDSCHUH, M. GURDAN, A. ZIMMERMANN, S. OCKERT, M. DOBRITZ, H.H. ECKSTEIN, M. ESSLER, *Imaging of acute and chronic aortic dissection by 18F-FDG PET/CT*, *J. Nucl. Med.* **51** (2010) 686–691.
- [174] P. RISSLAND, Y. ALEMU, S. EINAV, J. RICOTTA, D. BLUESTEIN, *Abdominal aortic aneurysm risk of rupture: Patient-specific FSI simulations using anisotropic model*, *J. Biomech. Eng.* **131** (2009) 031001–10.
- [175] P.J. ROUSSEEUW, A.M. LEROY, *Robust Regression and Outlier Detection*, John Wiley & Sons, Inc., 2003.
- [176] J.P. ROYSTON, *An extension of Shapiro and Wilk's W test for normality to large samples*, *J. Roy. Soc. Stat. C* **31** (1982) 115–124.
- [177] J.H.F. RUDD, K.S. MYERS, S. BANSILAL, J. MACHAC, M. WOODWARD, V. FUSTER, M.E. FARKOUH, Z.A. FAYAD, *Relationships among regional arterial inflammation, calcification, risk factors, and biomarkers / clinical perspective*, *Circ. Cardiovasc. Imaging* **2** (2009) 107–115.
- [178] N. SAKALIHASAN, H.V. DAMME, P. GOMEZ, P. RIGO, C. LAPIERE, B. NUSGENS, R. LIMET, *Positron emission tomography (PET) evaluation of abdominal aortic aneurysm (AAA)*, *Eur. J. Vasc. Endovasc. Surg.* **23** (2002) 431–436.
- [179] N. SAKALIHASAN, R. HUSTINX, R. LIMET, *Contribution of PET scanning to the evaluation of abdominal aortic aneurysm*, *Sem. Vasc. Surg.* **17** (2004) 144–153.
- [180] N. SAKALIHASAN, R. LIMET, O.D. DEFAWE, *Abdominal aortic aneurysm*, *The Lancet* **365** (2005) 1577–1589.
- [181] N. SAKALIHASAN, J.B. MICHEL, *Functional imaging of atherosclerosis to advance vascular biology*, *Eur. J. Vasc. Endovasc. Surg.* **37** (2009) 728–734.
- [182] M.J. SARNAK, *Cardiovascular complications in chronic kidney disease*, *Am. J. Kidney Dis.* **41** (2003) 11–17.
- [183] S. SCHILLER, *Modellierung räumlicher und patientenspezifischer Schwankungen der Gefäßwandeigenschaften beim abdominalen Aortenaneurysma*, Semesterarbeit, Lehrstuhl für Numerische Mechanik, Technische Universität München (2010).
- [184] H. SCHUMACHER, H.H. ECKSTEIN, F. KALLINOWSKI, J.R. ALLENBERG, *Morphometry and classification in abdominal aortic aneurysms: Patient selection for endovascular and open surgery*, *J. Endovasc. Surg.* **4** (1997) 39–44.
- [185] G.W.H. SCHURINK, J.M. VAN BAALEN, M.J.T. VISSER, J.H. VAN BOCKEL, *Thrombus within an aortic aneurysm does not reduce pressure on the aneurysmal wall*, *J. Vasc. Surg.* **31** (2000) 501–506.
- [186] R.A.P. SCOTT, THE MULTICENTRE ANEURYSM SCREENING STUDY GROUP, *The multicentre aneurysm screening study (MASS) into the effect of abdominal aortic aneurysm screening on mortality in men: A randomised controlled trial*, *The Lancet* **360** (2002) 1531–1539.
- [187] R.A.P. SCOTT, P.V. TISI, H.A. ASHTON, D.R. ALLEN, *Abdominal aortic aneurysm rupture rates: A 7-year follow-up of the entire abdominal aortic aneurysm population detected by screening*, *J. Vasc. Surg.* **28** (1998) 124–128.
- [188] S.S. SHAPIRO, M.B. WILK, *An analysis of variance test for normality (complete samples)*, *Biometrika* **52** (1965) 591–611.

- [189] J. SHUM, G. MARTUFI, E. DI MARTINO, C. WASHINGTON, J. GRISAFI, S. MULUK, E. FINOL, *Quantitative assessment of abdominal aortic aneurysm geometry*, Ann. Biomed. Eng. (2010) 1–10.
- [190] C.L. SIEGEL, R.H. COHAN, M. KOROBKIN, M.B. ALPERN, D.L. COURNEYA, R.A. LEDER, *Abdominal aortic aneurysm morphology: CT features in patients with ruptured and nonruptured aneurysms*, Am. J. Roentgenol. **163** (1994) 1123–1129.
- [191] J.C. SIMO, R.L. TAYLOR, *Penalty function formulations for incompressible nonlinear elastostatics*, Comput. Meth. Appl. Mech. Eng. **35** (1982) 107–118.
- [192] J.C. SIMO, R.L. TAYLOR, *Quasi-incompressible finite elasticity in principal stretches. Continuum basis and numerical algorithms*, Comput. Meth. Appl. Mech. Eng. **85** (1991) 273–310.
- [193] D.P. SOKOLIS, H. BOUDOULAS, P.E. KARAYANNACOS, *Assessment of the aortic stress-strain relation in uniaxial tension*, J. Biomech. **35** (2002) 1213–1223.
- [194] B. SONESSON, F. HANSEN, H. STALE, T. LÄNNE, *Compliance and diameter in the human abdominal aorta—The influence of age and sex*, Eur. J. Vasc. Surg. **7** (1993) 690–697.
- [195] L. SPEELMAN, A. BOHRA, E.M.H. BOSBOOM, G.W.H. SCHURINK, F.N. VAN DE VOSSE, M.S. MAKAROUN, D.A. VORP, *Effects of wall calcifications in patient-specific wall stress analyses of abdominal aortic aneurysms*, J. Biomech. Eng. **129** (2007) 105–109.
- [196] L. SPEELMAN, E. BOSBOOM, G. SCHURINK, J. BUTH, M. BREEUWER, M. JACOBS, F. VAN DE VOSSE, *Initial stress and nonlinear material behavior in patient-specific AAA wall stress analysis*, J. Biomech. **42** (2009) 1713–1719.
- [197] L. SPEELMAN, E.M.H. BOSBOOM, G.W.H. SCHURINK, F.A.M.V.I. HELLENTHAL, J. BUTH, M. BREEUWER, M.J. JACOBS, F.N. VAN DE VOSSE, *Patient-specific AAA wall stress analysis: 99-percentile versus peak stress*, Eur. J. Vasc. Endovasc. Surg. **36** (2008) 668–676.
- [198] H. STARY, *Natural history of calcium deposits in atherosclerosis progression and regression*, Z. Kardiol. **89** (2000) S028–S035.
- [199] H.C. STARY, A.B. CHANDLER, R.E. DINSMORE, V. FUSTER, S. GLAGOV, W. INSULL, M.E. ROSENFELD, C.J. SCHWARTZ, W.D. WAGNER, R.W. WISSLER, *A definition of advanced types of atherosclerotic lesions and a histological classification of atherosclerosis: A report from the committee on vascular lesions of the council on arteriosclerosis, american heart association*, Arterioscler., Thromb., Vasc. Biol. **15** (1995) 1512–1531.
- [200] S. SUGITA, T. MATSUMOTO, T. OHASHI, K. KUMAGAI, H. AKIMOTO, K. TABAYASHI, M. SATO, *Evaluation of rupture properties of thoracic aortic aneurysms in a pressure-imposed test for rupture risk estimation*, Cardiovasc. Eng. Technol. **3** (2012) 41–51.
- [201] T. SUSSMAN, K.J. BATHE, *A finite element formulation for nonlinear incompressible elastic and inelastic analysis*, Comput. Struct. **26** (1987) 357–409.
- [202] G. TAUBIN, *Curve and surface smoothing without shrinkage*, in: Computer Vision, 1995. Proceedings., Fifth International Conference on DOI - 10.1109/ICCV.1995.466848, 1995.
- [203] C.A. TAYLOR, C.A. FIGUEROA, *Patient-specific modeling of cardiovascular mechanics*, Annu. Rev. Biomed. Eng. **11** (2009) 109–134.
- [204] THE U.K. SMALL ANEURYSM TRIAL PARTICIPANTS WITH L. C. BROWN, J.T. POWELL, *Risk factors for aneurysm rupture in patients kept under ultrasound surveillance*, Ann. Surg. **230** (1999) 289–297.
- [205] G. THEWS, E. MUTSCHLER, P. VAUPEL, *Anatomie, Physiologie, Pathophysiologie des Menschen*, Wissenschaftliche Verlagsgesellschaft, 1999.
- [206] M.J. THUBRIKAR, F. LABROSSE, J. ROBICSEK, B. AL-SOUDI, M. FOWLER, *Mechanical properties of abdominal aortic aneurysm wall*, Jo. Med. Eng. Technol. **25** (2001) 133–142.
- [207] M. TONELLI, N. WIEBE, B. CULLETON, A. HOUSE, C. RABBAT, M. FOK, F. MCALISTER, A.X. GARG, *Chronic kidney disease and mortality risk: A systematic review*, J. Am. Soc. Nephrol. **17** (2006) 2034–2047.

- [208] J. TONG, T. COHNERT, P. REGITNIG, G.A. HOLZAPFEL, *Effects of age on the elastic properties of the intraluminal thrombus and the thrombus-covered wall in abdominal aortic aneurysms: Biaxial extension behaviour and material modelling*, Eur. J. Vasc. Endovasc. Surg. **42** (2011) 207–219.
- [209] I. TRÜBSWETTER, *Biaxiale Messung der mechanischen Eigenschaften von Schweinearterien*, Master's thesis, Lehrstuhl für Numerische Mechanik, Technische Universität München (2011).
- [210] M. TRUIJERS, H.A.J.M. KURVERS, S.J.H. BREDIE, W.J.G. OYEN, J.D. BLANKENSTEIJN, *In vivo imaging of abdominal aortic aneurysms: Increased FDG uptake suggests inflammation in the aneurysm wall*, J. Endovasc. Ther. **15** (2008) 462–467.
- [211] M. TRUIJERS, J.A. POL, L.J. SCHULTZEKOOL, S.M. VAN STERKENBURG, M.F. FILLINGER, J.D. BLANKENSTEIJN, *Wall stress analysis in small asymptomatic, symptomatic and ruptured abdominal aortic aneurysms*, Eur. J. Vasc. Endovasc. Surg. **33** (2007) 401–407.
- [212] M. TRUIJERS, T. RESCH, J.C. VAN DEN BERG, J.D. BLANKENSTEIJN, L. LÖNN, *Endovascular aneurysm repair: State-of-art imaging techniques for preoperative planning and surveillance*, J. Cardiovasc. Surg. **50** (2009) 423–438.
- [213] R.S. TUMINARO, M. HEROUX, S.A. HUTCHINSON, J.N. SHADID, *Official Aztec User's Guide: Version 2.1*, Sandia National Laboratories, Albuquerque, NM (December 1999).
- [214] R. UNTERHINNINGHOFEN, S. LEY, A. FRYDRYCHOWICZ, M. MARKL, *MRT-basierte tridirektionale Flussbildgebung*, Der Radiologe **47** (2007) 1012–1020.
- [215] S. VALLABHANANI, G. GILLING-SMITH, T. HOW, S. CARTER, J. BRENNAN, P. HARRIS, *Heterogeneity of tensile strength and matrix metalloproteinase activity in the wall of abdominal aortic aneurysms*, J. Endovasc. Ther. **11** (2004) 494–502.
- [216] E. VAN DAM, S. DAMS, G. PETERS, M. RUTTEN, G. SCHURINK, J. BUTH, F. VAN DE VOSSE, *Non-linear viscoelastic behavior of abdominal aortic aneurysm thrombus*, Biomech. Model. Mechanobiol. **7** (2008) 127–137.
- [217] M. VAN 'T VEER, J. BUTH, M. MERKX, P. TONINO, H. VAN DEN BOSCH, N. PIJLS, F. VAN DE VOSSE, *Biomechanical properties of abdominal aortic aneurysms assessed by simultaneously measured pressure and volume changes in humans*, J. Vasc. Surg. **48** (2008) 1401–1407.
- [218] J.P. VANDE GEEST, E.S. DI MARTINO, A. BOHRA, M.S. MAKAROUN, D.A. VORP, *A biomechanics-based rupture potential index for abdominal aortic aneurysm risk assessment*, Ann. N. Y. Acad. Sci. **1085** (2006) 11–21.
- [219] J.P. VANDE GEEST, M.S. SACKS, D.A. VORP, *Age dependency of the biaxial biomechanical behavior of human abdominal aorta*, J. Biomech. Eng. **126** (2004) 815–822.
- [220] J.P. VANDE GEEST, M.S. SACKS, D.A. VORP, *The effects of aneurysm on the biaxial mechanical behavior of human abdominal aorta*, J. Biomech. **39** (2006) 1324–1334.
- [221] J.P. VANDE GEEST, M.S. SACKS, D.A. VORP, *A planar biaxial constitutive relation for the luminal layer of intra-luminal thrombus in abdominal aortic aneurysms*, J. Biomech. **39** (2006) 2347–2354.
- [222] J.P. VANDE GEEST, D.H.J. WANG, S. WISNIEWSKI, M. MAKAROUN, D. VORP, *Towards a noninvasive method for determination of patient-specific wall strength distribution in abdominal aortic aneurysms*, Ann. Biomed. Eng. **34** (2006) 1098–1106.
- [223] J.A. VITA, M. HOLBROOK, J. PALMISANO, S.M. SHENOUDA, W.B. CHUNG, N.M. HAMBURG, B.R. ESKENAZI, L. JOSEPH, O.M. SHAPIRA, *Flow-induced arterial remodeling relates to endothelial function in the human forearm*, Circulation **117** (2008) 3126–3133.
- [224] J. VOLLMER, R. MENCL, H. MÜLLER, *Improved laplacian smoothing of noisy surface meshes*, Computer Graphics Forum **18** (1999) 131–138.
- [225] K.Y. VOLOKH, D.A. VORP, *A model of growth and rupture of abdominal aortic aneurysm*, J. Biomech. **41** (2008) 1015–1021.

- [226] D.A. VORP, P.C. LEE, D.H.J. WANG, M.S. MAKAROUN, E.M. NEMOTO, S. OGAWA, M.W. WEBSTER, *Association of intraluminal thrombus in abdominal aortic aneurysm with local hypoxia and wall weakening*, J. Vasc. Surg. **34** (2001) 291–299.
- [227] D.A. VORP, D.H.J. WANG, M.W. WEBSTER, W.J. FEDERSPIEL, *Effect of intraluminal thrombus thickness and bulge diameter on the oxygen diffusion in abdominal aortic aneurysm*, J. Biomech. Eng. **120** (1998) 579–583.
- [228] W.A. WALL, *Fluid-Struktur-Interaktion mit stabilisierten Finiten Elementen*, Ph.D. thesis, Universität Stuttgart (1999).
- [229] W.A. WALL, M.W. GEE, *Baci: A parallel multiphysics simulation environment*, Tech. rep., Institute for Computational Mechanics, Technische Universität München (2010).
- [230] D.H.J. WANG, M.S. MAKAROUN, M.W. WEBSTER, D.A. VORP, *Mechanical properties and microstructure of intraluminal thrombus from abdominal aortic aneurysm*, J. Biomech. Eng. **123** (2001) 536–539.
- [231] D.H.J. WANG, M.S. MAKAROUN, M.W. WEBSTER, D.A. VORP, *Effect of intraluminal thrombus on wall stress in patient-specific models of abdominal aortic aneurysm*, J. Vasc. Surg. **36** (2002) 598–604.
- [232] P. WATTON, N. HILL, *Evolving mechanical properties of a model of abdominal aortic aneurysm*, Biomech. Model. Mechanobiol. **8** (2009) 25–42.
- [233] J.W. WEISEL, *The mechanical properties of fibrin for basic scientists and clinicians*, Biophys. Chem. **112** (2004) 267–276.
- [234] C. WEISS, *Basiswissen Medizinische Statistik*, Springer, 2010.
- [235] F. WILCOXON, *Individual comparisons by ranking methods*, Biometrics Bulletin **1** (1945) 80–83.
- [236] M. XENOS, S. RAMBHIA, Y. ALEMU, S. EINAV, N. LABROPOULOS, A. TASSIOPOULOS, J. RICOTTA, D. BLUESTEIN, *Patient-based abdominal aortic aneurysm rupture risk prediction with fluid structure interaction modeling*, Ann. Biomed. Eng. **38** (2010) 3323–3337.
- [237] X.Y. XU, A. BORGHI, A. NCHIMI, J. LEUNG, P. GOMEZ, Z. CHENG, J.O. DEFRAIGNE, N. SAKALIHASAN, *High levels of 18F-FDG uptake in aortic aneurysm wall are associated with high wall stress*, Eur. J. Vasc. Endovasc. Surg. **39** (2010) 295–301.
- [238] Z. XU, N. CHEN, M.M. KAMOCCA, E.D. ROSEN, M. ALBER, *A multiscale model of thrombus development*, J. R. Soc. Interface **5** (2008) 705–722.
- [239] S. ZEINALI-DAVARANI, L. RAGUIN, D.A. VORP, S. BAEK, *Identification of in vivo material and geometric parameters of a human aorta: toward patient-specific modeling of abdominal aortic aneurysm*, Biomech. Model. Mechanobiol. **10** (2011) 689–699.
- [240] O.C. ZIENKIEWICZ, R.L. TAYLOR, *The Finite element method: Solid mechanics*, No. 2, Butterworth-Heinemann, 2000.







Verlag  
Dr. Hut

ISBN 978-3-8439-1066-8



"Advances in Computational Mechanics"  
Schriftenreihe des Lehrstuhls für Numerische Mechanik, TUM  
Herausgeber: Wolfgang A. Wall